NOVA SCHOOL OF SCIENCE & TECHNOLOGY

DEPARTMENT OF MATERIALS SCIENCE

LIGHT MANAGEMENT IN PEROVSKITE SOLAR CELLS WITH PHOTONIC STRUCTURES AND LUMINESCENT DOWN-SHIFTING LAYERS

SIRAZUL HAQUE

Master of Science in Electrical and Computer Engineering

DOCTORATE IN ADVANCED MATERIALS AND PROCESSING

NOVA University Lisbon

May, 2022

NOVA SCHOOL OF SCIENCE & TECHNOLOGY

DEPARTAMENT OF MATERIALS SCIENCE

LIGHT MANAGEMENT IN PEROVSKITE SOLAR CELLS WITH PHOTONIC STRUCTURES AND LUMINESCENT DOWN-SHIFTING LAYERS

SIRAZUL HAQUE

Master of Science in Electrical and Computer Engineering

Adviser: Rodrigo Ferrão de Paiva Martins
Full Professor, NOVA University Lisbon

Co-advisers: Maria Rute de Amorim e Sá Ferreira André
Associated Professor with Agregation , University of Aveiro

Manuel João de Moura Dias Mendes
Assistant Professor, NOVA University Lisbon

Examination Committee:

Chair: Luís Manuel Camarinha de Matos
Full Professor, NOVA University Lisbon

Rapporteurs: Maria João de Sousa Brites
Assistant Researcher, National Energy and Geology Laboratory

José Almeida Silva
Investigator, NOVA University Lisbon

Adviser: Rodrigo Ferrão de Paiva Martins
Full Professor, NOVA University Lisbon

Members: Pedro Manuel Parracho Salomé
Assistant Professor (Invited), University of Aveiro

Hugo Manuel Brito Águas
Associate Professor, NOVA University Lisbon

DOCTORATE IN ADVANCED MATERIALS AND PROCESSING

NOVA University Lisbon
May, 2022

Light Management in Perovskite Solar Cells with Photonic Structures and Luminescent Down-Shifting Layers

This thesis is dedicated to my parents, especially my father who passed away last year.

ACKNOWLEDGMENTS

I wanted to take a moment to thank everyone in CENIMAT-CEMOP, Department of Materials Science, NOVA School of Science and Technology, NOVA University of Lisbon, for their help, support and compassion throughout this PhD journey.

I would first like to express my gratitude to my supervisor, Prof. Rodrigo Martins for giving me this incredible opportunity and for his continued support, guidance and encouragement. Thank you so much to my other supervisor, Prof. Manuel Mendes, whose expertise was invaluable in formulating the research questions and methodology. Your insightful supervision and feedback pushed this work to reach the highest level. I would also like to acknowledge my co-supervisor, Prof. Maria Rute from University of Aveiro, for her patience, support and for all the opportunities I was given to advance my research.

I want to specially thank Prof. Elvira Fortunato, for the great deal of support, assistance and guidance that I have received. My appreciation also goes to Prof. Hugo Águas, for his advice and assistance during PhD.

I would like to acknowledge my colleagues (Dr. Christian S. Schuster and Dr. Kezheng Li) from University of York, UK, for their wonderful collaboration. I would particularly like to single out Dr. Christian S. Schuster and I want to thank him, for his guidance and the incredible brainstorming that we had, which resulted a novel work (flagshiped in the journal "Optica") that already reached out to an audience of more than 1 million worldwide.

I would like to thank MSc. Miguel Alexandre and Dr. António Vicente, for all the assistance and the stimulating discussions, which most definitely improved the quality of this work.

I would also like to thank our collaborators from 'Apolo' project, particularly, MSc. Clemens Baretzky and Prof. Uli Würfel from Fraunhofer, Germany, and Dr. Daniele Rossi, Prof. Francesca De Rossi, Prof. Francesca Brunetti and Prof. Matthias Auf der Maur from Tor Vergata, Italy, for their insightful collaboration.

I want to also thank the AdvaMTech PhD coordinator Prof. Teresa Cidade and all the secretaries of CEMOP, CENIMAT and DCM, especially Sara Oliveira and André Fonseca, for their assistance.

There are so many names left to mention here, but I would like to thank and send my gratitude from the bottom of my heart, to all of my friends and collegues, from CEMOP, CENIMAT and FCT-NOVA as well as from outside.

In addition, I would like to thank my parents (Azizul Haque and Rabia Akter) for their endless support, love and encouragement throughout my life. Special thanks to my sister (Chameli) and brothers (Masud, Ripon and Chuton), for their great care. Finally, I could not have completed this dissertation without the support of my wife, MSc. Syeda Rupaly Sultana, who provided stimulating discussions as well as happy distractions to rest my mind outside of my research.

"It is very simple to be happy, but it is very difficult to be simple."

Rabindranath Tagore

ABSTRACT

The path to achieve highly efficient, ultra-thin perovskite solar cells (PSCs) demands the use of advanced optical management techniques that can significantly boost cell absorption, thus offsetting the common losses expected from thinner absorber layers. In our research, we demonstrated unprecedented optical and electrical enhancements in ultrathin PSCs, by exploring and optimizing wave-optical nano/micro structures as well as by cleverly rearranging simple diffractive elements in a quasi-random fashion. Furthermore, the photonic-enhanced thin solar cells designed and studied ultimately support the reduction of material usage in PSC technology, which is especially beneficial to mitigate lead usage, without impacting the device's performance.

We developed and studied two novel photonic concepts, acting in the wave-optics regime, and applied them to PSCs with distinct thicknesses of the perovskite absorber (250-500 nm). Firstly, front-located photonic-structured electron transport layers (ETLs) were studied, demonstrating the best photocurrent improvement relative to unpatterned cells (up to 27% - value close to the fundamental Lambertian limit). Interestingly, these cells also showed a proclivity to protect (by absorbing the UV radiation) the absorber layer, that could play a pivotal role in maintaining PSCs stability. Furthermore, the otherwise lost UV radiation can still be exploited by adding one or more luminescent down-shifting (LDS) layers, that can convert the radiation of lower wavelengths into higher wavelengths (high energy photons are converted to lower energy photons) which can be effectively "trapped" in the cell without degrading the cells' stability. Secondly, PSCs conformally deposited on rather industrially-favorable photonic-structured substrates show also a comparable photocurrent enhancement to the previous structure (up to 25%) including a significant omni-directional optical response for angles up to 70 degrees. By studying the transport properties of these photonic-structured PSCs, it was shown that surface and charge carrier recombination can be offset by the increased optical gains resulting from the light trapping (LT), pointing at power conversion efficiencies (PCE) as high as 30%.

In addition to nano/micro structures, the smart arrangement of 1D grating lines can also show outstanding diffractive properties. We found that, using simple grating structures composed of checkerboard (CB) arrangements, the photocurrent of thin-film silicon cells can be realistically doubled (bulk current enhancement by 125%), thus revealing performance improvements at the level of the most sophisticated LT structures. Via careful optimization, it was shown that these structures can improve photocurrent and PCE by 24.9% and 28.2%, respectively, for ultra-thin PSCs. Furthermore, the CB pattern was shown to provide a crucial encapsulation effect — increasing photostability — by protecting the perovskite layer from harmful UV radiation. Subsequently, absorption and emission profiles of t-U (5000)/Eu^{3+} were used to predict how LDS can be employed to reuse these, otherwise lost, photons. Here, it was shown that 95% of the UV radiation can be effectively blocked and converted to non-harmful energies, thus providing extra stability without significantly compromising performance.

Keywords: Photovoltaics, Photonics, Luminescent Down-Shifting, Perovskite Solar Cells, Coupled Optical and Electrical Modelling.

RESUMO

A estratégia para alcançar células solares de perovskite (PSCs) ultrafinas e ultra eficientes exige o uso de técnicas avançadas de fotónica que permitam aumentar significativamente a absorção das células, compensando assim as perdas que as camadas absorventes mais finas estão sujeitas. Aqui são demonstradas pela primeira vez melhorias óticas e elétricas para PSCs ultrafinas que tiram partido de nano/micro-estruturas óticas e da organização de simples elementos difrativos semi-aleatórios. Além disso, as células solares finas projetadas com as estruturas fotónicas permitem uma menor quantidade de materiais na tecnologia PSC, o que é especialmente benéfico para mitigar o uso de compostos tóxicos (chumbo), sem afetar o desempenho dos dispositivos.

Foram desenvolvidos e estudados dois novos conceitos fotónicos que atuam no regime de ótica ondulatória, e posteriormente aplicados a PSCs com espessuras distintas para a camada de perovskite ativa (250-500 nm). Inicialmente, foram estudadas camadas frontais de transporte de eletrões estruturadas fotonicamente, que possibilitam um ganho expressivo da foto-corrente em relação às células não padronizadas (até 27% - valor próximo do limite Lambertiano fundamental). É interessante verificar que estas células também demostram uma propensão para proteger a camada de perovskite ao absorver parte da radiação UV que incide na célula e que tem um efeito nocivo na manutenção da estabilidade das PSCs. Além disso, esta mesma radiação UV, que é absorvida e maioritariamente perdida como calor, pode ainda ser aproveitada ao adicionar-se uma ou mais camadas luminescentes (LDS), que convertem a radiação UV em comprimentos de onda mais altos (fotões de alta energia são convertidos em fotões de energia mais baixa) que podem ser absorvidos pela célula sem causar foto-degradação. Em segundo lugar, as PSCs conformais com substratos estruturados fotónicos também apresentam um ganho na foto-corrente comparável à arquitetura anterior (até 25%), além de uma resposta ótica omnidirecional significativa para ângulos de incidência até 70 graus. Ao estudar as propriedades de transporte destas PSCs estruturadas fotonicamente, verificou-se que os efeitos adicionais de recombinação à superfície dos portadores de carga

podem ser compensados pelo aumento nos ganhos óticos resultantes do aprisionamento de luz (LT), o que permite apontar para eficiências de conversão de energia (PCE) até 30%.

Além das nano/micro-estruturas desenvolvidas, o arranjo em grelha 1D também apresenta excelentes propriedades difrativas. Descobriu-se que, usando uma grelha simples composta por arranjos axadrezados (CB), a corrente gerada na camada absorsora de células de silício de filme fino pode realisticamente aumentar em 125%. Trata-se de um desempenho equiparável às estruturas de LT mais sofisticadas. Após uma otimização cuidada, foi demonstrado que esse mesmo arranjo CB também permite melhorar a fotocorrente e a PCE em 24.9% e 28.2%, respectivamente, de PSCs ultrafinas. Além disso, o padrão CB pode também desempenhar um papel crucial no encapsulamento, protegendo a camada de perovskite da radiação UV prejudicial e consequentemente aumentando a sua fotoestabilidade. Por fim, os perfis de absorção e emissão de t-U (5000)/Eu^{3+} foram usados para prever como uma camada de LDS pode ser usada para aproveitar a radiação UV para a conversão em eletricidade. Aqui, foi demonstrado que 95% da radiação UV pode ser efetivamente bloqueada e convertida em energias não prejudiciais, proporcionando estabilidade extra sem comprometer o desempenho das células solares.

Palavras chave: Fotovoltaica, Fotónica, Luminescência para Conversão Espetral, Células Solares de Perovskite, Modelação Ótica e Elétrica Acoplada.

CONTENTS

1 INTRODUCTION 6

2 PHOTONIC-STRUCTURED TiO_2 FOR HIGH-EFFICIENCY, FLEXIBLE AND STABLE PEROVSKITE SOLAR CELLS 11

2.1 Introduction 11

2.2 Ray optics analysis 12

2.3 Numerical Method and Simulated Structures 13

2.4 Optimized photonic-enhanced Perovskite solar cells 15

2.4.1 Optimal dome front structures 17

2.4.2 Optimal void front structures 21

2.5 Discussion of results 23

2.6 Conclusions 25

3 DESIGN OF LUMINESCENT DOWN-SHIFTING PROPERTIES FOR PHOTONIC-ENHANCED PEROVSKITE SOLAR CELLS 27

3.1 Introduction 27

3.2 Simulation Method 29

3.3 Results and Discussion 30

3.4 Conclusions 36

4 WAVE-OPTICAL STRUCTURED SUBSTRATES FOR ULTRA-THIN PEROVSKITE SOLAR CELLS 39

4.1 Introduction 39

4.2 Modelling Method 41

4.3 Optimized photonic-structured perovskite solar cells 41

4.3.1 Photonic-enhanced PSCs in superstrate configuration 44
4.3.2 Photonic-enhanced PSCs in substrate configuration 47
4.4 Angle-resolved optical response 50
4.5 Discussion of results 51
4.6 Conclusions 54
5 COUPLED OPTICAL AND ELECTRONIC ANALYSIS OF PHOTONIC PEROVSKITE SOLAR CELLS 56
5.1 Introduction 56
5.2 Methodology and experimental considerations 58
5.3 Results and Discussion 60
5.3.1 Optical Modelling and Wave Optical Physics 60
5.3.2 Electrical Modelling and Device Physics 64
5.4 Conclusions 75
6 CHECKERBOARD LIGHT-TRAPPING STRUCTURES AND DESIGN RULES TO MAXIMIZE ABSORPTION 77
6.1 Introduction 77
6.2 Theoretical considerations 78
6.2.1 Grating lines 78
6.2.2 The photonic domain 79
6.3 Results 80
6.4 Discussion 83
6.4.1 Real-space considerations 83
6.4.2 Fourier-space considerations 85
6.5 Conclusions 87
7 PHOTON SHIFTING AND TRAPPING IN PEROVSKITE SOLAR CELLS FOR IMPROVED EFFICIENCY AND STABILITY 89
7.1 Introduction 89
7.2 Methodology 94
7.3 Results and Discussion 97

7.3.1 Photonic-enhanced PSCs with checkerboard pattern 98
7.3.2 Luminescent down-shifting properties in PSCs..... 103
7.4 Conclusions 110
8 CONCLUSIONS AND FUTURE PERSPECTIVES 111

LIST OF FIGURES

Figure 1: Representation of the relative spectral AM1.5 irradiance of sunlight at sea level.[43] 2

Figure 2: Sketch of different photonic-structured devices analyzed in this work using two different LT approaches, composed of TiO_2 features integrated on the front contact, ETM, of the PSCs coupled with a luminescent down-shifting layer (a), and via a conformal PSCs architecture formed by micro-structuring the substrate prior to the PSC deposition (b), for distinct perovskite thickness (250-500 nm). In c) it is shown the explored test cell with the checkerboard structure over c-Si (1 μm), while d) shows the checkerboard patterned in the TiO_2 in PSCs with a LDS layer over it. 8

Figure 3: Lambertian theoretical analysis of LT in Perovskite solar cells, in the geometrical optics regime. The maximum photocurrent (J_{ph} – solid lines) and J_{ph} enhancement (dashed line) are shown as a function of the Perovskite film thickness, for the case with a Lambertian scattering surface (with LT) relative to a flat surface without LT. The thinner the Perovskite film the lower is the maximum J_{ph} but the higher is the attainable enhancement with LT. The wavelength range considered for the calculations was 300-1000 nm. 13

Figure 4: Sketch of both types of LT structures analyzed in this work, composed of TiO_2 features integrated on the ETM of the PSCs. The PSCs have a substrate-type layer configuration, in which light comes into the devices from the film side. The LT structures consist in a hexagonal array (with pitch *p*) of vertically aligned semi-prolate features with radii R and R_Z, respectively along the in-plane direction and illumination axis. The parameters (R, R_Z, p, t_{TCO}, t_{ETM}) for the structure (a) and the parameters (R, R_Z, *p*, t_{TCO}, t_{LT}, t_{ETM}) for the structure (b) considered for optimization are indicated by the arrows. At normal incidence, light impinges from the top along the spheroids' axis of revolution (z). The rear side of the perovskite is coated with a 150-nm-thick Spiro-OMeTAD layer (HTM) and a 80 nm silver layer (metal contact)..... 14

Figure 5: a,b) Absorption (Abs) spectra attained with the optimized LT structures sketched in Figure 4a, composed of half-spheroidal domes (green lines, row 4 of Table 2), and with the reference cases of a cell with an optimized anti-reflection coating (blue lines, row 3), for Perovskite absorber layers with distinct thickness: a) 250 nm and b) 500 nm. Each graph shows the absorption occurring in Perovskite (solid lines) and the parasitic absorption in the other materials (colored regions above the lines). The inset profiles show the log-scale distribution of the corresponding total generation rate, G, along the xz cross-sectional plane of the structures passing by the spheroid center. c,d) Log-scale distributions of the absorption density, p_{ABS}, along the same xz plane of the structures, at the wavelengths of the peaks marked by the arrows in a) and b) respectively for the half-spheroids array on the 250 nm (c) and 500 nm (d) thick Perovskite absorbers. 19
Figure 6: Same as Figure 5 but for the LT structures sketched in Figure 4b, composed of semi-spheroidal voids in the TiO_2 film. a,b) Absorption (Abs) spectra attained with the optimized LT structures (green lines, row 5 of Table 2), and with the planar reference ARC cases (blue lines, row 3), for Perovskite layers with a) 250 nm and b) 500 nm thickness. Each graph shows the absorption occurring in Perovskite (solid lines) and the parasitic absorption in the other materials (colored regions above the lines). The inset profiles show the log-scale distribution of the corresponding generation rate, G, along the xz cross-sectional plane of the structures. c,d) Log-scale distributions of the absorption density, p_{ABS}, along the same plane, at the wavelengths of the peaks marked by the triangles in a) and b) respectively for the voids array on the 250 nm (c) and 500 nm (d) thick Perovskite. 22
Figure 7: Photocurrent enhancements attained with the optimized photonic structures (last 2 rows of Table 2) analyzed in section 4, relative to the planar double-layer ARC references (row 2 of Table 2). The absolute J_{ph} values were calculated by integrating the spectral absorption (eq. 2) in the UV-VIS-NIR wavelength range (300-1000 nm – with UV) and only in the VIS-NIR (400-1000 nm – without UV), for both Perovskite thicknesses (250 and 500 nm) analyzed in this work. 24
Figure 8: Schematic of the solar cell structures considered in the simulations. a) PC - Cell with planar structure used as reference, composed by the layers: Metal contact (Ag)/Hole Transport Layer (HTL, made of Spiro-OMeTAD)/Absorber (Perovskite)/ Electron Transport Layer (ETL, made of TiO_2), Transparent conductive oxide (TCO, made of ITO). b) LTC - cell with light trapping structures integrated in the n-contact (ETL) of the PSC. c) Plot illustrating the method used to emulate the process of down-shifting. In dashed green is the gaussian profile, in blue is the absorbed flux and in red is the emitted flux; d) schematic depicting the process of down-shifting by an LDS material. 29

Figure 9*:* Results for the PCs structure with $n_{Background}$ of 1.5. a) and b) are the absorption profiles calculated for the PCs with perovskite thickness of 250 and 500 nm, respectively. The black curve corresponds to the light absorption in the perovskite layer; in red, the perovskite+TiO_2 absorption; and, in green, the total absorption of the cell. The inset plots represent the absorbed power density through the cross section of the cell, calculated at specific wavelengths indicated by the arrows: the leftmost profile is the absorbed power for 350 nm and the rightmost graph is the absorbed power for 900 nm; c) and d) are the contour plots of the photocurrent density (J_{ph}) sweeps performed for the PC structure with 250 nm and 500 nm perovskite layer, respectively; the white contour line represents the pristine J_{ph}, i.e. the value attained with the AM1.5 incidence spectrum without any shifting. e) and f) are examples of the carrier generation profiles for the PC with 500 nm perovskite layer, considering the pristine and the optimized (using the λ_C and $\Delta\lambda$ corresponding to the maximum in d)) incidence spectrum, respectively. 32

Figure 10: Results for the LTCs with $n_{Background}$ of 1.5. a) and b) are the absorption profiles calculated for the LTCs perovskite thickness of 250 and 500 nm, respectively. The black curve corresponds to the light absorption in the perovskite layer; in red, the perovskite+TiO_2 absorption; and, in green, the total absorption of the cell. The inset plots represent the absorbed power density through the cross section of the cell, calculated at specific wavelengths indicated by the arrows: the leftmost profile is the absorbed power for 350 nm and the rightmost graphs is the absorbed power for 900 nm. c) and d) are the contour plots of the J_{ph} sweeps performed for the LTC structure with 250 nm and 500 nm perovskite layer, respectively; the thicker contour line represents the pristine J_{ph}, i.e. the value attained with the AM1.5 incidence spectrum without any shifting. e) and f) are examples of the carrier generation profiles for the LTC with 500 nm perovskite layer, considering the pristine and the optimized (using the λ_C and $\Delta\lambda$ corresponding to the maximum in d)) incidence spectrum, respectively..... 34

Figure 11: Bar charts summarizing the results from the photocurrent sweeps attained with the pristine (blue) and optimized (red) spectra incident on the PC and LTC PSCs with either 250 or 500 nm Perovskite thickness. a) J_{ph} values obtained considering the full UV-Visible-NIR wavelength range (300-1000 nm); b) UV photocurrent ($J_{ph\text{-}UV}$) values for wavelengths ranging from 300 to 400 nm. The more transparent bars refer to the devices with 250 nm perovskite thickness, while the others refer to those with 500 nm perovskite thickness. 36

Figure 12: Two types of photonic-patterned substrates were studied and optimized for two types of PSC architectures: the conventional superstrate configuration (a), compatible only with transparent substrates (e.g. flexible polymers as PEN/PET)[121], [170]; and the so-called "inverted" substrate configuration (b) enabling a larger variety of substrates (e.g. flexible

opaque materials as metal sheets)[101], [112], [121]. The LT structures patterned on the substrates are modelled as a hexagonal array (with pitch p) of vertically-aligned semi-prolate features with radii R and R_Z, respectively along the in-plane direction and illumination axis. The PSC layers are conformally deposited over such spheroidal features: a) superstrate-type layer configuration, in which light comes into the devices from the substrate side, composed of transparent conducting oxide (TCO, made of ITO/electron transport layer (ETL, made of SnO_2)/perovskite absorber (methylammonium lead iodide, $CH_3NH_3PbI_3$)/hole transport layer (HTL, made of Spiro-OMeTAD/rear metal contact (made of gold, Au); b) substrate-type layer configuration, in which light comes into the devices from the films' side, composed of TCO (made of ITO)/ETL (made of ZnO)/perovskite ($CH_3NH_3PbI_3$)/HTL (made of NiO_x)/rear contact (Au). 40

Figure 13: a,b) Absorption spectra obtained with the optimized LT structures sketched in Fig. 1a, for PSCs in superstrate configuration (red lines, row 3 of Table 5), compared the reference cases of optically-optimized planar cells (blue lines, row 3), for perovskite layers with distinct thickness: a) 300 nm and b) 500 nm. Each graph presents the absorption occurring in the perovskite (solid lines) and the parasitic absorption in the other materials (dashed lines). The inset profiles represent the log-scale distribution of the corresponding total generation rate, G, along the xz cross-sectional plane of the structures passing by the semi-spheroidal center. c,d) Log-scale distributions of the absorption density, p_{ABS}, along the same xz plane of the structures, at the wavelengths of the peaks marked by the arrows in a) and b), respectively for the PSCs with the 300 nm (c) and 500 nm (d) thick perovskite absorbers in superstrate configuration. 45

Figure 14: Similar to Figure 13 but for the PSCs in substrate configuration sketched in Figure 12b. a,b) Absorption spectra obtained with the optimized LT structures (green lines, row 5 of Table 5), compared with the reference cases of planar cells (grey lines, row 4), for perovskite layers with distinct thickness: a) 300 nm and b) 500 nm. The inset profiles represent the total generation rate, G, along the xz cross-sectional plane of the structures. c,d) Profiles of the absorption density, p_{ABS}, along the same xz plane, at the wavelengths of the peaks marked by the arrows in a) and b). 49

Figure 15: a) Sketch of sunlight illumination of a flexible LT-enhanced PSC. b, c) angle-resolved unpolarized photocurrent density, J_{ph}, given by the average between the current values attained with the TM and TE polarizations, for the two solar cells configurations: superstrate (b) and substrate (c). d) Color plots of the absorption spectra occurring in the 300 and 500 nm PSCs, as a function of the incidence angle, for both TM (top) and TE (bottom) polarization. The dashed brown curve plotted in the graphs corresponds to the angle-resolved photocurrent density obtained for each case (values in the right axes) 51

Figure 16: Improvement in photocurrent density, J_{ph}, achieved with the optimized photonic-structured PSCs (rows of 3 and 5 of Table 5) analyzed in section 3, relative to the planar references, as a function of the incidence angle (θ). The Lambertian limits of LT in PSCs, in the geometrical optics regime, are also indicated for normal incidence ($\theta=0^o$), by the solid and dashed horizontal black lines, respectively for the 300 and 500 nm perovskite absorbers. 52
Figure 17: Spectra of the absorption in the perovskite (top plots) and photocurrent density (J_{ph}, bottom plots) attained with a 20% variation (±10% deviation) in each geometrical parameter [R_Z, R and p, respectively in a), b) and c)], relative to the optimal parameter values (marked by the circles in bottom plots) for the superstrate photonic-enhanced PSC with 300 nm thick Perovskite (row 3 of Table 5, Figure 13a). 54
Figure 18: The photonic-structured substrates were studied and optimized for two types of PSC architectures with different metal contacts (Au, Ag and Ni): the conventional superstrate configuration (Figure 18a, left) in which light enters from the transparent substrate, and the so-called substrate configuration (Figure 18b, right) in which light impinges on the cell side. The LT structures patterned on the substrates are modelled as a hexagonal array (with pitch *p*) of vertically-aligned semi-prolate features with radii *R* and R_Z, respectively along the in-plane direction and illumination axis. The PSC layers are then conformally deposited over such spheroidal structures. Coupled optical and electrical simulations were performed to assess the full optoelectronic response of the solar cells following the process flow shown in b). First, 3D optical (electromagnetic) simulations are carried out using the FDTD solver, incorporating a particle swarm algorithm that optimizes the geometry of the photonic-structured PSCs. This was followed by the electrical simulations, here employing three FVM/FEM solvers for comparison and validation, which take as input the 3D-optically obtained generation profiles (original, raw *G*) from the FDTD solver as well as 3D, 2D or 1D planarized generation profiles resulting from planarizing the original *G* function using a binary matrix (3D-planarized) and further decreasing it to lower dimensions (2D and 1D planarized) when needed. Moreover, the electrical simulations were also carried out considering conceptual homogeneous (i.e. spatially-independent) generation profiles with a fixed value across the absorber region equal to the volume-averaged *G*..... 59
Figure 19: Improvement in photocurrent density (a), J_{PH}, achieved with the optimized photonic-structured PSCs for different cells configurations, metal contacts and distinct perovskite thicknesses (as shown in Table A1 in section of Appendix A2), relative to the planar references as indicated on the horizontal line (a). The profiles represent the total generation rate, *G*, along the xz cross-sectional plane of the structures for all the photonic-structured PSCs studied here (b). 62

Figure 20: Spectra of the absorption in the perovskite and photocurrent density (J_{PH}, dark line) attained with a 20% variation (±10% deviation) in each geometrical parameter (R_Z, R and p), relative to the optimal parameter values marked by the circles in the dark line (indicated in Table A1 of Appendix A2). This is shown for two cases of the photonic-enhanced PSCs with 300 nm thick perovskite layer and metal contact of Ag (*top plots*) or Au (*bottom plots*), in superstrate and substrate configurations, respectively. The white dotted lines qualitatively separate the effects of anti-reflection (stronger influence below ~450 nm wavelength) and guided-mode resonances (stronger influence above ~700 nm wavelength). 63
Figure 21: a) 1D device modelling and comparison with experimental planar flexible PSC with ~300 nm absorber thickness. The modelled JV curve in red considers the effect of an additional series resistance, R_S, to better fit the device response. b) SEM image of the cross-section of the experimentally fabricated PSC on flexible PET substrate..... 66
Figure 22: Comparison of electrical simulations of LT-structured and planar PSC. The 3D current generation profiles of LT (a) and planar (b) cells are shown together with the FVM and FEM simulation mesh. The plots in c,d) and e) represent the corresponding band diagrams for the LT (polarized at 0 and 1.14 V, respectively in c) and d) and planar (at 0 V in e) cells. The 4 curves in the band diagram (c,d,e) represent the conduction band (CB) minimum, quasi-fermi electron (QFermi Electron) and hole (QFermi Hole) levels, and valence band (VB) maximum. The inset images in (c,d,e) show the free electron and hole density used in the electrical simulations. The resulting J-V curves of both planar and LT-structured PSCs are presented in f). 68
Figure 23: Simulated J-V curves of the PSCs with the conventional 500 nm and thinner 300 nm perovskite layers for both superstrate (a) and substrate (b) configurations. The inset tables present the PV quantities of interest for the simulated devices..... 70
Figure 24: a, b) 3D inhomogeneous (original) and 3D homogenous (averaged) generation profiles used to evaluate the electrical PV performance. c, d) represent the radiative recombination profile at the maximum power point (c) within the perovskite absorber, and the band diagram of the structured PSC (d). e) J-V curves of the 1D (e) and 3D (f) device modelling using either the inhomogeneous or homogenous generation profiles, as well as with and without the effect of SRH recombination. 73
Figure 25: Depiction of different arrangements of diffractive elements (photonic domains) in square lattice structures. The rose (left) and zigzag (center) structures are based on the same diffractive element, i.e. a mono-pitched roof, which is rotated 90 degrees four times. The checkerboard structure (right) results from the simplification of the mono-pitched roof as a non-slanted grating line. Since all photonic domains contain one element, the computational unit cell encloses four..... 79

Figure 26: The arrangement of a simple diffractive element (a-e) controls the structural disorder. While periodicity can be disturbed via restructured photonic domains (bottom), this approach does not break mirror symmetry. Superior light-trapping structures repeat a periodic element quasi-randomly (e) or a QR element periodically (f). Whereas the former case offers flexibility in its design, fabrication and modification, the latter relies on accurate replication techniques. Since the unit cell is also the photonic domain of the QR supercell, design (f) from Ref. [85] cannot be generated from the quasi-random arrangement of a periodic element – in contrast to designs (c-e)..... 80
Figure 27: Representation of the checkerboard's photonic domain and computational unit cell (a). The parameter map shows the computed maximum achievable photocurrent density J_{max} as a function of the grating period and domain size (b). The inset shows the test cell with the checkerboard structure over it. The line width is here kept at half the grating period. The red dot marks the optimal parameter set that maximizes the broadband absorption in the 1 µm c-Si layer..... 81
Figure 28: Photocurrent depth profile, i.e. current generation per unit volume as a function of the absorber's depth x, determined by segmenting the total (1 µm) c-Si slab in thin slices with a step size of Δx = 10 nm. All current density profiles are calculated for the AM1.5G solar spectrum. While the current J generated in the surface pattern (0 – 190 nm depth) is equal for the checkerboard, photonic crystal and crossed grating lines, the current in the flat bulk layer (190 - 1000 nm depth) is the same for the checkerboard and supercell design from Ref. [85] Although the highest current is found within the QR supercell's surface texture, it will likely suffer the most from surface recombination effects. 82
Figure 29: Fourier energy spectrum in k-space for a) the QR supercell, b) the checkerboard and c) the crossed lines. For comparison, the energy distribution $ED(k_x,k_y)$ is normalized to the total diffracted intensity, given by the sum of all Fourier components in k-space. Here, each structure covers a 500 µm² area in real space; it is sampled at 5 nm resolution and expressed as a binary data matrix (see Appendix A3). Its Fourier transformation yields the desired Fourier-series components (after shifting the zero-frequency component to the center of the array). For their visualization only, they were appropriately smoothed. 85
Figure 30: The analysis of 84 different surface structures, that are etched 190 nm into a 1 µm thin c-Si slab (listed in Table A5 of Appendix A3), indicates a link between their Fourier-properties (Eq. 6) and the theoretical maximum achievable photocurrent $J_{max} = X \cdot J_{ref}$, with the planar reference J_{ref} =15 mA/cm². Some selected literature proposals are annotated with their references in brackets. For a fair comparison, all Fourier-series are based on the same aperture area of ca. 500 µm², sampled at 5 nm resolution and expressed as a binary data matrix. Although the root-mean-square-error *RMSE* (grey-toned area) implies a forecast that is often

greater than the mean-absolute-percentage-error (4.2%), the correlation coefficient R highlights a strong relationship between X and J_{max}. The mean-absolute-scaled-error (63%) shows that our (red) trendline is almost twice as good as the standard naive model. 87
Figure 31: Operating principles and primary processes and losses occurring in downshifting layers: 1) emission from the optical center (luminophore), 2) Fresnel reflection, 3) surface scattering, 4) waveguide attenuation, 5) transmitted radiation, 6) re-absorption by neighbor centers, 7) non-radiative relaxation, 8) emission within escape cone, and 9) radiation lost through the sides. Image adapted from [272]. 90
Figure 32: Molecular structures of the non-hydrolyzed organic–inorganic hybrid precursor, d-UPTES; and of the (b) $Eu(tta)_3 \cdot 2H_2O$ complex (tta=thenoyltrifluoroacetone). 94
Figure 33: Sketch of the layer architecture of planar (a) and photonic-enhanced (b) PSCs with an LDS encapsulant coating composed of t-U (5000)/Eu^{3+}. An innovative LT design is applied on the front contact of the PSCs (b), consisting of a symmetry-broken Escher-like checkerboard (CB) arrangement patterned in the TiO_2 electron transport layer (ETL). The geometrical parameters (h, w, g, l) for the CB patterns (b) considered for optimization are indicated by the arrows. Two distinct thicknesses (250 and 500 nm) were considered for the perovskite absorbers, which are compared with the corresponding planar reference cells (a, no LT), with and without the LDS layer. The thicknesses of the remaining layers in the PSCs are indicated in Table 10..... 96
Figure 34: a1, a2) Absorption spectra attained with the optimized CB pattern in PSCs, without LDSs layer, and with the reference cases of a cell with double-layer anti-reflection coating, for perovskite absorber layers with distinct thickness: a1) 250 nm and a2) 500 nm. Colors bar shows the absorption in different materials as well as reflection in PSCs with optimized CB pattern and the grey lines depict the absorption that occurred only in perovskite for the reference cases of planar cells without LT. b) Log-scale distributions of the absorption density, p_{ABS}, along the xz plane of the CB arrangement passing by the center of y plane, at the wavelengths of the interested absorption peaks on the 250 nm and 500 nm perovskites. The cumulative photocurrent density was calculated from the absorption profiles for the cells with and without LT present in c). d) illustrates the fast Fourier transform (FFT) analysis of CB patterns in PSC for perovskite thickness 250 nm (d1) and 500 nm (d2). e1) represents the angle-resolved unpolarized photocurrent density, J_{PH} determined for both planar and LT cells with 250 and 500 nm perovskite thickness and e2) shows the photocurrent improvement achieved with LT in respect to planar reference for oblique angles. 101
Figure 35: a, b) show the band diagram for PSC with 250 and 500 nm perovskite thickness and c, d) display the comparison of electrical simulations results of photonic-enhanced and planar PSC. The inset tables show PV performance of electrical simulations of PSCs..... 103

Figure 36: The excitation spectra taken for the t-U (5000)/Eu^{3+} LDS material. 105
Figure 37: a1, a2, a3) shows the optical properties of experimentally developed LDS material, t-U (500)/Eu^{3+}: refractive index (a1), normalized absorption (a2) and normalized emission (a3). b1, b2, b3, b4) illustrating the method used to emulate the process of the down-shifting feature of t-U (500)/Eu^{3+} in PSC. 106
Figure 38: Log-scale distributions of the optical generation profiles, G, along the *xz* plane of the PSC passing by the center of *y* plane for planar references (a) and LT-cells with CB pattern (b), with and without a LDS layer of t-U (500)/Eu^{3+}, for distinct perovskite thickness (250 and 500 nm). c, d) demonstrate the electrical simulation results for planar (c) and photonic-enhanced (d) PSCs with a LDS layer, for 250 and 500 nm perovskite thickness. The inset tables show PV performance of electrical modeling of PSCs. 108
Figure 39: Summary of main results. a) Comparison of the absolute PCE and photocurrent values attained with the planar (without LT) and photonic-enhanced (with LT) PSCs, with and without the LDS layer, for 250 and 500 nm perovskite thicknesses. b) Photocurrent generated only by the UV light, in the wavelength range of 300 to 400 nm, penetrating in the different perovskite absorbers for the planar and photonic-enhanced cells, comparing the results for a normal encapsulant layer (original AM1.5 illumination) and the LDS encapsulant (t-U (5000)/Eu^{3+}) layer (modified illumination spectrum). 109

LIST OF TABLES

Table 1: Overview of main photonic strategies applied in PSCs investigated in the literature [61]. 3
Table 2: Maximum J_{ph} values attained for the optimized LT structures placed on the two distinct PSCs, with 250 or 500 nm Perovskite layer thickness, considered in this work. The geometrical optimization parameters (R, R_Z, p, t_{TCO}, t_{ETM}) and (R, R_Z, p, t_{TCO}, t_{LT}, t_{ETM}), respectively for the Dome and Void structures, are defined in Figure 4. The results are compared with the reference ARC-patterned cases, as well as with the theoretical limits in the regime of geometrical optics attained with a Lambertian scattering surface. 17
Table 3: Summary of the main results from the photocurrent density sweeps performed in this work. $t_{Perovskite}$ represents the perovskite thickness, $n_{Background}$ is the refractive index used for the background medium, pristine J_{ph} is the value using the illumination spectrum without any shifting, optimized J_{ph} is the highest value obtained in the sweeps of Figure 9 and Figure 10, λ_C and $\Delta\lambda$ is the gaussian center and shifting parameter, respectively, corresponding to the maximum photocurrent value obtained in the sweeps. 35
Table 4: Summary of the photocurrent density values, $J_{ph\text{-}UV,}$ calculated only in the UV wavelength range (300-400 nm) for the perovskite layer with the pristine, i.e. the unaltered $AM_{1.5}$ spectrum, and the optimized spectrum, i.e. the spectrum using the optimized down-shifting parameters obtained in the photocurrent sweeps of Figure 9 and Figure 10. 36
Table 5: Highest J_{ph} values obtained for the optimized LT structures for two distinct PSCs, with 300 or 500 nm perovskite layer thicknesses, in two different solar cells configurations, superstrate and substrate-type, considered in this work. The geometrical optimization parameters (R, R_Z, p, t_{ITO}, t_{SnO2}, t_{Spiro}) and (R, R_Z, p, t_{ITO}, t_{ZnO}, t_{NiO}), for the LT structures in superstrate and substrate configurations, respectively, are sketched in Figure 12. The results are compared with the reference cases of planar PSCs having optically-optimized TCO/ETL and HTL thicknesses, as well as with the theoretical limits in the regime of geometrical optics attainable with a Lambertian scattering front surface. 42

Table 6: Main parameters attained by the electrical analysis performed in this sub-section to explore the effects of model dimensionality (3D vs. 1D simulations), the spatial distribution of photo-generation (inhomogeneous vs. homogeneous *G* profiles) and SRH recombination, for the optimized LT-structured PSCs with superstrate configuration, 300 nm perovskite thickness and Au rear contact. 74
Table 7: Recent theoretical proposals for light-trapping in thin-film c-Si solar cells. The crossed grating lines have a 242 nm width. The Light Trapping Efficiency *(LTE)* compares the actual current gain *via* surface structuring to the theoretical current gain *via* Lambertian scattering [228]. It thus aims at assessing the performance of the nanostructure itself, irrespective of the fabrication method and technology used. J_{max} not found in a reference were calculated using the published absorption spectra. 82
Table 8: Potential impact of surface structures on the carrier generation under AM1.5G solar spectrum illumination. All grating lines have a 242 nm width. The filling factor *FF* is defined as the area of the etched regions over the entire area of the unit cell. The surface/bulk current refers to carriers generated within/beyond 190 nm depth. Remarkably, grating lines can enhance the bulk current of a 1 μm thin c-Si slab by 125% *via* the checkerboard arrangement. 83
Table 9: Overview of improvement in PV performance using luminescent down-shifting (LDS) coatings reported in the literature. 91
Table 10: Maximum J_{PH} values obtained for the optimized CB arrangement placed on the two distinct PSCs, for 250 or 500 nm perovskite layer thickness, with and without a LDS layer, considered in this work. The geometrical optimization parameters (*h, w, g, l*) are defined in Figure 33 and the standard thicknesses of the cells' layers (t_{layer}) were fixed in the simulation. The results are compared with the reference ARC-patterned cases, for both with and without a LDS layer. 99

ACRONYMS

AR	Anti-Reflection.
ARC	Anti-Reflection Coating.
BC	Boundary Condition.
CB	Checkerboard
CL	Colloidal Lithography.
CIGS	Copper Indium Gallium Selenide.
CZTS	Copper Zinc Tin Sulfide.
DSL	Down-Shifting Layer.
DTL	Displacement Talbot Lithography.
ED	Energy Distribution.
ETL	Electron Transport Layer.
ETM	Electron Transport Materials.
FDTD	Finite Difference Time Domain.
FEM	Finite Element Method.
FF	Fill Factor.
FFT	Fast Fourier Transform.
FWHM	Full Width at Half Maximum.
FVM	Finite Volume Method.
G Profile	Generation Profile.
HTL	Hole Transport Layer.
HTM	Hole Transport Materials.
ITO	Indium Tin Oxide.
LDS	Luminescent Down-Shifting.
LT	Light Trapping.
LTC	Light Trapping Cells.
Ln	Lanthanide.

NIR	Near Infrared.
NiO	Nickel Oxide.
PC	Planar Cell.
PCE	Power Conversion Efficiency.
PET	Polyethylene Terephthalate.
PEN	Polyethylene Naphthalate.
PI	Polyimide.
PSC	Perovskite Solar Cells.
PSO	Particle Swarm Optimization.
PV	Photovoltaics.
PML	Perfect Matching Layer.
QR	Quasi Random.
RMS	Root Mean Square.
SAF	Surface Area Factor.
TCO	Transparent Conductive Oxide.
TE	Transverse Electric.
TM	Transverse Magnetic.
UV	Ultraviolet.
VIS	Visible.

SYMBOLS

$\mathbf{J_{ph}}$	Photocurrent.
$\mathbf{J_{sc}}$	Short-circuit current.
Voc	Open-circuit voltage.
n	Real part of the refractive index.
k	Imaginary part of the refractive index.
ω	Angular frequency.
e	Electron Charge.
h	Planck constant.
c	Free space light velocity.
$\mathbf{\lvert E \rvert^2}$	Electric field strength.
ε'	Real part of the dielectric permittivity.
ε"	Imaginary part of the dielectric permittivity.
λ	Wavelength.
$\mathbf{P_{ABS}}$	Power absorption density.
$g(\omega)$	Photon absorption rate.
AM1.5	Solar irradiance spectrum on Earth at sea level.
R	Recombination rate.
G	Generation rate.
n/p	Electron/hole carrier density.
ρ	Total charge density.
μ	Mobility.
D	Diffusivity.
V	Electrostatic potential.
E	Electric field.

MOTIVATION AND BACKGROUND

The ever-growing cost-competitiveness of photovoltaic (PV) technology is the main reason behind the recent growth in total global PV installed capacity (increasing from under 50 GW to above 400 GW from 2010 to 2017) [1]–[3]. Crystalline silicon (c-Si) solar cells have been the uncontested market leaders of this technology [2], [4]. However, the need to keep fueling this growth has turned the researchers' attention to other materials and light management techniques, as the sub-optimal absorption of c-Si is an obstacle in a scenario of ever-decreasing material thickness,[5], [6] which is a fundamental factor for low cost and flexible photovoltaics [7], [8]. Therefore, novel materials with excellent optical properties have been studied to achieve lower thickness without imperiling the device's performance.

The class of materials that, in recent years, has stood out from the rest are hybrid organic-inorganic perovskites, as they exhibit direct bandgap,[9]–[11] long carrier diffusion lengths,[12], [13] and high optical absorption coefficient [11], [12], [14]. Perovskite compounds are based on an ABX_3 atomic structure, where A and B are cations of different size and X is an anion [9], [15]. The first is an organic or inorganic ion (methylammonium, $CH_3NH_3^+$; ethylammonium, $CH_3CH_2NH_3^+$; formamidinium, $NH_2CH{=}NH_2^+$, Cs and Rb), the second a divalent metal cation (Ge^{2+}, Sn^{2+} and Pb^{2+}). The last element on the structure, X, is a monovalent halogen anion (F^-, Cl^-, Br^-, I^-) [9], [12], [15].

On the other hand, light trapping using periodic arrays of nanostructures has proven to be an effective method to solve the well-known dichotomy where thicker solar cells are optically favorable and electrically disadvantageous, and conversely for thinner devices, ultimately opening a new window of research possibilities pointing to cost-competitive photovoltaics (PV)[5], [16]–[18]. This method relies on improved anti-reflection and light scattering effects, that can be optimized to significantly enhance broadband light absorption in ultra-thin absorber layers, thereby increasing their power conversion efficiency[7], [19]. This reduction in solar cells thickness (single-junction) also enables several advantages, be it in electronic properties such as increasing open-circuit voltage and carrier collection, or even in other properties like cells' stability and mitigation of hazardous/toxic compounds (e.g. Pb) for the case of perovskite[19]–[25]. Furthermore, it also creates a conducive scenario to improve the performance of ultra-thin and low-cost solar cells for portable electronic devices with higher intrinsic mechanical flexibility[7], [8], [19], [21], [26].

As mentioned, organic-inorganic halide perovskite semiconductors have been extensively researched during the last decade due to their impressive optoelectronic properties[19]. Perovskite solar cells (PSCs) are a promising step in the recent evolution of PV due to their high light absorption coefficient[27], tunable band structure (1 eV-2.5 eV) [28], [29], high charge carrier mobility[30], [31], and low fabrication cost[32]. Based on the aforementioned characteristics, conjoined with a deeper understanding of materials and device interfaces brought out by the vast research in the area of materials science, the power conversion efficiency (PCE) of PSCs saw a rapid improvement, having grown from ~3.8% in 2009 to > 25% in 2021[33]–[38]. However, the progress in PSC technology hitherto has been mainly achieved by optimizing the process techniques of the perovskite and contact layers, as well as the quality of the cells' interfaces[32], [39]–[41].

Nevertheless, keeping a balance between generating and collecting carriers in PSCs remains a major challenge to overcome. In conventional PSCs, a perovskite layer with typically ~500 nm thickness is required to allow sufficient light absorption (hence, photocarrier generation) and maximize PCE. In contrast, thinner (~250 nm) absorber layers can reduce bulk recombination and facilitate carrier collection at the contacts[12]. Concomitantly, the use of less amount of absorber material is also an important means to mitigate the usage of toxic Pb in the perovskite[20]. However, reducing the absorber thickness comes at the expense of increasing the optical losses in PSCs; particularly for the longer sunlight wavelengths in the VIS-NIR range that correspond to a large portion of the solar spectrum (about half, as represented in Figure 1) but require a large travel path inside the absorber to generate photocurrent[42]. Therefore, effective **light trapping (LT)** strategies are crucial to improve performance in ultrathin solar cells, ultimately enabling highly efficient and flexible PSCs[7], [19].

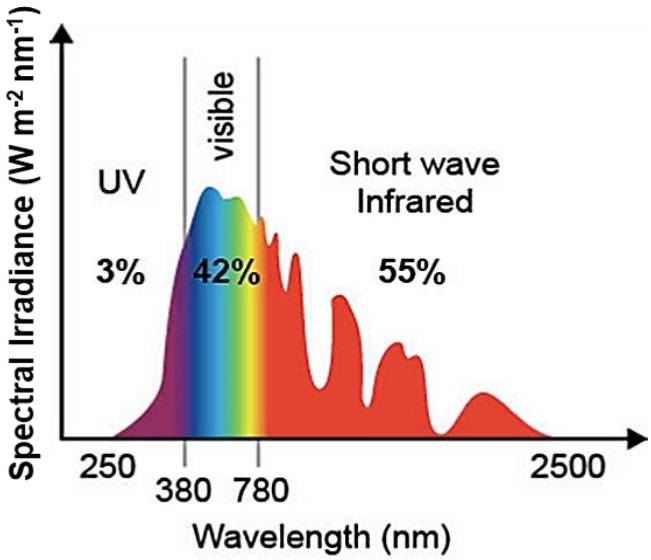

Figure 1: Representation of the relative spectral AM1.5 irradiance of sunlight at sea level.[43]

While silicon-based solar cells have been extensively tested regarding the implementation of advanced LT schemes, their application in PSCs is still in its infancy. This lethargy in LT adoption comes, understandably, from the high absorption properties of these perovskite materials. Regardless, for ultra-thin technology LT methodologies become viable to mitigate non-absorption losses[7], [19], [44]. Different LT approaches have been proposed in the last few years for PSCs, such as a micro lens or nanocone arrays[45]–[47], random pyramids[48], fiber array-based anti-reflection front electrodes[49], nanophotonic front[50] and back electrodes[24], nanophotonic perovskite layers[20], nano- and micro-patterned charge transport layers[51], [52], and corrugated substrates for single[53] and multijunction[54]–[56] PSCs, as well as the exploitation of surface plasmon resonances, e.g.: plasmonic nanoparticles[57]–[59] and light grating-coupled plasmons[59]. Table 1 summarizes the main photonic strategies employed in PSCs presented in the literature. Nonetheless, most of these approaches have yet to demonstrate pronounced absorption improvements that justify the efforts in their integration, or have even caused electrical deterioration of the devices.

Dielectric-based photonic features in the wave-optics regime are currently the most promising nano/micro-structures for light confinement in PV, as they can strongly capture and trap light in distinct absorbing media. For instance, this has allowed the demonstration of up to ~50% photocurrent enhancement in thin-film silicon solar cells [18]. Such a mechanism can be further improved when coupled with luminescent down-shifting materials, providing spectral matching of the impinging light [60].

Table 1: Overview of main photonic strategies applied in PSCs investigated in the literature [61].

No.	Photonic Structure	Location in cell	Initial PCE (%)	Final PCE (%)	PCE Gain (%)	Main Effects discussed	Reference (year)
1	Metal oxide honeycomb	Scaffold layer (ETL)	7.2	9.5	31.9	Lower shunt resistance + enhanced transmission	[62] (2015)
2	Periodic microstructure composite	HTL (Spiro-OMeTAD /P3HT)	14.8	17.7	19.4	Enhanced light-harvesting + increased hole conductivity	[59] (2015)
3	Textured FTO	TCO substrate	12.6	15.2	20.6	Light scattering	[63] (2016)
4	Nanocone patterned plastic substrates	Transparent substrate (PDMS, inside)	8.25	11.29	36.8	Light scattering	[64] (2016)

5	Textured FTO	TCO substrate	10.9	13.3	22.0	Enhanced light absorption and crystal growth	[65] (2017)
6	Whispering-gallery structure	Perovskite layer	15.3	19.8	29.4	Enhanced light-harvesting + improved film quality + carrier extraction	[66] (2018)
7	Diffraction-grating	Perovskite layer	16.7	19.71	18.0	Increased light-harvesting	[67] (2018)
8	Textured ITO	TCO substrate	14.8	18.6	25.7	Anti-reflection + light scattering	[68] (2019)
9	2D photonic crystal nanodisk array	ETL (TiO_2)	15.5	18.70	20.6	Photon confinement + light scattering + improved electron extraction	[69] (2019)
10	Coral-like nanostructures	Perovskite layer	17.2	19.47	13.3	Scattering + accelerated hole extraction	[70] (2019)

In the present work, the candidate has theoretically modelled and optimized wavelength-sized LT structures and luminescent down-shifting (LDS) layers for their unprecedented implementation in perovskite-based solar cells, motivated by recent breakthroughs showing outstanding record efficiencies (~25%) with solution-processed thin-film devices [71].

The main targets were to attain high-efficient (>25%) perovskite solar cells (PSCs) with minimal absorber layer thickness (<300nm) to allow increased flexibility (<1 cm bending radius). This has been pursued via the optimized combination of two promising photonic solutions (see Figure 2): 1) LT with dielectric-based wave-optical structures, and 2) UV-to-Visible spectral matching with down-shifting layers (DSLs). With these objectives, the candidate has been strongly devoted to theoretical simulation work, to provide deeper insight into the luminescent and interference-related wave-optical mechanisms that lead to absorption enhancement in the perovskite absorbers[5], and to determine the optimal parameters of both types of optical structures.

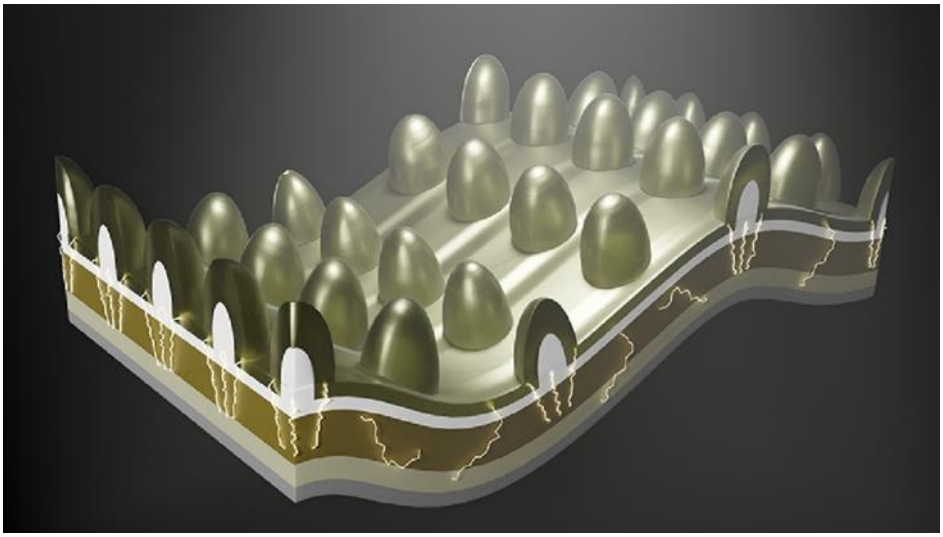

Cover illustration: *Representation of a light management scheme in a photonic-structured perovskite solar cell, which enhances the solar-to-electricity conversion performance of the device while allowing the use of ultra-thin perovskite layers to improve the mechanical flexibility. When fully optimized, wave-optical front structures are capable of effectively collecting and trapping the sunlight in the cell layers. In this way, the photocurrent generated by the devices (hence, their power conversion efficiency) is boosted in a wide spectral and incidence angular range.*

1 INTRODUCTION

Nowadays, photovoltaic (PV) industry is moving towards ultra-thin and low-cost solar cells for consumer-oriented electronic products with high intrinsic mechanical flexibility [7], [8], [72]. To achieve such challenging goal, nano/micro-structured photonic elements in the wave-optics regime are a promising solution, capable of capturing and trapping light within the cells' absorber, thus allowing the reduction of its thickness while boosting power conversion efficiency (PCE).

Recent findings in photonics demonstrated amazing possibilities to manipulate light in ways that greatly exceed traditional geometrical optical limits; for instance, allowing pronounced broadband LT (~50% photocurrent enhancement) within thin-film solar cells and spectral tuning of illumination[73], [74].

Light-trapping (LT) approaches conventionally applied in wafer-based solar cells rely on textured rear/front surfaces which provide: 1) anti-reflection, via geometrical refractive-index matching caused by the front facets, improving the short-wavelength (above absorber bandgap) photocurrent; and 2) light scattering which increases the longer-wavelength (near-bandgap) absorption via optical path-length amplification and coupling with waveguided modes confined within the structure of the cell [73], [74]. However, when applied in thin-film cells, the textures' size must be reduced along with the absorber thickness, which lowers their LT effects[75], [76]. Nonetheless, the main drawback is that texturing increases roughness (hence surface area) and defect density in the PV material, which deteriorates its electrical transport via recombination. Alternative strategies have been investigated, such as: diffraction gratings[77], micro-lenses[78], Mie features[79], [80] and plasmonic nanoparticles[81], [82]. However, many of these approaches also require structuring the PV layers, thus suffering from the same electrical compromise of texturing; and none has yet led to efficiencies superior to those attained with optimized periodic texturing[83].

The work undertaken in this PhD thesis involved key technological advances in the field of photonics for thin-film PV, regarding:

1) Photonic geometries – Novel LT designs have been explored and optimized, composed of semi-spheroidal dome/void arrays in the photonic media, which can provide higher degrees of light capturing/spreading within the absorbers and can be straightforwardly fabricated by high-throughput colloidal-lithographic methods[84]. In addition, while many diffrac-

tive LT structures have proven high absorption enhancements, their industrial application rather depends on simplicity concerning the integration to the solar cell architecture and the process technology. By optimizing smartly-designed 1D crossed-grating structures, composed of checkerboard and/or penta-like arrangements, we have shown that one can achieve photocurrent enhancements similar to the most sophisticated photonic strategies, such as with quasi-random supercell structures [85], in thin-film silicon and perovskite cells, but using much simpler and industrial-friendly geometries.

2) Photonic materials – the LT elements were formed by the same materials typically used in the front contact of the solar cell structures. For instance in PSCs, TiO_2 micro-structures coated with a transparent conductive oxide (TCO) were used. This way, the preferential materials for the devices' performance are maintained, but now their photonic structuring allows them to provide absorption gains while acting as the electron contact.

3) *Combination with down-shifting layers* - the coupling with luminescence down-shifting (LDS) coatings, commonly composed of organic-inorganic ureasils [86]–[93] materials modified by lanthanide ions (Ln^{3+}), was theoretically optimized for implementation on planar and LT-enhanced PSC devices.

4) Industrial-attractive optical schemes - the investigated photonic geometries are compatible with highly-scalable soft-lithographich processes, such as colloidal lithography. In addition, by micro-patterning the substrates with wavelength-sized semi-spheroidal features, it is possible to achieve high-performing LT-enhanced PSCs due to the conformal deposition of the cells' materials onto the photonic substrates, which allows carrying out separately the process of photonic structuring and PSCs fabrication, thus protecting the PSC layers from any damage while fabricating the LT structures[94].

Our wave-optics LT strategy, previously developed for thin-film Si cells[18], [84] and here investigated for thin-film PSCs, is nowadays considered the most effective approach for light management in PV as it can strongly boost absorption, via pronounced anti-reflection and scattering effects, but without affecting the cells' electrical performance (e.g; open circuit voltage, fill factor) [5], [95], [96]. It consists in implementing high-index dielectric (e.g. TiO_2) wavelength-sized features, with semi-spheroidal geometries, on the front surface.

On the other hand, to protect the PSCs from the harmful UV radiation, an encapsulant UV blocking layer has been commonly applied on the devices' front,[19]–[25] albeit compromising PV performance due to inevitable partial shading. Therefore, a preferential solution is the implementation of luminescent down-shifting (LDS) materials via their embedment in a polymeric matrix used as the cell's encapsulant [97]–[99], as these can convert the UV radiation into the non-harmful visible spectrum that penetrates the cell towards the perovskite absorber. Such LT solution, coupled with LDS spectral matching (Figure 2, a), offers best performance improvements and higher stability. Moreover, the conformal architecture (Figure 2, b) provides key technological advantages relative to previous photonic approaches for protecting

the PSCs from degrading during LT structuring process, thereby allowing significant practical benefits regarding its applicability, when compared with post-patterned photonic structures implemented on the front ETLs, since here the PSC layers are wet-coated by usual methods over a substrate already patterned with LT structures, hence making the photonic integration independent of the PSC's fabrication.

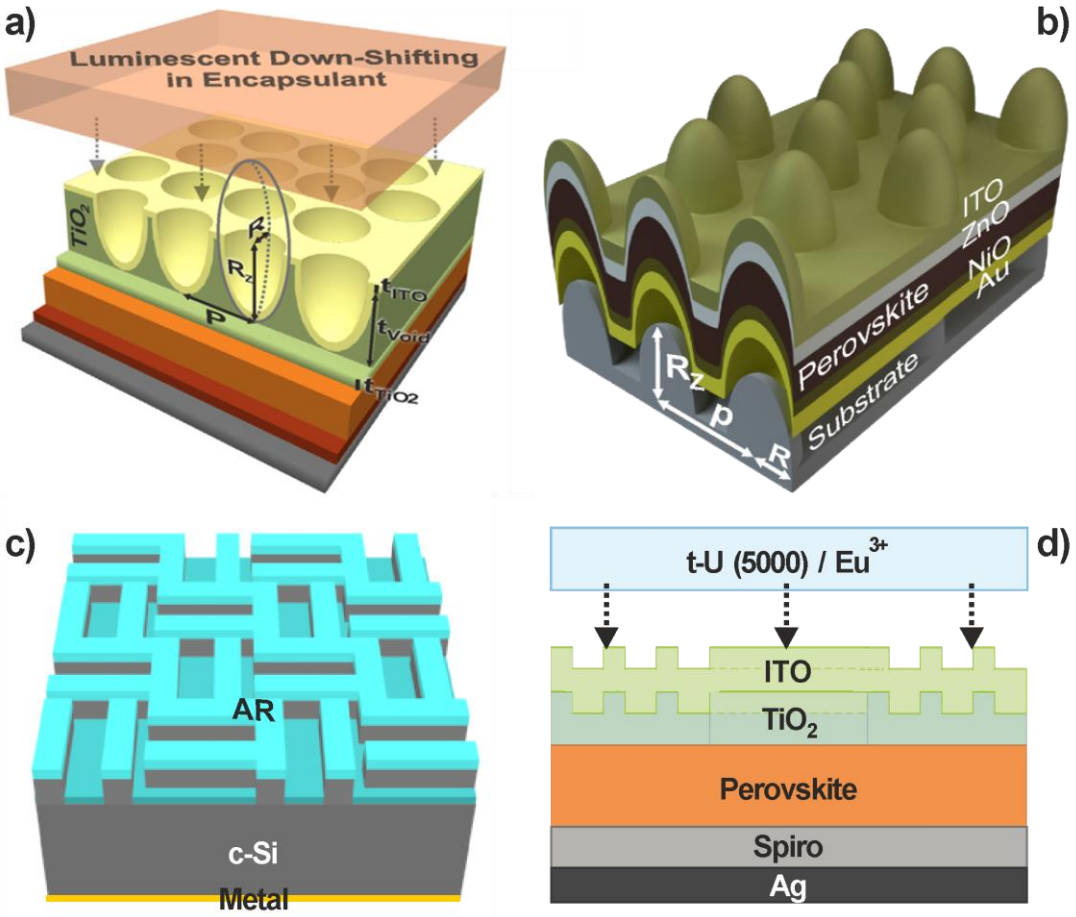

Figure 2: Sketch of different photonic-structured devices analyzed in this work using two different LT approaches, composed of TiO_2 features integrated on the front contact, ETM, of the PSCs coupled with a luminescent down-shifting layer (a), and via a conformal PSCs architecture formed by micro-structuring the substrate prior to the PSC deposition (b), for distinct perovskite thickness (250-500 nm). In c) it is shown the explored test cell with the checkerboard structure over c-Si (1 µm), while d) shows the checkerboard patterned in the TiO_2 in PSCs with a LDS layer over it.

In short, this work showed two main technological benefits that can be gained from the photonic solutions investigated:

1) *Optically-thicker absorbers* - The broadband absorption enhancement caused by the LT structures, and improved with the top-coated LDSs, allows lowering the PSC thickness while improving its photocurrent. This enables using thinner cells with increased efficiency, thus improving their bendability. As the flexural rigidity of a layer scales with the third power of its thickness, mechanical flexibility (and cost reduction) benefits from

lower thickness[100]. Here, the aim is to minimize the PSCs thickness to facilitate their integration on flexible substrates (e.g. polymers/plastics[100], fabrics[101], paper-based[26], [102]) of consumer-items as wearables, smart-packaging/labeling, mobile medical testing, etc.

2) *Improved Perovskite cell encapsulation* – Presently, a crucial issue of Perovskite technology is degradation upon UV and relative humidity exposure[103]. The innovative device architectures optimized in this work (see Figure 2) also contribute in improving the cell's long-term stability, as the front-coated LT and LDS structures can protect the underneath sensitive device layers from UV radiation and water penetration. Besides, the high aspect-ratio of the photonic structures renders the exposed surface superhydrophobic, thus providing *water-repellent* and *self-cleaning* functionalities[104]–[106].

Furthermore, one way to gain insight into the complex behavior of PSC devices is through the development of realistic simulation models, considering both optical and electrical effects [107] to account for carrier recombination, irregular field distribution and, thus, accurately predict device performance and allow modelling-aided design optimization, which can be of utmost importance for this emergent PV technology based on ultra-thin and flexible solar cells [108], [109]. However, most theoretical studies of LT in PSCs focus only on the optical effects at play [61], therefore not guaranteeing PCE improvement due to the lack of understanding of the behavior of LT-enhanced PSCs from an electrical standpoint, thus hindering the achievable gains for these devices. In this work, we developed a complete optoelectronic modelling procedure, from which it was determined that photonic-enhanced PSCs can indeed capitalize on the optical gains - particularly for ultrathin PSCs (perovskite layer: 300 nm) - and translate them to the electrical domain.

2

PHOTONIC-STRUCTURED TiO_2 FOR HIGH-EFFICIENCY, FLEXIBLE AND STABLE PEROVSKITE SOLAR CELLS

2.1 Introduction

Optical solutions are promising to improve not only the PSCs efficiency, by allowing physically thinner but optically thicker devices, but also facilitate their market applicability by enabling higher device flexibility due to the reduced thickness. The conventional best-performing PSCs exhibit high transparency in the near-infrared (NIR), thus are only able to exploit a reduced portion (about half) of the solar spectrum. The lower the Perovskite thickness the more challenging it becomes for optical strategies to compensate the losses in light absorption, mainly at the longer VIS-NIR wavelengths [110]. In addition, the application of such strategies in PV is conditioned by other factors, such as maintaining the electrical performance and compatibility with low cost and large area fabrication.

As previously introduced, several alternative approaches have been tested to increase the light harvesting of PSCs [111], [112], for instance by applying ultra-thin textures to the perovskite absorbers [113], [114] or the substrate [111], [112], applying ray optics by prism arrays [115], microlens [45] or nanocone [46], [47] arrays, plasmonic nanoparticles [58], [116], [117], light grating-coupled surface plasmon resonances [59] and embedding TiO_2 nanoparticles into the mesoporous TiO_2 layer [118]. However, most of these approaches also require nano/micro-structuring the Perovskite layers, thereby imposing a severe compromise between optical benefits and electrical deterioration; and none has yet led to efficiency enhancements superior to the state-of-the-art of optimized periodic texturing in thin film silicon-based cells [83].

This work started by investigating front-located wavelength-sized LT structures patterned on top of PSCs, operating in the wave-optics regime, which have been demonstrated to provide pronounced anti-reflection and scattering effects in thin film silicon PV [7], [119]. Since they do not require structuring the PV layers, this is a much more promising option to increase

the optical performance of thin film cells without increasing their roughness [18], [83], [95], [120]. For that, an inverted (substrate-type) PSC architecture is considered here, where the light enters through the cell side and not from the transparent substrate (as in conventional PSCs). Besides enabling the application of the PSCs in a much broader range of substrates (e.g. with flexible opaque materials), this inverted configuration can also be directly integrated onto multi-junction stacks to realize higher efficient tandem devices (e.g. Perovskite on Si or on CIGS) [56], [121], [122].

The wave-optical structures developed in this work for inverted PSCs are based on high-refractive index dielectric (TiO_2, n>2) micro-scale features, with semi-spheroidal geometries, which are shown to assist in three fundamental points of PSC technology: 1) photocurrent enhancement, 2) broader applicability due to higher device flexibility, such as portable electronic devices, and 3) higher stability against UV light degradation.

2.2 Ray optics analysis

The analytical Lambertian LT formalism has been used to determine the limit of maximum absorption in a slab of arbitrary thickness, in the geometric optics regime [123]. This is attained with an ideally rough surface where the incident light is randomly scattered, which can increase the average absorption in the slab by a factor of $4n^2$ compared to flat surfaces in the limit of weak absorption [74], where n is the real part of the refractive index of the slab. For a Perovskite with n~2.5 (at 300-1000 nm) the $4n^2$ limit means that the path length can be increased by a factor of ~25.

Such ray optics formalism was further developed to consider the full absorption by a slab with an arbitrary complex refractive index spectrum, allowing to estimate the photocurrent density (J_{ph}) enhancement that can be produced on the absorber with the implementation of Lambertian LT [124], [125]. Figure 3 shows the results of such calculation for the case of Perovskite absorbers with distinct thickness, considering that their back surface is coated with a perfect reflector and the front surface has an ideal Lambertian LT texture that disperses light rays at random angles towards the Perovskite [18]. For the two Perovskite thicknesses (250 and 500 nm) analyzed in this work, the limiting J_{ph} enhancements in the ray optics approximation are 31% and 25%, respectively. Such LT limits are only valid in the regime of geometric optics, and therefore are not applicable to the wave-optics regime of the thin film structures analyzed in this work where light interference effects play a major role. Nevertheless, the Lambertian results of Figure 3 can still provide a reasonable first-order prediction of the attainable J_{ph} values in PSCs improved with optimized LT, as the interference effects are mainly important for single wavelength calculations while the J_{ph} results from an integration over the solar spectrum that manipulates interference peaks.

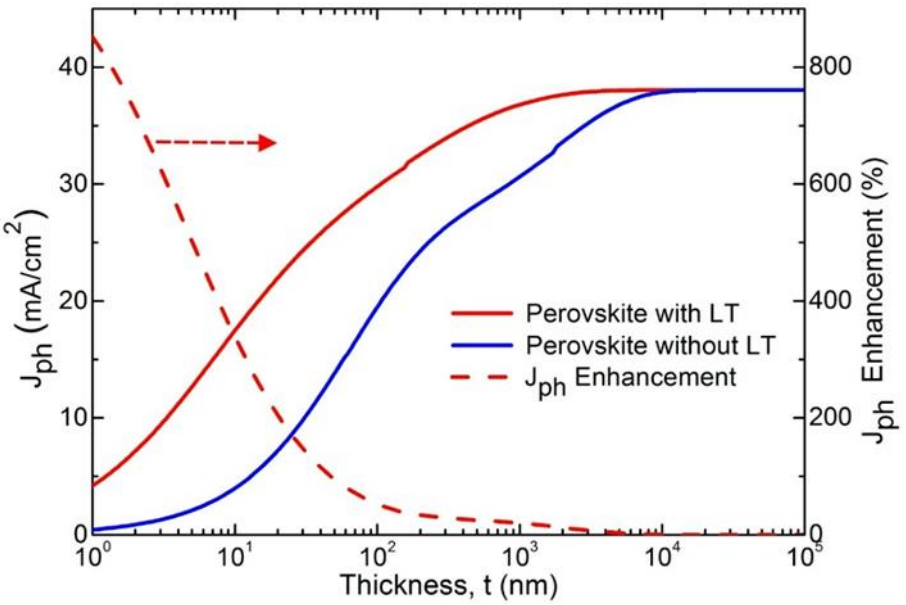

Figure 3: Lambertian theoretical analysis of LT in Perovskite solar cells, in the geometrical optics regime. The maximum photocurrent (J_{ph} – solid lines) and J_{ph} enhancement (dashed line) are shown as a function of the Perovskite film thickness, for the case with a Lambertian scattering surface (with LT) relative to a flat surface without LT. The thinner the Perovskite film the lower is the maximum J_{ph} but the higher is the attainable enhancement with LT. The wavelength range considered for the calculations was 300-1000 nm.

2.3 Numerical Method and Simulated Structures

The simulations of the electromagnetic field distribution in the thin film solar cell structures were carried out using a 3D Finite Difference Time Domain (FDTD) solver [126]. This is one of the preferential techniques to determine electromagnetic solutions in the wave-optics regime, specifically for PV light management [18], [107], since it is conceptually simple, versatile, and can accurately determine all the optical effects at play. Besides, since the computations are performed in the time-domain, the solutions can cover a broad frequency range over a single simulation run.

The complex refractive index of the materials composing the structures were taken from experimental data.(1) The Perovskite solar cell structure is composed of 5 layers coated on a substrate in the following order (see Figure 4): rear contact/mirror layer (silver, Ag), hole transport material (HTM made of Spiro-OMeTAD), Perovskite absorber (methylammonium

(1) We recall the physical relation between the real and imaginary parts of the complex refractive index, described by the well-known Kramers–Kronig relation, which correlates the real part of the index (n) with the absorption coefficient (a, directly related with the imaginary part), being ω and Ω the angular frequency, and c the light velocity in vacuum: $n(\omega) = 1 + \frac{c}{\pi} P \int_0^{+\infty} \frac{\alpha(\Omega)}{\Omega^2 - \omega^2} \, d\Omega$

lead iodide, $CH_3NH_3PbI_3$), electron transport material (ETM made of TiO_2) and front transparent contact (TCO made of ITO). The spectra of the refractive indices considered for all materials can be found elsewhere [19] and also plotted in Appendix A1.

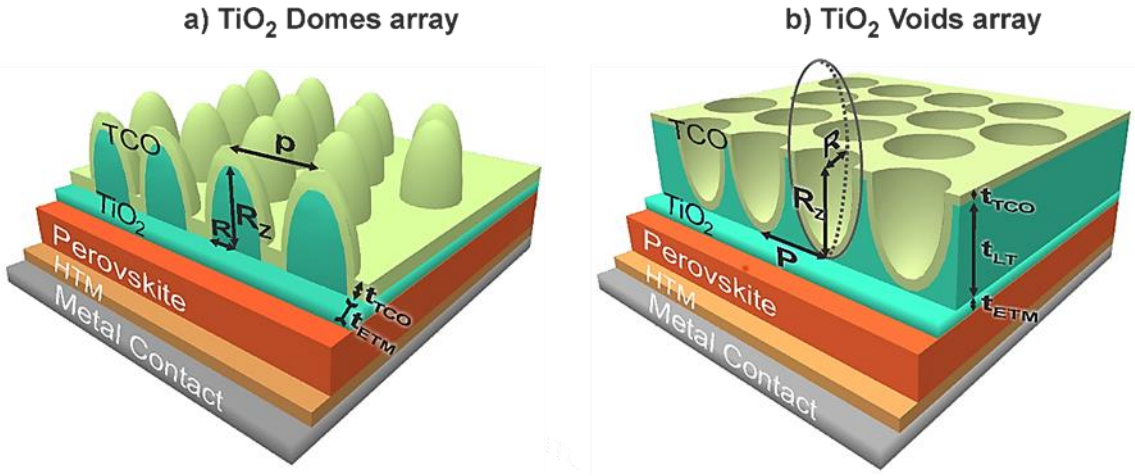

Figure 4: Sketch of both types of LT structures analyzed in this work, composed of TiO_2 features integrated on the ETM of the PSCs. The PSCs have a substrate-type layer configuration, in which light comes into the devices from the film side. The LT structures consist in a hexagonal array (with pitch p) of vertically aligned semi-prolate features with radii R and R_Z, respectively along the in-plane direction and illumination axis. The parameters (R, R_Z, p, t_{TCO}, t_{ETM}) for the structure (a) and the parameters (R, R_Z, p, t_{TCO}, t_{LT}, t_{ETM}) for the structure (b) considered for optimization are indicated by the arrows. At normal incidence, light impinges from the top along the spheroids' axis of revolution (z). The rear side of the perovskite is coated with a 150-nm-thick Spiro-OMeTAD layer (HTM) and a 80 nm silver layer (metal contact).

The illuminating source bandwidth is 300-1000 nm, since the AM1.5 solar photon flux outside this wavelength range is small (as shown in Figure 1) and corresponds to the most significant portion of the photocurrent spectrum of PSCs. The power absorbed per unit volume (P_{ABS}) in each element of the structures is given by the resulting electric field distribution established in its material:

$$P_{ABS} = \frac{1}{2}\omega\varepsilon''|\boldsymbol{E}|^2 \qquad (1)$$

where $|E|^2$ is the electric field strength, ω is the angular frequency of the light and ε" is the imaginary part of the dielectric permittivity. P_{ABS} is normalized by the energy source to obtain the absorption density (P_{ABS}, units of m^{-3}). The absorption of light with a certain wavelength (λ) is calculated by integrating P_{ABS} along the absorber volume: $Abs(\lambda) = \int p_{ABS}(\lambda)dV$. The number of photons absorbed per unit volume and per unit time is the photon absorption rate: $g(\omega)=P_{ABS}/E_{PH}$; where $E_{PH}=\hbar\omega$ is the photon energy. Here we assume that each absorbed photon excites one electron-hole pair, so g is equivalent to the optical generation rate. As the illumination is given by a broadband source, characterized by a spectral irradiance (instead of a power density to account for the wavelength dependence), the E-field is replaced by an electric

field spectral density such that its intensity, $|\mathbf{E}|^2$, becomes with units of $V^2m^{-2}Hz^{-1}$. In this way, g is generalized to a spectral generation rate (in units of $m^{-3}s^{-1}Hz^{-1}$) such that the total generation rate (G, units of $m^{-3}s^{-1}$) is calculated by integrating over the frequency range of the source bandwidth: $G = \int g(\omega)d\omega$ [126]. Since we are primarily concerned with the optical rather than the electrical transport properties of the solar cells, an internal quantum efficiency equal to one is also assumed (i.e. every photon absorbed in the Perovskite generates carriers collected by the contacts). As such, J_{ph} is determined by integrating the absorption in the Perovskite layer, convoluted with the solar power spectrum AM1.5 ($I_{AM\,1.5}$, units of $Wm^{-2}m^{-1}$), along the computation wavelength range (300-1000 nm):

$$J_{ph} = e \int \frac{\lambda}{hc} Abs(\lambda)\, I_{AM1.5}(\lambda) d\lambda \qquad (2)$$

where e is the electron charge, h is the Planck constant and c is the free space light velocity. This spectrally-integrated J_{ph} can be considered as an upper limit corresponding to the ideal case of no electrical losses, and is taken here as the figure of merit to optimize the performance of the photonic structures.

Using a particle swarm optimization algorithm (PSO) [126] in the FDTD programs, a complete screening of the geometrical parameters of the LT elements (indicated in Figure 4) was performed, searching for the set of parameters that produces the highest J_{ph}. The algorithm iteratively adjusts the geometry of the TiO_2 LT structures, and thickness of the TCO and ETM layers, to maximize absorption in the Perovskite region, minimizing optical losses (i.e. total reflection and absorption occurring in the TCO and TiO_2 materials). Population-based stochastic optimization techniques, such as the PSO, are preferred when operating with complex physical systems, as in the current wave-optical regime, where there is a strong correlation between all the parameters of the structures, making it practically unfeasible to precisely determine the global maximum of any figure of merit by simple sequential scanning of the parameters.

2.4 Optimized photonic-enhanced Perovskite solar cells

As demonstrated theoretically [7], [18], the absorption enhancements attained with wave-optical elements on the cells' front are maximized when the complex refractive index ($N=n+ik$) of their dielectric material has lowest imaginary part (k) at the sunlight wavelengths (to minimize parasitic optical losses), and has a real part (n) as close as possible to that of the underlying absorber (e.g. n~2.5 in Perovskite and n~4 in Si) to improve anti-reflection via geometric index matching. High values of n also boost the light scattering performance of the photonic features, since their scattering cross section increases with n. TiO_2 was shown to be one of the

preferential materials to fulfill such requirements in thin film silicon solar cells [18], [119], but it can perform even better in PSCs since its n~2.4-2.7 is much closer to that of Perovskite. Therefore, TiO_2 was the material considered for the photonic structures optimized in this work for PSCs (sketched in Figure 4). In fact, conventional PSCs already use compact (~20-30 nm thick) and/or mesoporous (~200-400 nm thick) TiO_2 layers as electron transporters, so the TiO_2 LT structures should be incorporated on such layers as a continuation of the cells' ETM. Due to the low electric conductivity of TiO_2, it must be coated with a transparent conductive oxide (TCO) acting as the front (n-type) electrode. Here we consider the most commonly used TCO composed of indium tin oxide (ITO) deposited conformally over the TiO_2 features.

The optimization method described in section 2.3 was applied to find the set of geometrical parameters of the two types of geometries depicted in Figure 4 that maximize the generated photocurrent in the underlying PSC. Here we consider a substrate-type PSC layer structure due to two main aspects: 1) To maintain the electrical performance (prevent increase of roughness and consequent recombination) of the PSCs after implementing the LT structures at the last processing steps and 2) To allow the integration of the devices on a wider range of substrates, including opaque ones, such as rigid (e.g. roof and wall tiles for BIPV, metallic coverage of vehicles, etc.) or flexible (e.g. PI, metal foils, fabrics [101], plastics [127], [128], paper-based [26]) materials.

LT can play a crucial role in the development of flexible solar cells, since it allows decreasing the cells' thickness without photocurrent loss, or even enhancing it as shown here. To explore that, the photonic structures of Figure 4 were optimized for both the conventional Perovskite layer thickness (500 nm) used in state-of-art devices, and for half that thickness (250 nm) to be applied in flexible devices. Note that a reduction of the absorber layer to half can enable a decrease up to about four times in the device flexural rigidity [127].

The geometry of the photonic structures is an hexagonal array of semi-spheroidal dome (Figure 4a) or void (Figure 4b) elements, as these are similar structures to those that can be fabricated by industrially-attractive patterning techniques such as colloidal lithography [7], [119], [120], which is an inexpensive soft-lithography method that can engineer any structure with nano/micrometer resolution and high uniformity throughout large areas [119]. The geometrical parameters considered for optimization are indicated in Figure 4. These are taken as variables by the PSO algorithm that iteratively searches for the best set of parameters that maximizes the photocurrent (J_{ph}, eq. 2) produced in the PSC, considering reasonable boundaries for their domains.

Table 2 presents the main outcomes of the optimization studies performed in this work, indicating the best parameters and the corresponding maximum J_{ph} values attained. The first line presents the theoretical *Lambertian* limits of geometrical optics, as described in section 2.2 (see Figure 3). The second line presents the optimized values for the thicknesses of the two flat layers of TiO_2 and TCO (composed of ITO) coated over the Perovskite, acting as a planar dou-

ble-layer anti-reflection coating (ARC), which is the reference LT case considered here for comparison with the results attained with the two types of TiO_2 micro-structures presented in the two last lines of Table 2 and sketched in Figure 4. The results and discussion of the optimization studies for the planar reference LT structures (ARC cases) are presented elsewhere [19].

Table 2: Maximum J_{ph} values attained for the optimized LT structures placed on the two distinct PSCs, with 250 or 500 nm Perovskite layer thickness, considered in this work. The geometrical optimization parameters (R, R_Z, p, t_{TCO}, t_{ETM}) and (R, R_Z, p, t_{TCO}, t_{LT}, t_{ETM}), respectively for the Dome and Void structures, are defined in Figure 4. The results are compared with the reference ARC-patterned cases, as well as with the theoretical limits in the regime of geometrical optics attained with a Lambertian scattering surface.

Light Trapping Structure	Absorber: **250 nm Perovskite layer**		Absorber: **500 nm Perovskite layer**	
	Optimal Parameters	$\mathbf{J_{ph}}$ | $\mathbf{J_{ph\_VIS\text{-}NIR}}$ (mA/cm²)	Optimal Parameters	$\mathbf{J_{ph}}$ | $\mathbf{J_{ph\_VIS\text{-}NIR}}$ (mA/cm²)
Lambertian surface *(Figure 3)*	-	**33.3 | 32.0**	**-**	**35.3 | 34.1**
Planar ARC	t_{TCO} = 50 nm t_{ETM} = 20 nm	**22.6 | 21.1**	t_{TCO} = 76 nm t_{ETM} =20 nm	**25.9 | 24.9**
Dome structures *(Figure 5)*	t_{TCO} = 50 nm t_{ETM} =159.1 nm R = 785.2 nm Rz = 1755 nm p = 1825.6 nm	**28.0 | 27.7**	t_{TCO} = 50 nm t_{ETM} = 132.7 nm R = 502.6 nm Rz = 1007 nm p = 1347.1 nm	**30.6 | 30.3**
Void structures *(Figure 6)*	t_{TCO} = 63.6 nm t_{ETM} = 20 nm R = 401.2 nm Rz = 1792 nm t_{LT} = 656.2 nm p = 882.7 nm	**28.6 | 28.3**	t_{TCO} = 62.3 nm t_{ETM} = 93.2 nm R = 388.0 nm Rz = 820.8 nm t_{LT} = 404.6 nm p = 865.3 nm	**31.3 | 30.8**

2.4.1 Optimal dome front structures

Figure 5 presents the results attained with the optimized set of geometrical parameters of the hexagonal array of TiO_2 half-spheroids, shaped like domes as shown in Figure 4a, and of the thicknesses of the flat ETM layer (t_{ETM}), placed between the domes and Perovskite, and front contact (t_{TCO}) coating the structure. These results (red curves) are compared to those of the planar reference cells (blue curves) with the optimized double-layer ARC, for the two Perovskite absorber thickness (250 and 500 nm) considered in this work.

The standard planar cell structure, with 500 nm Perovskite layer, exhibits high absorption in the Perovskite along 375 to 750 nm wavelengths. Above 750 nm there is an abrupt absorption drop of about 92%, occurring at the bandgap of the Perovskite material. In the case of the thinner (250 nm) Perovskite, there is a first smaller absorption drop at 600 to 750 nm wavelengths, and then above 750 nm there is a larger absorption drop at the bandgap of nearly 93%. The incorporation of the dome-like LT structures improves the optical performance of the cells mainly by decreasing such drops in absorption observed for the planar PSCs, namely in the visible range (600 to 750 nm wavelengths) for the thinner (250 nm) Perovskite and in the NIR (>750 nm wavelengths) for both the 250 and 500 nm Perovskite absorbers.

The enhancement in the visible range is due to a better light incoupling towards the Perovskite layer provided by the front TiO_2 structures, via two main mechanisms: 1) Anti-reflection due to the geometrical index matching caused by the cone-like shape of the TiO_2 features, which is favored by the proximity between the values of the real part of the refractive indices of TiO_2 and Perovskite. In fact, at a wavelength of approximately 600 nm, the n~2.41 of TiO_2 is equal to that of the Perovskite material, which highly contributes to the maximum of absorption (Abs= 0.96 and 0.98, respectively for Figure 5a,b) in the Perovskite occurring near such wavelength. 2) Near-field forward-scattering, since the domes act as micro-lenses creating an intense electric-field focus on the vicinity below their bottom surface, which is vital to confine the light specially in the thinner Perovskite layer. This effect is mostly relevant for wavelengths smaller than the dimensions of the scattering elements, in this case in the UV-visible range, as observed by the highly intense regions of localized electric field in the generation profiles of Figure 5a,b and in the p_{ABS} profiles of Figure 5c,d for the 412 and 601 nm wavelengths.

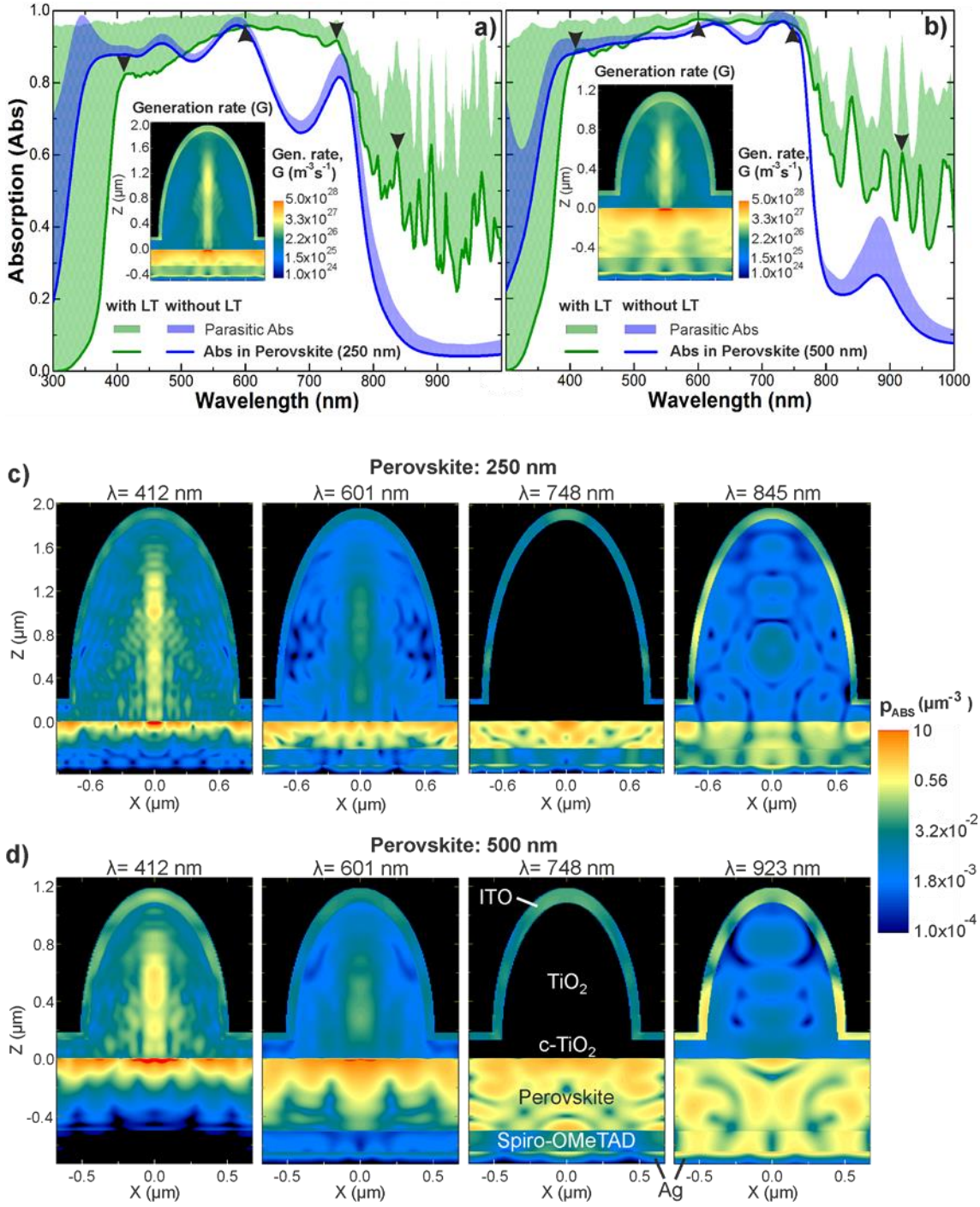

Figure 5: a,b) Absorption (Abs) spectra attained with the optimized LT structures sketched in Figure 4a, composed of half-spheroidal domes (green lines, row 4 of Table 2), and with the reference cases of a cell with an optimized anti-reflection coating (blue lines, row 3), for Perovskite absorber layers with distinct thickness: a) 250 nm and b) 500 nm. Each graph shows the absorption occurring in Perovskite (solid lines) and the parasitic absorption in the other materials (colored regions above the lines). The inset profiles show the log-scale distribution of the corresponding total generation rate, G, along the xz cross-sectional plane of the structures passing by the spheroid center. c,d) Log-scale distributions of the absorption density, p_{ABS}, along the same xz plane of the structures, at the wavelengths of the peaks marked by the arrows in a) and b) respectively for the half-spheroids array on the 250 nm (c) and 500 nm (d) thick Perovskite absorbers.

The enhancements observed in the NIR range are mainly caused by the strong far-field scattering effects of the TiO_2 domes, owing to their optimized shape and high real part of the refractive index, which increase the absorption in the Perovskite layer via optical path length amplification, by diverting the vertically incident light to more horizontal directions along the layers' plane, and coupling with waveguided modes trapped in the cell layers. This is evidenced by the distributed regions of higher p_{ABS} (hot-spots), observed in the profiles of Figure 5c,d for wavelengths >700 nm, which result from constructive and destructive interference between the light waves traveling along the incidence direction and the scattered light that travels along the plane of the cell layers suffering multiple reflections from the top surface and back reflector. These can be seen as 3D Fabry-Perot resonances, compared to the 1D Fabry-Perot resonances in planar layer structures, which lead to the sharp NIR peaks of absorption enhancement present in Figure 5a,b.

The light absorption in the Perovskite is the only one that can generate photocurrent, so the absorption in the other materials is referred as parasitic absorption, since it corresponds to optical losses not translated into electrical output by the cell. The main parasitic absorption in the planar references occurs chiefly in two spectral regions: 1) in the UV (300-400 nm wavelengths) since the imaginary part of the refractive index (k) of ITO and TiO_2 increases abruptly for wavelengths below 400 nm; 2) in the NIR (>800 nm wavelengths) due to the free carrier light absorption in the ITO, which leads to an increase of its k for the longer wavelengths, and absorption at the cell rear in the HTM (Spiro-OMeTAD). These parasitic losses can be observed in the generation rate and p_{ABS} profiles for the planar reference cells. In the structures with the TiO_2 domes the parasitic absorption occurs for the same reasons, but for shorter wavelengths it is more pronounced along a broader range (300-500 nm) extending to the visible spectrum, due to absorption by the LT features at the cells' front as seen in the generation profiles of Figure 5a,b and p_{ABS} profiles of Figure 5c,d at 412 nm wavelength. In the NIR, it can be seen from the plots of Figure 5c,d that the parasitic absorption happens mainly in the top ITO and in the bottom HTM, as occurred in the planar cells.

The severe parasitic absorption caused by the front TCO explains why the optimization algorithm converged to the minimum allowed thickness (t_{TCO}=50 nm) for the domes LT structures (see Table 2). Contrary to the planar cases, the anti-reflection LT effects caused by the domes structures are chiefly given by the geometrical index matching that they provide on the cell front. So, the TCO layer does not provide any beneficial optical contribution in these structures, and the thinner it is the better. However, a TCO layer with at least 50 nm thickness must be considered for electrical purposes, as it acts as the front n-electrode. On the other hand, the thickness of the underlying flat ETM layer (t_{ETM}~133-159 nm) converged to much higher values that those (t_{ETM}=20 nm) of the planar references, thus revealing that it is optically favorable to establish a separation between the bottom surface of the semi-spheroidal domes and the top surface of the Perovskite layer, in order to provide better light incoupling and confinement in the absorber.

2.4.2 Optimal void front structures

The results of the optimized LT structures based on spheroidal voids (sketched in Figure 4b) are presented in Figure 6. Despite the considerable differences in geometry, the absorption spectra and generation profiles of Figure 6a,b produced with the voids array are similar to those of Figure 5a,b attained with the domes. However, the voids provide a slightly higher absorption mainly at short visible wavelengths (400-500 nm) due to better anti-reflection, and in the NIR region due to improved scattering, both in the 250 and 500 nm Perovskite absorbers, thus leading to higher values of J_{ph} (last row of Table 2). The p_{ABS} profiles shown in Figure 6c,d reveal that the voids structure generally creates a more uniform spatial distribution of the absorption enhancement throughout the volume of the Perovskite layer, while the domes array generates more localized (confined) regions of highest electric field intensity due to the focal effect of their micro-lens shape. This explains the better performance of the voids structure for light scattering, i.e. bending of light waves, which justifies the higher values of absorption at the longer NIR wavelengths.

In the voids case, the optimal TCO thicknesses (t_{TCO}) indicated in Table 2 are higher than those of the domes since such front contact now improves the anti-reflection in the flat regions between voids on the top surface. On the other hand, the thicknesses of the flat ETM (t_{ETM}) are smaller, since this layer plays a lesser role for geometric index matching in this structure.

For the voids and domes structures, the optimized lateral (R) and vertical (Rz, tLT) dimensions of the TiO2 features are larger for the thinner 250 nm Perovskite, as the thinner the absorber the higher are the requirements for scattering: it needs to provide stronger path length enhancement for a broader wavelength range (i.e. extending to shorter wavelengths than those of thicker absorbers). This is achieved chiefly by enlarging the lateral sizes of the scattering elements, thus yielding higher scattering cross sections. Nevertheless, the optimal vertical size must also increase with the lateral size to maintain effective geometrical index matching provided by the front features, and consequent broadband anti-reflection. Since the thicker 500 nm Perovskite has a lower need for scattering, the optimized design of the TiO2 features converged to smaller dimensions and to larger array pitch (p) to also minimize the parasitic absorption of the LT structures.

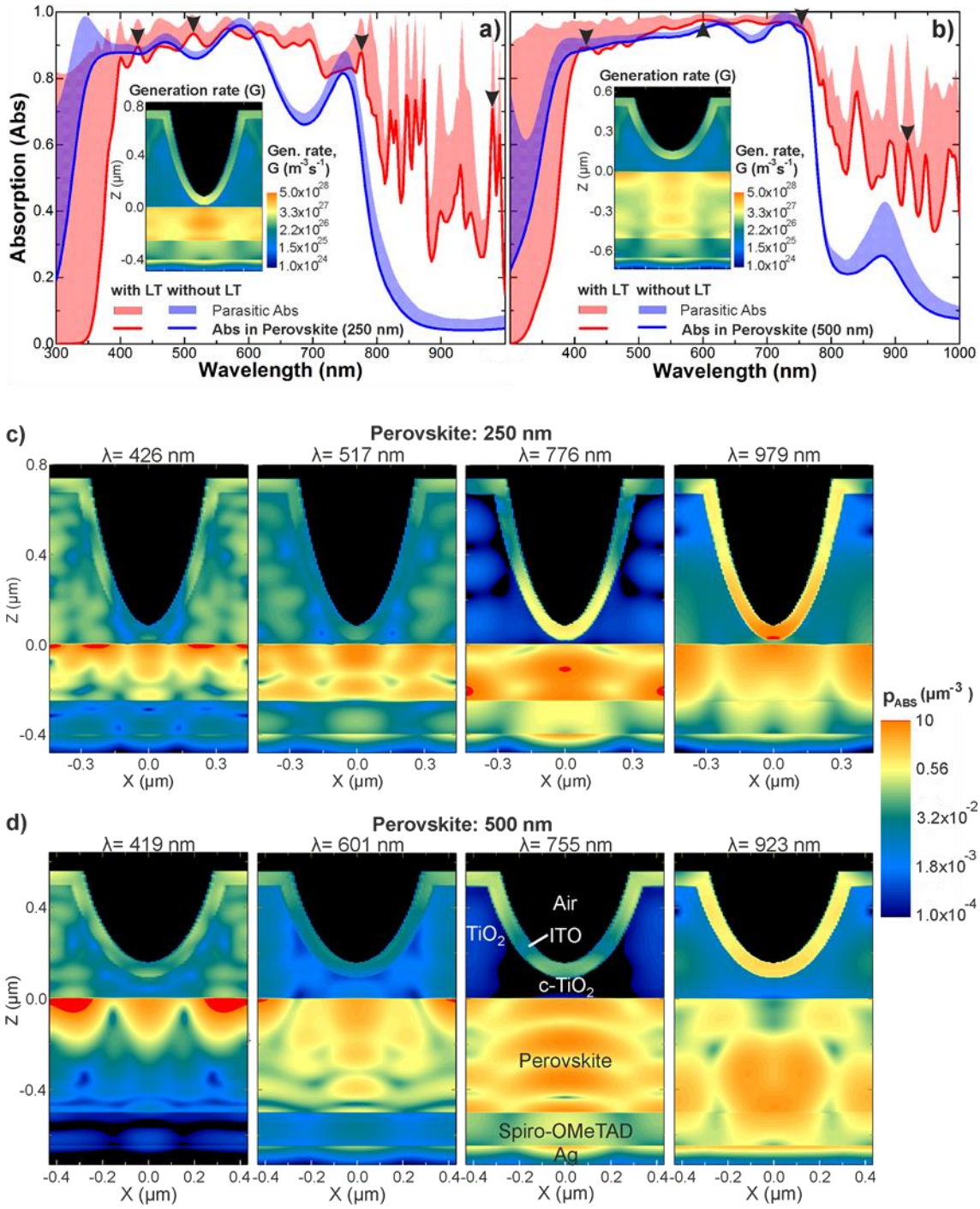

Figure 6: Same as Figure 5 but for the LT structures sketched in Figure 4b, composed of semi-spheroidal voids in the TiO_2 film. a,b) Absorption (Abs) spectra attained with the optimized LT structures (green lines, row 5 of Table 2), and with the planar reference ARC cases (blue lines, row 3), for Perovskite layers with a) 250 nm and b) 500 nm thickness. Each graph shows the absorption occurring in Perovskite (solid lines) and the parasitic absorption in the other materials (colored regions above the lines). The inset profiles show the log-scale distribution of the corresponding generation rate, G, along the xz cross-sectional plane of the structures. c,d) Log-scale distributions of the absorption density, p_{ABS}, along the same plane, at the wavelengths of the peaks marked by the triangles in a) and b) respectively for the voids array on the 250 nm (c) and 500 nm (d) thick Perovskite.

2.5 Discussion of results

The main distinguishing advantage of the LT schemes designed here, over the conventional texturing/structuring-based LT approaches mentioned in the Introduction, is that they can remarkably enhance light harvesting without creating roughness in the thin PV layers. This is because the photonic elements are placed on top of the unstructured planar solar cells. Thus, they do not increase the amount of defect states, that can strongly contribute to electrical deterioration particularly in PSCs [129], [130], allowing the geometry of the photonic structures to be fully optimized for maximum LT without constraints concerning the degradation of the electrical performance of the devices. Consequently, the voltage and fill factor of the cells is expected to be maintained (even possibly increased), while substantially boosting the photocurrent. Therefore, the efficiency gains resulting from the incorporation of the optimized LT structures are expected to be like their corresponding J_{ph} enhancements.

An important aspect of the absorption curves of Figure 5 and Figure 6 resulting from the incorporation of LT structures, is that the strongest parasitic absorption occurs in the UV range (300-400 nm) mainly due to the relatively large volume of the photonic structures and the significant *k* of their TiO_2 material below 400 nm wavelengths (see the reference [19]). Nevertheless, such optical losses in the UV can be quite advantageous for the stability of PSCs, as one of the main factors for the poor lifetime of this type of PV devices is their severe degradation upon UV illumination.

The mechanism responsible for UV light degradation in PSCs is attributed to the photocatalytic activity of TiO_2 occurring in the interface between the ETM and the Perovskite layer. Upon prolonged UV light exposure, the photo-generated holes react with the oxygen radicals adsorbed at surface oxygen vacancies, which become deep traps within the Perovskite increasing charge recombination [131]. Therefore, blocking UV photons from entering the PSCs has proven to be beneficial, yielding longer time of stabilized high efficiency [132], [133]. As such, here the TiO_2 structures advantageously act as a UV-protective layer that, at the same time, enhances the absorption of visible and NIR photons in the Perovskite absorber, thus leading to overall J_{ph} gains while contributing to the device robustness in standard sunlight exposure conditions.

Figure 7 represents such gains, relative to the optimized planar reference cells, determined from the J_{ph} values of Table 1 for the two types of LT geometries explored in this work (domes and voids) and both Perovskite thicknesses (250 and 500 nm). Besides, to analyze the aspect described in the previous paragraph, we also represent the enhancements considering the photocurrent density values ($J_{ph\_VIS\text{-}NIR}$) shown in Figure 7, determined from photon absorption in the Perovskite outside the UV range (i.e. restricting the integral of eq. 2 to the 400-1000 nm wavelength range, instead of the total 300-1000 nm range of Figure 5 and Figure 6). Such $J_{ph\_VIS\text{-}NIR}$ gains can be regarded as the improvements that would be achieved considering PSCs with a UV-blocking filter for better stability.

Figure 7 shows that the voids array outperforms the domes, as the present PSCs take more profit from the higher degree of light spreading provided by the voids, instead of the higher light focusing effect of the micro-lens shape of the domes. This can be advantageous for practical implementation, since void-like structures can be more straightforwardly fabricated than domes when employing scalable colloidal-lithography (CL) techniques. To form the desired void arrays, the CL processes use hexagonal arrays of colloidal microspheres as mask for the subsequent deposition of any material (in this case TiO_2) in the inter-spaces between the dry-etched spheres [119], [134], which results in nano/micro-patterned layers after the spheres lift-off. However, the better performance of LT structures composed of voids relative to domes may not apply to even thinner Perovskite layers that can take more advantage from the higher localization of the electric field enhancement in the ultra-thin Perovskite. This was seen in a previous work of the authors applied to thin film Si cells, in which for 100 nm thin a-Si cells the optimized domes provide higher enhancement than the voids [7].

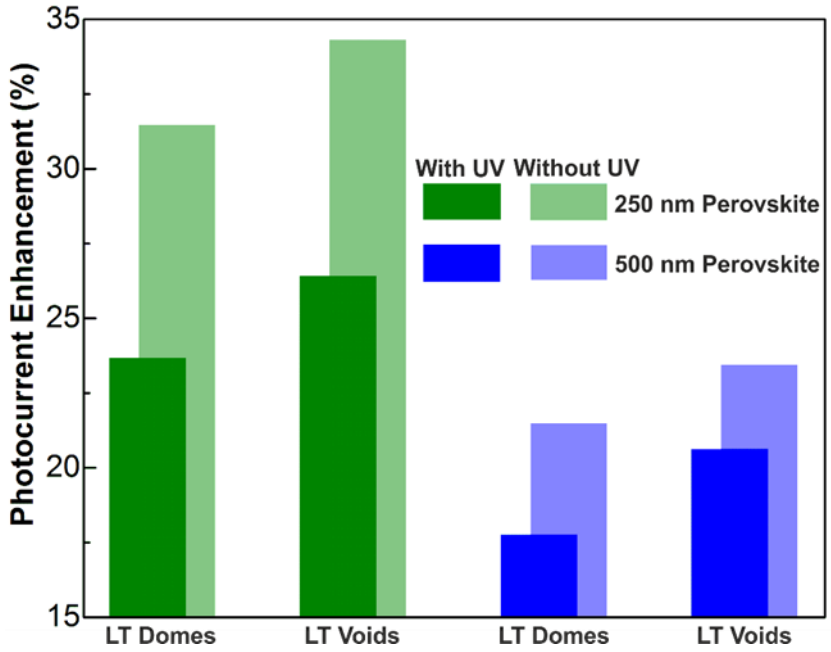

Figure 7: Photocurrent enhancements attained with the optimized photonic structures (last 2 rows of Table 2) analyzed in section 4, relative to the planar double-layer ARC references (row 2 of Table 2). The absolute J_{ph} values were calculated by integrating the spectral absorption (eq. 2) in the UV-VIS-NIR wavelength range (300-1000 nm – with UV) and only in the VIS-NIR (400-1000 nm – without UV), for both Perovskite thicknesses (250 and 500 nm) analyzed in this work.

Although the highest absolute photocurrent values are attained with 500 nm thick Perovskite (30.6 and 31.3 mA/cm², respectively with domes and voids), the optimized LT structures on the 250 nm absorber yield the highest enhancements (see Figure 7). The lower the absorber thickness the higher can be the absorption gain provided by optimized LT, as expected from the Lambertian ray optics analysis of Figure 3. The maximum values of the absolute J_{ph} (33.3 and 35.3 mA/cm², respectively for 250 and 500 nm thick Perovskites) and LT enhancement

(30.6% and 25.2%, respectively) determined with idealized Lambertian surfaces are close but above those attained in this work (see Figure 3 and Figure 7), which indicates that there is still room for further improvement of the optical schemes. The main reason for the lower photocurrents attained with the wave-optical structures, relative to the Lambertian limits, is the parasitic losses in the front TCO and TiO_2 materials. Therefore, the J_{ph} values of the optimized geometries would be closer to the Lambertian ones if no TCO was considered on top of the structures, or if distinct materials were investigated with lower extinction coefficient.

The most impactful result shown in Figure 7 is the J_{ph} enhancement (27% with UV and 34.3% within only VIS-NIR) attained with the optimized voids array on the 250 nm thick Perovskite, since it demonstrates an improved device architecture that can allow: 1) higher photocurrent (hence efficiency) relative to conventional planar PSCs with thicker (500 nm) Perovskite layers; 2) a potential 3-fold improvement in the device flexibility due to the thinner absorber, since the flexural rigidity of the cell scales with the third power of its total thickness; 3) a 2-fold reduction in the costs associated to the Perovskite material; and 4) potentially better PSC stability due to the role of the LT structure as a UV-blocking filter. In addition, such enhancement is considerably higher than the state-of-the-art enhancement (14.4% with 300 nm thick Perovskite absorber) achieved thus far using conventional texturing on the FTO/glass substrate [111], [135].

2.6 Conclusions

The novel front structures studied here allow remarkable photocurrent gains, indicated in Figure 7, which should translate into similar efficiency enhancements since the LT structures are patterned over the cells, therefore they are not expected to degrade the electric performance. These enhancements become increasingly pronounced with decreasing Perovskite thickness, thereby allowing thinning the cell absorber while increasing its photocurrent. For instance, the optimized void structures, which were shown to be more optically favorable than the domes, enable a PSC with a thin (250 nm) Perovskite thickness to supply a 28.62 mA/cm^2 photocurrent density, which is 10.3% higher than that (25.95 mA/cm^2) attained with the conventional Perovskite thickness (500 nm) coated with an optimized planar double-layer ARC.

It was also observed that there is a reasonable tolerance of the optimized results with respect to deviations in the geometrical parameters of the LT structures, since 5% variations in the values of each parameter result in <5% relative reduction in J_{ph}. The photocurrent close to the optimum point was seen to be mainly sensitive to the variations in the radius R and pitch p of the LT structures, which are the parameters that chiefly govern the scattering properties.

Lastly, in addition to their strong optical role, the developed front-located LT structures can allow important improvements in the operational stability of perovskite solar cells by blocking harmful UV radiation.

3

DESIGN OF LUMINESCENT DOWN-SHIFTING PROPERTIES FOR PHOTONIC-ENHANCED PEROVSKITE SOLAR CELLS

3.1 Introduction

Although PSCs display an impressive performance, competing with the best Si solar cells in terms of efficiency, they have several stability problems mainly related with exposure to moisture, oxygen and UV radiation, that are responsible for blocking its market implementation[15]. These degradation mechanisms are not yet fully understood, however several studies have defined many possible mechanisms[136]–[138]. Moisture and oxygen exposure can be mostly prevented via proper encapsulation[138], leaving UV exposure as the most important susceptibility to overcome. The UV degradation of PSCs has been attributed to photocatalytic effects caused by TiO_2, the material commonly used as electron transport layer (ETL). This effect was first reported by Leijtens *et. al.* where it was hypothesized that, upon electron excitation in TiO_2, deep trap states are created that capture photo-electrons generated in the absorber material, therefore hindering the cell's performance[139]. Ito *et. al.* also suggested that the formation of I_2, due to electron transfer to deep trap states in the TiO_2/perovskite interface, can then decompose the perovskite crystal by evaporation of volatile compounds[137]. Regarding perovskite degradation, excluding the effects of TiO_2, Quistch *et. al.* calculated the threshold energy between the perovskite's photo-brightening and photo-degradation, correlating it with the presence of residual PbI_2. This study indicated that I_2 can be created by the photolysis of PbI_2, leading to an equivalent degradation process to the aforementioned one[140].

Considering the above-mentioned problems, several techniques have been used to mitigate these degradation mechanisms, such as replacing TiO_2 by other non-harmful materials[139], depositing blocking layers between the TiO_2/perovskite interface to avoid electron exchange[137], as well as the use of either a UV filter or a DSL that prevents UV radiation from

reaching the cell[98], [99], [139], [141]. This latter case is the one that was unprecedentedly optimized in this study.

Down-shifting is the process where high energy photons are converted to lower energy photons[142], [143]. The main materials used for this process are quantum dots (QDs)[144]–[147], dyes [60], [148], [149] and rare-earth elements[89], [150], [151]. These materials have recently been applied to perovskite[152],[98], [141], organic[153] and dye sensitized solar cells[154] to improve their life-time without compromising their overall performance. When compared with the use of UV filters, which is the current common way of enhancing the UV stability of PSCs[139], using DSL benefits from the exploitation of the energy of otherwise lost photons, while still protecting the absorber material from the harmful UV radiation. One example, by Anizelli *et. al.*, compared the results against a UV filter obtaining a similar development of the device's parameters with prolonged UV exposure[98].

As stated earlier, the need for ever-decreasing thickness without compromising solar cell performance is a driver for research in the PV field. However, decreasing thickness leads to lower red-NIR absorption, as this radiation has higher penetration depth. Therefore, different LT methods have been studied to improve this low-energy absorption, such as the use of metallic or dielectric nanoparticles[155]–[157], front or rear texturing of the cell[6], [158], [159] and the use of high index dielectric structures on the cell front[7], [160], [161]. This latter LT method, operating in the regime of wave-optics, is the one considered in this work. Front-located high index photonic structures allow strong forward scattering of light, thus increasing its travel path within the PV absorber, as well as the creation of resonant modes, related with the structure's properties, that can greatly boost the cell's absorption. For periodic structures, this increase can even surpass the theoretical limit – the Tiedje-Yablonovitch limit – for specific wavelengths related with the LT structure's pitch[6], [107], [161].

In this study, two different types of solar cells were considered (Figure 8a,b) to the similar one studied in chapter 2 : First, a planar cell, henceforth PC, and a cell with light trapping structures, henceforth LTC. The absorber material considered in the PSCs is the conventional best-performing $CH_3NH_3PbI_3$ ($MAPbI_3$) perovskite[12], [15]. Two different thickness values for the perovskite layer were used, namely 250 and 500 nm, as the latter value is that conventionally used in PSCs while the former is of interest for the development of ultra-thin photonic-enhanced devices[8], [9], [121], [162]. The remaining solar cell dimensions and materials are based on previous results from optimizations centered on maximizing the optical performance of front LT structures on the PSCs[162]. A preferential implementation of luminescent down-shifting (LDS) materials is via their embedment in a polymeric matrix used as the cell's encapsulant[97]–[99], as sketched in Figure 8a,b, which is generally several micrometers thick[97], [99]. Therefore, such DS encapsulant layer was modelled as the background medium over the cells' structures. In the simulation, the background refractive index ($n_{Background}$) was set to n=1.5 as it is a common value for transparent polymeric materials used for this purpose such as PMMA,[98] EVA,[97] PVB [97] and PS[99]. This way, the light impinges on the cell from the

LDS embedded encapsulants. A base simulation with vacuum background index ($n_{Background}$) n= 1 was still made for the PCs, for comparison.

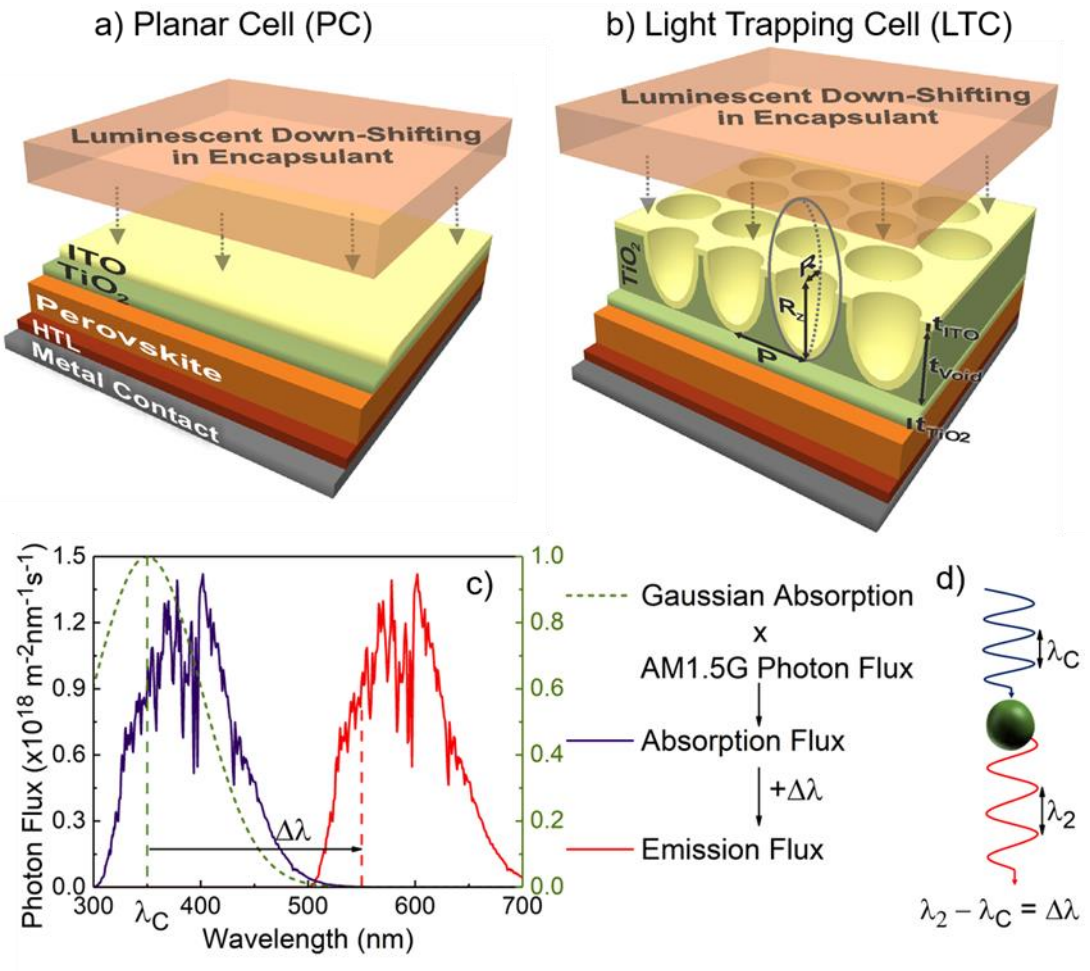

Figure 8: Schematic of the solar cell structures considered in the simulations. a) PC - Cell with planar structure used as reference, composed by the layers: Metal contact (Ag)/Hole Transport Layer (HTL, made of Spiro-OMeTAD)/Absorber (Perovskite)/ Electron Transport Layer (ETL, made of TiO_2), Transparent conductive oxide (TCO, made of ITO). b) LTC - cell with light trapping structures integrated in the n-contact (ETL) of the PSC. c) Plot illustrating the method used to emulate the process of down-shifting. In dashed green is the gaussian profile, in blue is the absorbed flux and in red is the emitted flux; d) schematic depicting the process of down-shifting by an LDS material.

3.2 Simulation Method

The present work shows how to ideally design the DS effect in order to attain: 1) maximum optical improvement in the PSCs, represented in terms of their overall photocurrent density, J_{ph}; 2) negligible UV degradation by minimizing both the light absorption in the TiO_2 across the full spectral range, and the UV photocurrent (i.e. carrier generation in the perovskite

due to UV absorption) calculated for wavelengths between 300 and 400 nm, henceforth $J_{ph\text{-}UV}$, as also addressed in chapter 2.

The results were obtained using a numerical solver (FDTD Solutions) provided by *Lumerical Inc.*[163] The use of this method allows for the calculation of the electric and magnetic fields in the entire simulation region as explained in details in section 2.3 of chapter 2. However, this an electromagnetic method based on Maxwell's equations, it cannot exactly simulate the effect of DS. Consequently, here DS was modelled by proper adaptation of the incident spectrum, as described in Figure 8c. Based on absorption and emission profiles of typical LDS materials, taken from several reports[60], [98], [149], [153], [164]–[166], a Gaussian profile was chosen to emulate these properties - Figure 8c) green dashed profile. Gaussian profiles have three main variables: the Gaussian root mean square (RMS) width, parameter related with the full width at half maximum (FWHM) which was fixed at 50 nm; the gaussian center, λ_C, that was left as a variable; and the amplitude, representing the peak absorption, that was fixed at unity. This gaussian absorption was then multiplied with the solar photon flux, based on the ASTM G-173 global irradiance spectra provided by NREL,[167] to calculate the hypothetical absorption flux in a thick DS layer - Figure 8c) blue profile. Subsequently, this absorbed flux is shifted to higher wavelengths, as shown in Figure *8*c), by a shifting parameter, $\Delta\lambda$, that was also left as a variable. Lastly, to create the "shifted" spectrum incident on the PSC, the absorbed flux was subtracted, while the emission flux was added to the pristine AM1.5G spectrum. For that, the resulting spectral irradiance plots for two different $\Delta\lambda$ and λ_C was calculated. It should be noted that the process used to emulate the DS process is an ideal one and, thus, does not account for effects such as isotropic emission, non-unitary quantum efficiency and reabsorption.

3.3 Results and Discussion

Firstly, the solar cells' absorption profiles were determined by the aforementioned method and are displayed in Figure 9a) and b) for the PCs and in Figure 10a) and b) for the LTCs, considering the $n_{Background} = 1.0$ and $n_{Background} = 1.5$. These absorption profiles only depend on the solar cells' structure and materials, being independent of the illumination spectrum. Therefore, they are suited to evaluate the device's optical performance. For red-NIR wavelengths there is a decrease in the cell absorption as sub-bandgap photons are harder to absorb. This is effectively shown by the absorbed power density plots shown for 900 nm wavelength (rightmost inset profiles in Figure 9 and Figure 10), as the absorption is rather uniform throughout the cell. Note that, for the LTCs, these losses are reduced using the photonic structures responsible for scattering light. For shorter wavelengths, the most notable aspect is the parasitic absorption from TiO_2 and ITO for both PCs and LTCs. The absorbed power density plots (leftmost inset plots in Figure 9 and Figure 10 at 350 nm wavelength) again serve to further verify this statement, as they show a pronounced absorption in the TiO_2 and ITO layers.

Furthermore, the LTCs show an effective UV shading of the perovskite, revealed by the red shaded area in the absorption spectra of Figure 10 a) and b) as well as the substantial absorbed power density in the front LT structures shown by the 350 nm inset profiles in Figure 10. This increase is due to the thick TiO_2 used in these structures, as it is the material responsible for the light trapping effects (i.e. improved broadband anti-reflection and scattering).[162] It should be noted that such UV shading is also beneficial for the perovskite cells, due to the UV instability problems.

Subsequently, sweeps were made for the different cells in study, where $\Delta\lambda$ and λ_C where varied between 100-400 nm and 300-400 nm, respectively. The resulting photocurrent contour plots for the PCs are shown in Figure 9 c) and d), and for the LTCs in Figure 10 c) and d). Firstly, one should note that the photocurrent contour plots (in Figure 9 and Figure 10) show a similar behavior, which is expected as these results are chiefly influenced by the absorption in the Perovskite layer, which is mostly similar in the 400-700 nm wavelength range for the different solar cells (Figure 9 a) and b) and Figure 10 a) and b)). At around 700 nm, value close to the perovskite's bandgap[10], [14], a significant drop in absorption occurs, as below-bandgap absorption is significantly reduced. Thus, it is expected that the photocurrent sweeps should also see this effect when the shifting occurs to higher wavelengths. Indeed this is the case, and, for the LTCs, this drop can be up to 7% lower than that of the corresponding pristine (without DS) structure (shown in Figure 10 c) and d) by the white line), while for the PC this value can be up to 12% lower. Therefore, it should be noted that the use of unoptimized LDS material properties can severely degrade the solar cell's performance.

Considering the photocurrent gains summarized in Table 3, when comparing the pristine AM1.5G spectrum with the shifted spectra, one can see that there is only a small increase in the cell's performance, even when considering the optimized λ_C and $\Delta\lambda$ values indicated in Table 3. For the LTCs, this J_{ph} increase was up to ~2% (~0.6 mA/cm^2), while for the PCs it was up to ~1% (0.2-0.3 mA/cm^2), with the main difference being attributed to higher TiO_2 thickness in the first, as this layer is mainly responsible for UV parasitic absorption. It should be noted that, when integrating the ASTM G-173 solar irradiance spectra in the UV wavelength range (i.e. from 300-400 nm), the maximum current density that can ideally be generated is only ~1.4 mA/cm^2, which sets the limit for the increase in photocurrent that can be attained using DS methods. Secondly, the outstanding perovskite's absorption properties are also a factor limiting further photocurrent increases. From the absorption profiles shown in Figure 9 and Figure 10, it can be seen that under 400 nm there is still some significant perovskite absorption. As such, and understandably, LDS materials cannot directly provide major photocurrent improvements in PSCs.

Nevertheless, it should be emphasized that the main objective of this method is to reduce the harmful effects of UV radiation on PSCs, and for that the optimized DS+LT solution presented here is shown to be outstanding. On the other hand, electrical effects were not taken into account here. However, considering that the sum of the $\Delta\lambda$ and λ_C values (resulting in the

wavelength to where the shifting occurs) is around 500 nm, an improved electrical performance would be expected as this value corresponds with the reported external quantum efficiency maximum[98], [121], [141], [168].

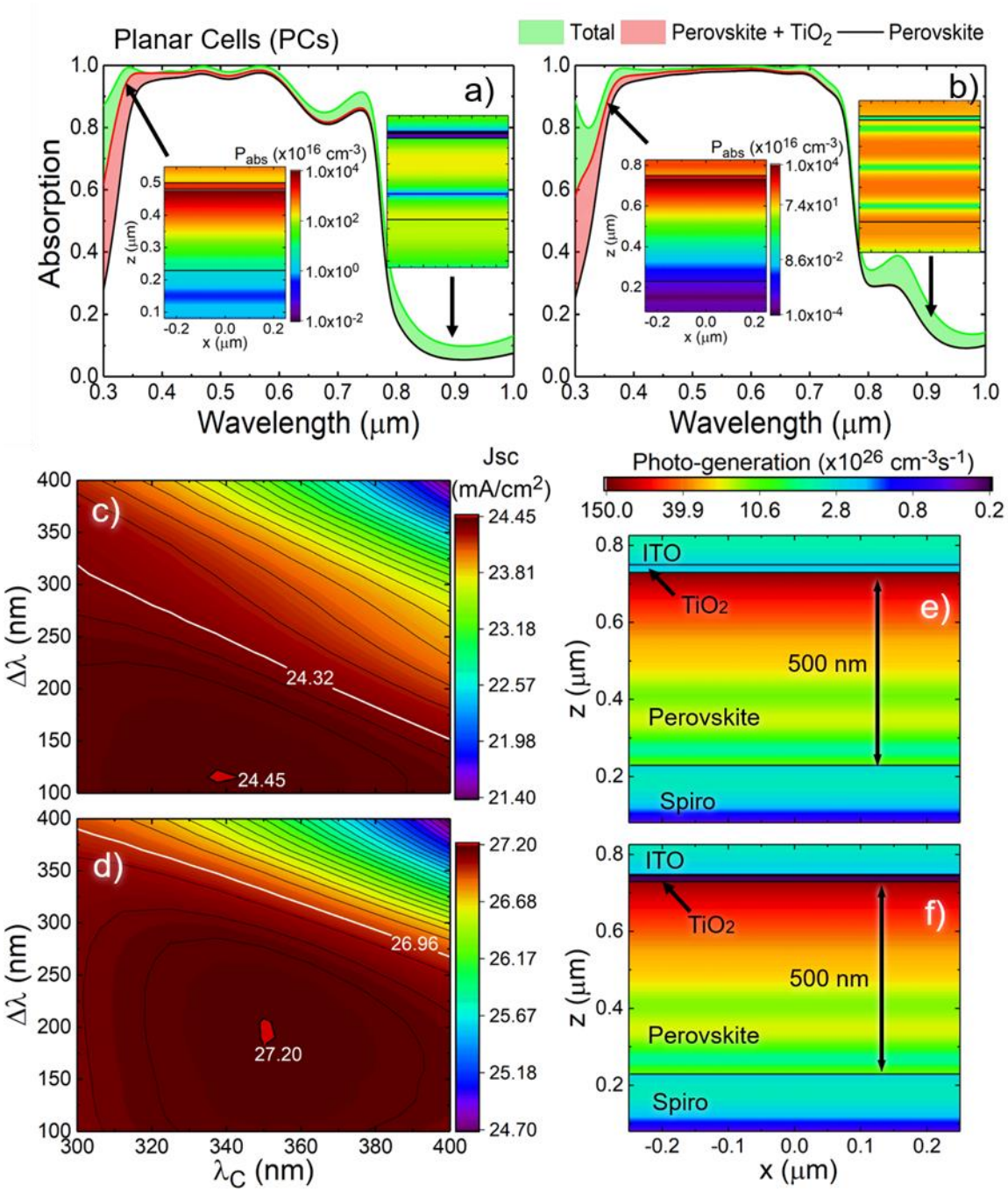

Figure 9*:* Results for the PCs structure with $n_{Background}$ of 1.5. a) and b) are the absorption profiles calculated for the PCs with perovskite thickness of 250 and 500 nm, respectively. The black curve corresponds to the light absorption in the perovskite layer; in red, the perovskite+TiO_2 absorption; and, in green, the total absorption of the cell. The inset plots represent the absorbed power density through the cross section of the cell, calculated at specific wavelengths indicated by the arrows: the leftmost profile is the absorbed power for 350 nm and the rightmost graph is the absorbed power for 900 nm; c) and d)

are the contour plots of the photocurrent density (J_{ph}) sweeps performed for the PC structure with 250 nm and 500 nm perovskite layer, respectively; the white contour line represents the pristine J_{ph}, i.e. the value attained with the AM1.5 incidence spectrum without any shifting. e) and f) are examples of the carrier generation profiles for the PC with 500 nm perovskite layer, considering the pristine and the optimized (using the λ_C and $\Delta\lambda$ corresponding to the maximum in d)) incidence spectrum, respectively.

Afterwards, the generation profiles were calculated using the optimum shifting parameters (λ_C, $\Delta\lambda$) obtained from the photocurrent sweeps (Table 3). These profiles are shown in Figure 9 e) and f) for the PC and Figure 10 e) and f) for the LTC, considering 500 nm perovskite thickness. In all these cases, a major reduction in the photo-generation of TiO_2 is observed resulting from the use of a shifted spectrum. Examining the LTC case (Figure 10 e) and f)), it can be seen that these values vary from around 1.6-0.2x10^{26} $cm^{-3}s^{-1}$ for the pristine spectrum to 0.1-0.02x10^{26} $cm^{-3}s^{-1}$ for the optimized spectrum, representing a pronounced change of one order of magnitude. Therefore, optimally-shifting the spectrum can almost eliminate the harmful photo-generation of TiO_2 and, in practice, lead to improved device stability. On the other hand, when comparing Figure 10 e) and f) it can also be seen a reduction in the absorption in the perovskite in the reddish "corner" region indicated by the arrow. This stems from the higher wavelength radiation incident upon the cell, that has a higher penetration depth, resulting in a higher solar cell bulk absorption instead of front surface absorption. A similar effect is also seen in Figure 9 f), where the bulk generation is higher from this effect. Electrically, this shift from surface to bulk absorption can also have a beneficial impact in the solar cell performance, as in surface absorption there is more electron recombination, particularly in PSCs[169].

Thereupon, the photocurrent values for wavelengths ranging from 300-400 nm ($J_{ph\text{-}UV}$ representing the UV absorption) were calculated using the pristine and optimized spectra, in order to assess how the shifting can impact the perovskite's UV absorption. These values are summarized in Table 4. Taking the example of the LTC with 250 nm perovskite thickness, for the pristine spectrum the calculated $J_{ph\text{-}UV}$ was 0.7 mA/cm^2, while for the optimized spectrum this value was 0.1 mA/cm^2, representing a reduction of 86% in the harmful UV photo-generation in the perovskite. The reductions for the other cases are all also around 80% (Figure 11 b)). Therefore, a remarkable reduction in the perovskite's UV absorption is determined as a result of the optimized shifting. Consequently, both the reduction in the perovskite's UV absorption and the lower harmful photo-generation of TiO_2, are expected to yield a pronounced improvement in the life-time of PSCs implementing such DS solution. From the generation profiles for the LTC (Figure 10 e) and f)), it can be seen that the photo-generation in the TiO_2 close to the perovskite interface (a critical region for the degradation mechanisms to occur)[137], [139] is lower than at the topmost part of the TiO_2 structures. This reduction occurs due to the UV shading effect that comes from the use of relatively-thick high index front structures, providing further protection against UV radiation for the device.

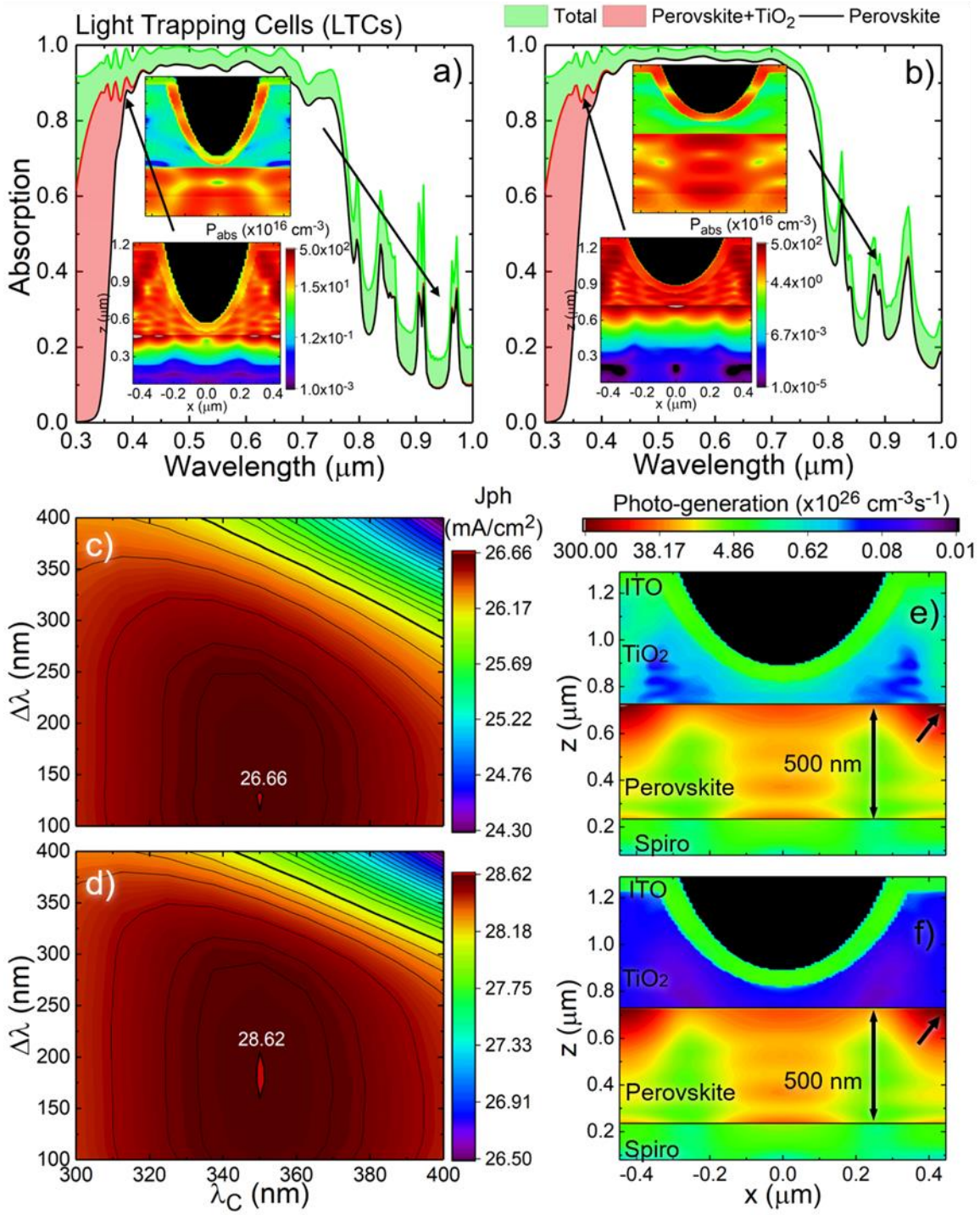

Figure 10: Results for the LTCs with $n_{Background}$ of 1.5. a) and b) are the absorption profiles calculated for the LTCs perovskite thickness of 250 and 500 nm, respectively. The black curve corresponds to the light absorption in the perovskite layer; in red, the perovskite+TiO_2 absorption; and, in green, the total absorption of the cell. The inset plots represent the absorbed power density through the cross section of the cell, calculated at specific wavelengths indicated by the arrows: the leftmost profile is the absorbed power for 350 nm and the rightmost graphs is the absorbed power for 900 nm. c) and d) are the contour plots of the J_{ph} sweeps performed for the LTC structure with 250 nm and 500 nm perovskite layer, respectively; the thicker contour line represents the pristine J_{ph}, i.e. the value attained with the AM1.5 incidence spectrum without any shifting. e) and f) are examples of the carrier generation profiles for the

LTC with 500 nm perovskite layer, considering the pristine and the optimized (using the λ_C and $\Delta\lambda$ corresponding to the maximum in d)) incidence spectrum, respectively.

Table 3: Summary of the main results from the photocurrent density sweeps performed in this work. $t_{Perovskite}$ represents the perovskite thickness, $n_{Background}$ is the refractive index used for the background medium, pristine J_{ph} is the value using the illumination spectrum without any shifting, optimized J_{ph} is the highest value obtained in the sweeps of Figure 9 and Figure 10, λ_C and $\Delta\lambda$ is the gaussian center and shifting parameter, respectively, corresponding to the maximum photocurrent value obtained in the sweeps.

	Planar Cell (PC)				LT Cell (LTC)	
$n_{Background}$	1		1.5		1.5	
$t_{Perovskite}$ (nm)	250	500	250	500	250	500
Pristine Jph (mA/cm²)	22.9	25.9	24.3	27.0	26.1	28.1
Optimized Jph (mA/cm²)	23.0	26.3	24.5	27.2	26.7	28.6
λ_C (nm)	387	400	337	350	350	350
$\Delta\lambda$ (nm)	145	205	115	205	130	190

The bar chart of Figure 11 summarizes the key results from this work. Starting with the photocurrent chart (Figure 11 a), a first point to be made is the higher current for the 500 nm PSCs, resulting from the thicker absorber. This difference is due to higher red-NIR radiation absorption, as demonstrated in Figure 9 b) for the PC and Figure 10 b) for the LTC. Secondly, the higher J_{ph} for the PC with $n_{Background}$ of 1.5, when compared to the equivalent cell with index of 1, stems from better index matching between the background and the front material in the cell (ITO). On the other hand, it can also be seen that the LTCs have higher J_{ph} when compared with their planar counterpart. This increase clearly demonstrates the benefits of using photonic structures for LT, allowing for optically thick but physically thin devices.

The graph also indicates small current increases when using the optimized spectrum. Considering that electrical losses are neglected in these studies, it can be inferred from Figure 11 a) that these materials do not show a pronounced increase in optical performance. However, these same effects, such as bulk instead of surface absorption and lower thermal losses that come with higher energy transitions, can be deciding factors leading to improved cell current.

Table 4: Summary of the photocurrent density values, $J_{ph\text{-}UV,}$ calculated only in the UV wavelength range (300-400 nm) for the perovskite layer with the pristine, i.e. the unaltered $AM_{1.5}$ spectrum, and the optimized spectrum, i.e. the spectrum using the optimized down-shifting parameters obtained in the photocurrent sweeps of Figure 9 and Figure 10.

	Planar Cell (PC)				LT Cell (LTC)	
$n_{Background}$	1		1.5		1.5	
$t_{Perovskite}$ (nm)	250	500	250	500	250	500
Pristine $J_{ph\text{-}UV}$ (mA/cm²)	1.0	1.0	1.2	1.1	0.7	0.7
Optimized $J_{ph\text{-}UV}$ (mA/cm²)	0.2	0.2	0.3	0.2	0.1	0.1

The bar chart analyzing the $J_{ph\text{-}UV}$ in Figure 11 b) shows that a remarkable reduction of around 80% is observed for all cases in the UV light absorption by the perovskite material. Therefore, by maintaining a similar optical current, while significantly reducing the harmful effects of UV radiation in these cells, an increased long-term performance is anticipated.

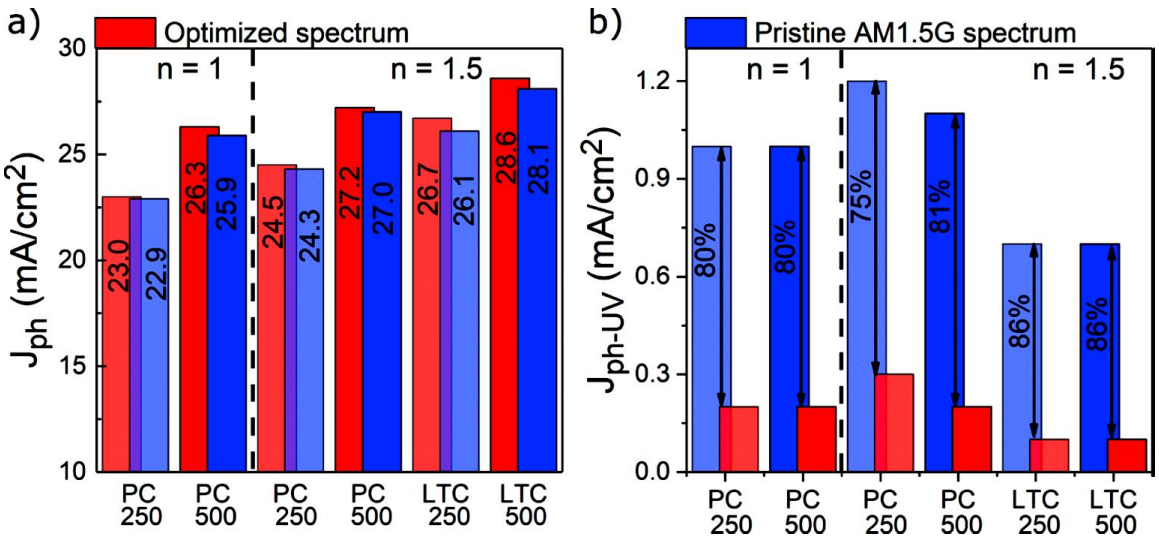

Figure 11: Bar charts summarizing the results from the photocurrent sweeps attained with the pristine (blue) and optimized (red) spectra incident on the PC and LTC PSCs with either 250 or 500 nm Perovskite thickness. a) J_{ph} values obtained considering the full UV-Visible-NIR wavelength range (300-1000 nm); b) UV photocurrent ($J_{ph\text{-}UV}$) values for wavelengths ranging from 300 to 400 nm. The more transparent bars refer to the devices with 250 nm perovskite thickness, while the others refer to those with 500 nm perovskite thickness.

3.4 Conclusions

The use of optimized DS materials in the PSCs' encapsulation revealed a marginal increase in photocurrent at best of 2% (~0.6 mA/cm²). This is due to the inevitable fact that there is not so much current that can be gained from exploiting the UV, and one is limited to the

maximum gain that can be obtained by absorbing all this radiation, which of only 1.4 mA/cm^2. On the other hand, the use of unoptimized $\Delta\lambda$ and λ_C revealed a severe impact in the optical performance of the cells, reducing the photocurrent by 7% and 12% for the worst cases simulated of the LTCs and PCs, respectively. The optimum $\Delta\lambda$ and λ_C implied a spectrum shift to wavelengths around 500 nm, matching well with the PSC's electrical performance peak.

Importantly, from the analysis of the perovskite stability, one obtained a significant reduction in the TiO_2 harmful photo-generation of one order of magnitude, coupled with an increase in the perovskite's bulk generation. The LTCs revealed a further decrease in the TiO_2 photo-generation near the perovskite/TiO_2 interface due to the UV shading effect provided by the LT structures. By assessing the perovskite UV photocurrent for the different simulated cells, reductions up to 86% were obtained when comparing J_{ph} values for the pristine and changed spectrum. Therefore, from these analyses, one can infer that the use of LDS avoids the unwanted effects of UV radiation on the perovskite, demonstrated by the hefty decrease in UV absorption coupled with the diminished TiO_2 photoactivity resulting from lower photo-generation.

4

WAVE-OPTICAL STRUCTURED SUBSTRATES FOR ULTRA-THIN PEROVSKITE SOLAR CELLS

4.1 Introduction

In earlier theoretical contributions[7], [18], [19] as presented in chapter 2, novel LT designs operating in the wave-optics regime were shown to allow pronounced photocurrent gains in thin-film solar cells via the incorporation of wavelength-sized pyramidal-like features in the front contact of PV devices with a substrate configuration. This enabled the demonstration of LT levels approaching the ideal Lambertian limits of geometric optics. However, the implementation of such LT architecture may be difficult to realize in practice, since the photonic elements need to be patterned on top of the planar cell layers, during the final processing stages, which may cause the degradation of the delicate materials of the devices during the micro-patterning fabrication[44], [119].

In this work, an unprecedented wave-optical solution was explored for PSC application, via the optimization of photonic-structured substrates supporting the cells. By micro-patterning the substrates with wavelength-sized semi-spheroidal features, it is possible to achieve high-performing LT-enhanced PSCs due to the conformal deposition of the cells' materials onto the photonic substrates. Such innovative industrially-attractive LT design is studied and optimized here for two different solar cell configurations: superstrate and substrate; considering distinct perovskite absorber thicknesses (300 and 500 nm), as sketched in Figure 12. This approach has significant practical benefits regarding its applicability, when compared with post-patterned photonic structures implemented on the ETLs, since here the PSC layers are wet-coated by usual methods over a substrate already patterned with LT structures, hence making the photonic integration independent of the PSC's fabrication. This is particularly beneficial in order to prevent the LT implementation from deteriorating not only the PSC layers

but also less robust polymeric substrates used in flexible devices[8], [170]. Besides, this enables the widespread application of the micro-structured substrates as generic photonic platforms to support other types of thin-film PV devices (based in Si[7], CIGS[171], CZTS[172], organic[8], tandems[173] etc.), after straightforward adaptation/tuning of the geometrical parameters of the LT structures.

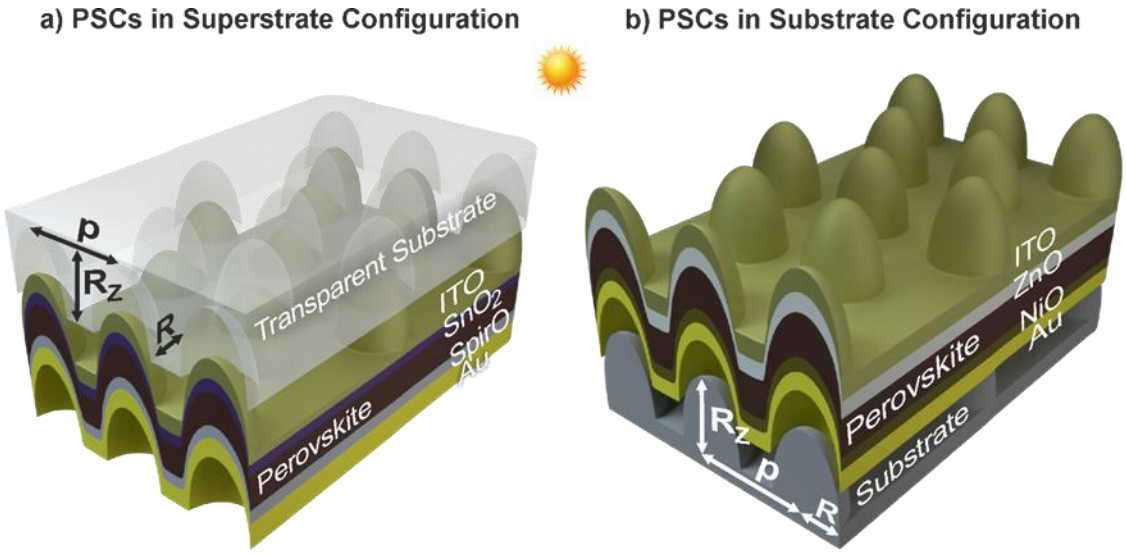

Figure 12: Two types of photonic-patterned substrates were studied and optimized for two types of PSC architectures: the conventional superstrate configuration (a), compatible only with transparent substrates (e.g. flexible polymers as PEN/PET)[121], [170]; and the so-called "inverted" substrate configuration (b) enabling a larger variety of substrates (e.g. flexible opaque materials as metal sheets)[101], [112], [121]. The LT structures patterned on the substrates are modelled as a hexagonal array (with pitch p) of vertically-aligned semi-prolate features with radii R and R_Z, respectively along the in-plane direction and illumination axis. The PSC layers are conformally deposited over such spheroidal features: a) superstrate-type layer configuration, in which light comes into the devices from the substrate side, composed of transparent conducting oxide (TCO, made of ITO/electron transport layer (ETL, made of SnO_2)/perovskite absorber (methylammonium lead iodide, $CH_3NH_3PbI_3$)/hole transport layer (HTL, made of Spiro-OMeTAD/rear metal contact (made of gold, Au); b) substrate-type layer configuration, in which light comes into the devices from the films' side, composed of TCO (made of ITO)/ETL (made of ZnO)/perovskite ($CH_3NH_3PbI_3$)/HTL (made of NiO_x)/rear contact (Au).

Previous work has shown that hexagonal arrays of high-index semi-spheroidal features patterned on the cells' illuminated front surface allow pronounced broadband absorption enhancement in the PV absorber of thin-film solar cells[7], [19], [44], [119]. Here, such type of features is produced in the cells' front due to the conformal deposition of the PSC layers over the patterned substrates (see Figure 12). Apart from allowing higher optical density with thinner absorber thickness, the LT geometries investigated here provide three other practical advantages: 1) the "round" spheroidal-type shapes can avoid losses associated with nanostructures having high spatial curvatures or sharp edges[17], [174]; 2) arrays of such semi-spheroidal features can be easily fabricated by industrially-attractive patterning methods such as col-

loidal lithography - a low cost soft-lithography process capable of engineering with nano/micrometer resolution with high uniformity throughout large areas[44], [119]; 3) the inherent wide angular acceptance of this type of structures is particularly important for flexible solar cells[7], [174], since their operation under bending implies the simultaneous conversion of light coming from a broad angular range.

4.2 Modelling Method

We employed a 3D finite difference time domain (FDTD) numerical method to rigorously model optical effects in the photonic-structured PSCs[7], [18], [19], [107]. This method is regarded as a preferential approach for solving electromagnetic problems in the wave-optics regime, especially for light management in solar cells, mainly owing to its conceptual simplicity and versatility[18]. Furthermore, its capability for single-run broadband simulations is of particular interest for application in photovoltaics[7], [17], [19]. The two different PSC architectures of Figure 12 were modelled, in which the solar cells are composed of 5 layers conformally coated onto micro-structured substrates. The optical response of the materials is determined by their complex refractive index ($N=n+ik$) spectra, which were taken from published experimental. The perovskite absorber material considered in this work is methylammonium lead iodide, $MAPbI_3$, taking a widely-used refractive index function fitted from measured values provided by Phillips *et al.*[14], available in a common database[175]. However contrarily to other more matured PV technologies, PSCs are still highly dependent on the specific fabrication conditions and process materials used. Therefore, there is presently no (n, k) dataset that can be taken as technological standard. In view of that, for comparison the main computations presented here were recalculated considering a different measured refractive index provided by Eerden *et al.*[176], whose results can be found elsewhere [94]. For the superstrate configuration (Figure 12 a), the refractive index of the transparent substrate was accounted for by a fixed real value, attributed to the background index of the simulation volume, equal to n=1.5 (e.g. similar to the index of PET)[175]. For the substrate configuration (Figure 12 b), a background index n=1.6 was taken in order to account for a typical transparent adhesive material used for encapsulation over the PSC layers[175].

The detailed procedures of optical simulation are given in section 2.3 of chapter 2.

4.3 Optimized photonic-structured perovskite solar cells

In this section we present the results of the optimized LT structures considering both configurations depicted in Figure 12. The superstrate configuration (Figure 12 a) is the current record efficiency holder in PSCs[38]. Nevertheless, the requirement for superstrate solar cells to be supported on transparent substrates is a major limiting factor if one is to achieve ultrathin and flexible devices. This can be mostly attributed to the proclivity for low degradation

temperatures, usually seen in bendable transparent materials (e.g. PEN, PET), that severely restricts the PSCs fabrication conditions[121]. Subsequently, there has been a shifting interest to the substrate configuration (Figure 12 b), since it allows for a more versatile gamut of materials to be used, such as the case of opaque and much more robust bendable materials (e.g. metal foils, PI)[101], [112], [121]. Besides, the substrate-type PSC structure is compatible with its application as sub-cell in monolithic tandem devices (e.g. perovskite top cells coupled with Si[173] or CIGS[121] bottom cells), which is another research line attracting much interest lately.

The materials considered for the PSCs' layer structure are based on state-of-the-art devices produced with low-temperature (< 200 °C) fabrication, to allow compatibility with polymeric flexible substrates. Different materials are considered for the ETL and HTL in each configuration: SnO_2 and ZnO are the materials taken for the ETLs, and Spiro-OMeTAD and NiO are those of the HTLs, respectively in the superstrate and substrate configuration. Apart from their low-temperature processing, both ETL materials have recently been revealing better stability and performance than the conventional TiO_2[38], [177], [178]. As for the HTLs, Spiro is the material that has allowed the highest efficiencies so far. However, due to its high cost, other HTLs have been investigated, being NiO-based materials those that appear to be the best alternative, especially for flexible applications that can particularly benefit from low-cost devices[179]. The conventional MAPI (methylammonium lead iodide) perovskite was taken for the absorber material, with two different thicknesses analyzed in this work: the standard 500 nm and a thinner 300 nm layer.

Table 5 shows the sets of relevant physical parameters optimized for the cell designs, where R, R_z and p define the geometry of the LT features patterned on the substrates (see Figure 12) and the values t_{layer} correspond to the thickness of specific flat layers. These quantities were taken as variables by the PSO algorithm that iteratively searched for the best set of parameters that maximizes the photocurrent (J_{ph}, equation 2) produced in the perovskite material. Row 1 of Table 5 shows the *Lambertian* limits of geometrical optics for the analyzed perovskite absorber layers, as described in chapter 2 [19]. In this case, the values of the LT enhancement were calculated relative to a cell without LT in the same regime of geometrical optics. Row 2 and 4 present the optically-optimized values for the thicknesses of the front contact of planar PSCs, which provides an anti-reflection coating (ARC) effect, and of the HTLs, respectively for superstrate and substrate configuration. These serve as reference results for comparison with the ones obtained with the photonic semi-spheroidal structures shown in rows 3 and 5, respectively.

Table 5: Highest J_{ph} values obtained for the optimized LT structures for two distinct PSCs, with 300 or 500 nm perovskite layer thicknesses, in two different solar cells configurations, superstrate and substrate-type, considered in this work. The geometrical optimization parameters (R, R_Z, p, t_{ITO}, t_{SnO2}, t_{Spiro}) and (R, R_Z, p, t_{ITO}, t_{ZnO}, t_{NiO}), for the LT structures in superstrate and substrate configurations, respectively, are sketched in Figure 12. The results are compared with the reference cases of planar PSCs

having optically-optimized TCO/ETL and HTL thicknesses, as well as with the theoretical limits in the regime of geometrical optics attainable with a Lambertian scattering front surface.

Light Trapping Structures	Absorber: **300 nm Perovskite layer**		Absorber: **500 nm Perovskite layer**		*Row index*
	Optimal Parameters	***Jph***, mA/cm² (LT enhancement)	Optimal Parameters	***Jph***, mA/cm² (LT enhancement)	
Lambertian surface	-	**33.8** (28.0%)	-	**35.3** (25.0%)	***1***
Optimized Planar PSCs in Superstrate Configuration	t_{ITO} = 50 nm t_{SnO2} = 25 nm t_{Spiro} = 50 nm	**25.0**	t_{ITO} = 50 nm t_{SnO2} = 25 nm t_{Spiro} = 50 nm	**27.1**	***2***
Optimized Photonic PSCs in Superstrate Configuration	t_{ITO} = 50 nm t_{SnO2} = 25 nm t_{Spiro} = 50 nm R = 219.2 nm Rz = 167.6 nm p = 558.6 nm	**30.7** (22.8%)	t_{ITO} = 50 nm t_{SnO2} = 25 nm t_{Spiro} = 50 nm R = 206.2 nm Rz = 259.8 nm p = 508.1 nm	**32.5** (20.0%)	***3***
Optimized Planar PSCs in Substrate Configuration	t_{ITO} = 50 nm t_{ZnO} = 100 nm t_{NiO} = 10 nm	**22.5**	t_{ITO} = 50 nm t_{ZnO} = 100 nm t_{NiO} = 10 nm	**25.1**	***4***
Optmized Photonic PSCs in Substrate Configuation	t_{ITO} = 50 nm t_{ZnO} = 100 nm t_{NiO} = 10.1 nm R = 239.0 nm Rz = 309.2 nm p = 480.1 nm	**28.0** (24.4%)	t_{ITO} = 50 nm t_{ZnO} = 100 nm t_{NiO} = 11.1 nm R = 200.2 nm Rz = 519.3 nm p = 484.4 nm	**30.2** (20.3%)	***5***

The PSO "smart search" was constrained to certain parameters' boundaries that were set based on reasonable values for their domains. Several optimization runs were performed with different initial parameter sets spanning the domain space, and it was found that the algorithm consistently converged to thicknesses of the selective contact layers (t_{ITO}, t_{SnO2}, t_{Spiro}, t_{ZnO}, t_{NiO}) at the minimum allowed value of the domain, defined to guarantee their electrical performance. Therefore, it is clear that such layers are optically undesirable, but their presence is electrically needed with a minimum thickness to guarantee effective current extraction[180], [181]. The variation of photocurrent with the thickness of such contact layers is analyzed and can be found here [94]. As the main goal here is the investigation of an optical scheme yielding the maximum degree of light trapping in PSCs, the present study considered optically-favorable values for such layer thicknesses indicated in Table 5, corresponding to the minimum

values within the defined "electrical limits" marked [94]. As can be observed these figures, different thicknesses would lead to slight deviations in the optimized parameters and resulting J_{ph} maxima, but would not imply significant differences in the overall trends and discussion given here[7], [18], [19].

4.3.1 Photonic-enhanced PSCs in superstrate configuration

We begin by analyzing the results obtained with the optimized set of geometrical parameters of PSCs in superstrate configuration (depicted in Figure 12a), which are presented in Figure 13. The absorption spectra of the optimized LT structures (corresponding to row 3 of Table 5) are compared to those of the planar reference cells (row 2 of Table 5) in Figure 13a,b, for the perovskite absorber thicknesses (300 and 500 nm) considered in this study. Figure 13c,d show the p_{ABS} profiles of PSCs with LT structures, along the *xz* plane passing by the center of a semi-spheroidal feature, for four different wavelengths along the illumination spectrum.

Looking at the reference planar cells (blue curves in Figure 13a,b), both 300 and 500 nm cells show a similar broadband behavior, with the 300 nm cell presenting an overall lower absorption, from the shorter light travel path in the absorber. The considerably high absorption in the perovskite active region (mainly corresponding to the 450-750 nm wavelength range in Figure 13) evidences well the outstanding perovskite optical properties, preceded by a small absorption drop in the UV-blue range (300-450 nm) due to reflection and parasitic absorption in the front contact (ITO and SnO_2 layers). This drop is slightly lower (~5%) for the 300 nm thick cell. In the near-infrared (NIR) there is a more abrupt absorption drop above 750 nm (nearing 86% and 89% for the 500 and 300 nm thickness, respectively) that coincides with the ~1.5 eV bandgap of the perovskite absorber. Regarding the photonic LT structures (red curves in Figure 13a,b), there is a pronouncedly higher broadband absorption occurring in the perovskite, brought out by the superior light management scenario created by the photonic features, as explained below.

The results of Figure 13 demonstrate a key optical advantage of using photonic-structured PSCs via conformal deposition over patterned substrates: the fact that it is the higher-index perovskite material that plays the main role in anti-reflection and light scattering, which causes the notable absorption gains and extremely low parasitic absorption (even lower than the reference planar cells) in most of the spectrum. The inset images of Figure 13a,b show the cross section of the solar-spectrum-weighted generation rate (*G*) along the PSCs with the optimized LT structures, computed over the 300-1000 nm wavelength range. It is notable from these inset profiles that the spectral-integrated absorption occurs primarily in the perovskite. However, Spiro-OMeTAD and Au also show some parasitic contribution, complementarily evidenced in the absorption density profiles (Figure 13 c,d), especially for longer NIR wavelengths.

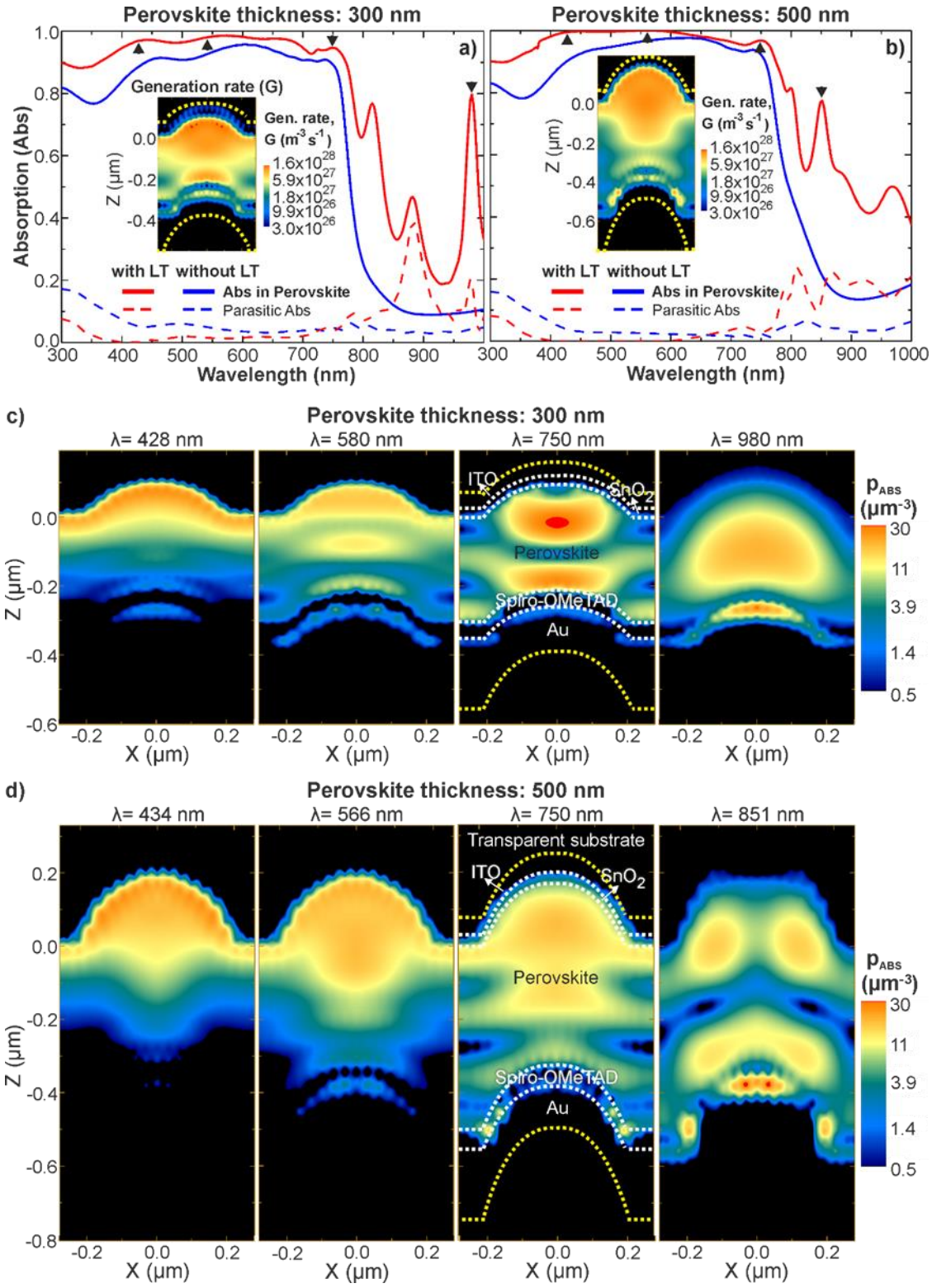

Figure 13: a,b) Absorption spectra obtained with the optimized LT structures sketched in Fig. 1a, for PSCs in superstrate configuration (red lines, row 3 of Table 5), compared the reference cases of optically-optimized planar cells (blue lines, row 3), for perovskite layers with distinct thickness: a) 300 nm and b) 500 nm. Each graph presents the absorption occurring in the perovskite (solid lines) and the parasitic absorption in the other materials (dashed lines). The inset profiles represent the log-scale dis-

tribution of the corresponding total generation rate, G, along the xz cross-sectional plane of the structures passing by the semi-spheroidal center. c,d) Log-scale distributions of the absorption density, p_{ABS}, along the same xz plane of the structures, at the wavelengths of the peaks marked by the arrows in a) and b), respectively for the PSCs with the 300 nm (c) and 500 nm (d) thick perovskite absorbers in superstrate configuration.

The absorption gains in the UV-VIS are attributed to a better light coupling towards the perovskite material by the semi-spheroidal LT features, as a consequence of two optical mechanisms: 1) superior anti-reflection owing to the geometrical index matching[7], [19] caused by the curvature of the front layers (ITO, SnO_2 and perovskite) coupled with the propinquity amongst the real part (n) of the refractive indices of ITO, SnO_2 and perovskite [94]. 2) Near-field forward-scattering[7], [19] due to the micro-lens effect of the curvature of these three layers, which causes the focal regions of intense electric-field in the top portion of the perovskite observed in the G profiles of Figure 13a,b and in the p_{ABS} profiles of Figure 13c,d (mainly for the indicated wavelengths of 580 nm and 566 nm, respectively). It should be noted that the absorption enhancement observed in this spectral range (<750 nm) cannot be due to the rear contact pattern, as the light is strongly absorbed before reaching the back.

In the NIR range, the remarkable absorption increase is chiefly due to the far-field forward scattering caused by the semi-spheroidal shape of both the front and rear features of the PSCs structure, which is favoured by the high real part (n) of the perovskite refractive index. This effect manipulates the vertically-impinging light and redirects it to paths closer to the horizontal plane, thereby leading to optical path length amplification within the cell and coupling with waveguided modes. This is evidenced by the "hot-spots" observed in the p_{ABS} profiles for wavelengths >700 nm, which result from constructive interference between the light waves traveling along the incidence direction and the scattered light that travels along the plane of the cell layers suffering multiple reflections from the top and bottom surfaces of the cell. In this longer wavelength region, the sharp absorption peaks observed in Figure 13a,b are mainly attributed to guided-mode resonances, as supported by related studies of LT-enhanced thin-film PV[7], [17]–[19], [182]. Such resonances were observed to be mostly sensitive to the variation of the in-plane dimension (radius R) and center-to-center distance (pitch, p) of the photonic elements. This is due to the fact that R is the chief parameter determining their scattering cross sections; while p establishes the periodicity and, thus, determines the trapping of waveguided modes in this spectral range[7], [18], [19]. Results on the LT sensitivity to variations in the geometrical parameters of the photonic structures are presented in Section 5.

Concerning the parasitic absorption, below 500 nm wavelengths it mainly occurs within the front ITO and SnO_2, as evidenced by the p_{ABS} plots of Figure 13c,d. For longer wavelengths it is mostly relegated to the cell's rear contact (Spiro-OMeTAD/Au), with also some contribution from SnO_2 as evidenced by its increasing imaginary part (k) of the refractive index in the NIR [94]. The p_{ABS} plots for >500 nm wavelengths illustrate well this effect. It should also be noted that, throughout the UV-VIS range, the photonic-structured devices show significantly

lower absorption losses when compared with the reference ones. This is mostly due to the geometrical index matching caused by the front curvature of the perovskite absorber, which provides a better coupling of light towards such material with high n, preventing its back-reflection towards the ITO/SnO_2 top layers. Nevertheless, in the NIR range (750-1000 nm wavelengths) the parasitic absorption is notably higher with LT structures due to the plasmonic effect caused by the corrugated Au metal layer[17], as seen in the G and p_{ABS} profiles of Figure 13, which does not occur in the flat metal present in the planar cells [94]. The periodic corrugations of the metallic layer lead to surface plasmon-polariton modes [17] that are confined in a near-field vicinity of the metal-HTL interface, so they mainly lead to enhanced parasitic light absorption within such rear contact. This is supported by the fact that, in the wavelength range (above ~700 nm) where the HTL and rear metal play a pronounced optical role, similar parasitic absorption is observed with the two different perovskite absorber properties considered by the aforementioned distinct refractive index functions of Phillips *et al.*[14].

Comparing this LT design to that of additional thick photonic structures coated on top of the solar cell, as analyzed in a previous study[19], the present implementation bypasses the parasitic absorption within such thick structures, especially for shorter wavelengths. This is because of two reasons: first, the optimized thicknesses of the structured front layers of ITO (50 nm) and SnO_2 (25 nm) are relatively small and the same as the reference cells, thence the parasitic absorption in these materials is quite low; and second, the perovskite is the main scattering material benefiting from an extremely high absorption coefficient (k values) in this range, which also helps mitigate parasitic absorption.

4.3.2 Photonic-enhanced PSCs in substrate configuration

In this section, we analyze the results obtained with the optimized set of geometrical parameters of PSCs in substrate configuration (Figure 12b), which are presented in Figure 14 (corresponding to rows 4 and 5 of Table 5). The absorption profiles of Figure 13 and Figure 14 show a similar overall optical behavior, despite the difference in cell architecture. However, the light confinement (focusing) in the front curvatures of the perovskite is more intense for the substrate-configuration PSCs, as seen by the higher values of the generation profiles (Figure 14a,b, insets) and of the p_{ABS} profiles (Figure 14c,d) at the first two wavelengths, due to the more elongated shape (higher R_Z) of these optimized features relative to those of the superstrate PSCs (see Table 5), for both 300 and 500 nm absorber thicknesses. A bigger height (R_Z) is needed in the substrate configuration to provide a higher effective geometrical index matching for stronger broadband anti-reflection in the UV-VIS range, since this configuration suffers from reduced absorption throughout the 300-700 nm wavelength range, relative to the superstrate configuration, as seen in the absorption spectra of the planar reference cells. At the same time, the structures must maintain a large scattering cross-section for path length amplification in the NIR, so the optimized lateral radii (R) are similar in the superstrate and substrate configuration.

Nonetheless, for the thinner 300 nm perovskite, stronger scattering is required to compensate for the reduced absorber thickness, which explains the larger *R* values of the thinner PSCs relative to the 500 nm ones. The optimal designs of the semi-spheroidal arrays converged to similar pitch (*p*) for both 300 and 500 nm perovskite, with optimal *p* values slightly above/below 500 nm for the superstrate/substrate configuration.

It can be seen that the substrate configuration suffers from higher parasitic absorption in most of the spectrum. At the shorter wavelengths <500 nm it is mostly attributed to the thicker 100 nm of ZnO that serves as ETL, in contrast to the 25 nm SnO_2 for the superstrate configuration. At the longer wavelengths in the NIR the high parasitic absorption occurs mainly at the rear contact, as revealed by the particularly intense hot spots present in the HTL and Au layers of these structures (see *G* and p_{ABS} profiles of Figure 14), which exhibit a much higher magnitude than those of Figure 13. The main reason for this is the fact that the HTL material (NiO_x) considered here has a considerably higher *n*, so the optical optimizations converged to HTL thicknesses (t_{NiO}~10-11 nm) much lower than those (50 nm) taken for the Spiro-OMeTAD used in the superstrate PSCs.

Overall, the absolute J_{ph} values attained with optimized LT are higher in the superstrate configuration, for both 300 and 500 nm perovskite, owing to the reduced parasitic absorption. However, the photocurrent improvement relative to the planar references is slightly higher in substrate configuration, mainly because the substrate-type planar cells also suffer comparably high parasitic absorption in the UV-VIS range. For this reason, the gains with optimized LT designs in substrate PSCs are superior to those achieved with superstrate architecture.

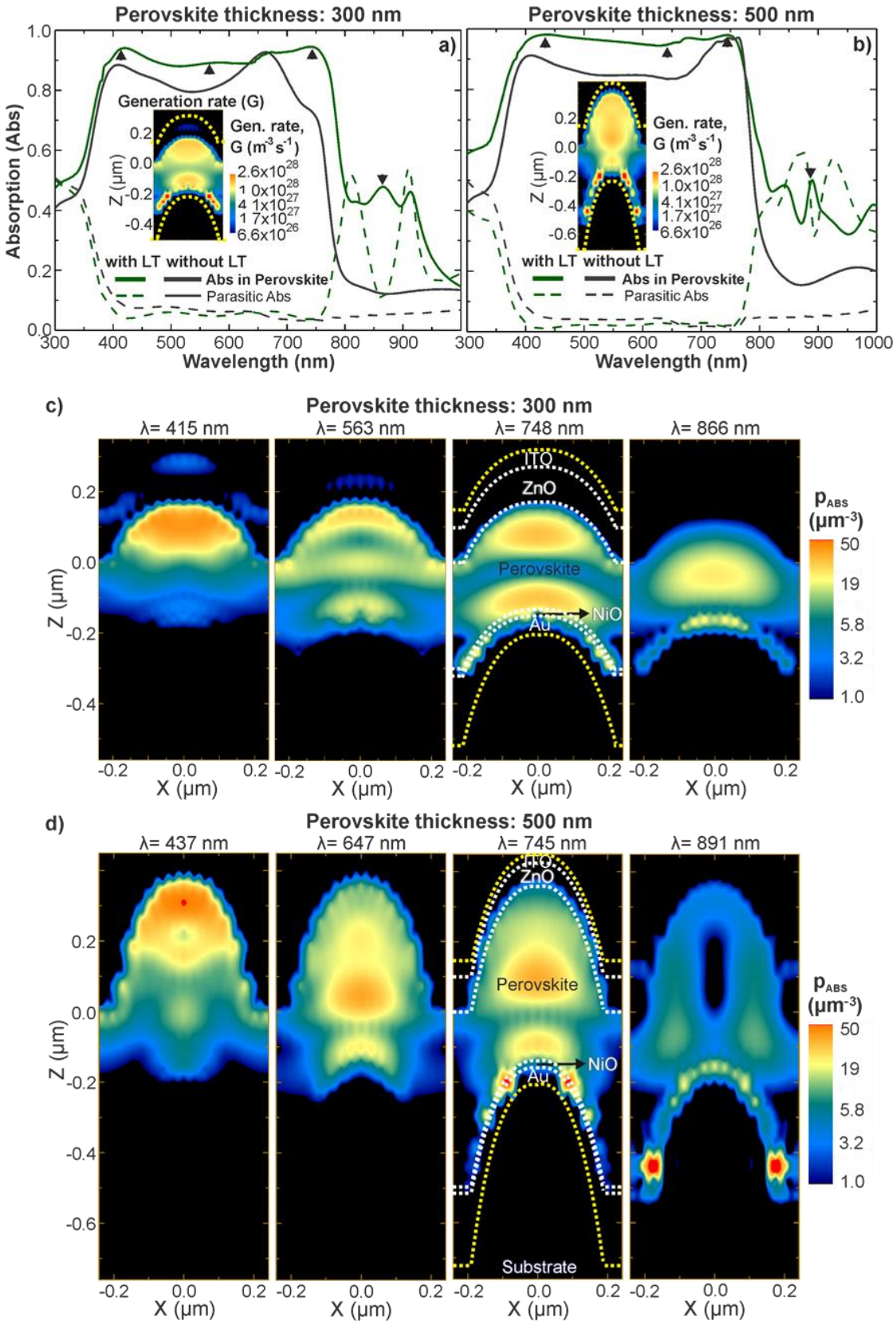

Figure 14: Similar to Figure 13 but for the PSCs in substrate configuration sketched in Figure 12b. a,b) Absorption spectra obtained with the optimized LT structures (green lines, row 5 of Table 5), compared with the reference cases of planar cells (grey lines, row 4), for perovskite layers with distinct

thickness: a) 300 nm and b) 500 nm. The inset profiles represent the total generation rate, G, along the xz cross-sectional plane of the structures. c,d) Profiles of the absorption density, p_{ABS}, along the same xz plane, at the wavelengths of the peaks marked by the arrows in a) and b).

4.4 Angle-resolved optical response

The dependence of the LT-enhanced PSCs performance with the incidence angle is of extreme relevance for their practical application, not only in conventional non-tracking PV installations, but specially importantly for thin-film cells integrated on bendable substrates[7], [183]. In such case, the flexible solar cells will likely operate with a certain curvature, so they will be illuminated by a cone of incidence angles along their active area. As such, it is crucial to evaluate the LT performance for oblique illumination. Even though the LT designs described in the previous section were optimized for normal incidence, they maintain broadband light absorption enhancement for a wide range of incidence angles, as analyzed next.

At normal incidence, due to the spheroidal shape of the LT features, the optical response of the cells is independent of the polarization of the incident light since the illumination is along the axis of revolution of the semi-spheroids. However, that is not the case for oblique incidence. As such, the TM (transverse magnetic) and TE (transverse electric) polarization components were computed separately, and the resulting photocurrent densities (TM J_{ph} and TE J_{ph}) are represented in Figure 15d. The output J_{ph} for unpolarized sunlight illumination was calculated by averaging the photocurrent values obtained with the TM and TE components, and is shown in Figure 15b,c.

In general, the planar PSCs exhibit a quite omni-directional response, particularly in the substrate configuration, since the unpolarized J_{ph} (in Figure 15b,c) is roughly constant up to ~60° and then starts decreasing only for higher angles, as these structures do not provide scattering effects. While the unpolarized J_{ph} of the LT-enhanced PSCs generally tends to decrease with increasing angle, but the maximum reduction is only of 3-4% for the substrate configuration and of 6-7% for the superstrate configuration, for 0-60° incidence angles. Such small reduction mainly occurs due to the relatively lower absorption in the perovskite in the NIR range, as seen in Figure 15d, as a consequence of slightly weaker scattering and waveguide mode coupling for larger angles. Nevertheless, such reduction with oblique incidence is significantly lower compared to that observed in thin-film silicon solar cells coated with optimized front LT structures[7]. This is attributed to the fact the present PSCs are conformally patterned on the photonic-structured substrates, so the corrugation of the PSC layers benefits a wider angular response with respect to LT-enhanced cells having a planar absorber. The more angle-independent J_{ph} of the substrate-type PSCs, relative to the superstrate configuration, is due to the fact that in substrate configuration the LT structures yield a higher fraction of absorption enhancement in the visible range (400-800 nm wavelengths) relative to NIR enhancement at

longer wavelengths, and the gains in the visible (chiefly via anti-reflection) are less affected by the increase of the incidence angle as compared with those in the NIR (via scattering).

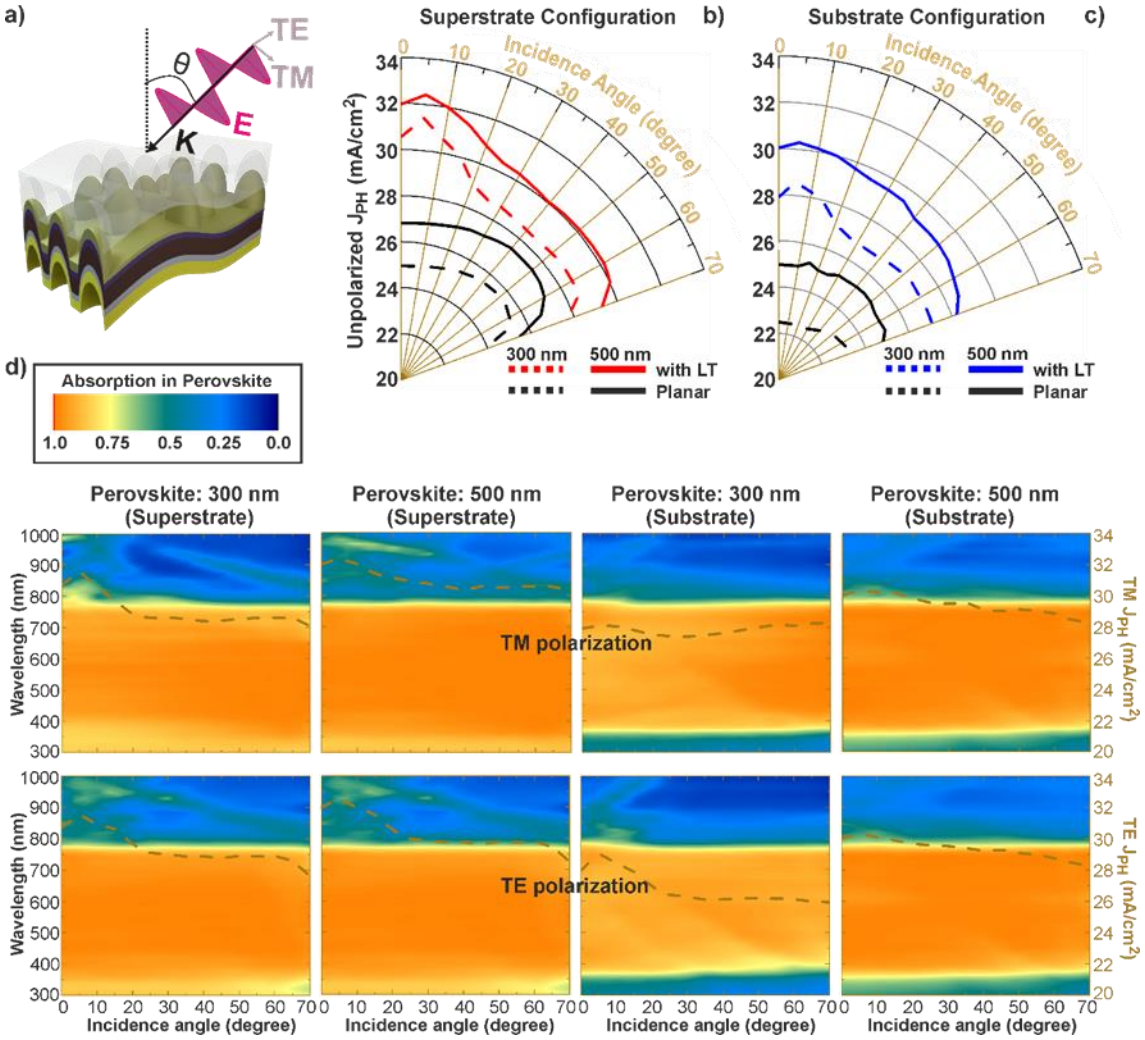

Figure 15: a) Sketch of sunlight illumination of a flexible LT-enhanced PSC. b, c) angle-resolved unpolarized photocurrent density, J_{ph}, given by the average between the current values attained with the TM and TE polarizations, for the two solar cells configurations: superstrate (b) and substrate (c). d) Color plots of the absorption spectra occurring in the 300 and 500 nm PSCs, as a function of the incidence angle, for both TM (top) and TE (bottom) polarization. The dashed brown curve plotted in the graphs corresponds to the angle-resolved photocurrent density obtained for each case (values in the right axes).

4.5 Discussion of results

By maximizing the broadband anti-reflection and light scattering properties of PSCs conformally deposited onto micro-structured substrates, optimized device architectures were presented with unprecedented photocurrent gains across the 300-1000 nm wavelength range of interest. Figure 16 summarizes the predicted enhancements, along the analyzed angular range, for the two distinct perovskite thicknesses of 300 and 500 nm with superstrate and substrate

cells' configurations, calculated relative to the corresponding optimized planar PSC reference cases. The gains are compared with those analytically obtained in the Lambertian cases of geometrical optics (see Table 5) at normal incidence. It should be noted that the Lambertian improvements were not calculated with respect to the same reference values of the planar PSCs, but instead relative to the same theoretical structure but without light scattering[7], [18], [19]. The results are compared for a distinct perovskite refractive index dispersion[94], [176], yielding slightly lower photocurrent enhancements than those of Table 5, but a much closer propinquity to the Lambertian limits for all cases.

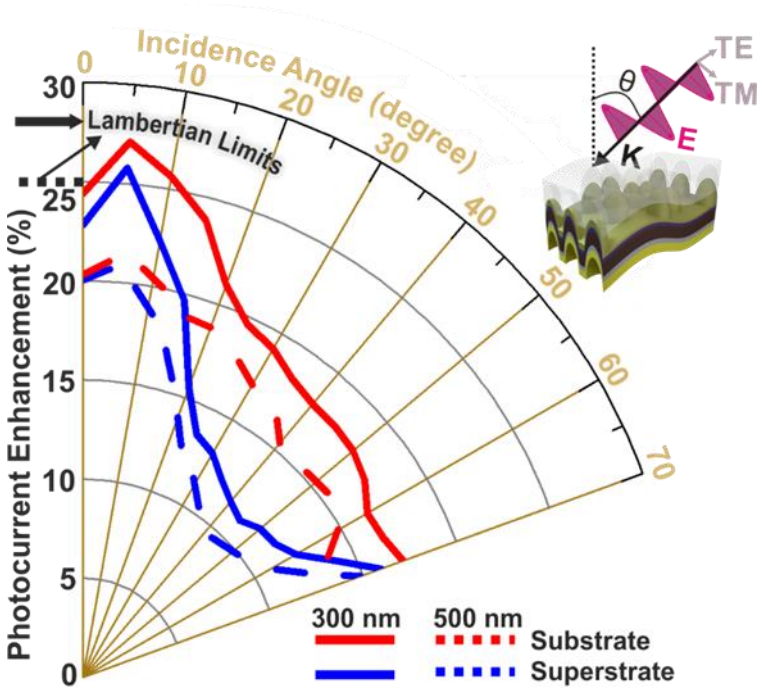

Figure 16: Improvement in photocurrent density, J_{ph}, achieved with the optimized photonic-structured PSCs (rows of 3 and 5 of Table 5) analyzed in section 3, relative to the planar references, as a function of the incidence angle (θ). The Lambertian limits of LT in PSCs, in the geometrical optics regime, are also indicated for normal incidence (θ=0º), by the solid and dashed horizontal black lines, respectively for the 300 and 500 nm perovskite absorbers.

The superstrate configuration led to higher absolute photocurrent for both perovskite thicknesses, mainly due to the thinner ETL thickness used in such architecture which yields lower parasitic absorption. Nevertheless, the substrate configuration ultimately showed ~3-4% higher gains when compared with the corresponding planar counterpart. As expected, the highest absolute photocurrents, J_{ph}, are achieved with the 500 nm thick perovskite (32.5 and 30.2 mA/cm², respectively in superstrate and substrate configuration at normal incidence). However, the LT structures on the 300 nm perovskite yield the highest photocurrent improvements (~3-4% higher gains compared to those with 500 nm perovskite at normal incidence), as shown in Figure 16. This matches the trend predicted from Lambertian ray optics analysis[19] - the thinner the absorber the higher the absorption enhancement that can be achieved

with LT. The photocurrent gains attained with our optimized LT structures are close to those predicted by the Lambertian limits. Nevertheless, the slight differences indicate that there is still some room for further improvement of the LT scheme, for instance by tuning the refractive indices of the front (e.g. less absorbing TCO) and rear (e.g. more reflective electrode as Ag) contact layers[17], [19], [174].

The substantial broadband absorption enhancement provided by the LT structures, relative to planar cells, was also demonstrated for a large range of incidence angles (0-70 degrees), as seen in Figure 16. The gains in the substrate configuration are clearly higher than those in superstrate configuration for most of the angular range, due to the spectral differences in which the absorption enhancements occur. It is noteworthy that the angular trends appear to be almost independent of the absorber thickness, since there is a roughly constant shift between the solid and dashed curves of Figure 16 for the 300 and 500 nm perovskites. For all cases, the angular dependences of the photocurrent improvements are significantly higher compared to those obtained in silicon solar cells with the best-performing LT front structures[7]. This is mainly due to two reasons: first, the optimized curvature of the PSC layers in the architectures developed in this work in which the cell is conformally coated onto structured substrates; and second, the lower real part of the refractive index of the perovskite absorber (n~2.3-2.5) and its better index matching with the contact layers (n~1.6-2.0) relatively to silicon-based absorbers (n~4), which reduces parasitic absorption and reflected light escaping the cell[7], [18], [184]. Therefore, the optimized conformal design demonstrated in this work is preferable for flexible PSCs, as it assists their operation under bending which implies illumination from a broad angular range.

It is also important to analyze the dependency of the solar cells' response with variations in the geometrical parameters of the LT structures around the optimal values. For that, we considered the PSC design with 300 nm perovskite in the superstrate configuration (Figure 13a), and present in Figure 17 the variation of its absorption spectrum and resulting photocurrent with a ±10% deviation in the geometrical parameters (R_Z, R, p). As observed in a previous work of the authors with photonic-enhanced PSCs supported of flat –rear-metal contacts [19], Figure 17a shows that the absorption in the perovskite in the shorter wavelength range (300-~450 nm) is mostly affected by variation of R_Z, since the absorption in this part of the spectrum is mostly enhanced by anti-reflection effects, due to the geometrical index matching caused by the high aspect-ratio of the front structures. The influence of R_Z in the absorption enhancement at the longer wavelengths is much less pronounced. Conversely, the in-plane radius, R, and array pitch, p, have a minor effect on the absorption gains in the shorter wavelengths, but have strong effect for the longer wavelengths (NIR region), as seen in Figure 17b,c. It is observed that these two parameters have almost the same effect on the perovskite absorption gains for wavelengths above ~700 nm, as they both set the grating properties of the photonic structure which determine the guided-mode trapping in such NIR wavelengths. For this reason, it is observed in Figure 17b1,c1 a higher sensitivity of the photocurrent with variation of these two

parameters (determining the waveguided modes) than with variation of *Rz* (determining the anti-reflection). These conclusions are in line with those of a recent study demonstrating similar optical absorption enhancement effects in ultra-thin CIGS solar cells[182].

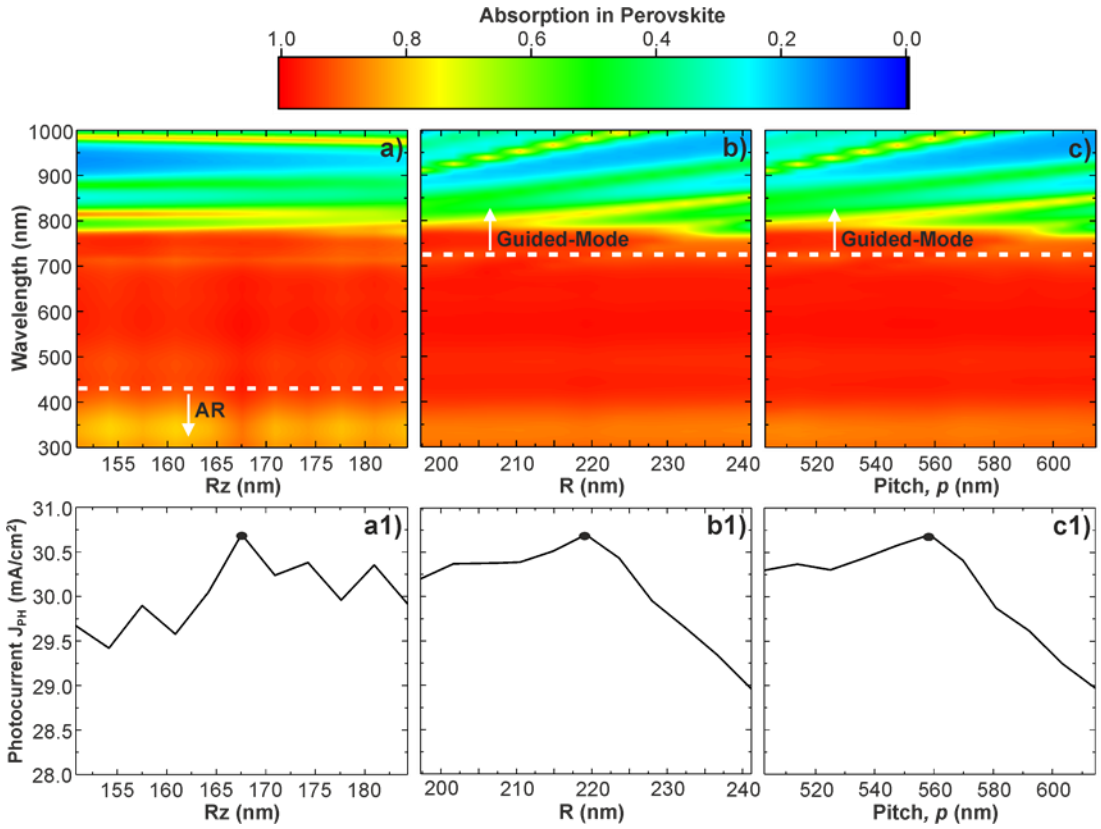

Figure 17: Spectra of the absorption in the perovskite (top plots) and photocurrent density (J_{ph}, bottom plots) attained with a 20% variation (±10% deviation) in each geometrical parameter [R_Z, R and p, respectively in a), b) and c)], relative to the optimal parameter values (marked by the circles in bottom plots) for the superstrate photonic-enhanced PSC with 300 nm thick Perovskite (row 3 of Table 5, Figure 13a).

4.6 Conclusions

We show that by carefully tuning the geometrical features on the substrates one can achieve levels of LT enhancement (up to 24.4% with 300 nm and 20.3% with 500 nm perovskite) comparable to those of the previous method[19], with the added benefit of a more omni-directional angular response (up to 70°) which is of paramount importance for flexible devices. In addition to the superior photocurrent (thus efficiency) improvements, the LT solutions designed here reveal that the perovskite thickness can be substantially reduced while maintaining high performance, as the J_{ph} values attained with the 300 nm LT-enhanced cells are considerably higher than those of the conventional 500 nm planar references (see Table 5). Such reduction in perovskite thickness from 500 to 300 nm can bring important competitive advantages: 1) an almost 2-fold reduction in the amount of the environmentally-toxic lead (Pb)

compound, as well as in the material costs associated to the perovskite material (with no additional material costs for the LT structures since they are incorporated in the substrates); 2) a potential 3-fold increase in the device flexibility due to the reduced absorber thickness.

Lastly, although outside the scope of this investigation, the rough PSC interfaces in the present LT-enhanced cell structure could raise the concern of possible electrical deterioration in practical devices fabricated with wet-coating processes. Nevertheless, the fast evolution in PSC technology has shown improved PSC deposition methods enabling conformal coating of the cell layers on micro-rough substrates and resulting in high efficiencies[185]. For instance, F. Wang et al. [68] developed a recrystallization treatment that allowed 18.6% PSC efficiency with a ~300 nm thick perovskite absorber conformally coated on textured glass having surface features on the order of the micrometer (as those in this study). These findings indicate that it is possible to develop non-planar PSCs without being considerably affected by the rough interfaces.

5

COUPLED OPTICAL AND ELECTRONIC ANALYSIS OF PHOTONIC PEROVSKITE SOLAR CELLS

5.1 Introduction

As highlighted in previous Chapters, PSCs have stormed the solar cell community in the past decade, and are now considered the most promising emergent photovoltaic (PV) technology [186]. Their non-vacuum solution-processing, which does not require highly specialized installations or expensive equipment, enabled many researchers around the globe to fabricate high performance PSC devices. It also brought forth a wave of worldwide effort aimed at improving and mitigating the shortcomings of PSCs technology in many different aspects such as: efficiency, stability, flexibility, reduction of harmful materials, etc. [38], [71], [94], [186], [187]. Despite the extraordinary growth of the PSCs' power conversion efficiency (PCE, now >25.5%) [38] over the years, from a theoretical standpoint, there are still many aspects of their intrinsic behavior that are inadequately understood, particularly concerning electrical effects (i.e. ionic transport, charge recombination and trapping, interplay at interfaces, inhomogeneous field generation, etc.). Therefore, an in depth fundamental analysis of the PSC properties is crucial to close the gap to the maximum achievable PCE (~30%) [188], [189].

In addition, there is now a growing market demand for flexible solar cells [108], [109], whose devices are required to be ultra-thin allowing improved intrinsic mechanical bendability [7], [8], [19], [171]. This, in part, requires a lower absorber material thickness, which is beneficial in PSCs as an effective means to attenuate the amount of hazardous/toxic compounds (e.g. Pb) present [94]. Furthermore, the lower material usage can also have manufacturing cost benefits and a broader range of potential applications that require improved flexibility [7], [94], [190].

To counterbalance the significant drop in light absorption and, consequently, in the device efficiency caused by the reduction of the thickness of the PSC layer, it is essential to develop ultra-thin absorber layers with state-of-the-art optoelectronic properties [7], [8], [19]. The design of optical enhancement strategies is another essential approach to manage these lower thicknesses without forfeiting performance [61], [94], [188]. Moreover, it has been shown that the same optical strategies also improve the stability of the PSC layer, which is an important limiting factor for the commercialization of PSCs [25], [61], [67]. Several advanced optical en-

hancement strategies have been proposed, such as anti-reflective coating [191], scattering media [192], texturing the charge transport layers [51] and/or absorber [20], nanophotonic front [193] and back electrodes [67], disordered micro-structuring [194], light harvesting using up-/down- converter coatings or nanoparticles [61], including plasmonic effects [195]. Despite the performance gains, these methods are generally contrasted by other unwanted mechanisms, such as parasitic absorption, complex integration with solar cells or unrealistic scale-up [94].

One way to gain insight into the complex behavior of PSC devices is through the development of realistic simulation models, considering both optical and electrical effects [107] to account for carrier recombination, irregular field distribution and, thus, accurately predict device performance and allow modelling-aided design optimization, which can be of utmost importance for this emergent PV technology based on ultra-thin and flexible solar cells [108], [109]. However, most theoretical studies of light trapping in PSCs focus only on the optical effects at play [61], therefore not guaranteeing PCE improvement due to the lack of understanding of the behavior of LT-enhanced PSCs from an electrical standpoint, thus hindering the achievable gains for these devices.

To overcome these shortfalls, the present work developed a complete optoelectronic modelling procedure, from which it was determined that photonic-enhanced PSCs can indeed capitalize on the optical gains - particularly for ultrathin PSCs (perovskite layer: 300 nm) - and translate them to the electrical domain, thus achieving close to 30% efficiency. The starting point is a conformal architecture designed for maximum optical density that can be achieved by depositing the PSC layers independently onto optimally patterned substrates. Such fabrication methodology represents a novel research direction as well, since the enhanced generated photocurrent achieved outperforms the most sophisticated optical strategies reported, without sacrificing scalability by making use of industrial-friendly geometries and fabrication methods. Besides, the study presented here reveals that the developed photonic-structuring of the PSCs does not lead to a significant increase in surface recombination, and also the performance is not affected by the inhomogeneous field generation caused by interference of the light waves scattered from the micro-structuring. The band-alignments of the photonic-structured PSCs reveal to be favorable for the carriers' transport towards the contacts. Hence, the electrons generated can be collected, even in the dense photon trapping regions.

Consequently, it is shown that photonic-structured PSCs with ultrathin perovskite (300 nm, higher flexibility) can outperform conventional planar PSCs with thicker perovskite (500 nm, rigid), and the electrical (PCE) performance improvement can be even slightly higher than the optical (photocurrent) enhancement caused by LT.

This work constitutes an important step towards high performance devices geared for consumers, such as portable electronics, BIPV, light-harvesting semi-transparent windows [196], wearable PV, solar-powered vehicles and self-powered smart electronics, which are promising PV market drivers. In addition, the design of the optical schemes presented herein

shows great potential to be forthwith incorporated in high-efficiency tandem [197]–[199] and triple-junction [54] PSCs devices.

5.2 Methodology and experimental considerations

A complete optoelectronic study of different photonic-structured PSC configurations was performed by optimizing first its design from an optical standpoint, depicted in Figure 18a, and then by using the resulting carrier generation profiles as input for the electrical drift-diffusion model of the devices, following the process flow shown in Figure 18b. The photonic features are modelled with a spheroidal geometry that is patterned on the substrate supporting the solar cells, in both superstrate-type and substrate-type PSC architectures, and arranged in a hexagonal array (honeycomb lattice). The five PSC layers are taken to be conformally deposited onto the substrate micro-patterns, as sketched in Figure 18a.

The Ansys Lumerical© FDTD [200] Solutions package was used to perform the complete optical analysis of the devices, due to the robustness and versatility of its finite-difference-time-domain (FDTD) algorithm, which can be used for electromagnetic simulations of arbitrarily shaped media. In addition, its ability to do single-run broadband simulations is also very beneficial for PV. The details regarding the FDTD simulation process and setup, including the refractive index spectra of the modelled materials (see Appendix A1), are provided in Chapter 2.

To adequately optimize the structures to achieve the ideal device dimensioning, several parameters need to be evaluated concerning the geometry of the photonic features (in-plane, R, and normal-to-plane, R_Z, spheroidal radii), array periodicity (pitch, p) and the thickness of the layers (t_{layer}), being the optical photocurrent, J_{PH}, the initial Figure of Merit. For that, stochastic optimization approaches are preferred due to their more efficient search within vast parameter spaces [19]; hence in this work, a particle swarm optimization algorithm (implemented in the FDTD solver) was used to achieve the device dimensioning that maximizes J_{PH} (more details given in Chapter 2) [19], [94].

The FDTD optical results were then combined with a finite volume method (FVM) and a finite element method (FEM) implementation of the charge transport equations (drift-diffusion plus Poisson), to model the electrical behavior of the devices. Three different solvers (TiberCAD [201], Lumerical-CHARGE [202], and Sentaurus Tcad [203]) were used to compare and corroborate the results. Standard values of the electronic properties of the cell materials were obtained from the literature and used as inputs to the electrical simulations. The collected literature values include, among others, the bandgap, dielectric permittivity, electron/hole effective mass, electron affinity, mobility, lifetime, doping, the density of states and series resistance (more details in Appendix A2) [122], [173]. Due to the complexity of the electrical simulations, in particular for PV technologies such as PSCs involving a combination of organic

and inorganic compounds, the modelling results obtained were also compared with experimental results for conventional planar PSCs, to both provide a strong reliable foundation for the simulation setup as well as to further refine the parameters of the device. A detailed description of the simulation process is provided in Appendix A2.

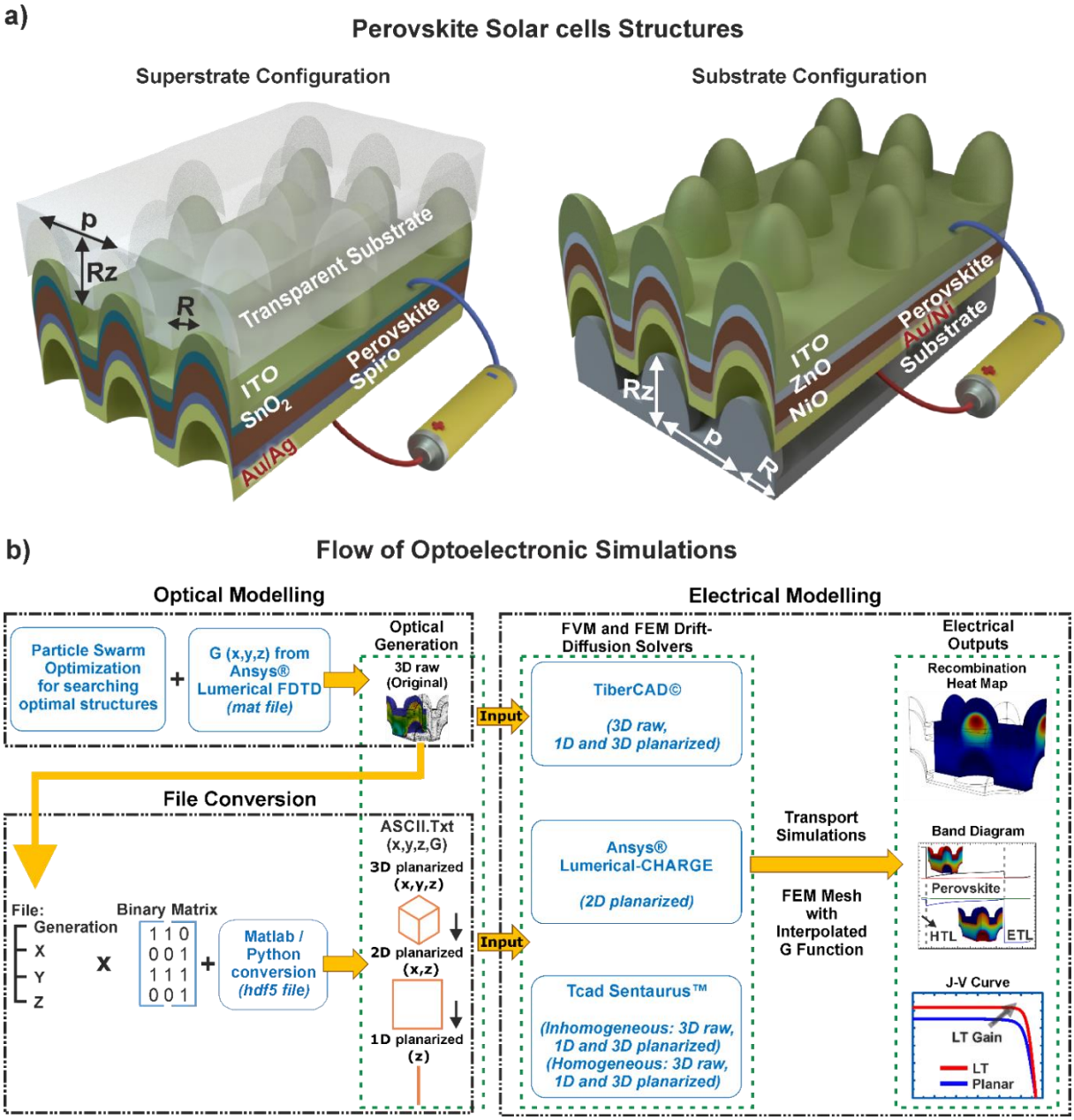

Figure 18: The photonic-structured substrates were studied and optimized for two types of PSC architectures with different metal contacts (Au, Ag and Ni): the conventional superstrate configuration (Figure 18a, left) in which light enters from the transparent substrate, and the so-called substrate configuration (Figure 18b, right) in which light impinges on the cell side. The LT structures patterned on the substrates are modelled as a hexagonal array (with pitch p) of vertically-aligned semi-prolate features with radii R and R_Z, respectively along the in-plane direction and illumination axis. The PSC layers are then conformally deposited over such spheroidal structures. Coupled optical and electrical simulations were performed to assess the full optoelectronic response of the solar cells following the process

flow shown in b). First, 3D optical (electromagnetic) simulations are carried out using the FDTD solver, incorporating a particle swarm algorithm that optimizes the geometry of the photonic-structured PSCs. This was followed by the electrical simulations, here employing three FVM/FEM solvers for comparison and validation, which take as input the 3D-optically obtained generation profiles (original, raw *G*) from the FDTD solver as well as 3D, 2D or 1D planarized generation profiles resulting from planarizing the original *G* function using a binary matrix (3D-planarized) and further decreasing it to lower dimensions (2D and 1D planarized) when needed. Moreover, the electrical simulations were also carried out considering conceptual homogeneous (i.e. spatially-independent) generation profiles with a fixed value across the absorber region equal to the volume-averaged *G*.

While planar multilayered solar cells can be accurately modelled via 1-2D simulations, the same may not be ensured for photonic-structured devices like the ones under study (Figure 1a), which demand higher modelling dimensionality (2-3D). However, since the exact electrical modelling becomes significantly more complex with an increase in dimensionality, simulations were also performed at different dimensionalities to compare 3D simulations (the most accurate geometric representation, but most limited in spatial resolution) with their 2D and 1D counterparts for a better insight into the real impacts of such simplifications.

From the complementarity of the optical and electrical results, it is possible to understand the main underlying physical mechanisms governing the response of the PSCs, with and without photonic structuring, thus enabling a complete modelling-aided design of the devices.

5.3 Results and Discussion

5.3.1 Optical Modelling and Wave Optical Physics

The semi-spheroidal LT structures provide a combination of geometrical gradual index matching and light scattering properties to, respectively, suppress reflection and effectively trap light inside the solar cells. These structures have also been shown to provide a broad angular acceptance, which is paramount for the proper functioning of the devices under bending conditions [94]. Apart from the optical benefits, the current photonic strategy studied here has also strong advantages in terms of experimental feasibility over most state-of-the-art LT schemes, as stated earlier. The biggest advantage is that these LT structures can be easily fabricated by a low-cost colloidal lithography (CL) process, which is capable of engineering any micro/nano-structures uniformly throughout large areas [44], [105], [106], [160]. The PSC layers are then wet-coated onto the patterned substrates, thereby becoming photonic-structured due to conformal deposition, as sketched in Figure 18a.

Apart from analyzing different PSC configurations, the influence of alternative materials on the PCE was also assessed. Namely, the properties of the rear metal contact were found to be particularly crucial for LT performance. Au is the metal contact of choice for PSCs, but its high cost brings a strong negative impact on the devices' scalability. Therefore, Ag and Ni were studied here as more affordable alternatives. Different materials for the electron transport layer (ETL) and hole transport layer (HTL) were also considered: SnO_2 and ZnO

were chosen for the ETLs, as they have shown better stability over typical TiO_2 [204], and Spiro-OMeTAD and NiO_x for the HTL, since the inorganic NiO_x has also revealed stability benefits relative to the conventionally-used organic Spiro-OMeTAD [205]. In addition, the cell layers' thicknesses are considered within reasonable ranges in accordance with the state-of-the-art of PSC technology (e.g. the minimum thickness allowed for the TCO, made of ITO, is 350 nm in the PSO optimization algorithm) [206].

We begin by optimizing the LT structured substrates (illustrated in Figure 18a) to achieve maximum photocurrent (J_{PH}) using the particle swarm optimization algorithm. Figure 19 summarizes the optimization results for the different structures (Figure 19a), and shows the cross-sectional optical generation rate (G, see Figure 2b) for comparison between different structures – 300/500 nm thick perovskite in superstrate and substrate configuration. From Figure 19a, one can see that, in all cases, the photonic-structured PSCs with ultrathin (300 nm) perovskite layer outperform the planar PSCs with the conventional (500 nm) perovskite thickness. The Ag contact allows similar performance as Au, while Ni contacts are optically worse in general. Nevertheless, the photonic-structured PSCs with Ni can perform as well as the optimized planar PSCs with Au and Ag metal contacts. Therefore, Ni is still a good candidate for PSC application, also if we consider its low price and the industrial advantage of allowing the fabrication of the NiO_x HTL layer simply by oxidizing the Ni rear contact in the same process run [207].

The observed gains are chiefly governed by two different optical mechanisms: anti-reflection and light scattering properties. The enhanced anti-reflection effect is predominately achieved from the geometrical index matching of the real part (n) between the semi-spheroidal structured front layers (TCO, ETLs and perovskite). This effect is mostly responsible for enhancing absorption in the UV-VIS range, due to the superior light coupling towards the absorber (perovskite) material. At the same time, strong near-field forward-scattering occurs because of the micro-lens effect arising from the optimized curvatures of the front layers, which generates high intensity electric fields in the top portion of the perovskite layer, as observed in the G profiles of Figure 19b. In this range below ~700 nm wavelength, light is easily absorbed by the cell, so that reflection in the back contact has a much-decreased impact on the overall absorption. For longer wavelengths (NIR region), the absorption enhancement is mostly governed by the far-field scattering caused by the semi-spheroidal shape of both the front and rear features of the photonic-structured PSCs, which benefits as well from the high real part (n) of the perovskite refractive index. This effect manipulates the light that falls vertically and redirects it to paths closer to the horizontal plane, thus leading to optical path increase and easier coupling into waveguided modes trapped in the absorber layer. This is evidenced by the "hot spots" observed in the rear side of the perovskite material, shown by the optical generation (G) profiles of Figure 19b. These "hot spots" result from the constructive interference between the light waves traveling along the incidence direction and the scattered light traveling along the plane of the cell layers that suffer multiple reflections from the top

and bottom surfaces of the cell. As such, the sharp absorption peaks seen in the NIR are a consequence of the 3D Fabry-Perot resonances resulting from such interference.

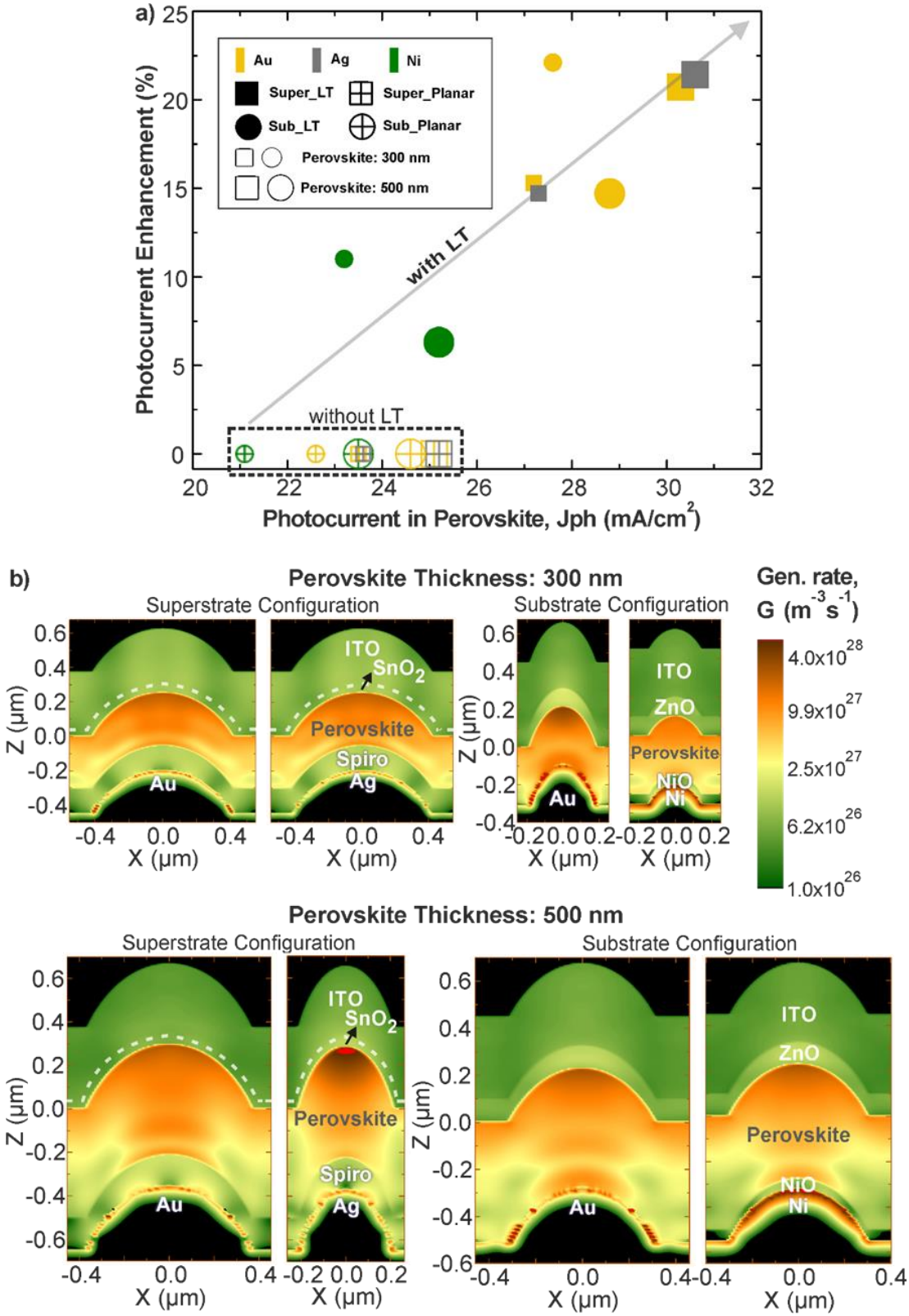

Figure 19: Improvement in photocurrent density (a), J_{PH}, achieved with the optimized photonic-structured PSCs for different cells configurations, metal contacts and distinct perovskite thicknesses (as

shown in Table A1 in section of Appendix A2), relative to the planar references as indicated on the horizontal line (a). The profiles represent the total generation rate, *G*, along the xz cross-sectional plane of the structures for all the photonic-structured PSCs studied here (b).

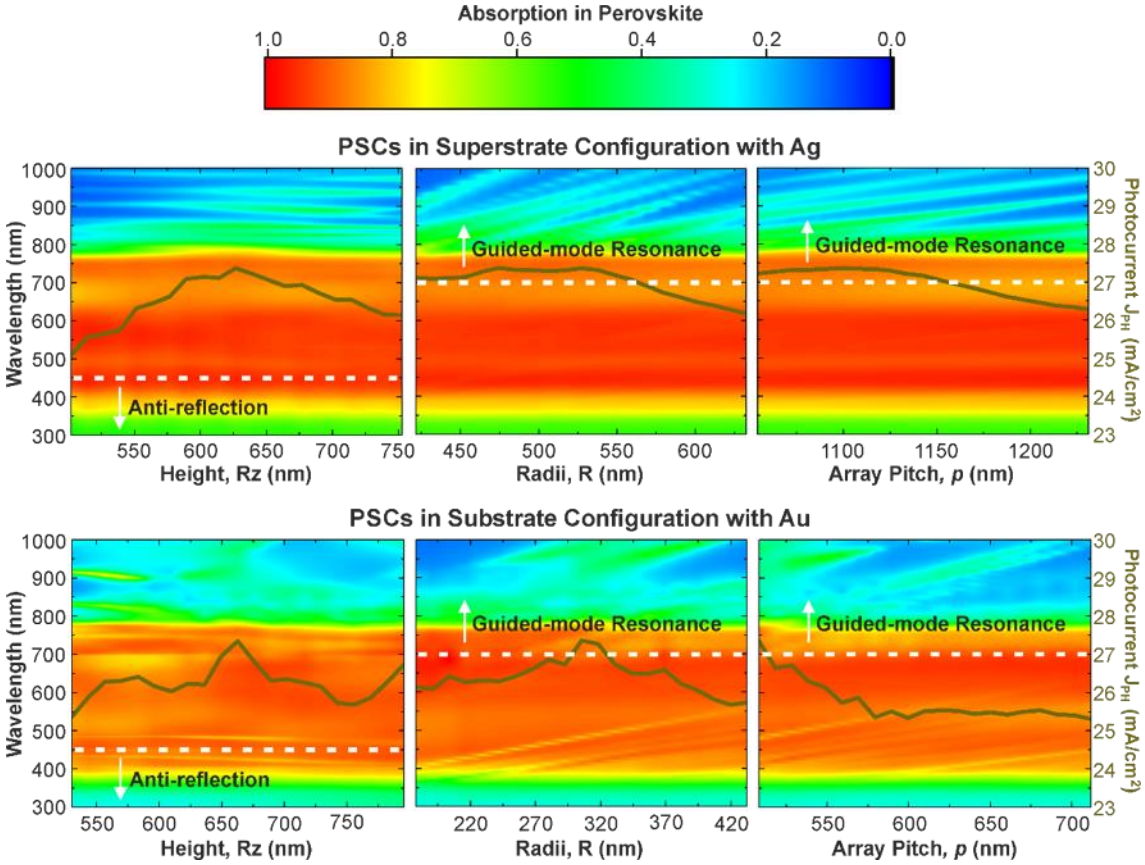

Figure 20: Spectra of the absorption in the perovskite and photocurrent density (J_{PH}, dark line) attained with a 20% variation (±10% deviation) in each geometrical parameter (R_Z, R and p), relative to the optimal parameter values marked by the circles in the dark line (indicated in Table A1 of Appendix A2). This is shown for two cases of the photonic-enhanced PSCs with 300 nm thick perovskite layer and metal contact of Ag (*top plots*) or Au (*bottom plots*), in superstrate and substrate configurations, respectively. The white dotted lines qualitatively separate the effects of anti-reflection (stronger influence below ~450 nm wavelength) and guided-mode resonances (stronger influence above ~700 nm wavelength).

The response of the solar cells with the variation of the geometrical parameters of the structures (R_z, R, p) around the optimal values was also analysed, focusing on the photonic-enhanced PSCs with 300 nm thick perovskite layer (see Figure 20). It further clarifies the above optical phenomena, since the influence of the structures' height, R_z, in the absorption enhancement for shorter wavelengths in UV-VIS is higher than for longer wavelengths in NIR, since R_z mostly affects the anti-reflection gain due to the geometrical index matching. Conversely, the lateral radius, R, and array pitch, p, have minor influence on the absorption gains in the shorter wavelengths but have a strong effect for the longer wavelengths. R and p set the grating

properties of the LT structures, which determine the guided-mode trapping in the longer NIR wavelengths. In general, it is noticeable that the photocurrent remains not far from the maximum within large (± 10%) variations of the geometrical parameters, demonstrating that the designed semi-spheroidal LT structures are adequately tolerant to fabrication imperfections, which is a key advantage from an industrial perspective.

5.3.2 Electrical Modelling and Device Physics

There has been an increasing interest in the PV-related community for the development of coupled optical and electrical models capable of exactly predicting and optimizing the full response of optoelectronic devices [208], as developed in this work and applied to the challenging case of photonic-structured PSCs.

As previously described (Figure 18b), this process involves a two-step approach: 1) detailed simulation of the solar cell optical response with an electromagnetic FDTD formalism, as presented in the previous section 5.3.1; and 2) the optical results are then used as input for the FVM and FEM model that determines the electrical behavior of the device, as the current density vs. voltage, *JV*, characteristic curve. Such approach has been thoroughly reported and extensively studied for the modelling of common (inorganic) PV semiconductor materials and cell architectures (single-junction and tandems) [122], whose behavior can be directly described by the traditional drift-diffusion formalism. However, the charge transport properties of solar cells composed of novel materials, as the hybrid organic-inorganic perovskites addressed in this work, have yet to be more clearly understood, in close interaction with experimental characterization. Namely, two main aspects make the electrical modelling of PSCs particularly complex:

1) heterojunction configuration - specifically the formalism employed by the numerical FVM and FEM solvers of the drift-diffusion/Poisson equations can break down with sharply varying electric fields, which is an intrinsic characteristic of heterojunctions as those in PSCs (namely at ETL/Perovskite/HTL interfaces [209]);

2) non-standard mechanisms observed, e.g. attributed to the presence of mobile ionic charge species in the perovskite, which can pronouncedly affect the optoelectronic response of PSCs, such as the JV hysteresis (i.e. the JV dependence on the direction/speed of the bias scan [210]), that cast doubts and make their charge transport behavior nebulous when compared to standard inorganic materials as c-Si.

In addition, the micro-structured PSCs studied here provide additional challenges, chiefly due to the curvature of the structures that increase the surface area and generate "hot-spots" (densely illuminated regions inside the cell). The "hotspots" derive from the locations of constructive interference of the light waves established within the periodically-structured devices, which can make their charge generation and transport properties more complicated when compared to planar cells.

Even though the actual charge-transport mechanisms in hybrid-perovskites can be influenced by their organic parts, it has been observed (mostly in high-performing devices) that it can be accurately modelled by approximating it to an inorganic semiconductor, even presenting properties resembling those of GaAs [211]. The same logic applies to the contact layers (HTL/ETL), where their hole/electron-separation role is modelled through fitting parameters that are as close as possible to the values known for these materials [209].

As mentioned before, the electrical simulations use as input the photo-generated charge carrier spatial distributions computed from the optical simulations described in the previous section. Considering such input, the present electrical models employ the classical drift-diffusion formalism, numerically computed via the FEM or the FVM implemented in different mesh-based charge transport solvers [201]–[203]. This is a physics-based electrical simulation tool for semiconductor devices that self-consistently solves the system of equations presented below, describing the drift-diffusion equation for the current density (Eq. S3), Poisson's equation for the electrostatic potential (Eq. S4), and the continuity equations for charge conservation (Eq. S5):

$$\boldsymbol{J}_{n,p} = q\,\mu_{n,p}\boldsymbol{E}n/p \pm\ qD_{n,p}\nabla n/p \tag{3}$$

$$-\nabla\ \cdot(\epsilon\nabla\mathbf{V}) = \mathrm{q}\rho \tag{4}$$

$$\frac{\partial n/p}{\partial t} = \pm\frac{1}{q}\nabla\cdot\boldsymbol{J}_{n,p} - R_{n,p} + G_{n,p} \tag{5}$$

here R and G are, respectively, the recombination and generation rates per unit volume (n and p subscripts indicate electron or hole, respectively), q the electron charge, n/p the electron/hole carrier density, ρ the total charge density, μ mobility, D diffusivity, V the electrostatic potential and $\boldsymbol{E}$ the electric field. Here, $R = R_n = R_p$ and $G = G_n = G_p$ since only local recombination/generation processes are considered which have to conserve locally the total number of carriers. Generation and recombination are major factors in the calculation of carrier behavior in the material, and these processes depend on temperature, doping, the E-field, current density and carrier concentration. The carriers move under two competing processes, drift due to the applied E-field and diffusion due to density gradients, appearing as the two terms in Eq. 3. Various domains are created and partitioned along the simulation region. Insulators, semiconductors and conductors' properties are specified in the simulation. Semiconductors use multi-coefficient models to describe the fundamental properties, mobility and recombination processes that are inherent and specific to the material. These models are employed in each vertex of the finite element discretization of the simulation domain, and the set of three partial differential Eq. (4) and (5) is discretized using FEM, reformulating the problem in weak form by projecting to a basis of piecewise linear functions, or using FVM by enforcing current continuity locally. The numerical solution of the resulting nonlinear set of algebraic equations provides the electrostatic potential and the carrier densities in each vertex. In this fashion, complex physics problems whose system of equations are unsolvable analytically are tackled, and the method

is widely used in other areas of engineering and physics. All simulations are conducted at a temperature of 300 K.

Here, a thorough assessment was first performed on the material parameters used for the electrical simulations, based on fabricated high-efficiency flexible PSCs as described in subsection 5.3.2.1. Subsequently, the different optically-optimized photonic-structured devices, in both superstrate and substrate configurations, were electrically modelled as described in section 5.3.2.2. Lastly, we explored the ultimate efficiency that can be achieved using LT, by considering the state-of-the-art highest efficient PSCs, as well as investigating the dimensionality of the simulation in the computed response, as described in section 5.3.2.3.

5.3.2.1 Electrical modelling and validation with experimental results

Given the promising application of photonic-enhanced PSCs for bendable devices [19], a potentially-flexible planar PSC deposited on PET substrate with high efficiency (measured PCE=18.5%, see Figure 21) was taken as a reference to extract the relevant electrical parameters (effective mass, bandgap, recombination properties, etc.) of the materials and refine the simulation model. The parameters used are summarized in section Appendix A2. For the fitting procedure, a simple 3D-optical/1D-electrical model implemented in TiberCAD was used. This benefits from significant improvements in simulation time and memory requirements, without the loss of accuracy in the results, since for flat multi-layered structures the optical generation only changes in the direction of light propagation (z axis). As such, for the electrical simulation, the 1D optical generation was obtained by averaging $G(x,y,z)$ in both the x and y directions.

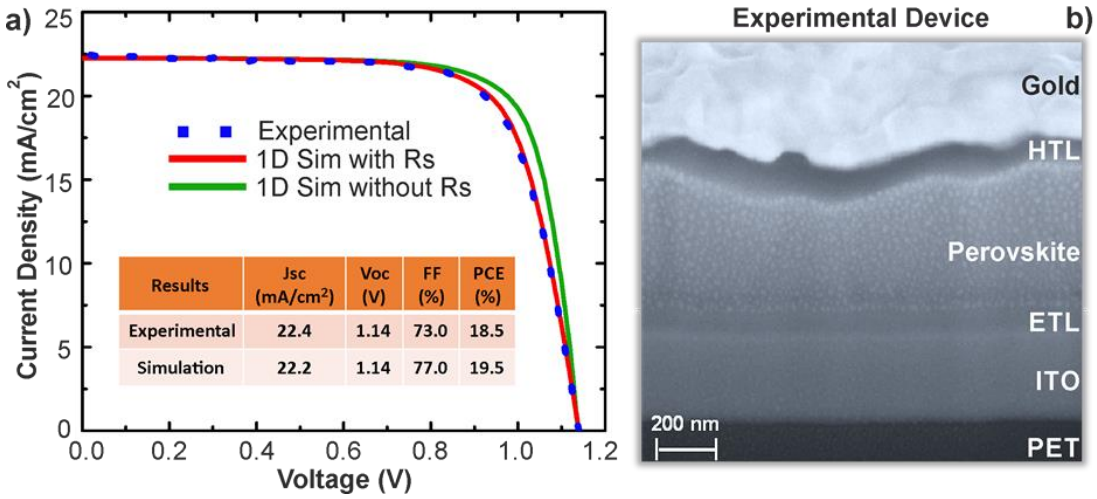

Figure 21: a) 1D device modelling and comparison with experimental planar flexible PSC with ~300 nm absorber thickness. The modelled JV curve in red considers the effect of an additional series

resistance, R_S, to better fit the device response. b) SEM image of the cross-section of the experimentally fabricated PSC on flexible PET substrate.

While 1D electrical simulations are sufficient for the accurate modelling of conventional planar PSCs, as in Figure 21, when considering structured devices such simplification in dimensionality needs to be reassessed as the optical generation profile is no longer uniform in x/y. The complex 3D behavior of the generation profile in the cases of the photonic-structured PSCs of Figure 18 can have a non-trivial impact when averaging the generation profile in the in-plane dimensions, which may lead to errors in the calculation. Hence, the rigorous 3D-optical/3D-electrical model to simulate the photonic-structured devices developed for this work and based on the electrical properties extracted from the experimental comparison (Figure 21).

Substrate-type PSCs, as shown in Figure 18a, were first modelled for a planar and photonic-structured device, using the previously mentioned set of material parameters. The planar cell [structure: Au (200 nm)/NiO_x (10 nm)/Perovskite (300 nm)/ZnO (100 nm)/Au (100 nm)] was simulated for both 1D-electrical and 3D-electrical cases. The current obtained was 22.6 mA/cm^2 for both simulations, thus reinforcing the validity of the above-made approximation. The photonic structured devices have the optimized hexagonally symmetrical structure (see Table A1 in Appendix A2) with period p=508.4 nm and radii R=254.2 nm and R_z=662.8 nm. The 3D charge carrier generation profiles obtained are shown in Figure 22a, b for the planar and photonic-structured PSCs. The optical modelling of these structures in section 5.3.1 pointed to a current density of J_{PH}=27.6 mA/cm^2, while the electric modelling resulted in a lower value of short-circuit current density J_{SC}=26.0 mA/cm^2. A lower value of J_{SC} is expected in the electrical simulations due to transport losses (mainly bulk and surface recombination) that are present in the drift-diffusion model, as well as because of the sampling error given by the different mesh sizes in optical and electrical modelling. Figure A2 of section Appendix A2 shows the radiative and Shockley-Read-Hall (SRH) recombination profiles for planar and LT-enhanced PSCs, where it is noticeable that SRH is the dominant recombination mechanism in the devices.

Figure 22c,d,e demonstrate that both LT and planar substrate cells have the same energetic band alignment, which is the expected behaviour. The band diagram should only depend on the materials used and not on the micro-structuring. It is observable from Figure 22d that at voltages close to V_{OC} (1.14 V) an inverse slope for the transport carriers appears in the perovskite bands. Such slope is not present at 0 V (Figure 22c,e) and can be correlated to the trapping and recombination of carriers before collection by the transport layers. The closer the polarization is to V_{OC}, the higher the recombination, up to the point where an equilibrium between generation and recombination of carriers occurs and the V_{OC} condition is achieved [212].

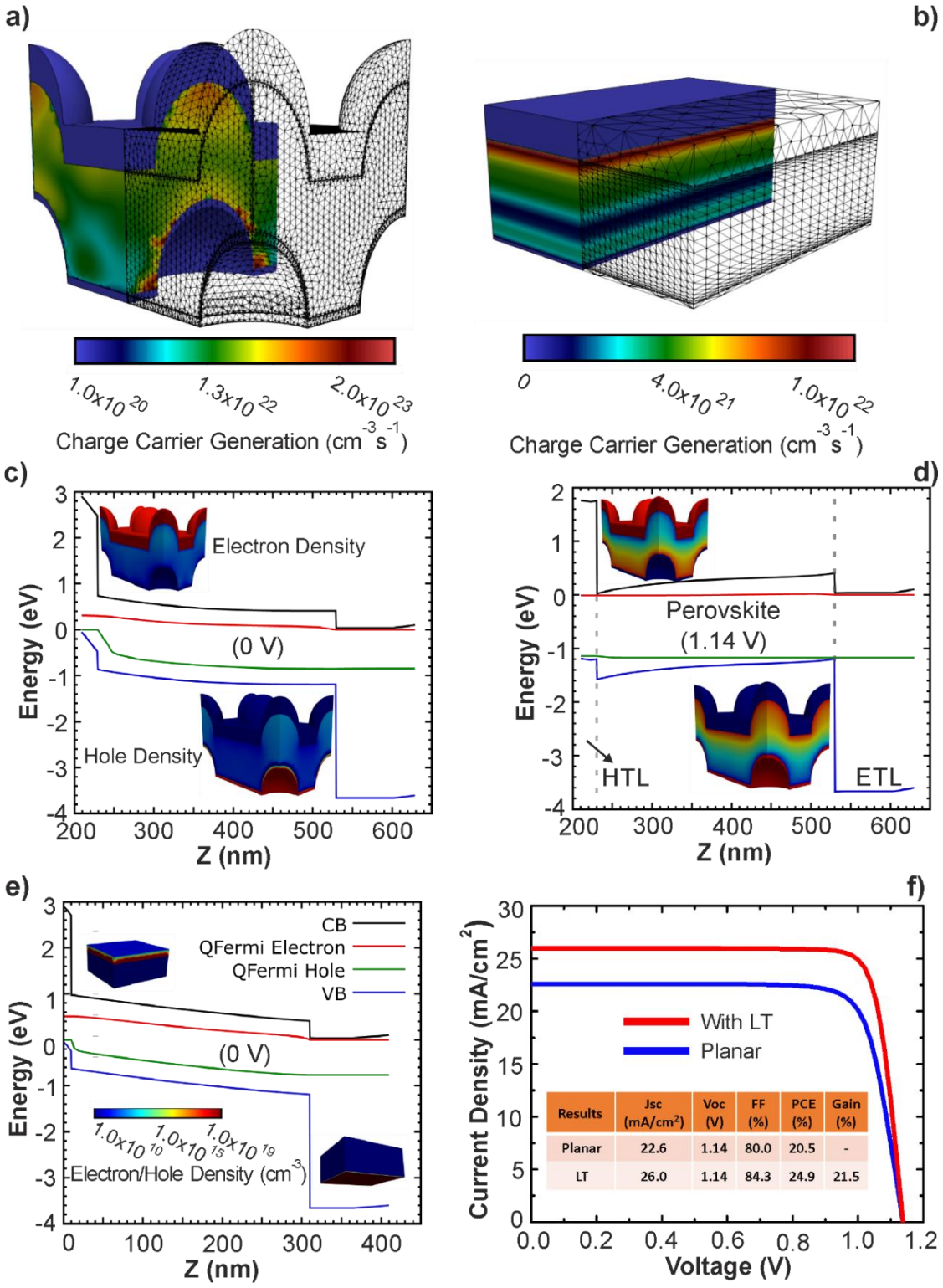

Figure 22: Comparison of electrical simulations of LT-structured and planar PSC. The 3D current generation profiles of LT (a) and planar (b) cells are shown together with the FVM and FEM simulation mesh. The plots in c,d) and e) represent the corresponding band diagrams for the LT (polarized at 0 and 1.14 V, respectively in c) and d) and planar (at 0 V in e) cells. The 4 curves in the band diagram (c,d,e) represent the conduction band (CB) minimum, quasi-fermi electron (QFermi Electron) and hole

(QFermi Hole) levels, and valence band (VB) maximum. The inset images in (c,d,e) show the free electron and hole density used in the electrical simulations. The resulting J-V curves of both planar and LT-structured PSCs are presented in f).

Nevertheless, from Figure 22f one can see that the higher degree of light confinement (absorption) attained with the photonic-structured PSCs significantly improves the photocurrent and, consequently, the efficiency. The studied planar cell with 20.5% efficiency can increase to 24.9% with the optimized photonic-structured counterpart, which represents a 21.5% gain. This enhancement is close to the 22.1% optical photocurrent gain computed in section 5.3.1 for the same photonic-structured PSC (Figure 19a).

5.3.2.2 Electrical modelling of photonic-structured PSC architectures

As described in the previous section, photonic-structured solar cells can be exactly modeled by 3D simulations, but the tradeoff is the highly demanding computational time and memory requirements. Yet, it is known that the high mobility of the perovskite material allows the carriers to travel quickly to the contact layers. Therefore, the authors propose the hypothesis whereby accurate electrical simulations can equally be obtained by planarizing and decreasing the 3D-optically obtained results to lower dimensions, which would reduce the computation time significantly. As such, the 3D-optical generation profiles, for both superstrate and substrate photonic configurations with perovskite thicknesses of 300 and 500 nm (i.e. for all the enumerated cases in section 5.3.1), were planarized and then averaged in the *y* in-plane dimension, resulting in a 2D generation profile to be used in the electrical simulations performed using Lumerical-CHARGE.

For the perovskite material ($CH_3NH_3PbI_3$) the charge transport is considered to be equal for both electrons and holes, although asymmetric transport is possible (e.g. by chloride addition into the iodide mixture; $CH_3NH_3PbI_{3-x}Cl_x$ [213]). Recently, the asymmetric featured HTL, synthesized by benzotrithiophenes small molecules, unveils full planarity that improves intermolecular π-stacking and charge transport, thereby leading to efficient HTL and higher efficiency PSCs. [214]. Furthermore, the complex behavior of the CH_3NH_3 ions can, in some cases, create hysteresis in the JV curves, as reported by several authors [210]. However, this behavior becomes much less pronounced in the highest-efficiency PSCs [215], so it is disregarded here. The ETLs (SnO_2 or ZnO) and HTLs (Spiro-OMeTAD or NiO_x) were modeled as semiconductors with doping profiles defined using a selective junction model, whose profile essentially depends on the density-of-states (DOS) of the materials set for the layers [173]. The electrode layers (ITO, Au) were taken as standard metallic materials described solely by their work function, Φ. The set of parameters used for the electrical simulations is provided in section Appendix A2.

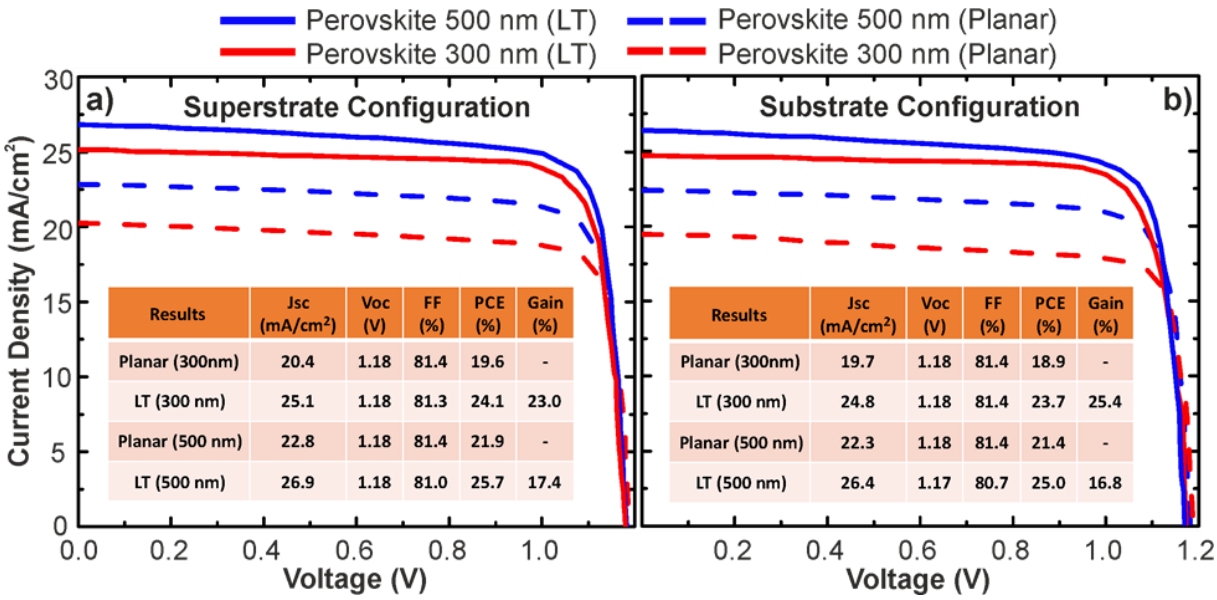

Figure 23: Simulated J-V curves of the PSCs with the conventional 500 nm and thinner 300 nm perovskite layers for both superstrate (a) and substrate (b) configurations. The inset tables present the PV quantities of interest for the simulated devices.

Figure 23 depicts the resulting JV curves attained by the 2D simulations for the planar references and their photonic structured counterparts. The main quantities resulting from these curves are summarized in the inset tables and are in good agreement with the most recent experimental values of high efficient PSCs [38], [186]. We also note that the response of the planar PSC with 300 nm perovskite is in good agreement with the previously calculated 1D simulation in section 5.3.2.1 (Figure 21), again reemphasizing the benefits of computationally efficient 1D simulation to model planar PSCs. The presence of photonic structures leads to a pronounced enhancement of the broadband light absorption across the perovskite layer, boosting the J_{SC}, while keeping the V_{OC} almost unchanged and only slightly reducing the FF following the 3D simulations presented in Figure 22. This results in overall PCE gains up to 25.4% due to LT, close to the optical photocurrent (J_{PH}) enhancements plotted in Figure 2a and listed in Table A2 of Appendix A2.

It is also observed that the J_{PH} values described in section 5.3.1 are consistently higher than the electrical J_{SC} values attained here. This is expected, since in the optical J_{PH} calculation all photo-generated carriers contribute to the current generated by the cell, while the J_{SC} takes into account the relevant electric losses within the layers and interfaces of the PSC structure, as a consequence of insufficient carrier transport (due to built-in E-field, recombination, potential barriers, etc.). These aspects are further discussed in the following section 5.3.2.3, again employing rigorous 3D simulations since the averaging (along y-axis) used for the 2D modelling prevents a complete assessment of the effects of surface recombination and inhomogeneous field distribution caused by the micro-structuring.

5.3.2.3 Analysis of interplay of interfaces and inhomogeneous generation in photonic-structured PSCs

Light management and interlayer engineering are two crucial factors to improve PSC efficiency. Here we combine the best optimized photonic structure with the approximated electronic properties of real, record-performing PSCs, in order to project the full potential of our LT scheme. We also address the question if, under these conditions, one can obtain accurate electrical simulations of complex 3D optical behavior by planarizing and projecting the 3D optical solutions to lower dimensions.

The selected architecture is the superstrate LT-structured PSC, with 300 nm perovskite thickness and Au rear contact (see Table A1 of Appendix A2 for a summary of the dimension of the used features), whose main electrical parameters are listed in Table A4 of Appendix A2. Based on the selected structure and the assumption of physical parameters of the PSC close to the published world record [216]–[221], the set of electrical simulations presented in this subsection explores the effects of three distinct physical parameters of the model:

1) **Dimensionality:** 3D vs. 1D electrical simulation, using the original 3D optical generation profile, $G(x,y,z)$, provided by Lumerical FDTD and shown in Figure 24a;
2) **Generation spatial distribution:** Inhomogeneous vs. homogeneous generation profile, in which a conceptual homogenous (constant) generation, $G(x,y,z)=\langle G \rangle$, is created by averaging the 3D-optical inhomogeneous generation across the absorber volume (see Figure 24b);
3) **Carrier recombination:** comparing the results with and without the effect of SRH recombination, shown in Figure A4 (b) of Appendix A2 in the perovskite bulk and interfaces. When neglecting SRH recombination we consider only radiative recombination, shown in Figure 24c, thus modelling a Shockley-Queisser-like scenario.

Firstly, we analyzed the maximum photocurrent (J_{PH}=27.2 mA/cm^2, see Figure 19) attainable from the 3D optical generation data, $G(x,y,z)$. Multiplying with the inferred voxel[2] volume and summing to total generation rate yielded a short-circuit current density J_{SC}=26.96 mA/cm^2, which is just slightly below J_{PH} due to sampling errors, over the first complete generation region without aliasing artifacts, which yields a 296.15 nm thick absorber, and multiplying the average with the full absorber thickness results in J_{SC}=27.08 mA/cm^2. The adjusted J_{SC} corresponds to an average generation rate of $\langle G \rangle = 5.628 \times 10^{21}$ cm^{-3}s^{-1} integrated for the absorber volume. This is the reference value used in the subsequent simulations that considered a homogeneous (constant) generation profile equal to $\langle G \rangle$ for the entire perovskite material, as shown in Figure 24b. The comparison of the *J-V* curves for inhomogeneous and homogene-

[2] Voxel denotes a 3-dimensional "grid point", i.e. a grid unit cell – see further details regarding the process in Appendix A2.

ous generation emphasizes the electrical effect of the spatial distribution of the photo-generation, and the increased interface area caused by the photonic structuring. For a direct comparison, the integral over the original generation profile within the absorber needs to be equal to the integral over the homogenous generation profile. Therefore, the homogenous generation rate was set up to generate as many charge carriers as the inhomogeneous generation rate.

For comparing the results between the 3D and 1D electrical simulations for the structured PSCs, the 3D-optically computed $G(x,y,z)$ data needed to be adequately normalized for the 1D simulations (as sketched in Figure 18,b) by first planarizing the 3D generation profile, G, and then integrating along the in-plane directions (x,y), thereby creating the 1D generation profile, shown in Figure A4 (a) of Appendix A2. For the 1D electrical simulations of homogenous generation, a constant generation profile (similar to the 3D, as shown in Figure 24, b) equal to $\langle G \rangle$ along the z axis was used as shown in Figure A4 (a) of Appendix A2. Here, to properly compare the influence of the increased surface area (and also dimensionalities) due to the curved structures (photonic-structured devices) to the planar structure (planarized devices), all electrical parameters as shown in Table A4 of Appendix A2 (including surface and bulk recombination coefficients) were kept the same in both cases. Finally, to analyze the effect of carrier recombination, the 1D and 3D simulations were performed with and without the SRH coefficient, which is the dominant recombination mechanism.

For the considered set of parameters listed in Table A4 of Appendix A2, Figure 24 highlights how the outcome of the drift-diffusion simulations does not seem to be strongly correlated with the structural geometry of the solar cells. The changes in PV performance are almost negligible, as seen in Table 6, which is mainly a consequence of the high mobility of the carriers in the perovskite material, aided by the ultra-low thickness of the perovskite layer (300 nm). The combination of both factors allows the charge carriers to quickly travel from the dense photon-trapped regions (localized "hot-spots") towards the contact layers where they can be extracted.

Nevertheless, one needs to define the parameter space more concisely, i.e., which materials and interface parameters increase the sensitivity of the simulations to the device geometry, to a point where the geometry must be explicitly considered to obtain reliable results. However, it can be said that electrical 1D simulations based on averaged optical generation can be regarded as a very good approximation of 3D approaches, as the PV outcomes are found to be almost identical to the inhomogeneous generation profiles. More generally, it can be inferred that the better the overall device performance with regard to carrier extraction and interface recombination the better the agreement between 1D and 3D simulations.

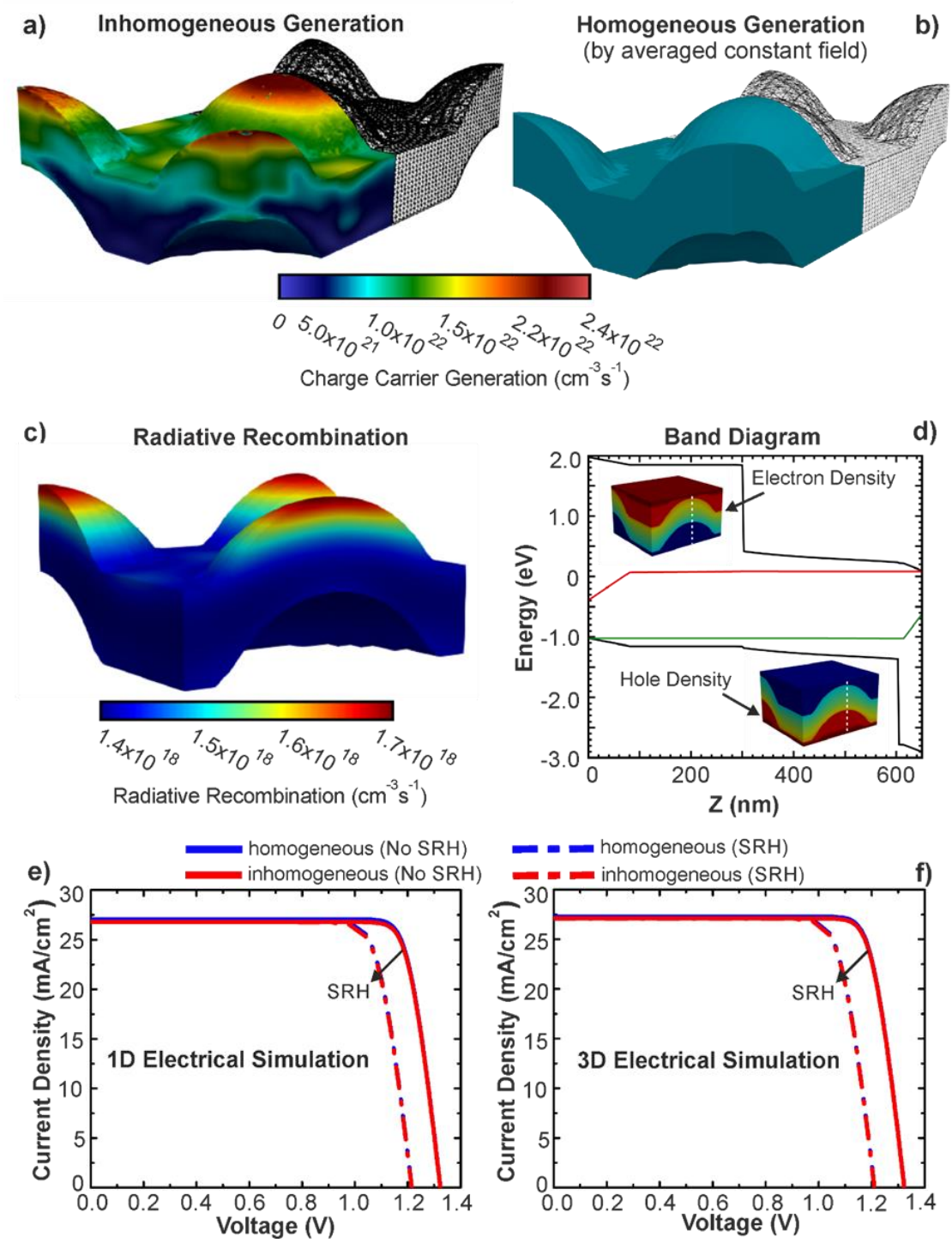

Figure 24: a, b) 3D inhomogeneous (original) and 3D homogenous (averaged) generation profiles used to evaluate the electrical PV performance. c, d) represent the radiative recombination profile at the maximum power point (c) within the perovskite absorber, and the band diagram of the structured PSC (d). e) J-V curves of the 1D (e) and 3D (f) device modelling using either the inhomogeneous or homogenous generation profiles, as well as with and without the effect of SRH recombination.

The moving from 3D to 1D computation is extremely important, as this change can speed up simulations by several orders of magnitude while reducing memory footprint. As an example, a typical 3D simulation of a photonic-structured PSC requiring about 16 hours and 128 Gb of memory, is reduced to 1.5 min and 30 Mb of memory when performed in 1D. Furthermore, it consolidates novel simulation techniques that can be used to study a broader range of devices.

Concerning the recombination effects, Figure A4 (b) of Appendix and Figure 24c depict the distribution of the two types of recombination mechanisms considered here: SRH (at interfaces and in the perovskite bulk) and radiative recombination. The SRH bulk and surface recombination parameters were chosen to reduce V_{OC} by 100 mV, respectively, or 140 mV when combined. While nonradiative recombination is generally considered to be the dominant loss mechanism in the highest efficiency PSCs, the distribution between bulk and interface is difficult to assess [189]. As such, a 50% contribution between the interfaces and bulk has been assumed. As expected, with activated SRH-recombination V_{OC} is significantly reduced. We note that the simulated interface area increases by 16% for the investigated photonic-structured PSC compared to the planar geometry, which leads to an increase in surface recombination. This in turn leads to an additional 5 mV reduction in V_{OC} for the photonic-structured PSC compared to the 1D structure, irrespective of the generation rate profile. Due to idealized extraction and a negligible influence of a potential shunt/parallel resistance, there is no slope observed at 0 V (J_{SC}) as seen in Figure 24d.

Table 6: Main parameters attained by the electrical analysis performed in this sub-section to explore the effects of model dimensionality (3D vs. 1D simulations), the spatial distribution of photo-generation (inhomogeneous vs. homogeneous *G* profiles) and SRH recombination, for the optimized LT-structured PSCs with superstrate configuration, 300 nm perovskite thickness and Au rear contact.

Description			Jsc	Voc	FF	PCE
Dimension	**Generation**	**Recombination**	**(mA/cm²)**	**(V)**	**(%)**	**(%)**
1D	**Homogeneous** $G(z) = \langle G \rangle$	**no SRH**	27.06	1.3234	84.05	30.1
1D	**Inhomogeneous** $G(z)$	**no SRH**	26.78	1.3232	84.11	29.8
1D	**Homogeneous** $G(z) = \langle G \rangle$	**with SRH**	27.06	1.2153	81.31	26.74
1D	**Inhomogeneous** $G(z)$	**with SRH**	26.78	1.2152	81.37	26.47
3D	**Homogeneous** $G(x,y,z) = \langle G \rangle$	**no SRH**	27.28	1.3234	84.00	30.32
3D	**Inhomogeneous** $G(x,y,z)$	**no SRH**	27.09	1.3232	84.04	30.13
3D	**Homogeneous** $G(x,y,z) = \langle G \rangle$	**with SRH**	27.28	1.2106	81.32	26.85
3D	**Inhomogeneous** $G(x,y,z)$	**with SRH**	27.09	1.2104	81.35	26.68

Overall, the electrical simulations using the optical generation profiles, originating from the advanced light-trapping structures computed by 3D FDTD, demonstrate the large potential gain for efficiency improvement of PSCs. Even though the study was not thorough in respect to the materials parameters, it does suggest that such increased surface area between the absorber and HTL/ETL does not significantly impact these results. The comparison between the 3D simulations based on the semi-prolate structure and the 1D simulation of flat surfaces show that the increased interface area has only little impact on V_{OC}, while the different generation profiles have none at all. Hence, it can be argued that the optical improvements achieved by the devices far outweigh the increased surface area.

The results here presented invite the experimental validation of these novel promising concepts. In that respect, recently F. Wang et al. [68] developed an isopropanol-assisted recrystallizing treatment for the perovskite. This method allows a practically conformal (pinholes-free) coating of the PSC layers onto photonic-textured glass substrates with micron-sized surface features having high aspect-ratio, identical to those considered in this work. With this conformal deposition, the authors reached 18.6% PCE for a ~300 nm thick perovskite and demonstrate that it is possible to overcome the trade-off between the optical enhancements and electrical deterioration caused by structured curvatures, thereby enabling the full exploitation of the maximum optical gains.

5.4 Conclusions

The outcomes from this study contribute to corroborating and providing a new understanding of the underlying physical effects occurring in this emerging type of photovoltaic devices. It was shown that photonic-enhanced PSCs with ultra-thin perovskite layer (300 nm) outperform state-of-the-art planar PSCs with conventionally thicker perovskite layer (500 nm) by a significant margin (25.4% PCE enhancement). It is also demonstrated that the ultra-thin photonic-enhanced PSCs can realistically reach remarkable 26.7% PCE values if we consider electronic properties similar to those of the state-of-the-art PSCs.
From an optical standpoint, the less-reflective (although inexpensive) Ni rear metal contact also showed higher photocurrent for photonic-structured PSCs compared to the planar PSCs with Au or Ag.

Nonetheless, of particular interest for any application of photonic solutions in PSCs, are the full device modelling studies developed here that help understand how light trapping can influence the electrical device performance. This study also unveils how the PV performance is practically independent of the type of field distribution (homogeneous/inhomogeneous: regular/irregular) generated by the optical strategy in the perovskite absorber, as demonstrated experimentally [68]. Furthermore, 1D and 3D electrical device modelling showed al-

most identical solar cell performance, which will certainly motivate the PV community to simulate solar cells with ever complex geometry in a less time-consuming and straightforward way, without significantly compromising accuracy.

6

CHECKERBOARD LIGHT-TRAPPING STRUCTURES AND DESIGN RULES TO MAXIMIZE ABSORPTION

6.1 Introduction

Broadband absorption of sunlight is key for solar cell technologies, so nanophotonic structures have emerged as a promising technique for their efficiency improvement. For instance, surface textures enable a reduction in surface reflection, enhancement of internal reflections, and optical path lengths in the active material [5].

One-dimensional surface gratings have become one of the most studied diffractive structures [222]. Simple grating lines now serve as test vehicles for theoretical concepts and fabrication methods [222], [223]. For example, while their superposition facilitates the analysis of more complicated designs [222], [224], gratings are commonly used in monochromators, spectrometers, wavelength-division multiplexing, cavity lasers, and sensors [225]. Some studies also proved their suitability for broadband mirrors [226] and radiative cooling applications [227].

Up to now, simple grating lines have only shown marginal absorption improvements in solar cell materials. The belief that they cannot be the pillar of advanced photonic concepts triggered a new research field to analyze more and more complicated and evermore efficient light-trapping schemes [228]–[230], at the expense of their complexity. Yet, the industry chooses (random) surface textures based on their easy processing and integration in photovoltaic devices. Simple grating lines thus could take a leverage position in large-scale implementations, if they outperform state-of-the-art approaches.

However, authors so far typically have focused on specific natural textures or computational algorithms [231]. Even though biological systems show a stunning diversity of surface structures [232]–[235], they serve multiple functions and result from complex morphological and chemical changes driven by natural selection. To replicate a natural absorption enhancement scheme, we thus first need to translate nature's idea back into simplified terms that are compatible with current fabrication and processing methods. For example, the excellent antireflective properties of foliage surfaces [236], [237], insect wings [238] and the moth-eye [239], [240] originate from densely packed, gradual-shaped structural features at the sub-wavelength

scale. Similarly, we can mimic these structures with artificially nanostructured arrays of domes, pillars, cones, or pyramids on solar cells [18], [19], [119].

The focus recently moved from the actual texture to its scattering and diffraction pattern. The absorption enhancement by rose petals [241], [242] and tropical butterfly-wings [243]–[245] originates from refractive and diffractive effects, respectively. Some studies try to link the superiority of a structure to the lower symmetry in its diffraction pattern [246], [247], but others refrain from conclusions based on symmetry group theory alone [247]. For example, the comparison of the dimple and rose structure [246] shows that coupling to higher diffraction orders does not necessarily translate to a greater current enhancement than coupling to lower orders. The actual principle for efficient light-trapping thus remains unclear.

If structural features cannot explain why some structures perform better than others, the research question must be approached from a different perspective. Here, we outline how a basic principle empowers grating lines to outperform state-of-the-art literature proposals. Finally, from a survey of a large and diverse range of structures, we derive four design criteria that directly link the Fourier-series of a structure to its implied photocurrent. They enable us, in turn, to explain the excellent performance of our design principle. It thus generally applies and is not restricted to particular structural features or the material.

6.2 Theoretical considerations

6.2.1 Grating lines

Simple grating lines are often regarded as disadvantageous because one-dimensionality (1D) cannot address both polarization states effectively at the same time. Lines mostly affect the absorption enhancement of a plane of incident angles instead of the full hemisphere. In addition, high periodicity leads to sharp and not broad resonance peaks in the absorption spectrum, restricting the absorption enhancement to only narrow wavelength intervals.

Once we look at two-dimensionality (2D), such as crossed 1D grating lines, we note a substantial gain in photocurrent compared to their 1D counterpart. Could 2D-periodicity cause this effect? 2D-periodic textures have received much interest due to their potential for higher light-trapping improvement over random textures [19], [224], [248]. Gjessing *et al.* optimized seven different 2D-periodic structures [246]. Although they found the lattice period that gives optimal light-trapping is comparable for all structures, the light-trapping ability differs between them [246]. 2D-periodicity thus cannot solely explain the high performance of a light-trapping structure.

However, when an appropriate level of short-range disorder is tuned into the structure via its Fourier-space representation, a better light-trapping solution is found [85], [222], [249]. Accordingly, the search for the optimum optical scheme has led to apparent-randomly distributed geometrical features arranged inside a large, periodically repeated unit cell.

In principle, the light-trapping problem then appears as solved by quasi-random (QR) nanostructures. However, a diffraction pattern does not define the desired structure. The abstract concept of Fourier-space engineering may not give clear guidance to a technologist, particularly in terms of simple fabrication and processing techniques. The opposite is instead a more natural approach, i.e. arranging simple periodic structures in a QR manner.

This proposal might be the way out for grating lines to overcome the one-dimensionality issue and gain a quasi-randomness appearance at the same time. We can show that the two approaches are complementary solutions to the light-trapping problem. Yet, gratings show distinct advantages for solar cell applications, as we highlight in the discussion section.

6.2.2 The photonic domain

Commonly, a unit cell defines the region of interest for optical (electromagnetic) modelling. It encloses the surface structure in a square or rectangle, to which periodic boundary conditions are applied to ease the simulation. While a convenient technique for computational analysis, this method does not highlight the relationship between the geometrical arrangement of the diffractive features and their unit cell.

To simplify the following discussion, we introduce the concept of the photonic domain. We define it as the region within a photonic structure in which a basic diffractive element is periodically arranged in a one-dimensional fashion. But the domain could comprise just a single element, too. For example, Gjessing *et al.* [246] used a mono-pitched roof as the building block, i.e. the photonic domain, for the rose and zigzag structures shown in Figure 25. Before displacing a roof next to another one, it is rotated by 90-degree.

Figure 25: Depiction of different arrangements of diffractive elements (photonic domains) in square lattice structures. The rose (left) and zigzag (center) structures are based on the same diffractive element, i.e. a mono-pitched roof, which is rotated 90 degrees four times. The checkerboard structure (right) results from the simplification of the mono-pitched roof as a non-slanted grating line. Since all photonic domains contain one element, the computational unit cell encloses four.

Therefore, it may not be difficult to increase the apparent randomness of a design with periodic grating lines. When we replace the mono-pitched roof of the rose or zigzag structure with lines, we get the checkerboard pattern shown in Figure 26c. Such trellised patterns were

proposed to control the wetting properties of surfaces [250], but have so far not been analyzed for light-trapping applications.

In addition, changing the shape of the photonic domain increases the design freedom. Whereas triangular, rectangular and hexagonal domains have been studied in the field [247], [251], [252], only a few authors proposed a pentagonal or heptagonal domain for light-trapping despite their superior characteristics [253]. But as the regular pentagon has a 72-degree rotational symmetry, it cannot tile a plane alone [254]. In Figure 26d, we thus propose an irregular pentagon with two different side lengths as the photonic domain for efficient light-trapping. Curiously, the alternate arrangement of such pentagons enables butterfly wings to absorb more sunlight [235], [239], [244].

Finally, modulating grating lines with a rotational operator, as in the farrago design (Figure 26e), allows for quantifying the introduced level of "randomness" by the number of different domains, e.g. 2 for the zigzag, checkerboard or pentagon, 4 for the rose and 72 for the farrago.

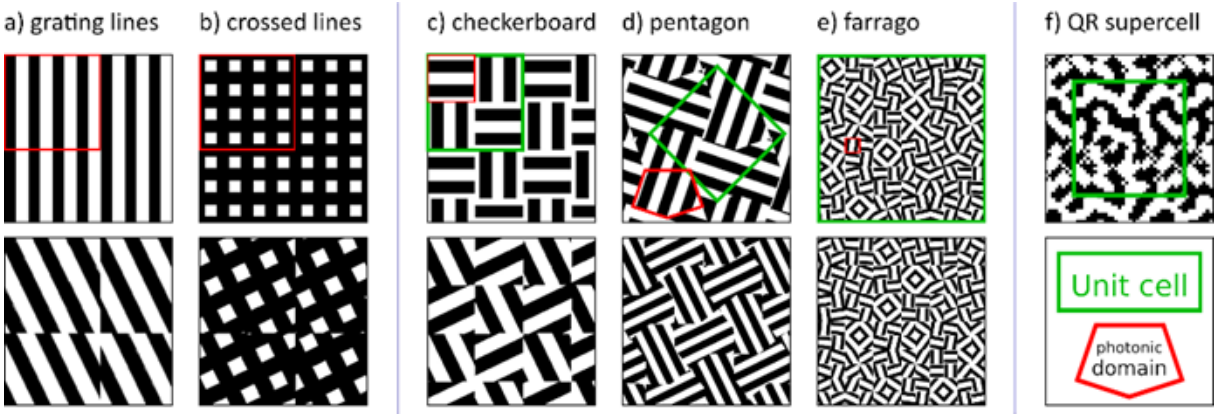

Figure 26: The arrangement of a simple diffractive element (a-e) controls the structural disorder. While periodicity can be disturbed via restructured photonic domains (bottom), this approach does not break mirror symmetry. Superior light-trapping structures repeat a periodic element quasi-randomly (e) or a QR element periodically (f). Whereas the former case offers flexibility in its design, fabrication and modification, the latter relies on accurate replication techniques. Since the unit cell is also the photonic domain of the QR supercell, design (f) from Ref. [85] cannot be generated from the quasi-random arrangement of a periodic element – in contrast to designs (c-e).

6.3 Results

We first optimize the checkerboard structure shown in Figure 26c. As its photonic domain comprises a 1D-grating only, the structure becomes defined solely by three design parameters: the side length of the photonic domain, the grating's line width and its period, see Figure 27a.

For a direct comparison of light-trapping performance, we follow the strategy set out in previous works [85][252], employing a test solar cell structure composed of crystalline silicon (c-Si) absorber material with an ideal back reflector:

- The thickness of the c-Si slab is set to 1 µm. At this thickness, light trapping has a great impact on absorption, and differences in photocurrent will manifest noticeably in the comparison of different textures [252].
- All photonic domains are etched on the front surface, whose depth is fixed at 190 nm which was found optimal in previous studies [85] for a 1 µm thickness.
- The c-Si surface is coated with a transparent dielectric medium of refractive index 1.65 and 70 nm thickness, conformally. This layer acts both as a passivating film for the etched regions as well as an anti-reflection coating.

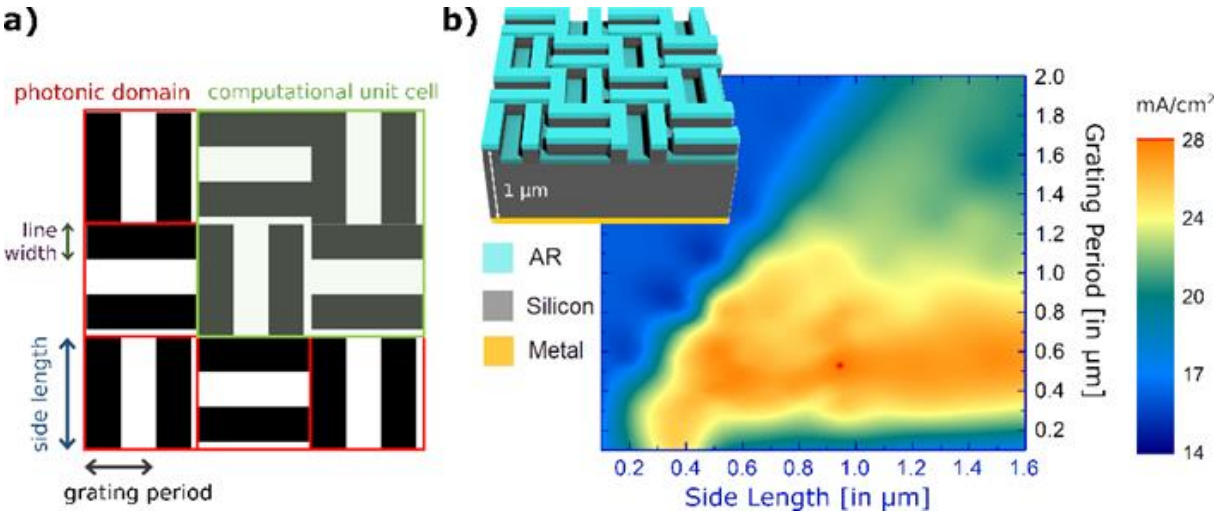

Figure 27: Representation of the checkerboard's photonic domain and computational unit cell (a). The parameter map shows the computed maximum achievable photocurrent density J_{max} as a function of the grating period and domain size (b). The inset shows the test cell with the checkerboard structure over it. The line width is here kept at half the grating period. The red dot marks the optimal parameter set that maximizes the broadband absorption in the 1 µm c-Si layer.

The photocurrent density produced in the c-Si material is taken as the figure of merit. It is equivalent to the maximum achievable photocurrent density J_{max} that would be generated by the cell. Here, we use the software package Lumerical FDTD Solutions to calculate J_{max} (the details about the procedures are given in Chapter 2) over the main spectral range of the AM1.5G solar spectrum, i.e. from 315 nm to 1150 nm wavelength.

From the parameter scan depicted in Figure 27b, we identify a high photocurrent region for grating periods between 0.3 and 0.9 µm, with the optimum period and domain size around 575 nm and 0.925 x 0.925 µm², respectively. Next, as the line width was kept at half of the grating period, we now study the impact of the line width on the J_{max}. We find 242 nm as the best parameter; that matches the line width of the optimized crossed grating design. Surprisingly, the checkerboard arrangement (28.4 mA/cm²) considerably outperforms the crossed design (25.2 mA/cm²), as shown in Figure 28, and demonstrates an excellent angular insensitivity up to a 60-degree angle of incidence. The structure surpasses recent proposals and even

rivals the exceptional performance of the QR supercell [85], see Table 7 and Table 8. This sophisticated design is termed supercell because the superposition of multiple gratings (with the same period) controls the phase shift between its diffraction orders [85].

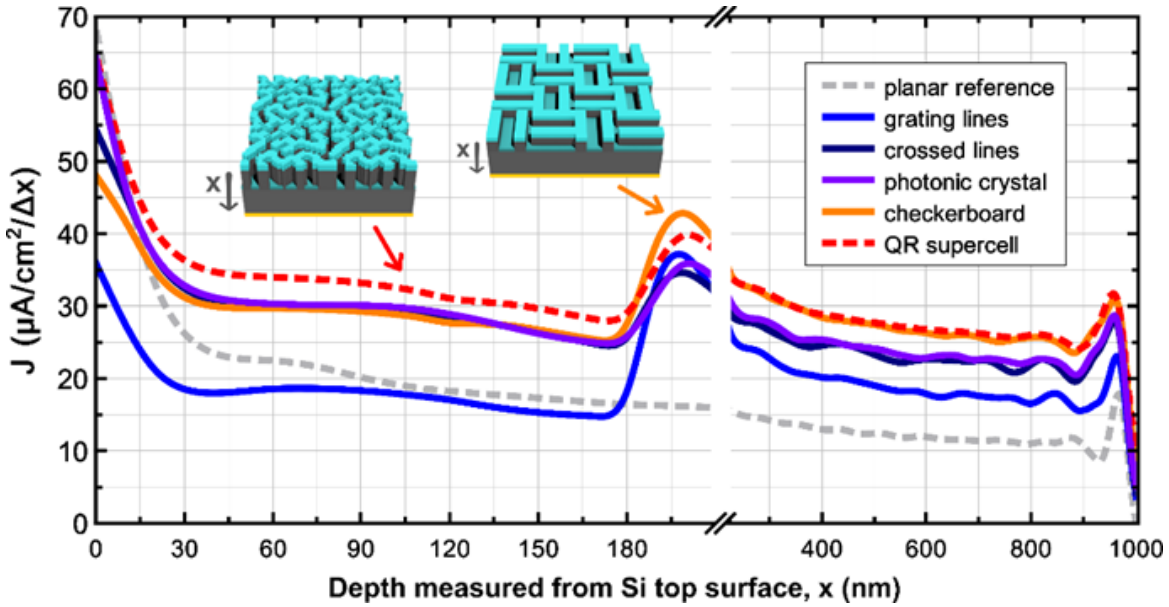

Figure 28: Photocurrent depth profile, i.e. current generation per unit volume as a function of the absorber's depth x, determined by segmenting the total (1 μm) c-Si slab in thin slices with a step size of Δx = 10 nm. All current density profiles are calculated for the AM1.5G solar spectrum. While the current J generated in the surface pattern (0 – 190 nm depth) is equal for the checkerboard, photonic crystal and crossed grating lines, the current in the flat bulk layer (190 - 1000 nm depth) is the same for the checkerboard and supercell design from Ref. [85] Although the highest current is found within the QR supercell's surface texture, it will likely suffer the most from surface recombination effects.

To verify that our parameter optimization was indeed unconditional, we extended our FDTD calculations to different domain sizes. Furthermore, we also changed the domain geometry from a square to an irregular pentagon with two different side lengths, as shown in Figure 26d, effectively adding a degree of freedom to the design. Yet, we optimized the pentagon only tentatively due to computational restraints [190], because we preferred to focus on the checkerboard's simpler geometry. Additional optimization steps thus may well reveal the pentagon's benefit.

Four parameters thus define our proposed light-trapping solution: the photonic domain size, the structural feature size, their periodicity and etching depth. Table 8 summarizes the transformative steps undergone by the photonic domain and the resulting quantitative changes in the J_{max}, which we cross-checked with a different simulation method (Rigorous Coupled Wave Analysis).

Table 7: Recent theoretical proposals for light-trapping in thin-film c-Si solar cells. The crossed grating lines have a 242 nm width. The Light Trapping Efficiency *(LTE)* compares the actual current

gain *via* surface structuring to the theoretical current gain *via* Lambertian scattering [228]. It thus aims at assessing the performance of the nanostructure itself, irrespective of the fabrication method and technology used. J_{max} not found in a reference were calculated using the published absorption spectra.

Structure name	**Total c-Si slab thickness (μm)**	***LTE***	**Maximum current (mA/cm²)**
Grating lines [this study]	1.0	0.31	19.5
Retina's fovea [255]	3.1	0.65	21.6
1D Periodic Fourier-series profile [256]	1.3	0.66	24.6
Crossed lines [this study]	1.0	0.68	25.2
Photonic Crystal [257]	1.0	0.73	25.9
Begonia's spiral [258]	1.5	0.83	26.2
Leaf-inspired scheme [259]	20.0	0.87	28.0
Checkerboard [this study]	1.0	0.89	28.4
QR supercell [259]	1.0	0.96	29.5

Table 8: Potential impact of surface structures on the carrier generation under AM1.5G solar spectrum illumination. All grating lines have a 242 nm width. The filling factor *FF* is defined as the area of the etched regions over the entire area of the unit cell. The surface/bulk current refers to carriers generated within/beyond 190 nm depth. Remarkably, grating lines can enhance the bulk current of a 1 μm thin c-Si slab by 125% *via* the checkerboard arrangement.

Photonic Structure	**Domain length (μm)**	**Unit cell**			**Surface current (mA/cm²)**	**Bulk current (mA/cm²)**
		Size (μm²)	FF (%)	Surface Area Increase (%)		
Planar reference	NA	NA	0	0	4.6	10.1
Grating lines	0.575	0.33	58	66	3.6	16.0
Crossed lines	0.575	0.33	34	77	5.9	19.3
Checkerboard	0.925	3.42	48	82	5.8	22.7
Photonic Crystal [257]	0.600	0.36	35	66	6.1	19.9
QR supercell [259]	1.792	3.21	50	188	6.6	22.9

6.4 Discussion

6.4.1 Real-space considerations

Like hierarchical structures in biological systems often vary a certain building block [234], we generate a set of different domains via the modulation of a basic photonic element. As such a set defines a unit cell dynamically, our simple principle introduces a new class of light-trapping structures, like the checkerboard, farrago or pentagon patterns shown in Figure 26.

Here, we focus on the checkerboard pattern that results from the displacement and π/2-rotation of periodic grating lines. This alternate arrangement increases the bulk current by

twice as much as a crossing of the lines can do. Therefore, the checkerboard light-trapping performance is close to that of the QR supercell design.

However, although both structures use the same silicon volume, the QR supercell has a 60% larger surface area, see Table 8, which increases surface recombination effects[260], as evident from its carrier generation profile[190]. In a preliminary experiment on commercial cells, we could also observe how these effects scale with the surface area to volume ratio. Therefore, we note the checkerboard's ability to shift its carrier generation further into the bulk, accomplished by [190]:

- choosing an up to 30% smaller line width,
- using an up to 30% shallower etching depth,
- extending its unit cell to three domains via π/3-rotated grating lines.

Consequently, the tolerance in width and depth of the large rectangular features makes the checkerboard structure more robust to fabrication imperfections. Noise in the line width may improve its angular response [234], and tapered lines couple better to incident light, as the optical density changes more gradually. The checkerboard thus mainly depends on the grating period, as shown in Figure 27b, permitting a fast turnaround from the design to its implementation up to potential modifications.

Since light beyond 600 nm wavelength is not absorbed within a double pass of the 1 µm silicon slab, one could select λ_0 = 600 nm as the target wavelength which in turn would define the grating period $P \approx \lambda_0$. If the grating height h and duty cycle D are then chosen such that the zero diffraction order cancels out, the light will be transmitted only at odd diffraction orders. So, the phase difference $\Delta\phi = 2\pi/\lambda_0 * h * \Delta n$ of the interfering waves must be equal to π and D=50% [261], implicating $h = \lambda_0/(2 \cdot \Delta n) \approx 130$ nm for an index contrast of $\Delta n = n_{Si} - n_{ARC} = 2.29$ at λ_0 = 600 nm. We note that these preliminary estimates are remarkably close to the outcome of the intensive FDTD computations performed in this work.

In addition, we also analyzed the checkerboard's performance to non-structural variations but found only 3 to 4% differences when the coating and c-Si layer thickness vary by 15% and 10%, respectively.

Finally, our study was motivated by the desire to reduce design complexity without loss in light-trapping performances. While the small 32 nm pixels of the QR supercell structure can rise complications in all the here mentioned lithography approaches, the simplicity of the checkerboard structure does not rely on a sophisticated fabrication technique: grating profiles are widely manufactured by holographic techniques, such as laser interference lithography, but also qualify for high-speed electron (multi) beam lithography [262], [263]. Sub-micrometer gratings can also be imprinted [263]. For example, Hamamatsu uses nanoimprinted gratings for its ultra-compact mini spectrometers, whereas Canon teamed up with Toshiba to develop 15 nm nanoimprint lithography for the high-volume manufacturing of semiconductor devices [264]. Immersion lithography, deep-UV lithography, and digital planar holography are other industrial methods [262]. We like to note that Displacement Talbot Lithography (DTL) [265]

could be a very promising large-area lithography technique for the checkerboard structure. However, as the current state-of-the-art seems to focus on strictly periodic patterns, it appears that only direct writing is capable of generating checkerboard patterns. As such, their feasibility remains to be tested. While some quasi-random [266] and complex periodic structures [267] were already produced via DTL, preliminary simulations seem to indicate that DTL might in principle create the checkerboard structure as well.

6.4.2 Fourier-space considerations

After highlighting the practical advantages of the checkerboard design, we now turn to the question of why its performance rivals the one from the QR supercell approach, whose functionality was tuned into its structure via Fourier-space considerations. The Fourier-spectrum of the QR supercell is rich, thereby giving the appearance of continuity, and concentrates all its energy distribution function $ED(k_x,k_y)$ in a ring region between 10 µm^{-1} and 25 µm^{-1}, see Figure 29a. In contrast, the checkerboard's Fourier-spectrum is not very broad and is mainly distributed along the principal axis, see Figure 29b. Still, both designs yield high performances.

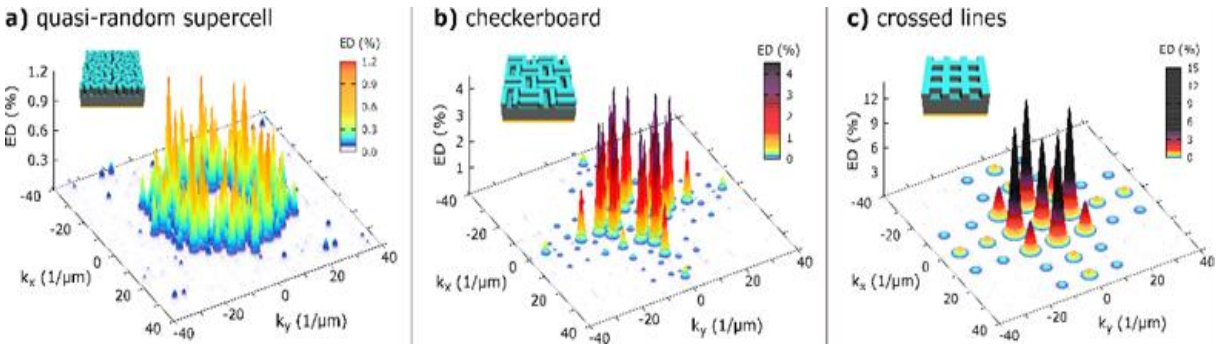

Figure 29: Fourier energy spectrum in *k*-space for a) the QR supercell, b) the checkerboard and c) the crossed lines. For comparison, the energy distribution $ED(k_x,k_y)$ is normalized to the total diffracted intensity, given by the sum of all Fourier components in *k*-space. Here, each structure covers a 500 µm^2 area in real space; it is sampled at 5 nm resolution and expressed as a binary data matrix (see Appendix A3). Its Fourier transformation yields the desired Fourier-series components (after shifting the zero-frequency component to the center of the array). For their visualization only, they were appropriately smoothed.

So, could the supercell concept ignore classes of structures that fail its ring criteria? This question inspired us to analyze the Fourier-series of a vast range of diverse structures (see Appendix A3), enabling us to identify four criteria that correlate with current gains:

1. high number N_{strong} of strong Fourier-series components,
2. low contribution of strong components ED_{strong} to the total diffracted energy ED_{tot} – a component is defined as strong (weak) if its Fourier energy exceeds (falls below) n% of the series' peak value;

3. low energy spread into the outer k-region $ED_{k>k^*}$, i.e. beyond the wave-number k^*,
4. high surface area factor (SAF) of the pattern – the SAF quantifies the increase in surface area compared to an unstructured slab while respecting the periodic boundary conditions of the unit cell.

It is $ED_{\text{weak}} + ED_{\text{strong}} = ED_{\text{tot}}$ and $ED_{\text{k<k*}} + ED_{\text{k>k*}} = ED_{\text{tot}}$. Our extensive study reveals a direct link between the Fourier-properties of a light-trapping structure and its resulting theoretical current enhancement $X = J_{max}/J_{ref}$ of a 1 µm c-Si slab, here, empirically defined by

$$X = 1 + \left(1 - \sqrt{f}\right)^p \quad \text{with} \quad 1/f = SAF \cdot \sqrt{\frac{ED_{\text{weak}}}{ED_{k>k^*}}} \cdot N_{\text{strong}}^q \cdot \left(\frac{ED_{k<k^*}}{ED_{\text{strong}}}\right)^p \tag{6}$$

in which the function *1/f* evaluates the four criteria in *k*-space, quantitatively. We find a high correlation coefficient $R=0.97$ between X and J_{max} for $p=1.87$ and $q=1.19$, which is robust to changes in n or k^* and is maximal for $n=15$ and $k^*=21$ µm^{-1} (see Table A5 and A6 of Appendix A3). According to Figure 30, point $X=1.7$ separates the surface structures with a single domain from those that yield the highest J_{max}.
Since our design principle meets the four criteria better than (crossed) grating lines alone, the checkerboard rivals the QR supercell structure, whose design does still fulfil them best:

a) uniformity in *k*-space increases the number of strong components N_{strong} but also weakens their contribution (criteria 1 and 2),
b) limiting the diffraction pattern to k=24.5 µm^{-1}, that is close to k^*=21 µm^{-1} (criteria 3),
c) the choice of small and squared pixels increases the SAF (criteria 4).

However, suppressing the lowest orders, as in Figure 29a, is not necessary (shown in Figure A5 of Appendix A3): their inclusion reduces the surface current by 0.5 mA/cm² but increases the bulk current by 0.2 mA/cm² (c.f. QR32_E0-E7 in Table A5 of Appendix A3), resulting in only a 0.3 mA/cm² lower photocurrent than the J_{max} of the original QR supercell design (c.f. QR32b Table A5 of Appendix A3).

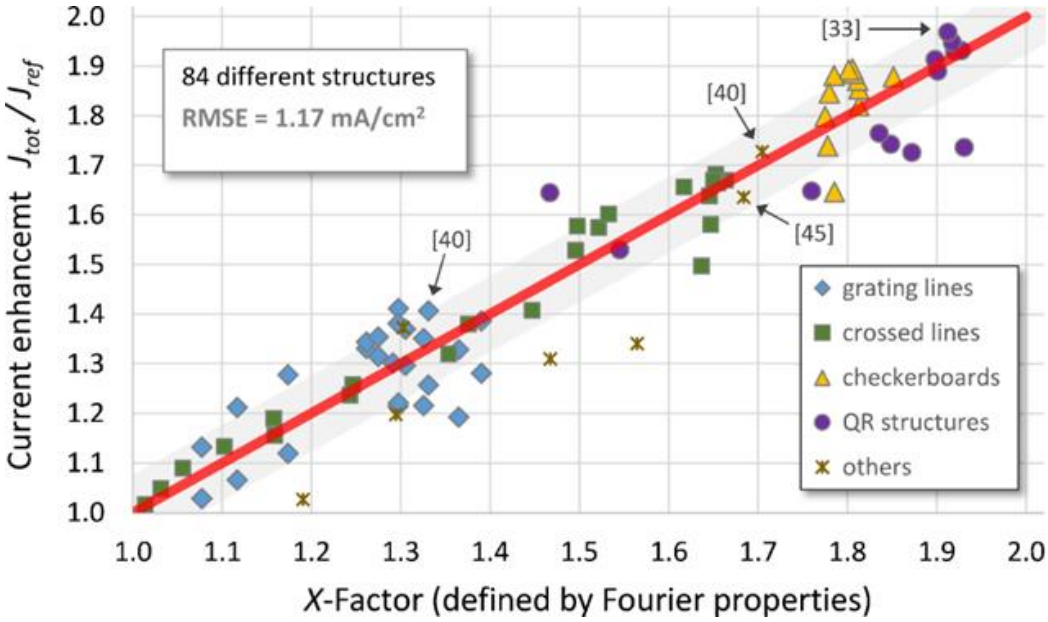

Figure 30: The analysis of 84 different surface structures, that are etched 190 nm into a 1 µm thin c-Si slab (listed in Table A5 of Appendix A3), indicates a link between their Fourier-properties (Eq. 6) and the theoretical maximum achievable photocurrent $J_{max} = X \cdot J_{ref}$, with the planar reference J_{ref} =15 mA/cm². Some selected literature proposals are annotated with their references in brackets. For a fair comparison, all Fourier-series are based on the same aperture area of ca. 500 µm², sampled at 5 nm resolution and expressed as a binary data matrix. Although the root-mean-square-error *RMSE* (grey-toned area) implies a forecast that is often greater than the mean-absolute-percentage-error (4.2%), the correlation coefficient *R* highlights a strong relationship between *X* and J_{max}. The mean-absolute-scaled-error (63%) shows that our (red) trendline is almost twice as good as the standard naive model.

Finally, since light-trapping structures inherently boost the surface recombination [238], considering this effect in the analysis relies on a full-device modelling approach and, therefore, greatly complicates the comparison of multiple proposals. We argue that the best light-trapping structure generates the greatest bulk current with the smallest increase in surface area. As such, when using the same surface passivation technology, the checkerboard structure will likely outperform the QR supercell design.

6.5 Conclusions

Surface textures increase the absorption of sunlight in photovoltaic materials. Although this strategy led to powerful designs, proposals often neglect their technological practicalities. For example, engineering the desired diffraction pattern into a structure via its k-space representation may result in its arbitrary appearance in real space, e.g. the QR supercell approach. Such a fine-tuned structure then becomes difficult to fabricate on a large scale, to monitor for imperfections and to modify, if needed later on.

On the other hand, our checkerboard pattern shows much simplicity in design, reduced surface area, and high robustness to imperfections but performs similar to the QR supercell. While we restricted our work to the cell level, any encapsulation material and protective glass cover will unlikely affect our conclusions. We expect their presence to reduce the charge generation in the surface structures. In addition, our concepts were tested on a 1µm slab of c-Si. Therefore, changing the etching depth, absorber thickness or material inevitably changes the optimal design parameters in real and Fourier space; both will be subject to a follow-up study. Whereas the supercell lacks a suitable parameter set to track such modifications, because its design must always be visualized and cannot be read off a current map, the checkerboard's optimal parameters can be listed in a look-up table or even intuitively found experimentally.

7

PHOTON SHIFTING AND TRAPPING IN PEROVSKITE SOLAR CELLS FOR IMPROVED EFFICIENCY AND STABILITY

7.1 Introduction

One area of particular interest for PSCs is consumer-oriented portable devices [42], [196]. The important requirements of such technologies, such as extremely low absorber thickness — for flexible and lightweight devices — are mitigated by the outstanding optoelectronic properties of perovskite absorbers, especially when compared with conventional materials such as c-Si and a-Si [7], [19], [190]. Nevertheless, the small absorber thicknesses required by these applications do negatively impact the optical performance of PSCs. Therefore, advanced light-management techniques can play a pivotal role in ultra-thin (potentially bendable) PSCs [44], [84], [94], by allowing the usage of physically thin but optically thick absorbers that have the flexibility benefits without the optical losses [11]. Furthermore, reducing the absorber thickness is also important to reduce the usage of hazardous/toxic elements, such as Pb, present in common perovskite compositions [20].

In PSCs, efforts have been devoted to improving light harvesting using advanced LT schemes at the expense of their complexity and implementation cost, for instance via micro-structured morphologies [51], such as a coarse surface [268] and periodic nanostructures, nanocone arrays, random pyramids, structured transport layers, corrugated substrates [61] and by periodic structuring of the perovskite layers [20]. Most of these features require sophisticated (expensive) fabrication processes, and can inevitably introduce defects in perovskite films (or in other cell layers) resulting in the electrical deterioration of the PV performance, and thereby hindering the achievable optical gains in real devices.

As presented in the previous chapter, smartly-designed 1D crossed-grating structures composed of checkerboard and/or penta-like arrangements were shown to provide photocurrent enhancements similar to the most sophisticated photonic strategies, such as quasi-random supercell structures, in thin-film silicon cells, but using much simpler and industrial-friendly geometries [190]. In addition, since the structures are top-coated as a final processing step, they do not lead to the structuring of the cells' absorber and, therefore, this creates a conducive path for optical enhancement in PSCs without electrical degradation.

PSCs also suffer from reduced stability due to different factors such as moisture, UV radiation, and elevated temperatures, as well as intrinsic instability due to the environmental-unfriendly composition of perovskites compounds [15], [269], [270]. Particularly, titanium dioxide (TiO_2), which is widely used as an electron transport layer (ETL) in high-performing PSCs, has been shown to trigger interfacial photocatalytic reaction to the perovskite films under UV radiation, which severely degrades the span of the device stability [25], [271]. In addition, combined oxygen vacancies with titanium interstitials can form non-stoichiometry defects in this ETL, which create deep sub-bandgap trap states that also reduce the PSCs performance [271].

One straightforward way to circumvent this photostability problem is by avoiding UV radiation from reaching the interface of TiO_2/perovskite layers, using a UV-shielding encapsulant layer in PSCs [25], [269]. However, a better solution can be realized with luminescent down-shifting (LDS) materials employed to convert these unwanted UV photons into lower energy photons that can be absorbed by the perovskite layer, but without affecting the device stability, as well as simultaneously functioning as front sealants [25], [60], [150], [152].

LDS coatings are mainly applied on the PV cell top surface in order to interact with the incident radiation and spectrally adjust it for improved power convertion at the solar cell [272], as illustrated in Figure 31. In this process, high-energy photons absorbed by the luminophores are converted to an equal number of low-energy photons, thereby potentially enhancing photocurrent since the active materials of the solar cells present a lower response in the UV spectral region (300–400 nm) than in the visible one [61], [272]. Thus, adding a LDS layer able to absorb the incident UV photons and convert them to visible ones is beneficial, by increasing the number of available visible photons for absorption by the cell (where the external quantum efficiency, EQE, of the PV device is higher, as is the case of PSCs [25]).

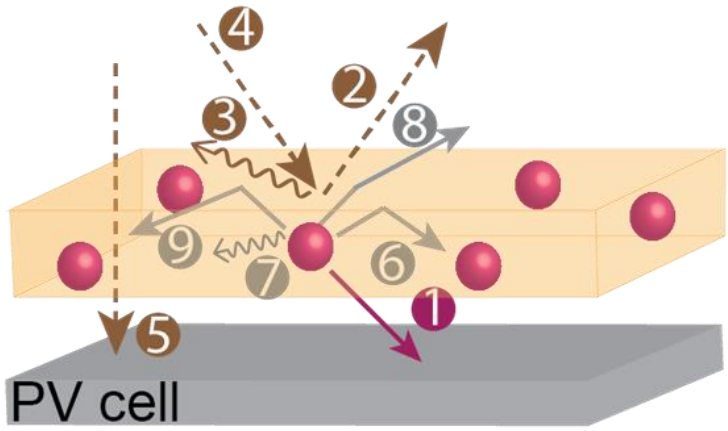

Figure 31: Operating principles and primary processes and losses occurring in downshifting layers: 1) emission from the optical center (luminophore), 2) Fresnel reflection, 3) surface scattering, 4) waveguide attenuation, 5) transmitted radiation, 6) re-absorption by neighbor centers, 7) non-radiative relaxation, 8) emission within escape cone, and 9) radiation lost through the sides. Image adapted from [272].

Table 9: Overview of improvement in PV performance using luminescent down-shifting (LDS) coatings reported in the literature.

LDS composition	PV absorber	Results	Ref. (year)
CaF_2 single crystals/Eu^{2+}	a-Si	PCE increase from 10% to 15%	[273] (1997)
PVA/$Eu(phen)_2](NO_3)_3$	c-Si	0.8–1% increase of total power (AM0)	[274] (2006)
PVA/$Eu(dbm)_3$phen/$Eu(tfc)_3$	c-Si	0.5% increase of total power	[275] (2009)
PMMA/ Lumogen 570 or Lumogen 083 or Lumogen 300.	c-Si	EQE ≈40 % enhancement (<400 nm)	[149] (2009)
$KMgF_3$:Sm	CdS/CdTe	PCE increased 5% relative to pure $KMgF_3$	[276] (2009)
CdS QD-embedded silica film	c-Si	J_{sc} increase by 4.0%	[277] (2010)
Lu_2O_3:(Tm^{3+}, Yb^{3+})	DSSC	PCE increase by 11.1%	[278] (2011)
EVA/Lumogen-F Violet 570	c-Si	EQE increase of 10% (300–400 nm); 0.18% higher module efficiency	[279] (2011)
PMMA/ Violet 570/ Yellow 083	CdTe	PCE Increase of 10%	[280] (2012)
PMMA/Eu(DPEPO)(hfac)3 (EuDH)	InGaP	Current density increase of ≈ 3.5%.	[281] (2013)
PMMA/CdSe/CdS/ZnS QDs	CdTe	EQE increase of 16% (at 300-430 nm)	[282] (2013)
PMMA/Eu(DPEPO)(hfac)3 (EuDH)	InGaP	Current density increase of ≈ 3.5%.	[281] (2013)
YVO_4: Bi^{3+}, Eu^{3+}	c-Si	EQE increase of ≈28% (UV); PCE increase from 16.6% to 17.3%; 4% reflectance decrease (UV)	[283] (2013)
PVA/$Eu(TTA)_3{\cdot}2H_2O$ with a bispinene-containing bipyridyl ligand	c-Si	PCE increase from 16.05% to 16.37%	[284] (2013)
Ba_2SiO_4:Eu^{2+}/SiO_2/Ag NPs	c-Si	J_{sc} from 41.18 to 42.04 mA/cm² (4% gain); PCE increase by 0.7%;	[285] (2013)
ZnO	c-Si	2.9% EQE enhancement (525-875 nm); 8.5% EQE enhancement (875-1100 nm), due to antireflective effect	[286] (2014)
Green and red emitting CdSe/ZnS and CdSe QDs	p-type Si	PCE enhancement for green emitting QDs by 0.93% and for red-light emitting QDs by 0.55%	[287] (2014)
CdTe QDs	CdTe/CdS	short-circuit current increase of 16%	[288] (2015)
YAG:Ce^{3+}	c-Si	PCE increase from 15.30% to 15.46%	[289] (2015)

Eu^{3+}-doped tri-ureasil (tU5Eu)	c-Si	Power and maximum EQE increase of 14% and 27%, respectively	[290] (2019)
Eu-PMMA	c-Si	PCE enhancements of ~5% (single-use of LDS layer) up to ~13% comparing with bare PV cell	[92] (2020)
Eu^{3+}-doped di-ureasil (dU6Eu)	Organic PV based on PTB7-Th:ITIC bulk hetero-junction	PCE enhancement of ~22% (from 3.1 to 3.8%)	[291] (2021)

Among distinct luminescent materials[292], such as organic dyes [279], [293], quantum dots (QDs) [293] and lanthanide metal ions/complexes [90], [92], as shown in Table 9, lanthanide-based beta-diketonate complexes stand out. The well-known Ln^{3+} luminescence sensitization, or antenna effect, may be seen as efficient light-conversion molecular devices. The ligand-induced large Stokes' shift and the ligand-to-Ln^{3+} energy transfer processes ensure efficient UV-downshifted emission towards the visible spectral range [294]. For instance, lanthanide (Ln^{3+}) based (such as, Ln = Eu and Tb) materials have shown significant potential acting as UV absorbers (absorbing maximum UV radiation at wavelengths around 300-400 nm) and efficiently shifting these photons into useful lower-energy visible photons [272], [291], [295]–[297]. This way, the otherwise lost UV light can be utilized for photo-current generation. LDS layers made of doped organic–inorganic hybrid materials with Eu^{3+} and Tb^{3+} displayed an absolute increase of the external quantum efficiency of ~27% in c-Si-based PV cells [90]. Recently, these materials have been also applied in PSC technology to improve PV response while protecting the cells from UV-induced degradation [298]–[300]. In particular, Rahman et al. [300] demonstrated ~14% enhancement of PCE in PSCs in combination with improved device stability by using LDS layers composed of Eu^{3+}.

This work explored a combination of two breakthrough optical strategies in PSCs using coupled optical and electrical modelling, grounded on experimental results.

First, the simple, yet powerful, checkerboard (CB) grating arrangement, with broken-symmetry in quasi-random fashion, was for the first time optimized for integration as LT structure in PSCs, which demonstrated pronounced broadband absorption and remarkable photocurrent gains over a large angular range (0–70°) with ultra-thin (250 nm, for superior flexibility) perovskites. Apart from higher short-circuit current, the LT-enhanced ultra-thin PSCs also revealed improved open-circuit voltage and fill factor, and thereby an unprecedented PCE enhancement (28%) was achieved. In addition, as the CB pattern is applied on the front (top) contact of the PSCs, this LT strategy is realized without causing morphological defects in the PSC layers [19]. Furthermore, the simple CB design can be fabricated in a highly-scalable fashion, for instance using a nano-imprinting technique [67], [193], [301] which is a high-resolution

low-cost micro-patterning method compatible with high throughput and with integration in PSCs technology.

Secondly, we studied the coupling of the optimized CB photonic front structure with an LDS encapsulant material composed of a tri-ureasil modified by lanthanides (t-U (5000)/Eu^{3+}). The ureasil is formed by a siliceous-based skeleton covalently grafted to the polymeric chain by urea bridges, as shown in Figure 32. The siliceous backbone provides compatibility with current microelectronics and confers enhanced thermal stability (onset of the decomposition temperature at ~339 °C) [302]. The tri-ureasils are processed using environment-friendly green solvents with tuneable viscosity, which makes them ideal low-cost inks to be easily printed in virtually any substrate (paper, plastic, and textile) similar to what occurred in printable electronic circuits [302]. In addition, the low refractive index $n \sim 1.5$ in UV/visible is preferable for reducing surface reflection [25], [94], [303]. The ureasils are intrinsically photoluminescent and can function as active hosts to tune the emission from luminescent dopants such as conjugated polymers, organic dyes and lanthanide complexe through energy transfer, leading to reduced re-absorption losses and harvesting a broader wavelength range of the solar spectrum [89], [90], [272], [291], [303]. Their facile sol–gel synthesis facilitates the controlled placement of luminophores within the ureasil matrix (host) via covalent grafting to the siliceous backbone, which can be used to both inhibit aggregation and/or promote specific packing (PFO-OH chains within the ureasil matrix) [303]. As mentioned, Eu^{3+} ions are widely used due to their potential for red emission, caused by their predominant $^5D_0 \rightarrow {}^7F_2$ transition emission [90], [291], but also excellent thermal and chemical stability as well as a desirable absorption in the UV region by Eu^{3+} [90]. Recently, Eu ions in a fiber waveguiding luminescent solar concentrator have shown the potential to convert 16% of the sunlight intensity available for down-shifting conversion, as a consequence of the wide overlap between the AM1.5 emission spectrum and their excitation spectra [78].

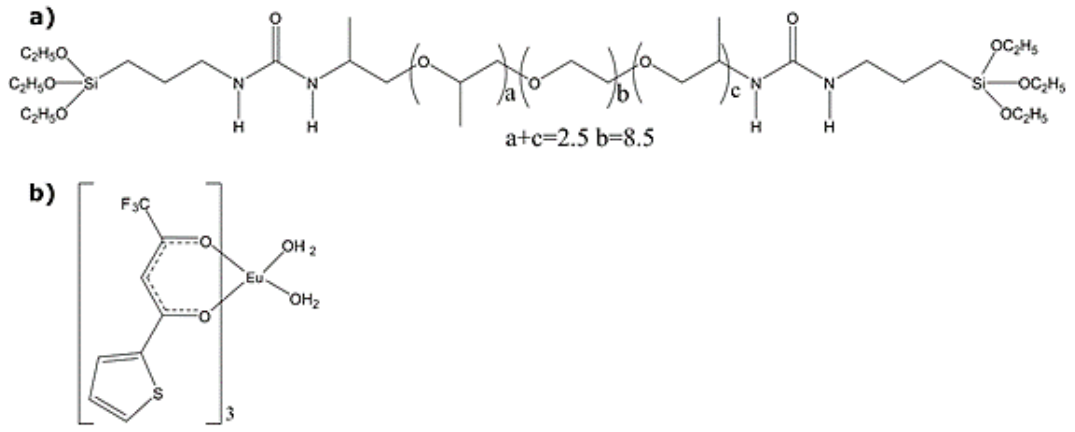

Figure 32: Molecular structures of the non-hydrolyzed organic–inorganic hybrid precursor, d-UPTES; and of the (b) $Eu(tta)_3 \cdot 2H_2O$ complex (tta=thenoyltrifluoroacetone).

The relevant optical features experimentally-obtained from such LDS coating materials are the refractive index, absorption and emission profiles, as detailed below. It was found that the luminescent layer blocks almost ~94% of the entire UV radiation in the spectral region of 300-400 nm. Subsequently, it was observed from our coupled optical and electrical modelling that the optical gains from the t-U (5000)/Eu^{3+} LDS can translate into the electrical domain in PSCs.

7.2 Methodology

The authors developed coupled optical and electrical simulations to model the response of PSCs and optimize the CB pattern for LT, as shown in Figure 33. Moreover, an LDS material composed of t-U (5000)/Eu^{3+} has been experimentally synthesized and its optical response was measured, inputting these results to the optoelectronic model to explore the addition of the LDS effect in the LT-enhanced PSCs.

The optoelectronic simulations were performed by a two-step process. Firstly, the optical (electromagnetic) modeling was carried out via a 3D FDTD formalism using Lumerical FDTD [200] to solve Maxwell's equations in arbitrary geometries, to explore all the relevant optical responses of both planar and photonic-enhanced PSCs. FDTD was chosen due to its capability to straightforwardly simulate complex 3D object configurations, being a method widely used in the literature [94]. The complex refractive indices ($N=n+ik$) of the materials were chosen from the experimentally verified literature [19], [94], [176] and shown in Appendix A1. Here we take a standard PSC layer structure (see Figure 33), composed of a common $MaPbI_3$ perovskite material by considering the refractive index of Eerden et al. [176], whose spectral response is significant in the 300–800 nm wavelength range, so this was the spectral window considered for the optical modeling. However, the measured dataset (n, k) of PSCs varied with

different fabrication conditions and process materials used. Given that, we calculated PSCs response in the 300–1000 nm wavelength range in previous Chapters, considering the measured refractive index provided by Phillip et al. [14].

Population-based stochastic optimization methods, such as the PSO algorithm, are ideal for rapidly screening a highly complex multi-variable system to determine a maximum/minimum state [18]. Here, such *smart-search* method was incorporated in the optical solver to determine the optimal parameter configuration — geometrical CB parameters, described in Figure 33 and Table 10 — that maximizes the overall device optical current, i.e. the useful absorption occurring in the perovskite material. Further details regarding the optical modeling and the PSO method are provided in Chapter 2 and in previous contributions [7], [19], [94].

In the second step, the electrical simulation was carried out using a FEM employing Lumerical-CHARGE solver [202]. For that, the optical output (photo-generation profile) of both planar and photonic-enhanced PSCs from FDTD was used as input to compute their PV response, i.e. the current density–voltage (J-V) characteristic curve of the solar cells for distinct perovskite thicknesses studied here. To perform a realistic prediction, a set of electronic transport properties about the bulk and surfaces of the materials were considered in the electrical simulations, which were taken from the state-of-the-art literature (see Chapter 6) and summarized in Appendix 2.

A detailed description of the electrical simulation methodology is given in Chapter 6.

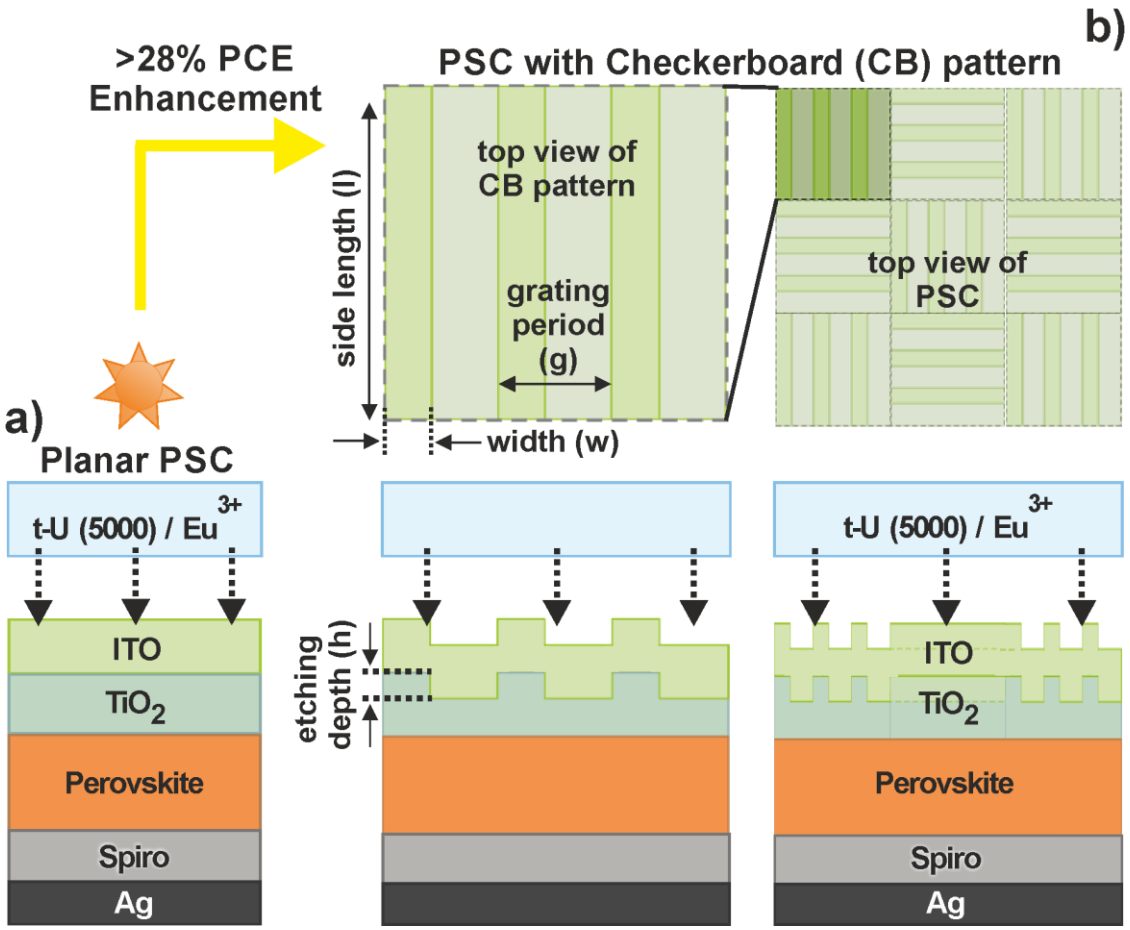

Figure 33: Sketch of the layer architecture of planar (a) and photonic-enhanced (b) PSCs with an LDS encapsulant coating composed of t-U (5000)/Eu^{3+}. An innovative LT design is applied on the front contact of the PSCs (b), consisting of a symmetry-broken Escher-like checkerboard (CB) arrangement patterned in the TiO_2 electron transport layer (ETL). The geometrical parameters (*h, w, g, l*) for the CB patterns (b) considered for optimization are indicated by the arrows. Two distinct thicknesses (250 and 500 nm) were considered for the perovskite absorbers, which are compared with the corresponding planar reference cells (a, no LT), with and without the LDS layer. The thicknesses of the remaining layers in the PSCs are indicated in Table 10.

As mentioned earlier, the LDS layer can perform a dual function in PV, improving UV photostability by blocking UV radiation while enhancing PV response by shifting these photons to the visible spectral region. Several materials have been studied for the LDS application, such as organic dyes [279], [293], quantum dots (QDs) [293], and lanthanide ions (Ln^{3+}) [90], [92]. The Ln^{3+} complexes (Ln^{3+}= Eu^{3+}, Tb^{3+}) have demonstrated to be better candidates, since they exhibit preferable absorption (absorbing maximum in UV radiation around 300-400 nm) and emission in the red and green spectral region, respectively [90]. Furthermore, the LDS layers composed of such Eu^{3+} and Tb^{3+} materials manifested larger ligands-induced Stokes shifts in comparison to other LDS materials, such as organic dyes or QDs, thereby posing smaller losses from self-absorption [90].

Therefore, to investigate the effects of an LDS encapsulant, a state-of-the-art LDS material (t-U (5000)/Eu^{3+} LDS) was considered, whose optical properties were experimentally obtained. Subsequently, to incorporate the LDS effect into the optoelectronic simulations a conversion procedure was applied to translate the experimentally measured data (absorption and emission profiles), as illustrated further below in Figure 37. Namely, the absolute absorption given by $1\text{-}10^{-A}$ (A is the absorbance) of the developed t-U (5000)/Eu^{3+} LDS material was multiplied by the solar photon flux (i.e. ASTM G-173 global irradiance spectra)[25], yielding the absorption flux of the LDS layer. Subsequently, this absorbed flux is subtracted from the original incident spectrum to account for the blocked absorption by the t-U (5000)/Eu^{3+} film. Lastly, the emission flux was added to this modified AM1.5G spectrum to output the "LDS-converted" spectrum incident on the PSC.
Afterwards, the CB pattern of the photonic-enhanced PSCs was again re-optimized in the optical solver using this spectrally-adjusted incident light, recalculating as well the response of the reference planar cells, followed by the electrical simulations of their PV response with the LDS effects.

7.3 Results and Discussion

The novel photonic CB design, presented for the first time by the authors [190] as described in Chapter 6, amazed the optics-for-PV community as it demonstrated unprecedented LT levels (>100% photocurrent gains) in ultra-thin (1 um) c-Si solar cells, which are quite close to the ideal Lambertian limits and, advantageously, realizable with quite simple cross-grating structures as depicted in Figure 33.

The application of these CB structures in PSC technology further benefits from the fact that they can be built atop the absorber material keeping it intact. This prevents the increase of surface roughness in the absorber and, thus, recombination — a common problem of many LT schemes. Another advantageous factor concerning the implementation of top-coated LT structures in PSCs is the propinquity of the real parts of the refractive indices (n~2.5) of the perovskite and the photonic-structured ETL contact (i.e. TiO_2/ITO as considered here, and in previous designs [19]), especially when compared with higher-n absorbers such as Si (n~3.5), which favors index matching and, therefore, lower reflection losses. In this work, we consider two different background index values (n=1 and n=1.5) of practical relevance. The case of n=1 corresponds to a substrate-type PSC configuration where the light is incident on the cell-side (transparent conductive oxide, TCO) without an encapsulant layer on the front [94]. Contrastingly, n=1.5 emulates the presence of a thick (hundreds of μm) encapsulant film (in this case embedded with LDS compounds) applied on the front TCO, since the n value of common encapsulant materials ([e.g.; doped Eu^{3+}] [304]) is ~1.5 [25]. The detailed results of coupled optical and electrical simulations of planar and photonic-enhanced PSCs with and without LDS are described in the following section 7.3.1 and 7.3.2, respectively.

7.3.1 Photonic-enhanced PSCs with checkerboard pattern

Considering the application of photonic-enhanced PSCs for flexible devices in portable electronics, we begin with optimizing the set of geometrical parameters of quasi-random CB patterns on the front contacts of PSCs, as depicted in Figure 33. The thicknesses of PSCs layers for TCO, ETL, HTL and metal contact (t_{ITO}, t_{TiO2}, t_{Spiro} and t_{Ag}) were restricted to a range that can easily be fabricated using low-cost process as shown in Table 10, thus flexible applications can benefit from being lower cost. The results of photonic-enhanced PSCs with optimized CB patterns are presented in Figure 34 and compared to those planar counterparts with double-layer ARC, for both ultrathin perovskite (250 nm) and conventional perovskite (500 nm) absorbers.

Figure 34 a1,2a2 show the absorption profiles for the reference planar cells as well as LT-enhanced cells (250 and 500 nm). Here, three main areas of interest can be emphasized. Firstly, for the UV range — 300–400 nm — both cells exhibit a strong absorption drop, mostly from reflection losses and parasitic absorption of the front contact. Secondly, for the visible range — 400–700 nm — the device shows its peak performance, where, even for the smaller thickness, it can consistently reach ~80 % absorption. Nevertheless, some limitations of the 250 nm cell can also be seen at ~650 nm, where there is a significant absorption drop, this reinforces the need for advanced light management techniques that mitigate these losses. Lastly, in the NIR region — 700–800 nm — the absorption drops, much like for the UV range, however, here the reason is the bandgap of the device. Upon optimization, a clear structure-aided absorption increase was obtained, as depicted in the cumulative photocurrent density profiles in Figure 34c.

The innovative design of optimized CB pattern on the front contacts in PSCs can enhance broadband light absorption by providing an improved ARC effect and strong light scattering. Here, there are several notable differences, in the optimized parameters, between the 250 and 500 nm cells. In the former, the structures tend to have smaller/thicker geometries (smaller h and bigger w, in Table 10), while the latter tends to have taller/thinner geometries (higher h and smaller w, in Table 10). This could indicate a preference for light in-coupling (taller structures) instead of AR for the thicker perovskite— the effective medium of the structures gets closer to the device refractive index as w increases and closer to vacuum otherwise — while the thinner cell prefers the AR effect in detriment of light in-coupling. This is reinforced by the power absorption density profiles in Figure 34b and the Fast Fourier Transform (FFT) profiles in Figure 34d1 and d2. The former shows visually, especially for longer wavelengths, that the possible horizontal maneuvering of light is much more limited in the thinner device, while the latter reinforces this by indicating that, in the 250 nm cell, these structures do not scatter light significantly. The FFT of the structures indicates the different scattering modes to which light can be dispersed, such that taller off-center peaks imply a stronger horizontal dispersion of light. In the case of Figure 34 d1 and d2, it is evident that the thinner perovskite shows a much

smaller sideways light scattering (less light in-coupling), when compared to the 500 nm cell. Concurrently, the cumulative photocurrent values from Figure 34c) show a bigger decrease in overall reflection for the 250 nm cell (from ~5 to ~2 mA/cm²) in comparison to the 500 nm cell (from ~3.7 to ~1.6 mA/cm²), stating thus that the structures are giving preferential treatment to AR in the smaller cell.

Table 10: Maximum J_{PH} values obtained for the optimized CB arrangement placed on the two distinct PSCs, for 250 or 500 nm perovskite layer thickness, with and without a LDS layer, considered in this work. The geometrical optimization parameters (*h, w, g, l*) are defined in Figure 33 and the standard thicknesses of the cells' layers (t_{layer}) were fixed in the simulation. The results are compared with the reference ARC-patterned cases, for both with and without a LDS layer.

Perovskite Solar Cells		Absorber layer: **250 nm perovskite**		Absorber layer: **500 nm perovskite**	
		Optimized parameters	**JPH**, mA/cm² (enhancement)	Optimized parameters	**JPH**, mA/cm² (enhancement)
No encapsulant (*n* = 1)	Planar ARC (ref.)	t_{ITO} = 350 nm t_{TiO2} = 400 nm t_{Spiro} = 150 nm t_{Ag} = 100 nm	**18.0**	t_{ITO} = 350 nm t_{TiO2} = 400 nm t_{Spiro} = 150 nm t_{Ag} = 100 nm	**19.9**
	CB pattern (with LT)	*h* = 283.1 nm *w* = 84.6 nm *g* = 577.2 nm *l* = 648.3 nm t_{ITO} = 350 nm t_{TiO2} = 400 nm t_{Spiro} = 150 nm t_{Ag} = 100 nm	**22.7** (25.9%)	*h* = 251.6 nm *w* = 153.7 nm *g* = 532.0 nm *l* = 653.9 nm t_{ITO} = 350 nm t_{TiO2} = 400 nm t_{Spiro} = 150 nm t_{Ag} = 100 nm	**23.6** (18.9%)
With LDS encapsulant (*n* = 1.5)	Planar ARC (ref.)	t_{ITO} = 350 nm t_{TiO2} = 400 nm t_{Spiro} = 150 nm t_{Ag} = 100 nm	**19.2**	t_{ITO} = 350 nm t_{TiO2} = 400 nm t_{Spiro} = 150 nm t_{Ag} = 100 nm	**21.3**
	CB pattern (with LT)	*h* = 270.5 nm *w* = 70.4 nm *g* = 435.6 nm *l* = 498.9 nm t_{ITO} = 350 nm t_{TiO2} = 400 nm t_{Spiro} = 150 nm t_{Ag} = 100 nm	**22.3** (16.1%)	*h* = 277.6 nm *w* = 42.6 nm *g* = 432.1 nm *l* = 426.1 nm t_{ITO} = 350 nm t_{TiO2} = 400 nm t_{Spiro} = 150 nm t_{Ag} = 100 nm	**24.0** (12.7%)

The pitch and finger size (*g* and *l* in Table 10, respectively) do not show a noticeable difference between devices. This could be due to their more preponderant effect being limited to

defining the wavelength range of action, i.e. the structure size and pitch is related to the range of wavelengths where the structures will be active. In this case, since both wavelength ranges and both starting absorptions (reference) are quite similar, the structures do not need to zone in a particular area to improve absorption and, instead, just have a global effect.

The light in-coupling effect, seen for the thicker perovskite, is most noticeable for longer wavelengths (600–700 nm) and is the chief responsible for the absorption gains seen in Figure 34 a2 (dashed and blue lines for planar and optimized configurations, respectively). The nature of the broken-symmetry of the quasi-random pattern and the optimized CB arrangement of the front contacts (ITO+TiO_2) causes a strong far-field scattering, which increases the optical path length, thereby boosting the absorption in perovskite material in the longer wavelengths. Figure 34 2d2 reiterates this scattering effect by showing several high-intensity off-center peaks.

Another fundamental component of ultrathin devices is the overall parasitic absorption from the other cell materials, as any loss mechanism should be mitigated to achieve an ideal device behavior. This unwanted absorption can be categorized into two different sections. Firstly, UV parasitic absorption (300–400 nm), which is most relevant in the top part of the cell, is thus mostly influenced by ITO and TiO_2, as seen in Figure 34a1. Secondly, NIR-IR parasitic absorption (>650 nm) from the HTL layer (Spiro-OmeTAD) and ITO, as seen in Figure 34a2. Interestingly, the structures act to reduce these unwanted absorptions, which reinforces the light trapping effect. This happens, since, by trapping light inside the absorber material, the structures mitigate lossy internal reflections that would lead to further absorption by the top layers. This can be seen in the cumulative photocurrent absorption plot (Figure 34c), where the topside parasitic absorptions (ITO and TiO_2) are reduced by adding the structures in both cases — lossy internal reflection mitigation — while the Spiro-OMeTAD parasitic absorption increases slightly, from the improved light travel path.

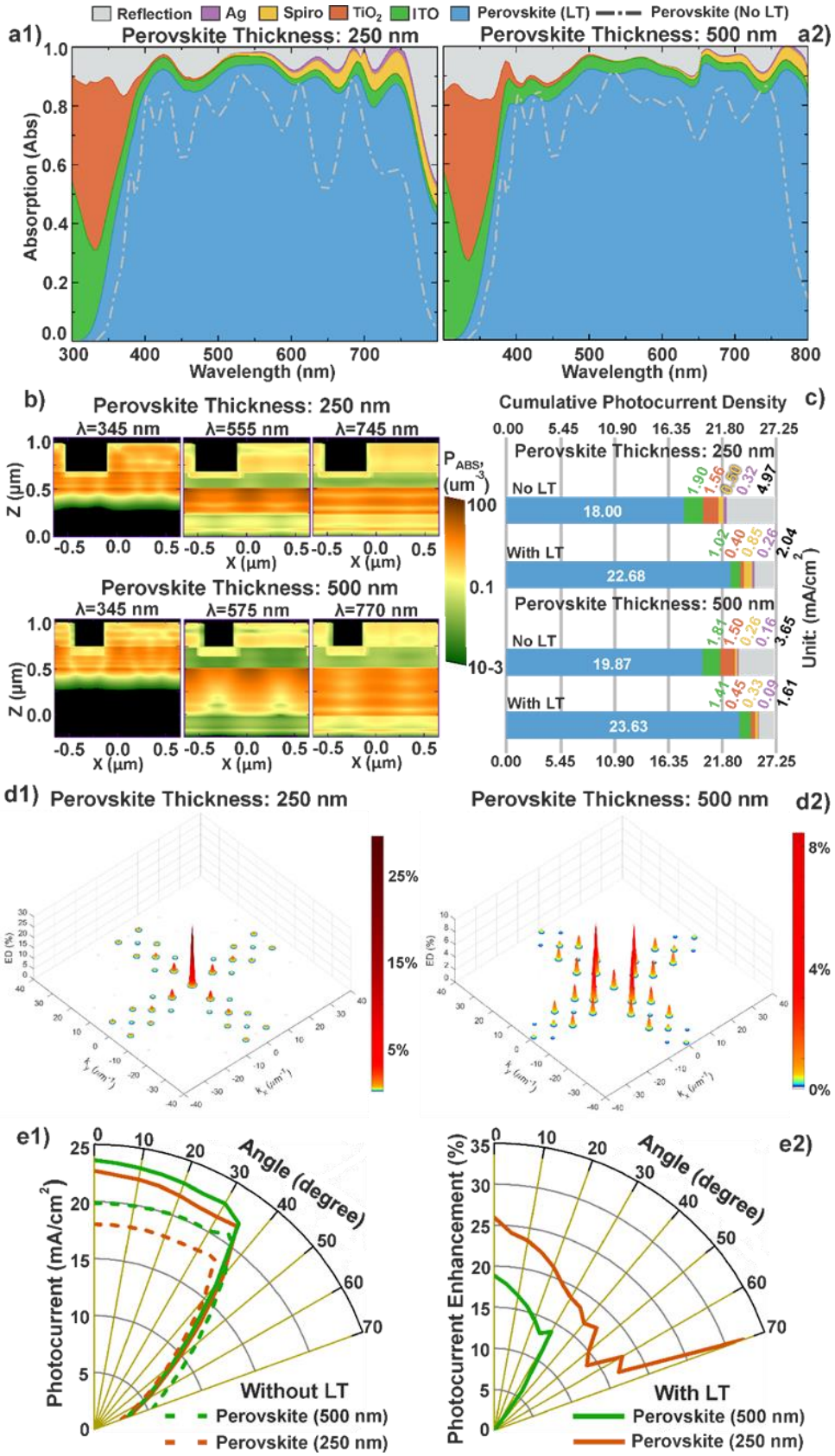

Figure 34: a1, a2) Absorption spectra attained with the optimized CB pattern in PSCs, without LDSs layer, and with the reference cases of a cell with double-layer anti-reflection coating, for perovskite absorber layers with distinct thickness: a1) 250 nm and a2) 500 nm. Colors bar shows the absorption in

different materials as well as reflection in PSCs with optimized CB pattern and the grey lines depict the absorption that occurred only in perovskite for the reference cases of planar cells without LT. b) Log-scale distributions of the absorption density, p_{ABS}, along the xz plane of the CB arrangement passing by the center of y plane, at the wavelengths of the interested absorption peaks on the 250 nm and 500 nm perovskites. The cumulative photocurrent density was calculated from the absorption profiles for the cells with and without LT present in c). d) illustrates the fast Fourier transform (FFT) analysis of CB patterns in PSC for perovskite thickness 250 nm (d1) and 500 nm (d2). e1) represents the angle-resolved unpolarized photocurrent density, J_{PH} determined for both planar and LT cells with 250 and 500 nm perovskite thickness and e2) shows the photocurrent improvement achieved with LT in respect to planar reference for oblique angles.

Figure 34 f1,f2 show photocurrent (total and relative, respectively) for both planar and photonic-enhanced PSCs for angles up to 70°, as determined from the J_{PH} values of Table 10. The most notable factor here is the stable angular response, even when the structures are added to the device, shown by the near constant photocurrent behavior up to 40°. Beyond that there is a significant drop in photocurrent. Furthermore, it is quite interesting how the ultrathin 250 nm cell outperforms the conventional 500 nm even for different incidence angles, which can offer a potential 3-fold improvement in the device flexibility as well as a 2-fold reduction in the costs and toxic lead consumption due to the reduced perovskite (absorber) material usage. Furthermore, it is found that the attained maximal photocurrent changes only 1–3% with a large (± 10%) variations of the optimized parameters of CB patterns. This high tolerance around optimal parameters provide high feasibility for fabrication imperfections, which is a key benefit from an industrial standpoint.

Figure 35 a,b summarizes the electrical results obtained from the previously optimized structures. Figure 35a shows the overall band structure, fundamental for these types of simulations, as it will define the drift electric field — one of the two major components of transport, along with diffusion. It is important to note that the electric field remains mostly unchanged when adding the structures, since it only depends on the materials properties (like, affinity and bandgap). The band structure can also be used to infer some of the final J-V curve behavior, for instance, in the perovskite layer, the long constant Ec/Ev region (~300–600 nm) reveals a weak electric field (constant potential) that could negatively impact charge transport, since the drift component is weaker. Ultimately, this effect is mostly bypassed by the excellent carrier lifetimes in perovskite [305], thus simply leading to a minor decrease in fill factor for the 500 nm cell when compared to the 250 nm cell (87.8 and 88.7, respectively). The most notable detail of Figure 35c,d is the significant Jsc increase in the LT-enhanced devices, which is the chief responsible for the PCE increase (28% for the 250 nm cell and 22% for the 500 nm cell). Interestingly, the PCE increases are very similar, percentage-wise, to the optical gains (26% and 19% for the 250 and 500 nm cells, respectively). The final short circuit current values are still smaller than their optical counterparts as result recombination losses. Lastly, the optimized CB structuring seems to have a more significant impact on the 250 nm cell (noted by

the bigger PCE increase) when compared to the 500 nm cell. This could be a direct result of the photonic-aided optical loss mitigation.

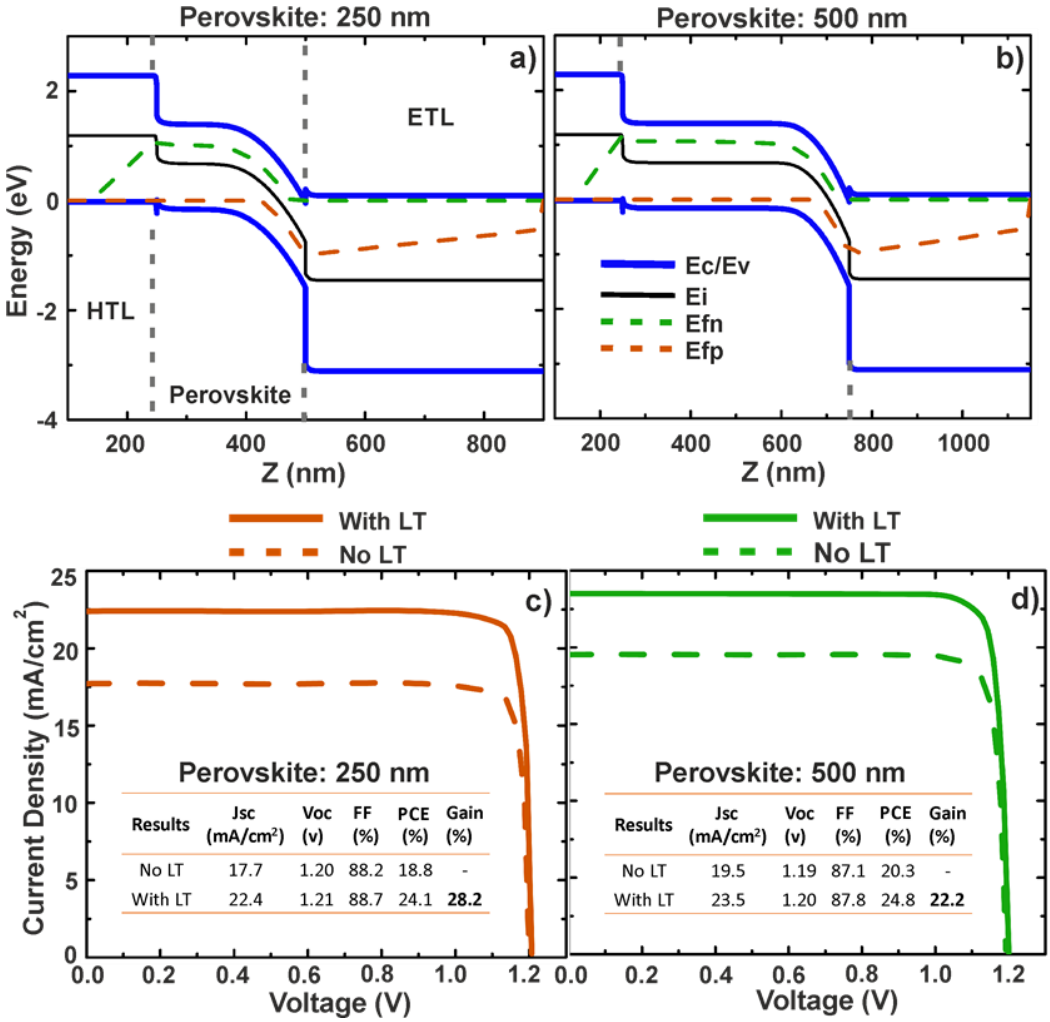

Figure 35: a, b) show the band diagram for PSC with 250 and 500 nm perovskite thickness and c, d) display the comparison of electrical simulations results of photonic-enhanced and planar PSC. The inset tables show PV performance of electrical simulations of PSCs.

7.3.2 Luminescent down-shifting properties in PSCs

The detailed mechanisms behind TiO_2 photocatalytic effects reveal that UV radiation can create deep trap states that capture photogenerated carriers from the perovskite (in the TiO_2/perovskite interface), leading to the formation of I_2 that then leads to the degradation of the perovskite structure [25]. Furthermore, the creation of I_2 from the photolysis of PbI_2 — present in the perovskite compound — can also lead to the evaporation of volatile compounds. These degradation processes mainly originated from, in the first case, the created deep trap states in TiO_2 that capture photogenerated electrons in the perovskite, leading to a decrease in cell performance [139]; in the second case, the generation of I_2 from the photocatalysis in TiO_2, which then reacts with the perovskite ions and leads to the evaporation of volatile compounds,

ultimately ending up degrading the crystalline structure of the perovskite [137]; and for the third case, there is the photolysis of residual PbI_2 that exists in the perovskite, turning it into I_2, which then leads to an equal decomposition of the perovskite [140] by the process mentioned in previous case.

These UV-generated degradation mechanisms can be mitigated by either blocking UV radiation (which completely loses these photons) or by converting it to lower — less harmful — energies. One such method for the latter is by using the LDS materials that convert high energy UV radiation into lower energies. Based on data from the lietrature [25], the t-U (5000)/Eu^{3+} LDS coating was applied to PSCs. Figure 37 a1,a2,a3 shows the experimental characterization of this LDS material: refractive index (a1) measured using spectroscopic ellipsometry and absorption (a2) and emission (a3) spectra. The averaged refractive index (n=1.5) was considered based on the dispersion curve shown in Figure 37a1, as considered above.

Figure 37 a2,a3 show the experimental absorption and emission profiles for t-U (5000)/Eu^{3+}, respectivelly, being the emission spectrum composed of the typical Eu^{3+} $^5D_0 \rightarrow {}^7F_{0\text{-}4}$ transitions, as studied in previous work [90]. The spectral characteristics of the t-U (5000)/Eu^{3+} LDS coatings allow for anticipating UV filtering in combination with downshifting to spectral regions where the PSCs exhibit higher spectral response. The absence of intrinsic emission from ligands and hybrids indicates effective energy transfer to the Eu^{3+} ions, as demonstrated in the excitation spectra that reveal three main components, peaking at ~280, ~330 and ~420 nm as shown in Figure 36, mainly ascribed to the hybrid host [87] and to the tta excited states [306], [307], respectively. The 330 and 420 nm components resemble those already observed for isolated $Eu(tta)_3.2H_2O$ [308] and for organic–inorganic hybrids incorporating Eu^{3+} complexes, being ascribed to the π-π* electronic transition of the organic ligands [309]. Apart from changes in the relative intensity, the absorption spectrum reveals the same components detected in the excitation spectra [90], [291].

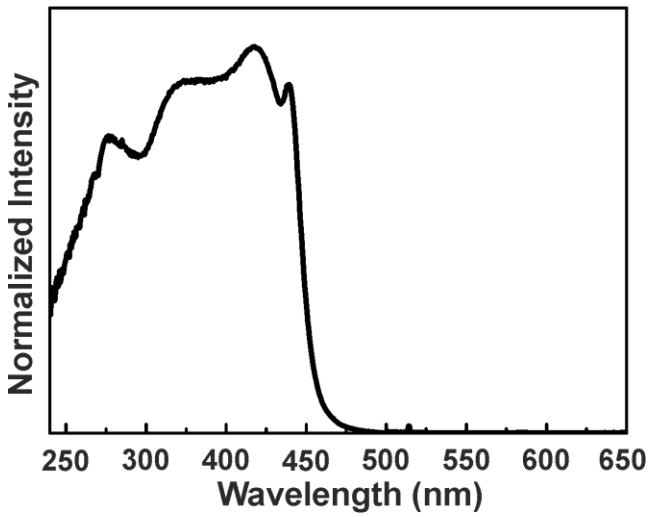

Figure 36: The excitation spectra taken for the t-U (5000)/Eu^{3+} LDS material.

Nevertheless, from the photocurrent generation perspective, it can be seen that there is a significant absorption for 300–400 nm followed by a clear emission peak for longer wavelengths (600–630 nm). The profiles also show an unwanted parasitic absorption for wavelengths above 400 nm, that could lead to negative impacts for the perovskite absorber. The performance of the LDS material can ultimately be determined by its conversion capabilities. On this note, it was determined that - considering an AM1.5G spectrum incidence - from 300-400 nm the amount of radiation that can be converted corresponds to a maximum current of 1.14 mA/cm^2, while in the 400-800 nm range the amount of parasitic absorption by the LDS coating corresponds to 0.73 mA/cm^2. In the case of the emission profile, it accounts for the photocurrent of 0.85 mA/cm^2. As such, it can be seen that there is still room for improvement in this material, namely by minimizing the absorption beyond 400 nm, and also maximizing the emission profile in the visible spectrum. Nevertheless, for the UV stability factor, this material is shown to be highly promising as it can mitigate most unwanted absorption.

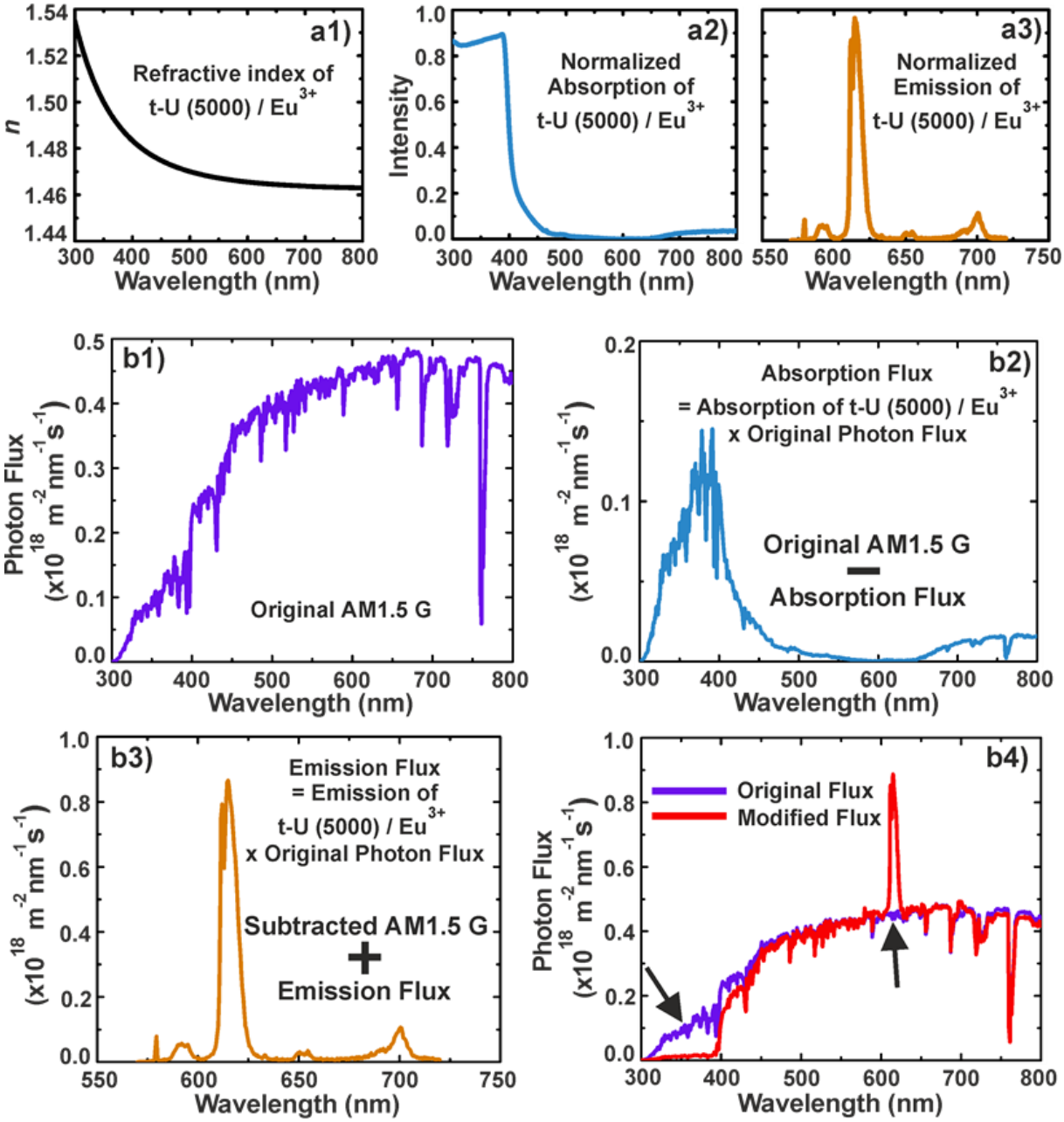

Figure 37: a1, a2, a3) shows the optical properties of experimentally developed LDS material, t-U (500)/Eu^{3+}: refractive index (a1), normalized absorption (a2) and normalized emission (a3). b1, b2, b3, b4) illustrating the method used to emulate the process of the down-shifting feature of t-U (500)/Eu^{3+} in PSC.

To incorporate the LDS effect of the t-U(5000)/Eu^{3+} material into the simulation a simple flux conservation scheme, consisting of 3 different steps, is proposed, based on previous work by Alexandre et. al. [25], also explained in section 3.2 of chapter 3, and summarized in Figure 37 b1,b2,b3,b4. Firstly, the absorption flux was obtained by multiplying the absorption of t-U(5000)/Eu^{3+} with the solar photon flux, based on the ASTM G-173 global irradiance spectra

provided by NREL. Then the absorption flux was subtracted from solar photon flux to implement the blocked UV absorption by t-U(5000)/Eu^{3+}. Lastly, the emission flux was acquired by multiplying the emission of t-U(5000)/Eu^{3+} with the solar photon flux, and subsequently was added to the subtracted solar photon flux to execute the shifted photons into higher wavelengths by t-U(5000)/Eu^{3+}.

The photocurrent values presented in Table 10 were calculated using the original and modified AM1.5 G irradiance for planar and photonic-enhanced PSCs without/with the t-U (5000)/Eu^{3+} LDS effect, respectively. For the photonic-enhanced PSCs, the CB geometry was again reoptimized using the modified AM1.5 G irradiance by employing same PSO algorithm for both perovskite thicknesses studied here (250 and 500 nm).

In a parenthesis, it should be noted that the optimal thickness for such LDS layer was found to be 90 nm, for both 250 and 500 nm perovskite absorbers. However, there is no significant variation in photocurrent observed for thicknesses of t-U (5000)/Eu^{3+} above ~200 nm. Since the typical thickness of LDS coatings in practical devices is in the range of several microns (much thicker than the cells' structure), it was found preferable to consider such coatings as a background index (n=1.5) over the PSCs, instead of a layer on top of the front contact, to account for realistic LDS effects.

Figure 38 shows the photo-generation profiles for planar and photonic-enhanced PSCs with and without LDS layer, for two distinct perovskite absorbers (250 and 500 nm). The optimized photocurrent values and geometrical parameters are summarized in Table 10. For the planar cells with t-U (5000)/Eu^{3+}, the photocurrent increased by 1.2 and 1.4 mA/cm^2 for perovskite absorbers of 250 and 500 nm, respectively. For the photonic-enhanced PSCs with t-U (5000)/Eu^{3+}, it is observed a much smaller increase in photocurrent (0.4 mA/cm^2) with the 500 nm perovskite, while no improvement was shown for the 250 nm perovskite.

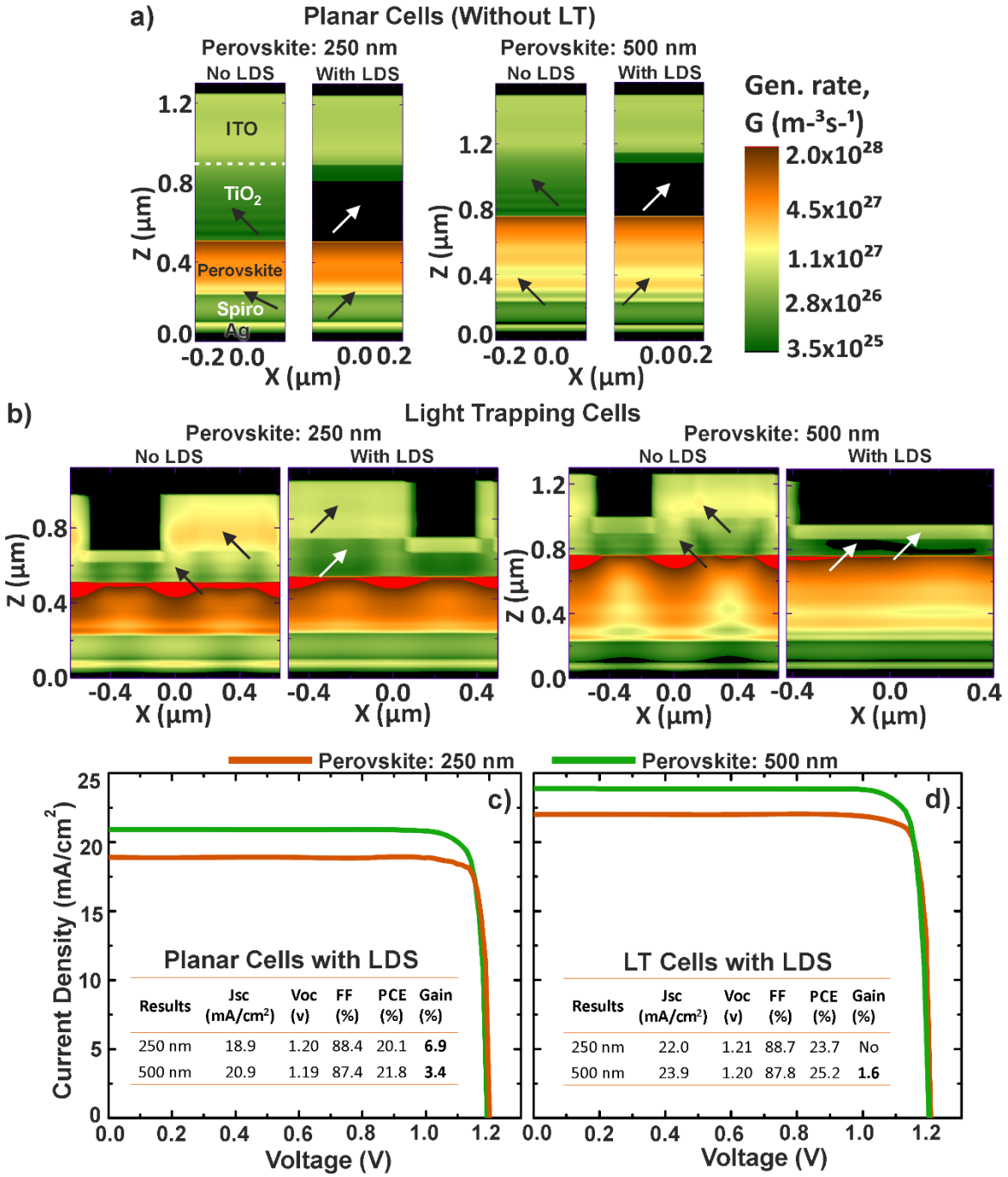

Results	Jsc (mA/cm²)	Voc (v)	FF (%)	PCE (%)	Gain (%)
250 nm	18.9	1.20	88.4	20.1	**6.9**
500 nm	20.9	1.19	87.4	21.8	**3.4**

Results	Jsc (mA/cm²)	Voc (v)	FF (%)	PCE (%)	Gain (%)
250 nm	22.0	1.21	88.7	23.7	No
500 nm	23.9	1.20	87.8	25.2	**1.6**

Figure 38: Log-scale distributions of the optical generation profiles, G, along the *xz* plane of the PSC passing by the center of *y* plane for planar references (a) and LT-cells with CB pattern (b), with and without a LDS layer of t-U (500)/Eu^{3+}, for distinct perovskite thickness (250 and 500 nm). c, d) demonstrate the electrical simulation results for planar (c) and photonic-enhanced (d) PSCs with a LDS layer, for 250 and 500 nm perovskite thickness. The inset tables show PV performance of electrical modeling of PSCs.

Nevertheless, it is demonstrated that the usage of an LDS layer can generally be advantageous for prolongued operation of the cells under illumination, since it clearly shows a reduction in UV absorption in the PSCs, particularly in the top layers (Figure 38a,b top arrows), due

to the red-shifting of such high-energy radiation. Notably, TiO_2 sees a massive photogeneration decrease, while ITO still shows some generation, which is mostly attributed to parasitic absorption from longer wavelengths (Figure 34a). The LDS effect can also be seen in the perovskite layers, particularly in planar cells, as depicted in the photo-generation profiles, owing to the converted photons in the visible wavelengths by the emission flux of t-U (5000)/Eu^{3+}. Therefore, it is ascertained that the overall PV performance can benefit from this higher bulk generation from UV photons conversion to higher wavelengths in PSCs by such LDS material.

Figure 38c,d summarizes the electrical results attained from planar and photonic-enhanced PSCs with the previously mentioned LDS layer composed of t-U (5000)/Eu^{3+}. It should be mentioned that the parameter settings used here for the electrical modelling are the same as those employed in the previous section. It is observed that the optical gains from the LDS layer in fact translate into the electrical domain in PSCs. The relative PCE gain (6.9%) was found almost the same as the optical enhancement (7.1%) for ultrathin planar PSCs (perovskite: 250 nm), whereas for 500 nm thicker perovskite, the PCE gain (3.4%) is slightly lower compared to the optical counterpart (6.7%), due to slight low Voc and FF with respect to the ultrathin perovskite, as shown in Figure 38c. As the optical gain is quite small for photonic-enhanced PSCs with LDS layer, this results in low PCE enhancements (no gain for 250 nm perovskite, whereas 2% optical/1.6% PCE improvement attained for 500 nm perovskite), as seen in Figure 38d. The optical and PCE gains due to the LDS layer of t-U (5000)/Eu^{3+} were calculated for planar and photonic-enhanced PSCs in comparison to their respective cells without the LDS layer presented in Table 10 (optical) and Figure 35c,d (PCE), and also shown in Figure 39a.

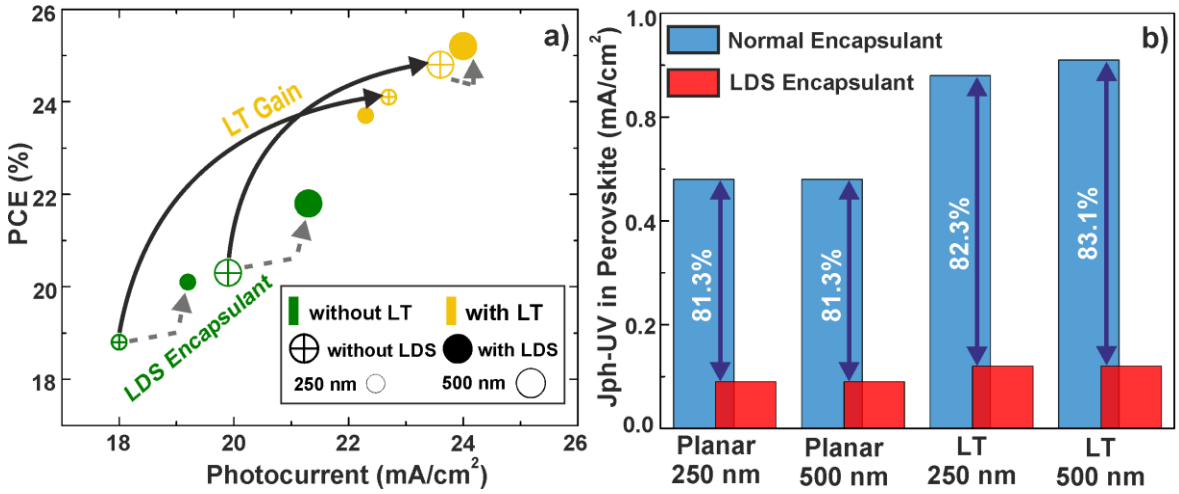

Figure 39: Summary of main results. a) Comparison of the absolute PCE and photocurrent values attained with the planar (without LT) and photonic-enhanced (with LT) PSCs, with and without the LDS layer, for 250 and 500 nm perovskite thicknesses. b) Photocurrent generated only by the UV light, in the wavelength range of 300 to 400 nm, penetrating in the different perovskite absorbers for the planar

and photonic-enhanced cells, comparing the results for a normal encapsulant layer (original AM1.5 illumination) and the LDS encapsulant (t-U (5000)/Eu^{3+}) layer (modified illumination spectrum).

From this analysis, it can be stated that planar PSCs can benefit more from the LDS encapsulant of t-U (5000)/Eu^{3+} in comparison to the LT-enhanced PSCs. Nonetheless, both planar and photonic-enhanced cells can highly benefit in terms of stability, due to the near absolute reduction of UV penetration caused by the LDS coating. It is observed that the LDS layer of t-U (5000)/Eu^{3+} can reduce 81-83% more the UV photocurrent in the perovskite absorbers in comparison to traditional encapsulant layers (without LDS), as presented in Figure 39b. Moreover, by considering total available UV photocurrent (~1.35 mA/cm^2), this LDS layer showed to be capable of blocking up to 91-94% of the harmful UV radiation from reaching the cells.

7.4 Conclusions

In this study an optimized quasi-random checkerboard (CB) pattern grating structure was applied and then coupled with the LDS on the front contacts of PSCs. It is demonstrated that ultrathin photonic-enhanced perovskite (250 nm) cells can particularly benefit from higher open circuit voltage and fill factor, thus reaching absolute PCEs as high as 24.1%, despite having a big portion of the UV radiation blocked by the front CB grating structure (which can lead to higher stability), since an unprecedented PCE improvement (>28%) is shown compared to their counterpart reference planar cell without the CB pattern.

Owing to its simple design, the CB grating pattern can be fabricated on the front contact of the PSCs by scalable micro-patterning techniques such as nanoimprint (NIL). This lithographic method does not use water in its process, unlike other soft-lithography processes (e.g. colloidal lithography), which is highly advantageous for perovskite-based PV since they are highly sensitive to moisture.

The experimentally developed LDS material (t-U(5000)/Eu^{3+}) is hereby shown to have potential in PSC technology, as a means of improving perovskite stability without sacrificing PV performance. From the analysis with this LDS material, it is shown that one can obtain a complete reduction (91-94%) in the harmful photo-generation in the TiO_2, as well as in the interface of perovskite/TiO_2 layers, coupled with an increase in the bulk photogeneration within the perovskite absorber.

The LDS materials theoretically studied here for PSC application were already experimentally verified, yielding a PCE increase in c-Si (~27% enhancement) [79] and in PTB7-Th:ITIC–based organic solar cells (~22% enhancement) [90], [291]. As such, similar gains are expected in perovskite-based PV using t-U(5000)/Eu^{3+}.

8
CONCLUSIONS AND FUTURE PERSPECTIVES

The high absorption coefficient and direct bandgap at appropriate energy of perovskite-based materials allow them to act as effective sunlight absorbers in thin film solar cells, thus having less need for absorption enhancement via LT solutions relative to Si-based thin-film PV. This explains why there have been little advances so far on photonic strategies applied to PSCs. Nevertheless, the novel optimized photonic designs presented here, based on different optical strategies, demonstrated unprecedented optical and electrical gains in PSCs.

In a first work (Chapter 2), the wave-optical TiO_2 front structures incorporated in the usual TiO_2 ETM of PSCs, were shown to improve substantially the absorption in the perovskite absorber for wavelengths above 600 nm, due to the strong anti-reflection (mainly in VIS) and light scattering (in NIR) effects. This allows remarkable photocurrent gains, which should translate into similar efficiency enhancements since the LT structures are patterned over the cells, therefore they are not expected to degrade the electric performance. These enhancements become increasingly pronounced with decreasing perovskite thickness, thereby allowing thinning the cell absorber while increasing its photocurrent. For instance, the optimized void structures, which were shown to be more optically favorable than the domes, enable a PSC with a thin (250 nm) Perovskite thickness to supply a 28.62 mA/cm^2 photocurrent density, which is 10.3% higher than that (25.95 mA/cm^2) attained with the conventional perovskite thickness (500 nm) coated with an optimized planar double-layer ARC.

In addition to their strong optical role, the developed front-located LT structures can allow important improvements in the operational stability of perovskite solar cells. On one hand, their TiO_2 material blocks almost all the UV light from entering the cell, thus protecting the device against degradation from such harmful radiation. On the other hand, the high aspect ratio of the photonic microstructures renders the top surface super-hydrophobic (i.e. water-repellent), allowing water droplets to easily roll-off, carrying away dust or other particles. This can therefore contribute to the outdoor robustness of the device, by improving the cell encapsulation against water ingress and allowing a self-cleaning functionality [104].

The second work (Chapter 3) consisted in a preliminary study of the coupling of LDS with the previously-optimized LT structures, which was important for a first analysis of the perovskite stability, as one obtained a significant reduction in the TiO_2 harmful photo-generation by one order of magnitude, coupled with an increase in the perovskite's bulk generation. The LT-enhanced cells revealed a further decrease in the TiO_2 photo-generation near the perovskite/TiO_2 interface due to the UV shading effect provided by the LT structures. By assessing the perovskite UV photocurrent for the different simulated cells, reductions up to 86% were

obtained when comparing J_{ph} values for the pristine and LDS-changed spectrum. Therefore, from these analyses, we found that the use of LDS avoids the unwanted effects of UV radiation on the perovskite, demonstrated by the hefty decrease in UV absorption coupled with the diminished TiO_2 photoactivity resulting from lower photo-generation.

In the third work (Chapter 4), we demonstrated the optical advantages of using photonic-structured substrates to fabricate electrically thin but optically thick solar cells, applied to perovskite PV. In the investigated LT design, the active cell materials are taken to be conformally deposited over the photonic substrates. This avoids the otherwise necessary costs associated with front-textured photonics applied to the device, as well as the deterioration of the cell layers during the implementation of such LT structures in post-processes. For instance, front-patterned TiO_2 LT coatings were proposed in the previous works described in chapters 2 and 3, and demonstrated high potential for efficiency and even UV stability improvement when integrated in the ETL of substrate-type PSCs[19]. This approach, however, requires an additional manufacturing step that can degrade the highly-sensitive PSC materials located underneath, thus posing challenges for its practical realization.

Furthermore, the solution presented in Chapter 4 can be an extremely cost effective approach due to the low material usage (no extra material is used in the photonic structuring), compared to those reported in the literature[19], [135], as well as being compatible with industrially-attractive processes as soft-lithography and roll-to-roll[119], since the PSCs are deposited with the established fabrication methods onto previously patterned substrates. To accommodate state-of-the-art fabrication procedures for the cells, different ETL and HTL materials were considered in the superstrate and substrate configurations[170]. Here, it is notable the resulting small thickness of the optimized ETL, HTL and TCO layers, since the optical (film-based) index-matching provides a smaller optical impact than the geometrical index-matching, thence creating a situation where smaller parasitic absorption is preferred.

We show that by carefully tuning the geometrical features on the substrates one can achieve levels of LT enhancement (up to 24.4% with 300 nm and 20.3% with 500 nm perovskite) comparable to those of the previous method[19], with the added benefit of a more omni-directional angular response (up to 70^o) which is of paramount importance for flexible devices. In addition to the superior photocurrent (thus efficiency) improvements, the LT solutions designed here reveal that the perovskite thickness can be substantially reduced while maintaining high performance, as the J_{ph} values attained with the 300 nm LT-enhanced cells are considerably higher than those of the conventional 500 nm planar references (see Table 5). Such reduction in perovskite thickness from 500 to 300 nm can bring important competitive advantages: 1) an almost 2-fold reduction in the amount of the environmentally-toxic lead (Pb) compound, as well as in the material costs associated to the perovskite material (with no additional material costs for the LT structures since they are incorporated in the substrates); 2) a potential 3-fold increase in the device flexibility due to the reduced absorber thickness.

Lastly, photonic substrates as those investigated here can also be straightforwardly adapted to different types of thin-film solar cells (e.g. Si-based, CIGS, CZTS, Organic, etc.) via a fine-tuning of the geometrical parameters using a similar methodology.

Next, in Chapter 5 we extended our modelling methodology to account for the electrical mechanisms of PSCs, and thereby simulate their full optoelectronic response. The outcomes from this study contribute to corroborating and providing a new understanding of the underlying physical effects occurring in this emerging type of photovoltaic devices. It was shown that photonic-enhanced PSCs with ultra-thin perovskite layer (300 nm) outperform state-of-the-art planar PSCs with conventionally thicker perovskite layer (500 nm) by a significant margin (25.4% PCE enhancement). It is also demonstrated that the ultra-thin photonic-enhanced PSCs can realistically reach remarkable 26.7% PCE values if we consider electronic properties similar to those of the state-of-the-art PSCs.

From an optical standpoint, the less-reflective (although inexpensive) Ni rear metal contact also showed higher photocurrent for photonic-structured PSCs compared to the planar PSCs with Au or Ag.

Nonetheless, of particular interest for any application of photonic solutions in PSCs, are the full device modelling studies developed here that help understand how light trapping can influence the electrical device performance. This study also unveils how the PV performance is practically independent of the type of field distribution (homogeneous/inhomogeneous: regular/irregular) generated by the optical strategy in the perovskite absorber, as demonstrated experimentally [68]. Furthermore, 1D and 3D electrical device modelling showed almost identical solar cell performance, which will certainly motivate the PV community to simulate solar cells with ever complex geometry in a less time-consuming and straightforward way, without significantly compromising accuracy.

In another remark, although carrier recombination effects can significantly reduce the performance of PSCs, the increase in surface recombination arising from the higher surface area of the photonic structures is more than compensated from the photocurrent gain; further supporting the case towards the adoption of high efficiency and flexible PSCs fusing LT structuring. Moreover, this also indicates that the prospective design of powerful optical strategies for PSCs should primarily focus on the optimization of the broadband absorption in the perovskite material via industrially-viable LT designs, without imposing electrical-based constraints that restrict the photonic domains.

In summary, this work constitutes an unprecedented step for the rigorous modelling of PSCs, contributing to the development of accurate simulation tools that can be of great use by the PV industry - where the prediction of the full optoelectronic response of the devices is of extreme importance. Besides, the build-up of tools to import and simulate arbitrary device geometries and generation profiles opens new pathways to investigate novel design concepts.

Chapter 6 presents an exploration of unprecedented LT designs, which deserved strong attention by the photonics and PV community. It is known fact that surface textures increase

the absorption of sunlight in photovoltaic materials, therefore, the optical strategies leading to powerful LT often neglect their technological practicalities. For example, engineering the desired diffraction pattern into a structure via its k-space representation may result in its arbitrary appearance in real space, e.g. the QR supercell approach. Such a fine-tuned structure then becomes difficult to fabricate on a large scale, to monitor for imperfections and to modify, if needed later on.

Here, we moved the focus from the structure to the arrangement of its basic element. We outlined how arranging grating lines yields the same high performance of sophisticated designs but with practical advantages. We thereby introduced the concept of the photonic domain and show how the combination of Fourier analysis and current depth profile allows to fully assess all relevant aspects of light-trapping designs for solar cells. For example, the checkerboard pattern shows much simplicity in design, reduced surface area, and high robustness to imperfections. We expect our simple design principle to impact not only in the solar cell or LED sector but also in applications where a disruptive function is required on large areas, such as acoustic noise shields, wind break panels, anti-skid surfaces, liquid control devices, biosensors and atomic cooling [310].

In the last work (Chapter 7), motivated by the previous results of Chapter 6 and Chapter 3, an optimized quasi-random checkerboard (CB) pattern grating structure was applied and then coupled with an LDS coating on the front contacts of PSCs. The structures showed both an important increase in photocurrent (25%) and an omnidirectional response over large oblique angles (0–70 degrees). Electrically, it is also shown that the ultra-thin devices also benefit from an increased open circuit voltage and fill factor, leading to an absolute PCE as high as 24.1% — corresponding to a >28% gain compared to the reference planar cell. Regardless, a large portion of UV radiation is being blocked by the front CB grating — thus also contributing to the perovskite stability.

This study demonstrates how the experimentally developed LDS material (t-U (5000)/Eu^{3+}) has the potential to improve perovskite stability without sacrificing PV performance. It is shown that this LDS material can reduce by ~94% the harmful photo-generation in the TiO_2 layer as well as in the interface of perovskite/TiO_2 layers. Despite t-U (5000)/Eu^{3+} acting as a perfect UV encapsulant layer, the overall device performance is expected to even improve slightly. The gain in PCE is more noticeable for planar PSCs without LT (+6.9%) compared to LT-enhanced PSCs (+1.6%). The improvements demonstrated in our theoretical analysis for the studied LDS layer in PSCs are expected to be attained experimentally in real solar cells, as the LDS layer composed of such materials has already allowed pronounced gains in c-Si and PTB7-Th:ITIC–based organic solar cells shown experimentally.

Considering all the benefits demonstrated by the innovative photonic schemes studied throughout this thesis, the next step for this work is to test them in real PSC devices with a highly promising potential to boost efficiency and stability. As a future prospect, these optical

micro-structures (particularly the CB gratings) also offer the possibility to realize different structural colors, which would improve the aesthetic appeal of PV technology.

BIBLIOGRAPHY

[1] SolarPower Europe, "Global market outlook for Solar Power 2017-2021." Solarpower Europe, 2017.

[2] S. Philipps and W. Warmuth, "©Fraunhofer ISE: Photovoltaics Report." p. 45, 2018.

[3] International Energy Agency, "Snapshot of global photovoltaic markets." 2017.

[4] M. A. Green, "Commercial progress and challenges for photovoltaics," *Nat. Energy*, vol. 1, no. 1, p. 15015, Jan. 2016, doi: 10.1038/nenergy.2015.15.

[5] M. L. Brongersma, Y. Cui, and S. Fan, "Light management for photovoltaics using high-index nanostructures," *Nat. Mater.*, vol. 13, no. 5, pp. 451–460, May 2014, doi: 10.1038/nmat3921.

[6] O. Isabella, R. Vismara, D. N. P. Linssen, K. X. Wang, S. Fan, and M. Zeman, "Advanced light trapping scheme in decoupled front and rear textured thin-film silicon solar cells," *Sol. Energy*, vol. 162, no. October 2017, pp. 344–356, Mar. 2018, doi: 10.1016/j.solener.2018.01.040.

[7] M. J. Mendes *et al.*, "Optimal-Enhanced Solar Cell Ultra-thinning with Broadband Nanophotonic Light Capture," *iScience*, vol. 3, pp. 238–254, May 2018, doi: 10.1016/j.isci.2018.04.018.

[8] A. T. Vicente *et al.*, "Multifunctional cellulose-paper for light harvesting and smart sensing applications," *J. Mater. Chem. C*, vol. 6, no. 13, pp. 3143–3181, Mar. 2018, doi: 10.1039/C7TC05271E.

[9] J.-P. Correa-Baena *et al.*, "Promises and challenges of perovskite solar cells," *Science (80-.).*, vol. 358, no. 6364, pp. 739–744, 2017, doi: 10.1126/science.aam6323.

[10] M. R. Filip, C. Verdi, and F. Giustino, "GW Band Structures and Carrier Effective Masses of CH 3 NH 3 PbI 3 and Hypothetical Perovskites of the Type APbI 3 : A = NH 4 , PH 4 , AsH 4 , and SbH 4," *J. Phys. Chem. C*, vol. 119, no. 45, pp. 25209–25219, 2015, doi: 10.1021/acs.jpcc.5b07891.

[11] W.-J. Yin, J.-H. Yang, J. Kang, Y. Yan, and S.-H. Wei, "Halide perovskite materials for solar cells: a theoretical review," *J. Mater. Chem. A*, vol. 3, no. 17, pp. 8926–8942, 2015, doi: 10.1039/C4TA05033A.

[12] T. M. Brenner, D. A. Egger, L. Kronik, G. Hodes, and D. Cahen, "Hybrid organic—inorganic perovskites: low-cost semiconductors with intriguing charge-transport properties," *Nat. Rev. Mater.*, vol. 1, no. 1, p. 15007, Jan. 2016, doi: 10.1038/natrevmats.2015.7.

[13] N. J. Jeon *et al.*, "Compositional engineering of perovskite materials for high-performance solar cells," *Nature*, vol. 517, no. 7535, pp. 476–480, Jan. 2015, doi: 10.1038/nature14133.

[14] L. J. Phillips *et al.*, "Dispersion relation data for methylammonium lead triiodide perovskite deposited on a (100) silicon wafer using a two-step vapour-phase reaction process," *Data Br.*, vol. 5, pp. 926–928, Dec. 2015, doi: 10.1016/J.DIB.2015.10.026.

[15] M. I. Asghar, J. Zhang, H. Wang, and P. D. Lund, "Device stability of perovskite solar cells – A review," *Renew. Sustain. Energy Rev.*, vol. 77, no. July 2016, pp. 131–146, 2017, doi: 10.1016/j.rser.2017.04.003.

[16] H. A. Atwater and A. Polman, "Plasmonics for improved photovoltaic devices," *Nat. Mater.*, vol. 9, no. 3, pp. 205–213, Mar. 2010, doi: 10.1038/nmat2629.

[17] V. E. Ferry, A. Polman, and H. A. Atwater, "Modeling Light Trapping in Nanostructured Solar Cells," *ACS Nano*, vol. 5, no. 12, pp. 10055–10064, Dec. 2011, doi: 10.1021/nn203906t.

[18] M. J. Mendes *et al.*, *Design of optimized wave-optical spheroidal nanostructures for photonic-enhanced solar cells*, vol. 26. Elsevier, 2016, pp. 286–296. doi: 10.1016/J.NANOEN.2016.05.038.

[19] S. Haque, M. J. Mendes, O. Sanchez-Sobrado, H. Águas, E. Fortunato, and R. Martins, "Photonic-structured TiO2 for high-efficiency, flexible and stable Perovskite solar cells," *Nano Energy*, vol. 59, pp. 91–101, 2019, doi: 10.1016/J.NANOEN.2019.02.023.

[20] R. Schmager, G. Gomard, B. S. Richards, and U. W. Paetzold, "Nanophotonic perovskite layers for enhanced current generation and mitigation of lead in perovskite solar cells," *Sol. Energy Mater. Sol. Cells*, vol. 192, pp. 65–71, Apr. 2019, doi: 10.1016/J.SOLMAT.2018.12.012.

[21] A. V. Shah *et al.*, "Thin-film silicon solar cell technology," *Prog. Photovoltaics Res. Appl.*, vol. 12, no. 23, pp. 113–142, Mar. 2004, doi: 10.1002/pip.533.

[22] D. L. Staebler and C. R. Wronski, "Reversible conductivity changes in discharge-produced amorphous Si," *Appl. Phys. Lett.*, vol. 31, no. 4, pp. 292–294, Aug. 1977, doi: 10.1063/1.89674.

[23] Y. Xu, T. Gong, and J. N. Munday, "The generalized Shockley-Queisser limit for nanostructured solar cells.," *Sci. Rep.*, vol. 5, p. 13536, Sep. 2015, doi: 10.1038/srep13536.

[24] J. Wei *et al.*, "Enhanced Light Harvesting in Perovskite Solar Cells by a Bioinspired Nanostructured Back Electrode," *Adv. Energy Mater.*, vol. 7, no. 20, p. 1700492, Oct. 2017, doi: 10.1002/aenm.201700492.

[25] M. Alexandre *et al.*, "Optimum Luminescent Down-Shifting Properties for High Efficiency and Stable Perovskite Solar Cells," *ACS Appl. Energy Mater.*, vol. 2, no. 4, pp. 2930–2938, Apr. 2019, doi: 10.1021/acsaem.9b00271.

[26] H. Águas *et al.*, "Thin Film Silicon Photovoltaic Cells on Paper for Flexible Indoor Applications," *Adv. Funct. Mater.*, vol. 25, no. 23, pp. 3592–3598, Jun. 2015, doi: 10.1002/adfm.201500636.

[27] Q. Chen *et al.*, "Under the spotlight: The organic–inorganic hybrid halide perovskite for optoelectronic applications," *Nano Today*, vol. 10, no. 3, pp. 355–396, Jun. 2015, doi: 10.1016/J.NANTOD.2015.04.009.

[28] Y. Ogomi *et al.*, "$CH_3NH_3Sn_xPb_{(1-x)}I_3$ Perovskite Solar Cells Covering up to 1060 nm," *J. Phys. Chem. Lett.*, vol. 5, no. 6, pp. 1004–1011, Mar. 2014, doi: 10.1021/jz5002117.

[29] J. H. Noh, S. H. Im, J. H. Heo, T. N. Mandal, and S. Il Seok, "Chemical Management for Colorful, Efficient, and Stable Inorganic–Organic Hybrid Nanostructured Solar Cells," *Nano Lett.*, vol. 13, no. 4, pp. 1764–1769, Apr. 2013, doi: 10.1021/nl400349b.

[30] C. S. Ponseca *et al.*, "Organometal Halide Perovskite Solar Cell Materials Rationalized: Ultrafast Charge Generation, High and Microsecond-Long Balanced Mobilities, and Slow Recombination," *J. Am. Chem. Soc.*, vol. 136, no. 14, pp. 5189–5192, Apr. 2014, doi: 10.1021/ja412583t.

[31] H. Oga, A. Saeki, Y. Ogomi, S. Hayase, and S. Seki, "Improved Understanding of the Electronic and Energetic Landscapes of Perovskite Solar Cells: High Local Charge Carrier Mobility, Reduced Recombination, and Extremely Shallow Traps," *J. Am. Chem. Soc.*, vol. 136, no. 39, pp. 13818–13825, Oct. 2014, doi: 10.1021/ja506936f.

[32] F. Huang, M. Li, P. Siffalovic, G. Cao, and J. Tian, "From scalable solution fabrication of perovskite films towards commercialization of solar cells," *Energy Environ. Sci.*, vol. 12, no. 2, pp. 518–549, Feb. 2019, doi: 10.1039/C8EE03025A.

[33] A. Kojima, K. Teshima, Y. Shirai, and T. Miyasaka, "Organometal Halide Perovskites as

Visible-Light Sensitizers for Photovoltaic Cells," *J. Am. Chem. Soc.*, vol. 131, no. 17, pp. 6050–6051, May 2009, doi: 10.1021/ja809598r.

[34] M. Saliba *et al.*, "Cesium-containing triple cation perovskite solar cells: improved stability, reproducibility and high efficiency," *Energy Environ. Sci.*, vol. 9, no. 6, pp. 1989–1997, Jun. 2016, doi: 10.1039/C5EE03874J.

[35] D. Bi *et al.*, "Polymer-templated nucleation and crystal growth of perovskite films for solar cells with efficiency greater than 21%," *Nat. Energy*, vol. 1, no. 10, p. 16142, Sep. 2016, doi: 10.1038/nenergy.2016.142.

[36] W. S. Yang *et al.*, "Iodide management in formamidinium-lead-halide-based perovskite layers for efficient solar cells.," *Science*, vol. 356, no. 6345, pp. 1376–1379, Jun. 2017, doi: 10.1126/science.aan2301.

[37] Y. Cheng, F. So, and S.-W. Tsang, "Progress in air-processed perovskite solar cells: from crystallization to photovoltaic performance," *Mater. Horizons*, 2019, doi: 10.1039/C9MH00325H.

[38] "Best Research-Cell Efficiency Chart | Photovoltaic Research | NREL." https://www.nrel.gov/pv/cell-efficiency.html (accessed Jan. 12, 2022).

[39] J. Burschka *et al.*, "Sequential deposition as a route to high-performance perovskite-sensitized solar cells," *Nature*, vol. 499, no. 7458, pp. 316–319, Jul. 2013, doi: 10.1038/nature12340.

[40] W. Nie *et al.*, "High-efficiency solution-processed perovskite solar cells with millimeter-scale grains," *Science (80-.).*, vol. 347, no. 6221, pp. 522–525, Jan. 2015, doi: 10.1126/SCIENCE.AAA0472.

[41] N. Arora *et al.*, "Perovskite solar cells with CuSCN hole extraction layers yield stabilized efficiencies greater than 20%," *Science (80-.).*, vol. 358, no. 6364, pp. 768–771, Nov. 2017, doi: 10.1126/SCIENCE.AAM5655.

[42] E. Della Gaspera *et al.*, "Ultra-thin high efficiency semitransparent perovskite solar cells," *Nano Energy*, vol. 13, pp. 249–257, Apr. 2015, doi: 10.1016/J.NANOEN.2015.02.028.

[43] "What is solar gain?" https://www.es-so-database.com/index.php/knowledge/appendices

[44] O. Sanchez-Sobrado *et al.*, "Lightwave trapping in thin film solar cells with improved photonic-structured front contacts," *J. Mater. Chem. C*, vol. 7, no. 21, pp. 6456–6464, May 2019, doi: 10.1039/C8TC06092D.

[45] A. Peer, R. Biswas, J.-M. Park, R. Shinar, and J. Shinar, "Light management in perovskite solar cells and organic LEDs with microlens arrays," *Opt. Express*, vol. 25, no. 9, p. 10704, May 2017, doi: 10.1364/OE.25.010704.

[46] H. Wang, B. Cai, and X. Yuan, "Significant light absorption improvement in perovskite/CIGS tandem solar cells with dielectric nanocone structures," *J. Phys. Conf. Ser.*, vol. 844, p. 012004, Jun. 2017, doi: 10.1088/1742-6596/844/1/012004.

[47] N. Horiuchi, "Photonic nanojets," *Nat. Photonics*, vol. 6, no. 3, pp. 138–139, Mar. 2012, doi: 10.1038/nphoton.2012.43.

[48] B. Dudem, J. H. Heo, J. W. Leem, J. S. Yu, and S. H. Im, "$CH_3NH_3PbI_3$ planar perovskite solar cells with antireflection and self-cleaning function layers," *J. Mater. Chem. A*, vol. 4, no. 20, pp. 7573–7579, May 2016, doi: 10.1039/C6TA01800A.

[49] T. K. Nguyen, P. T. Dang, and K. Q. Le, "Numerical design of thin perovskite solar cell with fiber array-based anti-reflection front electrode for light-trapping enhancement," *J. Opt.*, vol. 18, no. 12, p. 125901, Dec. 2016, doi: 10.1088/2040-8978/18/12/125901.

[50] U. W. Paetzold, W. Qiu, F. Finger, J. Poortmans, and D. Cheyns, "Nanophotonic front electrodes for perovskite solar cells," *Appl. Phys. Lett.*, vol. 106, no. 17, p. 173101, Apr.

2015, doi: 10.1063/1.4918751.
[51] S. M. Kang *et al.*, "Moth-Eye TiO $_2$ Layer for Improving Light Harvesting Efficiency in Perovskite Solar Cells," *Small*, vol. 12, no. 18, pp. 2443–2449, May 2016, doi: 10.1002/smll.201600428.
[52] S.-J. Ha, J. H. Heo, S. H. Im, and J. H. Moon, "Mesoscopic CH $_3$ NH $_3$ PbI $_3$ perovskite solar cells using TiO $_2$ inverse opal electron-conducting scaffolds," *J. Mater. Chem. A*, vol. 5, no. 5, pp. 1972–1977, Jan. 2017, doi: 10.1039/C6TA07004C.
[53] Y. Luo, S. Liu, N. Barange, L. Wang, and F. So, "Perovskite Solar Cells on Corrugated Substrates with Enhanced Efficiency," *Small*, vol. 12, no. 46, pp. 6346–6352, Dec. 2016, doi: 10.1002/smll.201601974.
[54] J. Werner *et al.*, "Perovskite/Perovskite/Silicon Monolithic Triple-Junction Solar Cells with a Fully Textured Design," *ACS Energy Lett.*, vol. 3, no. 9, pp. 2052–2058, Sep. 2018, doi: 10.1021/acsenergylett.8b01165.
[55] D. Chen *et al.*, "Nanophotonic light management for perovskite–silicon tandem solar cells," *J. Photonics Energy*, vol. 8, no. 02, p. 1, Mar. 2018, doi: 10.1117/1.JPE.8.022601.
[56] M. I. Hossain, W. Qarony, V. Jovanov, Y. H. Tsang, and D. Knipp, "Nanophotonic design of perovskite/silicon tandem solar cells," *J. Mater. Chem. A*, vol. 6, no. 8, pp. 3625–3633, Feb. 2018, doi: 10.1039/C8TA00628H.
[57] J. Hao *et al.*, "Light Trapping Effect in Perovskite Solar Cells by the Addition of Ag Nanoparticles, Using Textured Substrates.," *Nanomater. (Basel, Switzerland)*, vol. 8, no. 10, Oct. 2018, doi: 10.3390/nano8100815.
[58] R. T. Ginting *et al.*, "Plasmonic Effect of Gold Nanostars in Highly Efficient Organic and Perovskite Solar Cells," *ACS Appl. Mater. Interfaces*, vol. 9, no. 41, pp. 36111–36118, Oct. 2017, doi: 10.1021/acsami.7b11084.
[59] M. Long *et al.*, "Ultrathin efficient perovskite solar cells employing a periodic structure of a composite hole conductor for elevated plasmonic light harvesting and hole collection," *Nanoscale*, vol. 8, no. 12, pp. 6290–6299, Mar. 2016, doi: 10.1039/C5NR05042A.
[60] R. Rondão *et al.*, "High-Performance Near-Infrared Luminescent Solar Concentrators," *ACS Appl. Mater. Interfaces*, vol. 9, no. 14, pp. 12540–12546, Apr. 2017, doi: 10.1021/acsami.7b02700.
[61] C. Chen, S. Zheng, H. Song, Cong Chen, Shijian Zheng, and Hongwei Song, "Photon management to reduce energy loss in perovskite solar cells," *Chem. Soc. Rev.*, vol. 50, no. 12, pp. 7250–7329, Jun. 2021, doi: 10.1039/D0CS01488E.
[62] M. T. Hörantner, W. Zhang, M. Saliba, K. Wojciechowski, and H. J. Snaith, "Templated microstructural growth of perovskite thin films via colloidal monolayer lithography," *Energy Environ. Sci.*, vol. 8, no. 7, pp. 2041–2047, Jul. 2015, doi: 10.1039/C5EE01169H.
[63] G. Editors *et al.*, "(LMTD,Re,Nu,Pr,to get h,etc with flowchart) Targeting and Design of Evacuated-Tube Solar Collector Networks," *Chem. Eng. Trans.*, vol. 52, 2016, Accessed: May 03, 2022. [Online]. Available: https://www.aidic.it/cet/16/52/144.pdf
[64] M. M. Tavakoli *et al.*, "Efficient, flexible and mechanically robust perovskite solar cells on inverted nanocone plastic substrates," *Nanoscale*, vol. 8, no. 7, pp. 4276–4283, 2016, doi: 10.1039/C5NR08836D.
[65] Y. Wang *et al.*, "Metal oxide charge transport layers in perovskite solar cells—optimising low temperature processing and improving the interfaces towards low temperature processed, efficient and stable devices," *J. Phys. Energy*, vol. 3, no. 1, p. 012004, Dec. 2020, doi: 10.1088/2515-7655/ABC73F.
[66] Y. Wang, M. Li, X. Zhou, P. Li, X. Hu, and Y. Song, "High efficient perovskite whispering-gallery solar cells," *Nano Energy*, vol. 51, pp. 556–562, Sep. 2018, doi:

10.1016/J.NANOEN.2018.06.085.
[67] Y. Wang *et al.*, "Diffraction-Grated Perovskite Induced Highly Efficient Solar Cells through Nanophotonic Light Trapping," *Adv. Energy Mater.*, vol. 8, no. 12, Apr. 2018, doi: 10.1002/AENM.201702960.
[68] F. Wang *et al.*, "Toward ultra-thin and omnidirectional perovskite solar cells: Concurrent improvement in conversion efficiency by employing light-trapping and recrystallizing treatment," *Nano Energy*, vol. 60, pp. 198–204, Jun. 2019, doi: 10.1016/j.nanoen.2019.03.059.
[69] D. H. Choi, S. K. Nam, K. Jung, and J. H. Moon, "2D photonic crystal nanodisk array as electron transport layer for highly efficient perovskite solar cells," *Nano Energy*, vol. 56, pp. 365–372, Feb. 2019, doi: 10.1016/J.NANOEN.2018.11.050.
[70] Y. A. Lu *et al.*, "Coral-like perovskite nanostructures for enhanced light-harvesting and accelerated charge extraction in perovskite solar cells," *Nano Energy*, vol. 58, pp. 138–146, Apr. 2019, doi: 10.1016/J.NANOEN.2019.01.014.
[71] M. Saliba *et al.*, "Cesium-containing Triple Cation Perovskite Solar Cells: Improved Stability, Reproducibility and High Efficiency," *Energy Environ. Sci.*, vol. 9, no. 6, pp. 1989–1997, 2016, doi: 10.1039/C5EE03874J.
[72] M. Ye, X. Hong, F. Zhang, and X. Liu, "Recent advancements in perovskite solar cells: flexibility, stability and large scale," *J. Mater. Chem. A*, vol. 4, no. 18, pp. 6755–6771, May 2016, doi: 10.1039/C5TA09661H.
[73] L. C. Andreani, A. Bozzola, P. Kowalczewski, and M. Liscidini, "Photonic light trapping and electrical transport in thin-film silicon solar cells," *Sol. Energy Mater. Sol. Cells*, vol. 135, pp. 78–92, Apr. 2015, doi: 10.1016/J.SOLMAT.2014.10.012.
[74] A. Ingenito, O. Isabella, and M. Zeman, "Experimental Demonstration of 4 n^2 Classical Absorption Limit in Nanotextured Ultrathin Solar Cells with Dielectric Omnidirectional Back Reflector," *ACS Photonics*, vol. 1, no. 3, pp. 270–278, Mar. 2014, doi: 10.1021/ph4001586.
[75] M. S. Branham *et al.*, "Empirical Comparison of Random and Periodic Surface Light-Trapping Structures for Ultrathin Silicon Photovoltaics," *Adv. Opt. Mater.*, vol. 4, no. 6, pp. 858–863, Jun. 2016, doi: 10.1002/adom.201500667.
[76] F.-J. Haug and C. Ballif, "Light management in thin film silicon solar cells," *Energy Environ. Sci.*, vol. 8, no. 3, pp. 824–837, Mar. 2015, doi: 10.1039/C4EE03346A.
[77] A. Mellor, I. Tobías, A. Martí, M. J. Mendes, and A. Luque, "Upper limits to absorption enhancement in thick solar cells using diffraction gratings," *Prog. Photovoltaics Res. Appl.*, vol. 19, no. 6, pp. 676–687, Sep. 2011, doi: 10.1002/pip.1086.
[78] Z. Yang, P. Gao, C. Zhang, X. Li, and J. Ye, "Scattering effect of the high-index dielectric nanospheres for high performance hydrogenated amorphous silicon thin-film solar cells," *Sci. Rep.*, vol. 6, no. 1, p. 30503, Sep. 2016, doi: 10.1038/srep30503.
[79] D. Zhou *et al.*, "Optimization of the optical properties of nanostructured silicon surfaces for solar cell applications," *J. Appl. Phys.*, vol. 115, no. 13, p. 134304, Apr. 2014, doi: 10.1063/1.4870236.
[80] C. van Lare, F. Lenzmann, M. A. Verschuuren, and A. Polman, "Dielectric Scattering Patterns for Efficient Light Trapping in Thin-Film Solar Cells," *Nano Lett.*, vol. 15, no. 8, pp. 4846–4852, Aug. 2015, doi: 10.1021/nl5045583.
[81] M. J. Mendes, S. Morawiec, F. Simone, F. Priolo, and I. Crupi, "Colloidal plasmonic back reflectors for light trapping in solar cells.," *Nanoscale*, vol. 6, no. 9, pp. 4796–805, 2014, doi: 10.1039/c3nr06768h.
[82] M. J. Mendes *et al.*, "Broadband light trapping in thin film solar cells with self-organized plasmonic nano-colloids," *Nanotechnology*, vol. 26, no. 13, p. 135202, Mar. 2015, doi:

10.1088/0957-4484/26/13/135202.
[83] "Triple-junction thin-film silicon solar cell fabricated on periodically textured substrate with a stabilized efficiency of 13.6%," *Appl. Phys. Lett.*, vol. 106, no. 21, p. 213902, May 2015, doi: 10.1063/1.4921794.
[84] O. Sanchez-Sobrado *et al.*, "Colloidal-lithographed TiO2 photonic nanostructures for solar cell light trapping," *J. Mater. Chem. C*, 2017, doi: 10.1039/C7TC01756A.
[85] E. R. Martins *et al.*, "Deterministic quasi-random nanostructures for photon control," *Nat. Commun. 2013 41*, vol. 4, no. 1, pp. 1–7, Oct. 2013, doi: 10.1038/ncomms3665.
[86] "RCAAP - Luminescent urea cross-linked tripodal siloxane-based hybrids." https://www.rcaap.pt/detail.jsp?id=oai:ria.ua.pt:10773/19196 (accessed May 03, 2022).
[87] V. T. Freitas *et al.*, "Luminescent urea cross-linked tripodal siloxane-based hybrids," *J. Sol-Gel Sci. Technol.*, vol. 65, no. 1, pp. 83–92, Jan. 2013, doi: 10.1007/S10971-012-2770-2/FIGURES/7.
[88] S. F. H. Correia *et al.*, "Large-Area Tunable Visible-to-Near-Infrared Luminescent Solar Concentrators," *Adv. Sustain. Syst.*, vol. 2, no. 6, p. 1800002, Jun. 2018, doi: 10.1002/ADSU.201800002.
[89] S. F. H. Correia *et al.*, "Scale up the collection rea of luminescent solar concentrators towards metre-length flexible waveguiding photovoltaics," *Prog. Photovoltaics Res. Appl.*, vol. 24, pp. 1178–1193, 2016, doi: 10.1002/pip.
[90] S. F. H. Correia *et al.*, "Lanthanide-based downshifting layers tested in a solar car race," *Opto-Electronic Adv.*, vol. 2, no. 6, pp. 190006–1, 2019, doi: 10.29026/OEA.2019.190006.
[91] S. F. H. Correia, V. De Zea Bermudez, S. J. L. Ribeiro, P. S. André, R. A. S. Ferreira, and L. D. Carlos, "Luminescent solar concentrators: challenges for lanthanide-based organic–inorganic hybrid materials," *J. Mater. Chem. A*, vol. 2, no. 16, pp. 5580–5596, Mar. 2014, doi: 10.1039/C3TA14964A.
[92] M. A. Cardoso *et al.*, "Solar spectral conversion based on plastic films of lanthanide-doped ionosilicas for photovoltaics: Down-shifting layers and luminescent solar concentrators," *J. Rare Earths*, vol. 38, no. 5, pp. 531–538, May 2020, doi: 10.1016/J.JRE.2020.01.007.
[93] S. F. H. Correia *et al.*, "Scale up the collection area of luminescent solar concentrators towards metre-length flexible waveguiding photovoltaics," *Prog. Photovoltaics Res. Appl.*, vol. 24, no. 9, pp. 1178–1193, Sep. 2016, doi: 10.1002/pip.2772.
[94] S. Haque, M. Alexandre, M. J. Mendes, H. Águas, E. Fortunato, and R. Martins, "Design of wave-optical structured substrates for ultra-thin perovskite solar cells," *Appl. Mater. Today*, vol. 20, p. 100720, Sep. 2020, doi: 10.1016/J.APMT.2020.100720.
[95] A. Polman and H. A. Atwater, "Photonic design principles for ultrahigh-efficiency photovoltaics," *Nat. Mater.*, vol. 11, no. 3, pp. 174–177, Mar. 2012, doi: 10.1038/nmat3263.
[96] M. J. Mendes, I. Tobías, A. Martí, and A. Luque, "Light concentration in the near-field of dielectric spheroidal particles with mesoscopic sizes," *Opt. Express*, vol. 19, no. 17, p. 16207, Aug. 2011, doi: 10.1364/OE.19.016207.
[97] T. Uekert *et al.*, "Nanostructured organosilicon luminophores in highly efficient luminescent down-shifting layers for thin film photovoltaics," *Sol. Energy Mater. Sol. Cells*, vol. 155, pp. 1–8, Oct. 2016, doi: 10.1016/j.solmat.2016.04.019.
[98] H. S. Anizelli *et al.*, "Application of luminescence downshifting materials for enhanced stability of CH 3 NH 3 PbI 3(1-x) Cl 3x perovskite photovoltaic devices," *Org. Electron.*, vol. 49, pp. 129–134, Oct. 2017, doi: 10.1016/j.orgel.2017.06.056.
[99] A. Gheno, T. Trigaud, J. Bouclé, P. Audebert, B. Ratier, and S. Vedraine, "Stability

assessments on luminescent down-shifting molecules for UV-protection of perovskite solar cells," *Opt. Mater. (Amst).*, vol. 75, pp. 781–786, Jan. 2018, doi: 10.1016/j.optmat.2017.11.027.
[100] M. Ye, X. Hong, and X.-Y. Liu, "Recent Advancements in Perovskite Solar Cells: Flexibility, Stability and Large Scale," *J. Mater. Chem. A*, vol. 4, pp. 6755–6771, 2016, doi: 10.1039/C5TA09661H.
[101] L. Qiu, J. Deng, X. Lu, Z. Yang, and H. Peng, "Integrating Perovskite Solar Cells into a Flexible Fiber," *Angew. Chemie Int. Ed.*, vol. 53, no. 39, pp. 10425–10428, Sep. 2014, doi: 10.1002/anie.201404973.
[102] A. Vicente *et al.*, "Solar cells for self-sustainable intelligent packaging," *J. Mater. Chem. A*, vol. 3, no. 25, pp. 13226–13236, 2015, doi: 10.1039/c5ta01752a.
[103] S. N. Habisreutinger, D. P. McMeekin, H. J. Snaith, and R. J. Nicholas, "Research Update: Strategies for improving the stability of perovskite solar cells," *APL Mater.*, vol. 4, no. 9, p. 091503, Sep. 2016, doi: 10.1063/1.4961210.
[104] M. M. Tavakoli *et al.*, "Highly Efficient Flexible Perovskite Solar Cells with Antireflection and Self-Cleaning Nanostructures," *ACS Nano*, vol. 9, no. 10, pp. 10287–10295, Oct. 2015, doi: 10.1021/acsnano.5b04284.
[105] R. D. Oliveira *et al.*, "Colloidal Lithography for Photovoltaics: An Attractive Route for Light Management," *Nanomater. 2021, Vol. 11, Page 1665*, vol. 11, no. 7, p. 1665, Jun. 2021, doi: 10.3390/NANO11071665.
[106] J. L. N. Boane *et al.*, "Soft-Microstructured Transparent Electrodes for Photonic-Enhanced Flexible Solar Cells," *Micro 2021, Vol. 1, Pages 215-227*, vol. 1, no. 2, pp. 215–227, Oct. 2021, doi: 10.3390/MICRO1020016.
[107] M. G. Deceglie, V. E. Ferry, A. P. Alivisatos, and H. A. Atwater, "Design of Nanostructured Solar Cells Using Coupled Optical and Electrical Modeling," *Nano Lett.*, vol. 12, no. 6, pp. 2894–2900, Jun. 2012, doi: 10.1021/nl300483y.
[108] J. Chung *et al.*, "Record-efficiency flexible perovskite solar cell and module enabled by a porous-planar structure as an electron transport layer," *Energy Environ. Sci.*, vol. 13, no. 12, pp. 4854–4861, Dec. 2020, doi: 10.1039/D0EE02164D.
[109] J. Zhang, W. Zhang, H. M. Cheng, and S. R. P. Silva, "Critical review of recent progress of flexible perovskite solar cells," *Mater. Today*, vol. 39, pp. 66–88, Oct. 2020, doi: 10.1016/J.MATTOD.2020.05.002.
[110] Q. Lin, A. Armin, R. C. R. Nagiri, P. L. Burn, and P. Meredith, "Electro-optics of perovskite solar cells," *Nat. Photonics*, vol. 9, no. 2, pp. 106–112, Feb. 2015, doi: 10.1038/nphoton.2014.284.
[111] B. Shi *et al.*, "Enhanced light absorption of thin perovskite solar cells using textured substrates," *Sol. Energy Mater. Sol. Cells*, vol. 168, pp. 214–220, Aug. 2017, doi: 10.1016/J.SOLMAT.2017.04.038.
[112] M. Jošt *et al.*, "Efficient Light Management by Textured Nanoimprinted Layers for Perovskite Solar Cells," *ACS Photonics*, vol. 4, no. 5, pp. 1232–1239, May 2017, doi: 10.1021/acsphotonics.7b00138.
[113] L. Zheng *et al.*, "Improved light absorption and charge transport for perovskite solar cells with rough interfaces by sequential deposition," *Nanoscale*, vol. 6, no. 14, pp. 8171–8176, 2014, doi: 10.1039/C4NR01141D.
[114] A. R. Pascoe *et al.*, "Enhancing the Optoelectronic Performance of Perovskite Solar Cells via a Textured $CH_3NH_3PbI_3$ Morphology," *Adv. Funct. Mater.*, vol. 26, no. 8, pp. 1278–1285, Feb. 2016, doi: 10.1002/adfm.201504190.
[115] D.-L. Wang, H.-J. Cui, G.-J. Hou, Z.-G. Zhu, Q.-B. Yan, and G. Su, "Highly efficient light management for perovskite solar cells," *Sci. Rep.*, vol. 6, no. 1, p. 18922, May 2016, doi:

10.1038/srep18922.
[116] M. Omelyanovich, S. Makarov, V. Milichko, and C. Simovski, "Enhancement of Perovskite Solar Cells by Plasmonic Nanoparticles," *Mater. Sci. Appl.*, vol. 07, no. 12, pp. 836–847, 2016, doi: 10.4236/msa.2016.712064.
[117] Q. Luo *et al.*, "Plasmonic Effects of Metallic Nanoparticles on Enhancing Performance of Perovskite Solar Cells," *ACS Appl. Mater. Interfaces*, vol. 9, no. 40, pp. 34821–34832, Oct. 2017, doi: 10.1021/acsami.7b08489.
[118] J. Yin, H. Qu, J. Cao, H. Tai, J. Li, and N. Zheng, "Light absorption enhancement by embedding submicron scattering TiO_2 nanoparticles in perovskite solar cells," *RSC Adv.*, vol. 6, no. 29, pp. 24596–24602, 2016, doi: 10.1039/C6RA01894G.
[119] O. Sanchez-Sobrado *et al.*, "Colloidal-lithographed TiO_2 photonic nanostructures for solar cell light trapping," *J. Mater. Chem. C*, vol. 5, no. 27, pp. 6852–6861, Jul. 2017, doi: 10.1039/C7TC01756A.
[120] M. Karg *et al.*, "Colloidal self-assembly concepts for light management in photovoltaics," *Mater. Today*, vol. 18, no. 4, pp. 185–205, May 2015, Accessed: Mar. 05, 2018. [Online]. Available: https://www.sciencedirect.com/science/article/pii/S1369702114004076
[121] F. Fu *et al.*, "High-efficiency inverted semi-transparent planar perovskite solar cells in substrate configuration," *Nat. Energy*, vol. 2, no. 1, p. 16190, Dec. 2016, doi: 10.1038/nenergy.2016.190.
[122] G. W. P. Adhyaksa, E. Johlin, and E. C. Garnett, "Nanoscale Back Contact Perovskite Solar Cell Design for Improved Tandem Efficiency," *Nano Lett.*, vol. 17, no. 9, pp. 5206–5212, Sep. 2017, doi: 10.1021/acs.nanolett.7b01092.
[123] E. Yablonovitch and G. D. Cody, "Intensity enhancement in textured optical sheets for solar cells," *IEEE Trans. Electron Devices*, vol. 29, no. 2, pp. 300–305, Feb. 1982, doi: 10.1109/T-ED.1982.20700.
[124] M. A. Green, "Lambertian light trapping in textured solar cells and light-emitting diodes: analytical solutions," *Prog. Photovoltaics Res. Appl.*, vol. 10, no. 4, pp. 235–241, Jun. 2002, doi: 10.1002/pip.404.
[125] A. Bozzola, M. Liscidini, and L. C. Andreani, "Photonic light-trapping versus Lambertian limits in thin film silicon solar cells with 1D and 2D periodic patterns," *Opt. Express*, vol. 20, no. S2, p. A224, Mar. 2012, doi: 10.1364/OE.20.00A224.
[126] "FDTD Solutions | Lumerical's Nanophotonic FDTD Simulation Software." https://www.lumerical.com/tcad-products/fdtd/ (accessed Jan. 12, 2022).
[127] K. J. Yu *et al.*, "Light Trapping in Ultrathin Monocrystalline Silicon Solar Cells," *Adv. Energy Mater.*, vol. 3, no. 11, pp. 1401–1406, Nov. 2013, doi: 10.1002/aenm.201300542.
[128] J. Nam *et al.*, "Transfer Printed Flexible and Stretchable Thin Film Solar Cells Using a Water-Soluble Sacrificial Layer," *Adv. Energy Mater.*, vol. 6, no. 21, p. 1601269, Nov. 2016, doi: 10.1002/aenm.201601269.
[129] U. Mehmood, A. Al-Ahmed, M. Afzaal, F. A. Al-Sulaiman, and M. Daud, "Recent progress and remaining challenges in organometallic halides based perovskite solar cells," *Renew. Sustain. Energy Rev.*, vol. 78, pp. 1–14, 2017, doi: 10.1016/j.rser.2017.04.105.
[130] H. Uratani and K. Yamashita, "Charge Carrier Trapping at Surface Defects of Perovskite Solar Cell Absorbers: A First-Principles Study," *J. Phys. Chem. Lett.*, vol. 8, no. 4, pp. 742–746, Feb. 2017, doi: 10.1021/acs.jpclett.7b00055.
[131] Y. Sun *et al.*, "Enhanced UV-light stability of organometal halide perovskite solar cells with interface modification and a UV absorption layer," *J. Mater. Chem. C*, vol. 5, no. 34, pp. 8682–8687, Aug. 2017, doi: 10.1039/C7TC02603J.
[132] L. Jiang *et al.*, "Enhancing the Photovoltaic Performance of Perovskite Solar Cells with

a Down-Conversion Eu-Complex," *ACS Appl. Mater. Interfaces*, vol. 9, no. 32, pp. 26958–26964, Aug. 2017, doi: 10.1021/acsami.7b10101.

[133] J. Jin *et al.*, "Improving Efficiency and Light Stability of Perovskite Solar Cells by Incorporating YVO_4:Eu^{3+}, Bi^{3+} Nanophosphor into the Mesoporous TiO_2 Layer," *ACS Appl. Energy Mater.*, vol. 1, no. 5, pp. 2096–2102, May 2018, doi: 10.1021/acsaem.8b00192.

[134] Y. Zhang *et al.*, "Ultra-Broadband Directional Scattering by Colloidally Lithographed High-Index Mie Resonant Oligomers and Their Energy-Harvesting Applications," *ACS Appl. Mater. Interfaces*, vol. 10, no. 19, pp. 16776–16782, May 2018, doi: 10.1021/acsami.8b03718.

[135] H. Zhang and J. Toudert, "Optical management for efficiency enhancement in hybrid organic-inorganic lead halide perovskite solar cells," *Sci. Technol. Adv. Mater.*, vol. 19, no. 1, pp. 411–424, Dec. 2018, doi: 10.1080/14686996.2018.1458578.

[136] S.-W. Lee *et al.*, "UV Degradation and Recovery of Perovskite Solar Cells," *Sci. Rep.*, vol. 6, no. 1, p. 38150, Dec. 2016, doi: 10.1038/srep38150.

[137] S. Ito, S. Tanaka, K. Manabe, and H. Nishino, "Effects of Surface Blocking Layer of Sb 2 S 3 on Nanocrystalline TiO 2 for CH 3 NH 3 PbI 3 Perovskite Solar Cells," *J. Phys. Chem. C*, vol. 118, no. 30, pp. 16995–17000, Jul. 2014, doi: 10.1021/jp500449z.

[138] A. Farooq *et al.*, "Spectral Dependence of Degradation under Ultraviolet Light in Perovskite Solar Cells," *ACS Appl. Mater. Interfaces*, vol. 10, no. 26, pp. 21985–21990, Jul. 2018, doi: 10.1021/acsami.8b03024.

[139] T. Leijtens, G. E. Eperon, S. Pathak, A. Abate, M. M. Lee, and H. J. Snaith, "Overcoming ultraviolet light instability of sensitized TiO2with meso-superstructured organometal tri-halide perovskite solar cells," *Nat. Commun.*, vol. 4, pp. 1–8, 2013, doi: 10.1038/ncomms3885.

[140] W.-A. Quitsch *et al.*, "The Role of Excitation Energy in Photobrightening and Photodegradation of Halide Perovskite Thin Films," *J. Phys. Chem. Lett.*, vol. 9, no. 8, pp. 2062–2069, Apr. 2018, doi: 10.1021/acs.jpclett.8b00212.

[141] N. Chander *et al.*, "Reduced ultraviolet light induced degradation and enhanced light harvesting using YVO 4 :Eu 3+ down-shifting nano-phosphor layer in organometal halide perovskite solar cells," *Appl. Phys. Lett.*, vol. 105, no. 3, p. 033904, Jul. 2014, doi: 10.1063/1.4891181.

[142] E. Klampaftis, D. Ross, K. R. McIntosh, and B. S. Richards, "Enhancing the performance of solar cells via luminescent down-shifting of the incident spectrum: A review," *Sol. Energy Mater. Sol. Cells*, vol. 93, no. 8, pp. 1182–1194, Aug. 2009, doi: 10.1016/j.solmat.2009.02.020.

[143] N. Liu, H. Xue, Y. Ji, and J. Wang, "ZnSe/ZnS core-shell quantum dots incorporated with Ag nanoparticles as luminescent down-shifting layers to enhance the efficiency of Si solar cells," *J. Alloys Compd.*, vol. 747, pp. 696–702, May 2018, doi: 10.1016/j.jallcom.2018.03.060.

[144] R. Lesyuk *et al.*, "Simulation study of environmentally friendly quantum-dot-based photovoltaic windows," *J. Mater. Chem. C*, vol. 5, no. 45, pp. 11790–11797, 2017, doi: 10.1039/C7TC02945D.

[145] R. Lesyuk, V. Marinov, E. K. Hobbie, A. Elbaradei, I. Tarnavchyk, and Y. Bobitski, "Toward cadmium-free spectral down-shifting converters for photovoltaic applications," *Sol. Energy Mater. Sol. Cells*, vol. 151, pp. 52–59, Jul. 2016, doi: 10.1016/j.solmat.2016.02.021.

[146] A. J. Chatten, K. W. J. Barnham, B. F. Buxton, N. J. Ekins-Daukes, and M. A. Malik, "A new approach to modelling quantum dot concentrators," *Sol. Energy Mater. Sol. Cells*,

vol. 75, no. 3–4, pp. 363–371, Feb. 2003, doi: 10.1016/S0927-0248(02)00182-4.
[147] A. J. Chatten, K. W. J. Barnham, B. F. Buxton, N. J. Ekins-Daukes, and M. A. Malik, "Quantum dot solar concentrators," *Semiconductors*, vol. 38, no. 8, pp. 909–917, Aug. 2004, doi: 10.1134/1.1787111.
[148] B. Lipovšek *et al.*, "Optical model for simulation and optimization of luminescent down-shifting layers filled with phosphor particles for photovoltaics," *Opt. Express*, vol. 23, no. 15, p. A882, Jul. 2015, doi: 10.1364/OE.23.00A882.
[149] K. R. McIntosh *et al.*, "Increase in external quantum efficiency of encapsulated silicon solar cells from a luminescent down-shifting layer," *Prog. Photovoltaics Res. Appl.*, vol. 17, no. 3, pp. 191–197, May 2009, doi: 10.1002/pip.867.
[150] S. F. H. Correia, P. P. Lima, P. S. André, M. R. S. Ferreira, and L. A. D. Carlos, "High-efficiency luminescent solar concentrators for flexible waveguiding photovoltaics," *Sol. Energy Mater. Sol. Cells*, vol. 138, pp. 51–57, Jul. 2015, doi: 10.1016/j.solmat.2015.02.032.
[151] J. W. E. Wiegman and E. van der Kolk, "Building integrated thin film luminescent solar concentrators: Detailed efficiency characterization and light transport modelling," *Sol. Energy Mater. Sol. Cells*, vol. 103, pp. 41–47, Aug. 2012, doi: 10.1016/j.solmat.2012.04.016.
[152] J. Farinhas *et al.*, "Ultraviolet-Filtering Luminescent Transparent Coatings for High-Performance PTB7-Th:ITIC–Based Organic Solar Cells," *Front. Nanotechnol.*, vol. 0, p. 12, Apr. 2021, doi: 10.3389/FNANO.2021.635929.
[153] J. Kettle *et al.*, "Printable luminescent down shifter for enhancing efficiency and stability of organic photovoltaics," *Sol. Energy Mater. Sol. Cells*, vol. 144, pp. 481–487, Jan. 2016, doi: 10.1016/j.solmat.2015.09.037.
[154] J. Llanos, I. Brito, D. Espinoza, R. Sekar, and P. Manidurai, "A down-shifting Eu 3+ -doped Y 2 WO 6 /TiO 2 photoelectrode for improved light harvesting in dye-sensitized solar cells," *R. Soc. Open Sci.*, vol. 5, no. 2, p. 171054, Feb. 2018, doi: 10.1098/rsos.171054.
[155] G. Yin, P. Manley, and M. Schmid, "Light trapping in ultrathin CuIn 1-x Ga x Se 2 solar cells by dielectric nanoparticles," *Sol. Energy*, vol. 163, no. January, pp. 443–452, Mar. 2018, doi: 10.1016/j.solener.2018.01.096.
[156] D. G. Baranov *et al.*, "All-dielectric nanophotonics: the quest for better materials and fabrication techniques," vol. 4, no. 7, 2017, doi: 10.1364/OPTICA.4.000814.
[157] J. Bhattacharya, N. Chakravarty, S. Pattnaik, W. Dennis Slafer, R. Biswas, and V. L. Dalal, "A photonic-plasmonic structure for enhancing light absorption in thin film solar cells," *Appl. Phys. Lett.*, vol. 99, no. 13, p. 131114, Sep. 2011, doi: 10.1063/1.3641469.
[158] J. Xiao *et al.*, "Paths to light trapping in thin film GaAs solar cells," *Opt. Express*, vol. 26, no. 6, p. A341, Mar. 2018, doi: 10.1364/OE.26.00A341.
[159] Y. J. Donie *et al.*, "Light trapping in thin film silicon solar cells via phase separated disordered nanopillars," *Nanoscale*, vol. 10, no. 14, pp. 6651–6659, 2018, doi: 10.1039/C8NR00455B.
[160] O. Sanchez-Sobrado *et al.*, "Colloidal-lithographed TiO2photonic nanostructures for solar cell light trapping," *J. Mater. Chem. C*, vol. 5, no. 27, pp. 6852–6861, 2017, doi: 10.1039/c7tc01756a.
[161] J. Grandidier, M. G. Deceglie, D. M. Callahan, and H. A. Atwater, "Simulations of solar cell absorption enhancement using resonant modes of a nanosphere array," in *Physics, Simulation, and Photonic Engineering of Photovoltaic Devides*, Feb. 2012, vol. 8256, p. 825603. doi: 10.1117/12.909677.
[162] S. Haque, M. J. Mendes, O. Sanchez-Sobrad, H. Aguas, E. Fortunato, and R. Martins, "Photonic-structured TiO2 for high-efficiency, flexible and stable Perovskite solar cells".
[163] "Lumerical Inc."

[164] F. Purcell-Milton and Y. K. Gun'ko, "Quantum dots for Luminescent Solar Concentrators," *J. Mater. Chem.*, vol. 22, no. 33, p. 16687, 2012, doi: 10.1039/c2jm32366d.
[165] B. Wang, B. Li, T. Shen, M. Li, and J. Tian, "ZnSe quantum dots downshifting layer for perovskite solar cells," *J. Energy Chem.*, vol. 27, no. 3, pp. 736–741, May 2018, doi: 10.1016/j.jechem.2017.11.021.
[166] B. S. Richards and K. R. McIntosh, "Overcoming the poor short wavelength spectral response of CdS/CdTe photovoltaic modules via luminescence down-shifting: ray-tracing simulations," *Prog. Photovoltaics Res. Appl.*, vol. 15, no. 1, pp. 27–34, Jan. 2007, doi: 10.1002/pip.723.
[167] "National Energy Renewable Laboratory (NREL)."
[168] X. Hou, T. Xuan, H. Sun, X. Chen, H. Li, and L. Pan, "High-performance perovskite solar cells by incorporating a ZnGa2O4:Eu3+ nanophosphor in the mesoporous TiO2 layer," *Sol. Energy Mater. Sol. Cells*, vol. 149, pp. 121–127, May 2016, doi: 10.1016/j.solmat.2016.01.021.
[169] Y. Yang *et al.*, "Top and bottom surfaces limit carrier lifetime in lead iodide perovskite films," *Nat. Energy*, vol. 2, no. 2, p. 16207, Jan. 2017, doi: 10.1038/nenergy.2016.207.
[170] D. Yang, R. Yang, S. Priya, and S. F. Liu, "Recent Advances in Flexible Perovskite Solar Cells: Fabrication and Applications," *Angew. Chemie Int. Ed.*, vol. 58, no. 14, pp. 4466–4483, Mar. 2019, doi: 10.1002/anie.201809781.
[171] P. M. P. Salomé *et al.*, "Passivation of Interfaces in Thin Film Solar Cells: Understanding the Effects of a Nanostructured Rear Point Contact Layer," *Adv. Mater. Interfaces*, vol. 5, no. 2, p. 1701101, Jan. 2018, doi: 10.1002/admi.201701101.
[172] F. Neves *et al.*, "Investigation of single phase $Cu2ZnSnxSb1-xS4$ compounds processed by mechanochemical synthesis," *Phys. Rev. Mater.*, vol. 2, no. 7, p. 075404, Jul. 2018, doi: 10.1103/PhysRevMaterials.2.075404.
[173] M. Chapa, M. F. Alexandre, M. J. Mendes, H. Águas, E. Fortunato, and R. Martins, "All-Thin-Film Perovskite/C–Si Four-Terminal Tandems: Interlayer and Intermediate Contacts Optimization," *ACS Appl. Energy Mater.*, vol. 2, no. 6, pp. 3979–3985, Jun. 2019, doi: 10.1021/acsaem.9b00354.
[174] V. E. Ferry, M. A. Verschuuren, M. C. van Lare, R. E. I. Schropp, H. A. Atwater, and A. Polman, "Optimized Spatial Correlations for Broadband Light Trapping Nanopatterns in High Efficiency Ultrathin Film a-Si:H Solar Cells," *Nano Lett.*, vol. 11, no. 10, pp. 4239–4245, Oct. 2011, doi: 10.1021/nl202226r.
[175] "Refractive index database." https://refractiveindex.info/ (accessed Jun. 01, 2018).
[176] M. van Eerden *et al.*, "Optical Analysis of Planar Multicrystalline Perovskite Solar Cells," *Adv. Opt. Mater.*, vol. 5, no. 18, p. 1700151, Sep. 2017, doi: 10.1002/adom.201700151.
[177] Q. Jiang, X. Zhang, and J. You, "SnO_2: A Wonderful Electron Transport Layer for Perovskite Solar Cells," *Small*, vol. 14, no. 31, p. 1801154, Aug. 2018, doi: 10.1002/smll.201801154.
[178] P. Zhang *et al.*, "Perovskite Solar Cells with ZnO Electron-Transporting Materials," *Adv. Mater.*, vol. 30, no. 3, p. 1703737, Jan. 2018, doi: 10.1002/adma.201703737.
[179] A. Al Mamun *et al.*, "Effect of hot-casted NiO hole transport layer on the performance of perovskite solar cells," *Sol. Energy*, vol. 188, pp. 609–618, Aug. 2019, doi: 10.1016/J.SOLENER.2019.06.040.
[180] G.-W. Kim, D. V. Shinde, and T. Park, "Thickness of the hole transport layer in perovskite solar cells: performance versus reproducibility," *RSC Adv.*, vol. 5, no. 120, pp. 99356–99360, 2015, doi: 10.1039/C5RA18648J.
[181] D. Liu and T. L. Kelly, "Perovskite solar cells with a planar heterojunction structure

prepared using room-temperature solution processing techniques," *Nat. Photonics*, vol. 8, no. 2, pp. 133–138, Feb. 2014, doi: 10.1038/nphoton.2013.342.
[182] H.-L. Chen *et al.*, "A 19.9%-efficient ultrathin solar cell based on a 205-nm-thick GaAs absorber and a silver nanostructured back mirror," *Nat. Energy*, vol. 4, no. 9, pp. 761–767, Sep. 2019, doi: 10.1038/s41560-019-0434-y.
[183] P. Spinelli, M. A. Verschuuren, and A. Polman, "Broadband omnidirectional antireflection coating based on subwavelength surface Mie resonators," *Nat. Commun.*, vol. 3, no. 1, p. 692, Jan. 2012, doi: 10.1038/ncomms1691.
[184] W. Qarony, M. I. Hossain, A. Salleo, D. Knipp, and Y. H. Tsang, "Rough versus planar interfaces: How to maximize the short circuit current of perovskite single and tandem solar cells," *Mater. Today Energy*, vol. 11, pp. 106–113, Mar. 2019, doi: 10.1016/J.MTENER.2018.10.001.
[185] S. A. Lukas Kegelmann, Philipp Tockhorn, Max Grischek, José A. Márquez, Thomas Unold, Wilfried Lövenich, Dieter Neher, "SpiDOT: mixtures of undoped Spiro-OMeTAD and PEDOT to reduce charge recombination and absorption losses in monolithic perovskite/silicon tandem solar cells." [Online]. Available: https://www.nanoge.org/proceedings/HOPV19/5c530c600044c8385969dadb
[186] J. Y. Kim, J.-W. Lee, H. S. Jung, H. Shin, and N.-G. Park, "High-Efficiency Perovskite Solar Cells," *Chem. Rev.*, vol. 120, no. 15, pp. 7867–7918, Aug. 2020, doi: 10.1021/ACS.CHEMREV.0C00107.
[187] G. Yang *et al.*, "Stable and low-photovoltage-loss perovskite solar cells by multifunctional passivation," *Nat. Photonics 2021 159*, vol. 15, no. 9, pp. 681–689, Jul. 2021, doi: 10.1038/s41566-021-00829-4.
[188] T. Kirchartz, "Photon Management in Perovskite Solar Cells," *J. Phys. Chem. Lett.*, vol. 10, no. 19, pp. 5892–5896, Oct. 2019, doi: 10.1021/ACS.JPCLETT.9B02053.
[189] J. Diekmann *et al.*, "Pathways toward 30% Efficient Single-Junction Perovskite Solar Cells and the Role of Mobile Ions," *Sol. RRL*, vol. 5, no. 8, p. 2100219, Aug. 2021, doi: 10.1002/solr.202100219.
[190] K. Li *et al.*, "Light trapping in solar cells: simple design rules to maximize absorption," *Opt. Vol. 7, Issue 10, pp. 1377-1384*, vol. 7, no. 10, pp. 1377–1384, Oct. 2020, doi: 10.1364/OPTICA.394885.
[191] A. S. R. Chesman *et al.*, "Solution-processed antireflective coating for back-contact perovskite solar cells," *Opt. Express, Vol. 28, Issue 9, pp. 12650-12660*, vol. 28, no. 9, pp. 12650–12660, Apr. 2020, doi: 10.1364/OE.384039.
[192] H. Kwak *et al.*, "Light absorption enhancement in ultrathin perovskite solar cells using light scattering of high-index dielectric nanospheres," *Opt. Express, Vol. 29, Issue 22, pp. 35366-35376*, vol. 29, no. 22, pp. 35366–35376, Oct. 2021, doi: 10.1364/OE.440989.
[193] K. Deng, Z. Liu, M. Wang, and L. Li, "Nanoimprinted Grating-Embedded Perovskite Solar Cells with Improved Light Management," *Adv. Funct. Mater.*, vol. 29, no. 19, May 2019, doi: 10.1002/ADFM.201900830.
[194] N. R. Thangavel *et al.*, "Disordered Polymer Antireflective Coating for Improved Perovskite Photovoltaics," *ACS Photonics*, vol. 7, no. 8, pp. 1971–1977, Aug. 2020, doi: 10.1021/ACSPHOTONICS.0C00805.
[195] W. R. Erwin, H. F. Zarick, E. M. Talbert, and Rizia Bardhan, "Light trapping in mesoporous solar cells with plasmonic nanostructures," *Energy Environ. Sci.*, vol. 9, no. 5, pp. 1577–1601, May 2016, doi: 10.1039/C5EE03847B.
[196] S. Rahmany and L. Etgar, "Semitransparent Perovskite Solar Cells," *ACS Energy Lett.*, vol. 5, no. 5, pp. 1519–1531, May 2020, doi: 10.1021/ACSENERGYLETT.0C00417.
[197] M. Shahiduzzaman *et al.*, "Spray Pyrolyzed TiO 2 Embedded Multi-Layer Front Contact

Design for High-Efficiency Perovskite Solar Cells," 123AD, doi: 10.1007/s40820-020-00559-2.
[198] E. L. Warren *et al.*, "A Taxonomy for Three-Terminal Tandem Solar Cells," *ACS Energy Lett.*, vol. 5, no. 4, pp. 1233–1242, Apr. 2020, doi: 10.1021/ACSENERGYLETT.0C00068/SUPPL_FILE/NZ0C00068_SI_001.PDF.
[199] T. C. J. Yang, P. Fiala, Q. Jeangros, and C. Ballif, "High-Bandgap Perovskite Materials for Multijunction Solar Cells," *Joule*, vol. 2, no. 8, pp. 1421–1436, Aug. 2018, doi: 10.1016/J.JOULE.2018.05.008.
[200] "Nanophotonic FDTD Simulation Software - Lumerical FDTD." https://www.lumerical.com/products/fdtd/ (accessed Jan. 12, 2022).
[201] "tiberCAD | DEVELOPER COMMUNITY." http://www.tibercad.org/ (accessed Jan. 12, 2022).
[202] "CHARGE solver introduction – Lumerical Support." https://support.lumerical.com/hc/en-us/articles/360034917693-CHARGE-solver-introduction (accessed Jan. 12, 2022).
[203] "Sentaurus Device - Technology Computer Aided Design (TCAD) | Synopsys." https://www.synopsys.com/silicon/tcad/device-simulation/sentaurus-device.html (accessed Jan. 12, 2022).
[204] R. He *et al.*, "Scalable Preparation of High-Performance ZnO–SnO2 Cascaded Electron Transport Layer for Efficient Perovskite Solar Modules," *Sol. RRL*, p. 2100639, 2021, doi: 10.1002/SOLR.202100639.
[205] R. Li *et al.*, "NiOx/Spiro Hole Transport Bilayers for Stable Perovskite Solar Cells with Efficiency Exceeding 21%," *ACS Energy Lett.*, vol. 5, no. 1, pp. 79–86, Jan. 2020, doi: 10.1021/ACSENERGYLETT.9B02112/SUPPL_FILE/NZ9B02112_SI_001.PDF.
[206] Z. Chen, W. Li, R. Li, Y. Zhang, G. Xu, and H. Cheng, "Fabrication of highly transparent and conductive indium-tin oxide thin films with a high figure of merit via solution processing," *Langmuir*, vol. 29, no. 45, pp. 13836–13842, Nov. 2013, doi: 10.1021/LA4033282/SUPPL_FILE/LA4033282_SI_001.PDF.
[207] S. Pang *et al.*, "Efficient NiO x Hole Transporting Layer Obtained by the Oxidation of Metal Nickel Film for Perovskite Solar Cells," *ACS Appl. Energy Mater.*, vol. 2, no. 7, pp. 4700–4707, Jul. 2019, doi: 10.1021/ACSAEM.9B00169/SUPPL_FILE/AE9B00169_SI_001.PDF.
[208] J. Piprek, "HANDBOOK OF OPTOELECTRONIC DEVICE MODELING AND SIMULATION : lasers.," *CRC Press*, 2021, doi: 10.4324/9781315152318.
[209] P. K. Patel, "Device simulation of highly efficient eco-friendly CH3NH3SnI3 perovskite solar cell," *Sci. Reports 2021 111*, vol. 11, no. 1, pp. 1–11, Feb. 2021, doi: 10.1038/s41598-021-82817-w.
[210] P. Liu *et al.*, "Fundamental Understanding of Photocurrent Hysteresis in Perovskite Solar Cells," *Adv. Energy Mater.*, vol. 9, no. 13, p. 1803017, Apr. 2019, doi: 10.1002/AENM.201803017.
[211] G. Létay, M. Hermle, and A. W. Bett, "Simulating single-junction GaAs solar cells including photon recycling," *Prog. Photovoltaics Res. Appl.*, vol. 14, no. 8, pp. 683–696, Dec. 2006, doi: 10.1002/PIP.699.
[212] T. M. Burke *et al.*, "Beyond Langevin Recombination: How Equilibrium Between Free Carriers and Charge Transfer States Determines the Open-Circuit Voltage of Organic Solar Cells," *Adv. Energy Mater.*, vol. 5, no. 11, p. 1500123, Jun. 2015, doi: 10.1002/AENM.201500123.
[213] L. Huang *et al.*, "Improvement on performance of hybrid CH3NH3PbI3−xClx perovskite solar cells induced sequential deposition by low pressure assisted solution

processing," *Sol. Energy*, vol. 199, pp. 826–831, Mar. 2020, doi: 10.1016/J.SOLENER.2020.02.080.

[214] W. Budiawan *et al.*, "Asymmetric Benzotrithiophene-based hole transporting materials provide high-efficiency perovskite solar cells," *ACS Appl. Mater. Interfaces*, vol. 12, no. 26, pp. 29143–29152, 2020, doi: 10.1021/ACSAMI.0C02204/SUPPL_FILE/AM0C02204_SI_001.PDF.

[215] C. Geffroy *et al.*, "p-Doping of a Hole Transport Material via a Poly(ionic liquid) for over 20% Efficiency and Hysteresis-Free Perovskite Solar Cells," *ACS Appl. Energy Mater.*, vol. 3, no. 2, pp. 1393–1401, Feb. 2020, doi: 10.1021/ACSAEM.9B01819/SUPPL_FILE/AE9B01819_SI_001.PDF.

[216] T. Kirchartz, L. Krückemeier, and E. L. Unger, "Research Update: Recombination and open-circuit voltage in lead-halide perovskites," *APL Mater.*, vol. 6, no. 10, p. 100702, Oct. 2018, doi: 10.1063/1.5052164.

[217] T. W. Crothers *et al.*, "Photon Reabsorption Masks Intrinsic Bimolecular Charge-Carrier Recombination in CH3NH3PbI3 Perovskite," *Nano Lett.*, vol. 17, no. 9, pp. 5782–5789, Sep. 2017, doi: 10.1021/ACS.NANOLETT.7B02834/SUPPL_FILE/NL7B02834_SI_001.PDF.

[218] M. A. Green, E. D. Dunlop, J. Hohl-Ebinger, M. Yoshita, N. Kopidakis, and A. W. Y. Ho-Baillie, "Solar cell efficiency tables (Version 55)," *Prog. Photovoltaics Res. Appl.*, vol. 28, no. 1, pp. 3–15, Jan. 2020, doi: 10.1002/PIP.3228.

[219] L. Bertoluzzi *et al.*, "Mobile Ion Concentration Measurement and Open-Access Band Diagram Simulation Platform for Halide Perovskite Solar Cells," *Joule*, vol. 4, no. 1, pp. 109–127, Jan. 2020, doi: 10.1016/J.JOULE.2019.10.003.

[220] D. Walter *et al.*, "Transient photovoltage in perovskite solar cells: Interaction of trap-mediated recombination and migration of multiple ionic species," *J. Phys. Chem. C*, vol. 122, no. 21, pp. 11270–11281, May 2018, doi: 10.1021/ACS.JPCC.8B02529/SUPPL_FILE/JP8B02529_SI_001.PDF.

[221] M. Stolterfoht *et al.*, "The impact of energy alignment and interfacial recombination on the internal and external open-circuit voltage of perovskite solar cells," *Energy Environ. Sci.*, vol. 12, no. 9, pp. 2778–2788, Sep. 2019, doi: 10.1039/C9EE02020A.

[222] E. R. Martins, J. Li, Y. Liu, J. Zhou, and T. F. Krauss, "Engineering gratings for light trapping in photovoltaics: The supercell concept," *Phys. Rev. B - Condens. Matter Mater. Phys.*, vol. 86, no. 4, p. 041404, Jul. 2012, doi: 10.1103/PHYSREVB.86.041404/FIGURES/5/MEDIUM.

[223] S. Schauer *et al.*, "Disordered diffraction gratings tailored by shape-memory based wrinkling and their application to photovoltaics," *Opt. Mater. Express, Vol. 8, Issue 1, pp. 184-198*, vol. 8, no. 1, pp. 184–198, Jan. 2018, doi: 10.1364/OME.8.000184.

[224] R. Dewan, S. Shrestha, V. Jovanov, J. Hüpkes, K. Bittkau, and D. Knipp, "Random versus periodic: Determining light trapping of randomly textured thin film solar cells by the superposition of periodic surface textures," *Sol. Energy Mater. Sol. Cells*, vol. 143, pp. 183–189, Dec. 2015, doi: 10.1016/J.SOLMAT.2015.06.014.

[225] P. Kozma *et al.*, "Grating coupled interferometry for optical sensing," *Appl. Phys. B 2009 971*, vol. 97, no. 1, pp. 5–8, Aug. 2009, doi: 10.1007/S00340-009-3719-1.

[226] C. F. R. Mateus, M. C. Y. Huang, L. Chen, C. J. Chang-Hasnain, and Y. Suzuki, "Broad-band mirror (1.12-1.62 μm) using a subwavelength grating," *IEEE Photonics Technol. Lett.*, vol. 16, no. 7, pp. 1676–1678, Jul. 2004, doi: 10.1109/LPT.2004.828514.

[227] A. Hervé, J. Drévillon, Y. Ezzahri, and K. Joulain, "Radiative cooling by tailoring surfaces with microstructures: Association of a grating and a multi-layer structure," *J. Quant. Spectrosc. Radiat. Transf.*, vol. 221, pp. 155–163, Dec. 2018, doi:

10.1016/J.JQSRT.2018.09.015.
[228] A. Bozzola, C. S. Schuster, L. C. Andreani, and T. F. Krauss, "How to assess light trapping structures versus a Lambertian Scatterer for solar cells?," *Opt. Express, Vol. 22, Issue S2, pp. A542-A551*, vol. 22, no. 102, pp. A542–A551, Mar. 2014, doi: 10.1364/OE.22.00A542.
[229] S. Morawiec *et al.*, "Experimental quantification of useful and parasitic absorption of light in plasmon-enhanced thin silicon films for solar cells application," *Sci. Reports 2016 61*, vol. 6, no. 1, pp. 1–10, Mar. 2016, doi: 10.1038/srep22481.
[230] A. Araújo *et al.*, "Ultra-fast plasmonic back reflectors production for light trapping in thin Si solar cells," *Sol. Energy*, vol. 174, pp. 786–792, Nov. 2018, doi: 10.1016/J.SOLENER.2018.08.068.
[231] R. A. Gouvêa, M. L. Moreira, and J. A. Souza, "Evolutionary design algorithm for optimal light trapping in solar cells," *J. Appl. Phys.*, vol. 125, no. 4, p. 043105, Jan. 2019, doi: 10.1063/1.5078745.
[232] W. Barthlott, M. Mail, B. Bhushan, and K. Koch, "Plant Surfaces: Structures and Functions for Biomimetic Innovations," *Nano-Micro Lett. 2016 92*, vol. 9, no. 2, pp. 1–40, Jan. 2017, doi: 10.1007/S40820-016-0125-1.
[233] P. Ball, "Life's lessons in design," *Nat. 2001 4096818*, vol. 409, no. 6818, pp. 413–416, Jan. 2001, doi: 10.1038/35053198.
[234] B. Bhushan, "Biomimetics: lessons from naturean overview," *Philos. Trans. R. Soc. A Math. Phys. Eng. Sci.*, vol. 367, no. 1893, pp. 1445–1486, Apr. 2009, doi: 10.1098/RSTA.2009.0011.
[235] Z. Han *et al.*, "Biomimetic multifunctional surfaces inspired from animals," *Adv. Colloid Interface Sci.*, vol. 234, pp. 27–50, Aug. 2016, doi: 10.1016/J.CIS.2016.03.004.
[236] Z. Huang, S. Yang, H. Zhang, M. Zhang, and W. Cao, "Replication of Leaf Surface Structures for Light Harvesting," *Sci. Reports 2015 51*, vol. 5, no. 1, pp. 1–10, Sep. 2015, doi: 10.1038/srep14281.
[237] Z. Huang, T. Shi, H. Zhang, M. Zhang, M. Huttula, and W. Cao, "A computational study of antireflection structures bio-mimicked from leaf surface morphologies," *Sol. Energy*, vol. 131, pp. 131–137, Jun. 2016, doi: 10.1016/J.SOLENER.2016.02.041.
[238] R. H. Siddique, G. Gomard, and H. Hölscher, "The role of random nanostructures for the omnidirectional anti-reflection properties of the glasswing butterfly," *Nat. Commun. 2015 61*, vol. 6, no. 1, pp. 1–8, Apr. 2015, doi: 10.1038/ncomms7909.
[239] Z. W. Han *et al.*, "Antireflective surface inspired from biology: A review," *Biosurface and Biotribology*, vol. 2, no. 4, pp. 137–150, Dec. 2016, doi: 10.1016/J.BSBT.2016.11.002.
[240] J. Sun *et al.*, "Biomimetic Moth-eye Nanofabrication: Enhanced Antireflection with Superior Self-cleaning Characteristic," *Sci. Reports 2018 81*, vol. 8, no. 1, pp. 1–10, Apr. 2018, doi: 10.1038/s41598-018-23771-y.
[241] R. Hünig *et al.*, "Flower Power: Exploiting Plants' Epidermal Structures for Enhanced Light Harvesting in Thin-Film Solar Cells," *Adv. Opt. Mater.*, vol. 4, no. 10, pp. 1487–1493, Oct. 2016, doi: 10.1002/ADOM.201600046.
[242] K. Li, R. Wu, Y. Ruan, L. Zhang, and H. Zhen, "Numerical analysis of the angular insensitive photovoltaic light harvesting with the biomimetic scattering film inspired by the rose petal epidermal topography," *Sol. Energy*, vol. 170, pp. 800–806, Aug. 2018, doi: 10.1016/J.SOLENER.2018.05.098.
[243] Z. Han, S. Niu, C. Shang, Z. Liu, and L. Ren, "Light trapping structures in wing scales of butterfly Trogonoptera brookiana," *Nanoscale*, vol. 4, no. 9, pp. 2879–2883, Apr. 2012, doi: 10.1039/C2NR12059C.
[244] Z. Han *et al.*, "A High-Transmission, Multiple Antireflective Surface Inspired from

Bilayer 3D Ultrafine Hierarchical Structures in Butterfly Wing Scales," *Small*, vol. 12, no. 6, pp. 713–720, Feb. 2016, doi: 10.1002/SMLL.201502454.
[245] R. H. Siddique *et al.*, "Bioinspired phase-separated disordered nanostructures for thin photovoltaic absorbers," *Sci. Adv.*, vol. 3, no. 10, Oct. 2017, doi: 10.1126/SCIADV.1700232/SUPPL_FILE/1700232_SM.PDF.
[246] J. Gjessing, A. S. Sudbø, and E. S. Marstein, "Comparison of periodic light-trapping structures in thin crystalline silicon solar cells," *J. Appl. Phys.*, vol. 110, no. 3, p. 033104, Aug. 2011, doi: 10.1063/1.3611425.
[247] S. E. Han and G. Chen, "Toward the lambertian limit of light trapping in thin nanostructured silicon solar cells," *Nano Lett.*, vol. 10, no. 11, pp. 4692–4696, Nov. 2010, doi: 10.1021/NL1029804/SUPPL_FILE/NL1029804_SI_001.PDF.
[248] C. Battaglia *et al.*, "Light trapping in solar cells: Can periodic beat random?," *ACS Nano*, vol. 6, no. 3, pp. 2790–2797, Mar. 2012, doi: 10.1021/NN300287J/ASSET/IMAGES/NN300287J.SOCIAL.JPEG_V03.
[249] W. K. Lee *et al.*, "Concurrent design of quasi-random photonic nanostructures," *Proc. Natl. Acad. Sci. U. S. A.*, vol. 114, no. 33, pp. 8734–8739, Aug. 2017, doi: 10.1073/PNAS.1704711114/SUPPL_FILE/PNAS.1704711114.SAPP.PDF.
[250] X. Zhang, Y. Cai, and Y. Mi, "Anisotropic wetting on checkerboard-patterned surfaces," *Langmuir*, vol. 27, no. 15, pp. 9630–9637, Aug. 2011, doi: 10.1021/LA200342W/ASSET/IMAGES/LA200342W.SOCIAL.JPEG_V03.
[251] Z. Yu, A. Raman, and S. Fan, "Fundamental limit of nanophotonic light trapping in solar cells," *Proc. Natl. Acad. Sci. U. S. A.*, vol. 107, no. 41, pp. 17491–17496, Oct. 2010, doi: 10.1073/PNAS.1008296107/SUPPL_FILE/PNAS.1008296107_SI.PDF.
[252] P. Wang and I. M. Peters, "Impact of structure symmetry on light trapping properties of periodic nanostructures: A systematic discussion and quantification," *J. Appl. Phys.*, vol. 119, no. 8, p. 083101, Feb. 2016, doi: 10.1063/1.4942167.
[253] X. Guo, D. Wang, B. Liu, Y. Zhou, and S. Li, "Quick design of high efficiency light trapping nanostructures for thin film silicon solar cells," *Opt. Commun.*, vol. 395, pp. 122–126, Jul. 2017, doi: 10.1016/J.OPTCOM.2016.08.076.
[254] "The Nobel Prize in Chemistry 2011 - Press release." https://www.nobelprize.org/prizes/chemistry/2011/press-release/ (accessed Apr. 11, 2022).
[255] G. Shalev, S. W. Schmitt, H. Embrechts, G. Brönstrup, and S. Christiansen, "Enhanced photovoltaics inspired by the fovea centralis," *Sci. Reports 2015 51*, vol. 5, no. 1, pp. 1–7, Feb. 2015, doi: 10.1038/srep08570.
[256] B. Liu, D. Wang, S. Li, X. Guo, and X. Sheng, "Enhanced light absorption in thin film silicon solar cells with Fourier-series based periodic nanostructures," *Opt. Express, Vol. 24, Issue 2, pp. A408-A413*, vol. 24, no. 2, pp. A408–A413, Jan. 2016, doi: 10.1364/OE.24.00A408.
[257] A. Bozzola, L. C. Andreani, and M. Liscidini, "Photonic light-trapping versus Lambertian limits in thin film silicon solar cells with 1D and 2D periodic patterns," *Opt. Express, Vol. 20, Issue S2, pp. A224-A244*, vol. 20, no. 102, pp. A224–A244, Mar. 2012, doi: 10.1364/OE.20.00A224.
[258] J. Hou *et al.*, "Biomimetic spiral grating for stable and highly efficient absorption in crystalline silicon thin-film solar cells," *Opt. Express, Vol. 25, Issue 20, pp. A922-A931*, vol. 25, no. 20, pp. A922–A931, Oct. 2017, doi: 10.1364/OE.25.00A922.
[259] S. Das *et al.*, "A leaf-inspired photon management scheme using optically tuned bilayer nanoparticles for ultra-thin and highly efficient photovoltaic devices," *Nano Energy*, vol. 58, pp. 47–56, Apr. 2019, doi: 10.1016/J.NANOEN.2018.12.072.

[260] Y. Da *et al.*, "Role of surface recombination in affecting the efficiency of nanostructured thin-film solar cells," *Opt. Express, Vol. 21, Issue S6, pp. A1065-A1077*, vol. 21, no. 106, pp. A1065–A1077, Nov. 2013, doi: 10.1364/OE.21.0A1065.

[261] A. Y. Meshalkin, V. V. Podlipnov, A. V. Ustinov, and E. A. Achimova, "Analysis of diffraction efficiency of phase gratings in dependence of duty cycle and depth," *J. Phys. Conf. Ser.*, vol. 1368, no. 2, p. 022047, Nov. 2019, doi: 10.1088/1742-6596/1368/2/022047.

[262] K. Li *et al.*, "High speed e-beam writing for large area photonic nanostructures — a choice of parameters," *Sci. Reports 2016 61*, vol. 6, no. 1, pp. 1–10, Sep. 2016, doi: 10.1038/srep32945.

[263] M. Esashi, A. Kojima, N. Ikegami, H. Miyaguchi, and N. Koshida, "Development of massively parallel electron beam direct write lithography using active-matrix nanocrystalline-silicon electron emitter arrays," *Microsystems Nanoeng. 2015 11*, vol. 1, no. 1, pp. 1–8, Nov. 2015, doi: 10.1038/micronano.2015.29.

[264] R. Seki *et al.*, "Template development for sub15nm nanoimprint lithography," *https://doi.org/10.1117/12.2567043*, vol. 11178, pp. 212–218, Jan. 2020, doi: 10.1117/12.2567043.

[265] L. Wang, F. Clube, C. Dais, H. H. Solak, and J. Gobrecht, "Sub-wavelength printing in the deep ultra-violet region using Displacement Talbot Lithography," *Microelectron. Eng.*, vol. 161, pp. 104–108, Aug. 2016, doi: 10.1016/J.MEE.2016.04.017.

[266] C. Dais, F. Clube, L. Wang, and H. H. Solak, "High rotational symmetry photonic structures fabricated with multiple exposure Displacement Talbot Lithography," *Microelectron. Eng.*, vol. 177, pp. 9–12, Jun. 2017, doi: 10.1016/J.MEE.2017.01.021.

[267] E. Le Boulbar, P. A. Shields, P. Chausse, and P.-M. Coulon, "“Double” displacement Talbot lithography: fast, wafer-scale, direct-writing of complex periodic nanopatterns," *Opt. Express, Vol. 27, Issue 22, pp. 32037-32046*, vol. 27, no. 22, pp. 32037–32046, Oct. 2019, doi: 10.1364/OE.27.032037.

[268] J. F. Wang *et al.*, "Surface engineering of perovskite films for efficient solar cells," *Sci. Reports 2017 71*, vol. 7, no. 1, pp. 1–9, Nov. 2017, doi: 10.1038/s41598-017-14920-w.

[269] D. Wang, M. Wright, N. K. Elumalai, and A. Uddin, "Stability of perovskite solar cells," *Sol. Energy Mater. Sol. Cells*, vol. 147, pp. 255–275, Apr. 2016, doi: 10.1016/J.SOLMAT.2015.12.025.

[270] T. Chen, J. Xie, and P. Gao, "Ultraviolet Photocatalytic Degradation of Perovskite Solar Cells: Progress, Challenges, and Strategies," *Adv. Energy Sustain. Res.*, p. 2100218, Feb. 2022, doi: 10.1002/AESR.202100218.

[271] S. K. Pathak *et al.*, "Performance and Stability Enhancement of Dye-Sensitized and Perovskite Solar Cells by Al Doping of TiO2," *Adv. Funct. Mater.*, vol. 24, no. 38, pp. 6046–6055, Oct. 2014, doi: 10.1002/ADFM.201401658.

[272] R. A. S. Ferreira, S. F. H. Correia, A. Monguzzi, X. Liu, and F. Meinardi, "Spectral converters for photovoltaics – What's ahead," *Mater. Today*, vol. 33, pp. 105–121, Mar. 2020, doi: 10.1016/J.MATTOD.2019.10.002.

[273] K. Kawano, K. Arai, H. Yamada, N. Hashimoto, and R. Nakata, "Application of rare-earth complexes for photovoltaic precursors," *Sol. Energy Mater. Sol. Cells*, vol. 48, no. 1–4, pp. 35–41, 1997, doi: 10.1016/S0927-0248(97)00066-4.

[274] S. Marchionna *et al.*, "Photovoltaic quantum efficiency enhancement by light harvesting of organo-lanthanide complexes," *J. Lumin.*, vol. 118, no. 2, pp. 325–329, Jun. 2006, doi: 10.1016/J.JLUMIN.2005.09.010.

[275] A. Le Donne, M. Acciarri, D. Narducci, S. Marchionna, and S. Binetti, "Encapsulating Eu3+ complex doped layers to improve Si-based solar cell efficiency," *Prog. Photovoltaics Res. Appl.*, vol. 17, no. 8, pp. 519–525, Dec. 2009, doi: 10.1002/PIP.902.

[276] K. Kawano, B. C. Hong, K. Sakamoto, T. Tsuboi, and H. J. Seo, "Improvement of the conversion efficiency of solar cell by rare earth ion," *Opt. Mater. (Amst).*, vol. 31, no. 9, pp. 1353–1356, Jul. 2009, doi: 10.1016/J.OPTMAT.2008.10.012.
[277] Z. Cheng, F. Su, L. Pan, M. Cao, and Z. Sun, "CdS quantum dot-embedded silica film as luminescent down-shifting layer for crystalline Si solar cells," *J. Alloys Compd.*, vol. 494, no. 1–2, pp. L7–L10, Apr. 2010, doi: 10.1016/J.JALLCOM.2010.01.047.
[278] Q. Li *et al.*, "Enhancing photovoltaic performance of dye-sensitized solar cell by rare-earth doped oxide of Lu2O3:(Tm3+, Yb3+)," *Electrochim. Acta*, vol. 56, no. 14, pp. 4980–4984, May 2011, doi: 10.1016/J.ELECTACTA.2011.03.125.
[279] E. Klampaftis and B. S. Richards, "Improvement in multi-crystalline silicon solar cell efficiency via addition of luminescent material to EVA encapsulation layer," *Prog. Photovoltaics Res. Appl.*, vol. 19, no. 3, pp. 345–351, May 2011, doi: 10.1002/PIP.1019.
[280] L. Danos, T. Parel, T. Markvart, V. Barrioz, W. S. M. Brooks, and S. J. C. Irvine, "Increased efficiencies on CdTe solar cells via luminescence down-shifting with excitation energy transfer between dyes," *Sol. Energy Mater. Sol. Cells*, vol. 98, pp. 486–490, Mar. 2012, doi: 10.1016/J.SOLMAT.2011.11.009.
[281] X. Sheng *et al.*, "Enhanced ultraviolet responses in thin-film InGaP solar cells by down-shifting," *Phys. Chem. Chem. Phys.*, vol. 15, no. 47, pp. 20434–20437, Nov. 2013, doi: 10.1039/C3CP54096K.
[282] S. D. Hodgson, W. S. M. Brooks, A. J. Clayton, G. Kartopu, V. Barrioz, and S. J. C. Irvine, "Enhancing blue photoresponse in CdTe photovoltaics by luminescent down-shifting using semiconductor quantum dot/PMMA films," *Nano Energy*, vol. 2, no. 1, pp. 21–27, Jan. 2013, doi: 10.1016/J.NANOEN.2012.07.006.
[283] C. K. Huang, Y. C. Chen, W. B. Hung, T. M. Chen, K. W. Sun, and W. L. Chang, "Enhanced light harvesting of Si solar cells via luminescent down-shifting using YVO4:Bi3+, Eu3+ nanophosphors," *Prog. Photovoltaics Res. Appl.*, vol. 21, no. 7, pp. 1507–1513, Nov. 2013, doi: 10.1002/PIP.2222.
[284] J. Liu, K. Wang, W. Zheng, W. Huang, C. H. Li, and X. Z. You, "Improving spectral response of monocrystalline silicon photovoltaic modules using high efficient luminescent down-shifting Eu3+ complexes," *Prog. Photovoltaics Res. Appl.*, vol. 21, no. 4, pp. 668–675, Jun. 2013, doi: 10.1002/PIP.1251.
[285] J.-Y. Chen, C. K. Huang, W. B. Hung, K. W. Sun, and T. M. Chen, "Efficiency improvement of Si solar cells using metal-enhanced nanophosphor fluorescence," 2013, doi: 10.1016/j.solmat.2013.08.039.
[286] A. Apostoluk *et al.*, "Improvement of the solar cell efficiency by the ZnO nanoparticle layer via the down-shifting effect," *Microelectron. Eng.*, vol. 127, pp. 51–56, Sep. 2014, doi: 10.1016/J.MEE.2014.04.025.
[287] S. W. Baek *et al.*, "Effect of core quantum-dot size on power-conversion-efficiency for silicon solar-cells implementing energy-down-shift using CdSe/ZnS core/shell quantum dots," *Nanoscale*, vol. 6, no. 21, pp. 12524–12531, Oct. 2014, doi: 10.1039/C4NR02472A.
[288] G. Griffini *et al.*, "Multifunctional Luminescent Down-Shifting Fluoropolymer Coatings: A Straightforward Strategy to Improve the UV-Light Harvesting Ability and Long-Term Outdoor Stability of Organic Dye-Sensitized Solar Cells," *Adv. Energy Mater.*, vol. 5, no. 3, p. 1401312, Feb. 2015, doi: 10.1002/AENM.201401312.
[289] G. Shao, C. Lou, and D. Xiao, "Enhancing the efficiency of solar cells by down shifting YAG: Ce3+ phosphors," *J. Lumin.*, vol. 157, pp. 344–348, Jan. 2015, doi: 10.1016/J.JLUMIN.2014.08.064.
[290] S. F. H. Correia, A. R. N. Bastos, L. Fu, L. D. Carlos, P. S. André, and R. A. S. Ferreira,

"Lanthanide-based downshifting layers tested in a solar car race," *Opto-Electron Adv*, vol. 2, no. 6, p. 190006, 2019, doi: 10.29026/oea.2019.190006.

[291] J. Farinhas *et al.*, "Ultraviolet-Filtering Luminescent Transparent Coatings for High-Performance PTB7-Th:ITIC–Based Organic Solar Cells," *Front. Nanotechnol.*, vol. 3, Apr. 2021, doi: 10.3389/FNANO.2021.635929/.

[292] J. C. G. Bünzli and C. Piguet, "Taking advantage of luminescent lanthanide ions," *Chem. Soc. Rev.*, vol. 34, no. 12, pp. 1048–1077, Nov. 2005, doi: 10.1039/B406082M.

[293] E. Klampaftis, D. Ross, K. R. McIntosh, and B. S. Richards, "Enhancing the performance of solar cells via luminescent down-shifting of the incident spectrum: A review," *Sol. Energy Mater. Sol. Cells*, vol. 93, no. 8, pp. 1182–1194, Aug. 2009, doi: 10.1016/J.SOLMAT.2009.02.020.

[294] J. F. C. B. Ramalho, A. N. Carneiro Neto, L. D. Carlos, P. S. André, and R. A. S. Ferreira, "Lanthanides for the new generation of optical sensing and Internet of Things," *Handb. Phys. Chem. Rare Earths*, Feb. 2022, doi: 10.1016/BS.HPCRE.2021.12.001.

[295] B. M. Van Der Ende, L. Aarts, and A. Meijerink, "Lanthanide ions as spectral converters for solar cells," *Phys. Chem. Chem. Phys.*, vol. 11, no. 47, pp. 11081–11095, Nov. 2009, doi: 10.1039/B913877C.

[296] X. Huang, S. Han, W. Huang, and X. Liu, "Enhancing solar cell efficiency: the search for luminescent materials as spectral converters," *Chem. Soc. Rev.*, vol. 42, no. 1, pp. 173–201, Dec. 2012, doi: 10.1039/C2CS35288E.

[297] T. Heumueller *et al.*, "Reducing burn-in voltage loss in polymer solar cells by increasing the polymer crystallinity," *Energy Environ. Sci.*, vol. 7, no. 9, pp. 2974–2980, Aug. 2014, doi: 10.1039/C4EE01842G.

[298] W. Chen *et al.*, "Effects of down-conversion CeO2:Eu3+ nanophosphors in perovskite solar cells," *J. Mater. Sci. Mater. Electron.*, vol. 28, no. 15, pp. 11346–11357, Aug. 2017, doi: 10.1007/S10854-017-6928-0/FIGURES/10.

[299] C. W. Kim *et al.*, "Dual-Function Au@Y2O3:Eu3+ Smart Film for Enhanced Power Conversion Efficiency and Long-Term Stability of Perovskite Solar Cells," *Sci. Reports 2017 71*, vol. 7, no. 1, pp. 1–9, Jul. 2017, doi: 10.1038/s41598-017-07218-4.

[300] N. U. Rahman *et al.*, "A promising europium-based down conversion material: organic–inorganic perovskite solar cells with high photovoltaic performance and UV-light stability," *J. Mater. Chem. A*, vol. 7, no. 11, pp. 6467–6474, Mar. 2019, doi: 10.1039/C9TA00551J.

[301] M. A. Verschuuren, M. Megens, Y. Ni, H. Van Sprang, and A. Polman, "Large area nanoimprint by substrate conformal imprint lithography (SCIL)," *Adv. Opt. Technol.*, vol. 6, no. 3–4, pp. 243–264, Jun. 2017, doi: 10.1515/AOT-2017-0022/MACHINEREADABLECITATION/RIS.

[302] J. F. C. B. Ramalho *et al.*, "Super modules-based active QR codes for smart trackability and IoT: a responsive-banknotes case study," *npj Flex. Electron. 2020 41*, vol. 4, no. 1, pp. 1–9, Jun. 2020, doi: 10.1038/s41528-020-0073-1.

[303] I. Meazzini *et al.*, "Ureasil organic-inorganic hybrids as photoactive waveguides for conjugated polyelectrolyte luminescent solar concentrators," *Mater. Chem. Front.*, vol. 1, no. 11, pp. 2271–2282, Nov. 2017, doi: 10.1039/C7QM00264E.

[304] J. Farinhas *et al.*, "Ultraviolet-Filtering Luminescent Transparent Coatings for High-Performance PTB7-Th:ITIC–Based Organic Solar Cells," *Front. Nanotechnol.*, vol. 3, p. 12, Apr. 2021, doi: 10.3389/FNANO.2021.635929/BIBTEX.

[305] J. Jiang *et al.*, "Carrier lifetime enhancement in halide perovskite via remote epitaxy," *Nat. Commun. 2019 101*, vol. 10, no. 1, pp. 1–12, Sep. 2019, doi: 10.1038/s41467-019-12056-1.

[306] C. Molina *et al.*, "Enhanced emission from Eu(III) β-diketone complex combined with ether-type oxygen atoms of di-ureasil organic–inorganic hybrids," *J. Lumin.*, vol. 104, no. 1–2, pp. 93–101, Jun. 2003, doi: 10.1016/S0022-2313(02)00684-1.

[307] M. M. Nolasco *et al.*, "Engineering highly efficient Eu(III)-based tri-ureasil hybrids toward luminescent solar concentrators," *J. Mater. Chem. A*, vol. 1, no. 25, pp. 7339–7350, Jun. 2013, doi: 10.1039/C3TA11463E.

[308] J. Kai, M. C. F. C. Felinto, L. A. O. Nunes, O. L. Malta, and H. F. Brito, "Intermolecular energy transfer and photostability of luminescence-tuneable multicolour PMMA films doped with lanthanide–β-diketonate complexes," *J. Mater. Chem.*, vol. 21, no. 11, pp. 3796–3802, Mar. 2011, doi: 10.1039/C0JM03474F.

[309] M. Fernandes *et al.*, "Highly photostable luminescent poly(ε-caprolactone)siloxane biohybrids doped with europium complexes," *Chem. Mater.*, vol. 19, no. 16, pp. 3892–3901, Aug. 2007, doi: 10.1021/CM062832N/SUPPL_FILE/CM062832NSI20070419_060640.PDF.

[310] C. C. Nshii *et al.*, "A surface-patterned chip as a strong source of ultracold atoms for quantum technologies," *Nat. Nanotechnol. 2013 85*, vol. 8, no. 5, pp. 321–324, Apr. 2013, doi: 10.1038/nnano.2013.47.

[311] L. J. Phillips *et al.*, "Maximizing the optical performance of planar CH3NH3PbI3 hybrid perovskite heterojunction stacks," *Sol. Energy Mater. Sol. Cells*, vol. 147, pp. 327–333, Apr. 2016, doi: 10.1016/J.SOLMAT.2015.10.007.

A

APPENDIX

A.1 Material data

The complex refractive indices (N=n+ik) of the materials considered in FDTD simulations performed in this work were taken from literature databases [19], [175] and are plotted in Figure A1.

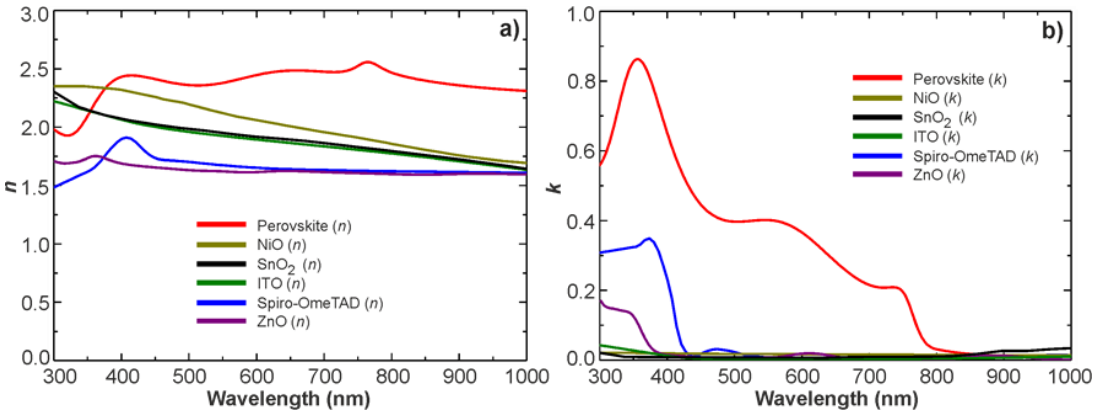

Figure A1: Spectra of the real, n (a), and imaginary, k (b), parts of the complex refractive indices of the materials used in this work.

The perovskite absorber material is taken to be methylammonium lead iodide, $MAPbI_3$, with a widely-used refractive index function fitted from measured values provided by L. J. Phillips *et al.*[175], [311]. However, the measured dataset (n, k) of PSCs are varied with different fabrication conditions and process materials used. Given that, the optical simulations also performed considering a different measured refractive index provided by M. V. Eerden *et al.* [176], in this work.

A.2 Supporting material for optoelectronic modelling

Table A1: Geometrical parameters of the photonic-structured PSCs as sketched in Chapter 5 that allow the maximum photocurrent (J_{PH}) determined by the optical PSO optimizations. The values of the photocurrent gain relative to the reference (planar) PSCs are indicated in brackets. R, Rz and *p* define the geometry of the designed LT structures patterned on the substrates, and the t values represent the thickness of specific layers. These quantities were chosen as variables in the optimization algorithm that iteratively searched for the optimal set of parameters that maximizes the photocurrent produced by the perovskite material.

Light Trapping Structures	**300 nm Perovskite layer**		**500 nm Perovskite layer**	
	Optimal Parameters	J_{PH}, mA/cm² (LT enhancement)	Optimal Parameters	J_{PH}, mA/cm² (LT enhancement)
Superstrate Configuration				
Optimized Planar PSCs with **Au** metal contact	t_{ITO} = 350 nm t_{SnO2} = 25 nm t_{Spiro} = 150 nm t_{Au} = 200 nm	**23.5**	t_{ITO} = 350 nm t_{SnO2} = 25 nm t_{Spiro} = 150 nm t_{Au} = 200 nm	**25.1**
Optimized Structured PSCs with **Au** Metal Contact	t_{ITO} = 350 nm t_{SnO2} = 25 nm t_{Spiro} = 150 nm t_{Au} = 200 nm R = 518.4 nm Rz = 627.4 nm p = 1100.6 nm	**27.2** (15.3%)	t_{ITO} = 350 nm t_{SnO2} = 25 nm t_{Spiro} = 150 nm t_{Au} = 200 nm R = 445.4 nm Rz = 669.7 nm p = 907.3 nm	**30.3** (20.7%)
Optimized Planar PSCs with **Ag** Metal Contact	t_{ITO} = 350 nm t_{SnO2} = 25 nm t_{Spiro} = 150 nm t_{Ag} = 200 nm	**23.6**	t_{ITO} = 350 nm t_{SnO2} = 25 nm t_{Spiro} = 150 nm t_{Ag} = 200 nm	**25.2**
Optimized Structured PSCs with **Ag** Metal Contact	t_{ITO} = 350 nm t_{SnO2} = 25 nm t_{Spiro} = 150 nm t_{Ag} = 200 nm R = 527.1 nm Rz = 627.4 nm p = 1096.8 nm	**27.3** 14.7%	t_{ITO} = 350 nm t_{SnO2} = 25 nm t_{Spiro} = 150 nm t_{Ag} = 200 nm R = 263.0 nm Rz = 655.4 nm p = 526.0 nm	**30.6** (21.4%)
Substrate Configuration				
Optimized Planar PSCs with **Au** Metal Contact	t_{ITO} = 350 nm t_{ZnO} = 100 nm t_{NiO} = 50 nm t_{Ni} = 200 nm	**22.6**	t_{ITO} = 350 nm t_{ZnO} = 100 nm t_{NiO} = 50 nm t_{Ni} = 200 nm	**24.6**

Optmized Structured PSCs with **Au** Metal Contact	t_{ITO} = 350 nm t_{ZnO} = 100 nm t_{NiO} = 10 nm t_{Au} = 200 nm R = 254.2 nm Rz = 662.8 nm p = 508.4 nm	**27.6** (22.1%)	t_{ITO} = 350 nm t_{ZnO} = 100 nm t_{NiO} = 10 nm t_{Au} = 200 nm R = 420.8 nm Rz = 677.1 nm p = 920.2 nm	**28.8** (14.7%)

Subsequently, as described in Chapter 5, three different software packages were used for the electrical simulations: TiberCAD [201], Lumerical-CHARGE [202] and Sentaurus Tcad [203], for the realistic prediction of the PV performance of PSCs. Each solver requires adapting the simulation environment differently, as explained next for each case.

- **TiberCAD**

The transport simulations presented in sub-section 5.3.2.1 employed the drift-diffusion model implemented in the simulation software TiberCAD [201], discretized with FEM and employing a Newton method with line search for the solution of the non-linear equations. The model follows the previously-described formalism, based on the generalized van Roosbroeck equations consisting of a system of partial differential equations, namely the Poisson equation and the continuity equation for each carrier is considered. However, here the Poisson equation determines the electrostatic potential V from the sum of charge densities resulting from all free charged carriers *(n, p)* as well as from ionized donors (N_d^-) and acceptors (N_a^+). The continuity equations describe the transport of carriers included in the system. The carrier fluxes are written in terms of the gradient of quasi-Fermi potentials. Mobilities are assumed to be constant, with values used as fitting parameters. For the recombination terms, we use standard models, in particular bi-molecular (radiative) recombination and trap-assisted (Shockley-Read-Hall, SRH) recombination. The latter can be parameterized via explicitly introducing trap states, or via fixed SRH life times. In our fitting procedure, we used SRH lifetimes to keep the number of parameters small, and because trap density and capture cross-section are highly correlated (only their product enters the lifetime).

Table A2: Parameters used for the electrical simulations in sub-section 5.3.2.1, considering the PSC structure in Chapter 5 with a 300 nm thick perovskite absorber.

Material	Parameters	Value	Unit
Perovskite Absorber	Conduction band minimum	-3.93	eV
	Valence band maximum	-5.53	eV
	Bandgap	1.6	eV
	Effective density of states of the conduction band	$1.5x10^{18}$	cm^{-3}
	Effective density of states of the valence band	$1.8x10^{18}$	cm^{-3}
	Dielectric permittivity (relative)	25	
	Electron mobility	5	$cm^2\ (Vs)^{-1}$
	Hole mobility	10	$cm^2\ (Vs)^{-1}$
	Radiative recombination coefficient	$2x10^{-9}$	$cm^3\ s^{-1}$
	SRH lifetime bulk	$2.0x10^{-7}$	s
Absorber/HTL Interface	Interface recombination parameter, *C*	10^{-19}	$cm^4\ s^{-1}$

In an intermediate step, the optical generation files are read in Matlab and rewritten into an ASCII text file in column format "x y z G", which is read by TiberCAD. Based on the data points, a FEM mesh is generated, on which the data can be interpolated. Then, the transport simulation is performed on the device mesh, taking the generation data on the integration points by interpolation. The implementation is parallelized, which considerably accelerates the 3D simulations. In these simulations, a speedup factor of 11 and 19 has been measured, for 16 and 32 processes, respectively. A critical issue in such coupled simulations is the translation of the generation rate from the optical to the electrical modeling, due to the grid change. For that, to minimize interpolation errors, we accurately matched the optical grid with the electrical grid.

The list of electronic properties that were used is presented in Table A2. Our simulation accounts for two main bulk recombination mechanisms: radiative and SRH, whose profiles along the planar and structured PSCs are shown in Figure A2 and commented in sub-section 5.3.2.1 of Chapter 5. As expected, it can be seen that higher recombination occurs in the regions of higher carrier generation. In addition a bimolecular interface recombination rate at the perovskite/HTL interface is included, given by $R = C \cdot n_{PSK} p_{HTL}$, with parameter *C* given in units of $cm^4\ s^{-1}$, and n_{PSK} and p_{HTL} being the electron and hole densities in the two layers at the interface.

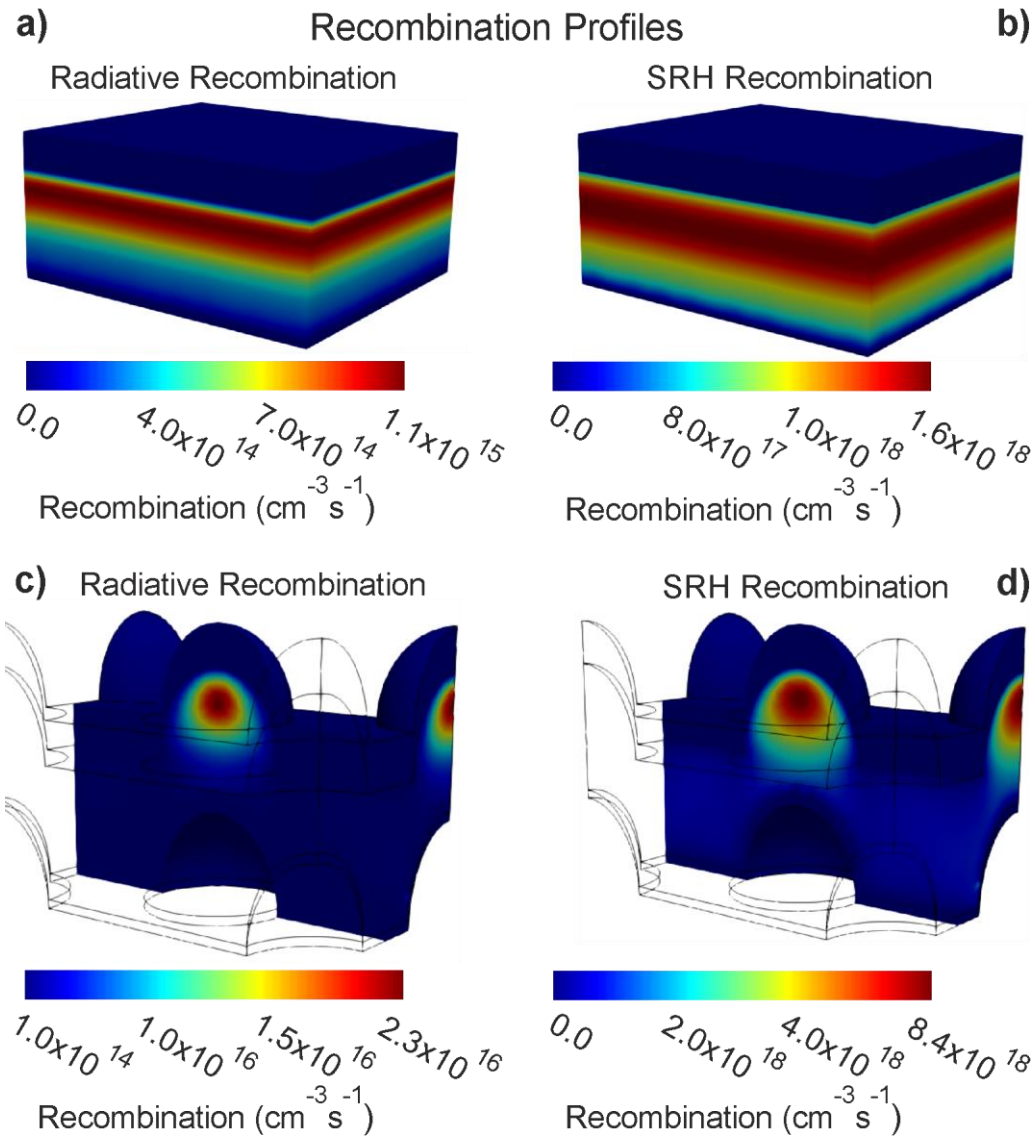

Figure A2: Radiative (a,c) and SRH (b,d) recombination profiles, obtained from the 3D electrical simulations in TiberCAD, for the cases of optimized planar and structured PSCs, respectively, in substrate configuration with perovskite thickness of 300 nm and Au metal contact (see Table A1).

- **<u>Lumerical-CHARGE</u>**

As described in Chapter 5, 1D electrical simulations are sufficient to rigorously model conventional solar cells composed of a flat multi-layered structure, as the reference PSCs without LT features. In such common planar cases, the photo-generation profile varies only along the vertical direction (z axis), but is constant along the in-plane axes (x and y).

Nevertheless, when micro-structuring is applied to create the LT effects, the photo-generation profile varies along the 3 spatial directions. In such cases, the use of 3D simulations would be the most realistic/exact procedure, to avoid spatially averaging the 3D photo-generation profiles in the x and/or y planes. However, 3D simulations require heavy time and

memory costs when performed with the fine meshes used for the accurate FEM electrical modelling of photonic-structured PSCs. To circumvent this without significant loss of computational accuracy, 2D simulation routines were implemented which can be computed within a reasonable time and with the available processing/memory capabilities.

Table A3: Electrical parameters considered for the materials (ITO/SnO_2/PSK/Spiro/Au) composing the planar and LT-enhanced PSCs with the geometrical parameters listed in Table A1 with Au and Ag metal contacts.

	PSK	**SnO_2**	**Spiro$^+$**	**ITO**	**Au**	**Ag**
Intrinsic properties						
dc permittivity	6.5	9.0	3.0			
Φ (eV)	3.93	4.9	3.80	4.50	5.1	4.9
E_g (eV)	1.55	3.7	2.30			
$^{\#}m^*_e$	0.104	1.18	0.05			
$^{\#}m^*_h$	0.104	0.81	1.00			
$^{o}\mu_e$ (cm^2/V s)	30.0	0.2	2.0			
$^{o}\mu_h$ (cm^2/V s)	30.0	0.1	0.001			
$^{X}SRH_h$ (s)	5^{-9}	$5x10^{-9}$	$1x10^{-10}$			
$^{X}SRH_e$ (s)	5^{-9}	$1x10^{-9}$	$1x10^{-10}$			
Doping properties						
Dopant type	*n*	*p*	*p*			
Conc. (cm^{-3})	$7x10^{16}$	$1x10^{12}$	$2x10^{20}$			

The electrical simulations performed in section 5.3.2.2 employed the Lumerical-CHARGE FEM solver [202]. This package receives the photo-generation distribution, *G(x,y,z)*, across the unit cell of the PSCs structure computed in the 3D optical simulations performed with the Lumerical-FDTD solver. The 3D photo-generation is then spatially averaged along the *y* axis to convert it to a 2D distribution, *G(x,z)*, which is imported to the 2D Lumerical-CHARGE program. The FEM calculations are then performed by first applying a 2D coarse mesh (with 30 nm maximum length constraints), and auto-mesh refinements (typically <10 times smaller than the geometrical sizes) across the regions with the highest E-field variations, as those where there are changes in doping density. A boundary condition controlling the bias is set on both Au metal (emitter contact) and TCO (base contact) where a steady-state DC sweep is run from 0.0 to 1.5 V applied voltage (0.025 V interval). Newton's numerical method was used for a self-consistent control of the calculation, iterating between calculating the drift-diffusion equation and using it as an input to solve Poisson's (electrostatic potential) equation, and vice versa. This iteration was carried out until an absolute tolerance $<10^{-6}$ V is reached for convergence. The output containing the spatial information of the electrostatic potential, the electron-hole distribution, recombination rates, and mobility is used to compute the PSC characteristic JV curves. The list of electronic properties used in this simulation is represented in Table A3.

In what concerns the recombination processes, the dominant recombination pathway in PSCs is found to be trap-assisted (SRH), as shown in Figure A2. Therefore, to simplify the simulations and minimize the number of involved parameters to the most fundamental ones, SRH was the only recombination process considered here, while the other two recombination processes (radiative and Auger) were taken to be negligible relative to SRH.

- **Sentaurus Tcad**

The electrical simulations presented in sub-section 5.3.2.3 employed the drift-diffusion model implemented in the commercial semiconductor software Sentaurus Tcad (from Synopsys Inc.) [203]. It is based on solving the drift-diffusion partial differential equations together with the Poisson equation (eqs. S3-5) in spatial dimensions with a finite volume method. Here we considered the list of electronic properties presented in Table A4.

The simulations performed using this tool focused on the interplay of interfaces and spatial distribution of the generation profiles, which is a crucial aspect for structured devices such as those analyzed here (see Chapter 5) patterned with the light-trapping features. To this end, we created 2D, planar 3D (Cuboid) and 3D-structures representing the superstrate configuration with Au contacts. A decisive question addressed here is whether a 3D-structure really requires a complete 3-D electrical simulation (with its corresponding CPU and Memory demand) or whether 1- or 2-D electrical simulations based on homogenized optical data could lead to very similar results, thus reducing the computational effort significantly.

To work on the 3D structure, the simulation flow had to be adapted to be able to synthesize the discrete topography from the provided geometric descriptions (see Table A1) and to integrate the provided 3D-generation data [$G(x,y,z)$, see Chapter 5]. Especially the integration of the optical generation data proved challenging to align correctly. As the generation data was provided in a cubic voxel grid, but the geometric structure is continuous, simple overlaying would lead to aliasing effects at the interfaces, reducing the generated current. To counteract this problem, the generation data was pre-processed to constantly extrapolate the generation values at the interfaces outwards, to later intersect the data with the continuous geometric structure (see Figure A3).

The aliasing effects also play a role in the vertex-centered simulation mesh. Specifically, the discontinuous generation profile leads to problems of current over-accounting at the interfaces. The 1D simulations can be executed with a mesh resolution of 1000 steps per nanometer which does not lead to measurable over-accounting. However, this resolution cannot be maintained for the present 3D-simulations, in which the mesh resolution drops to 1 step per every 2 nanometers at the interfaces and 1 step every 20 nanometers in the bulk.

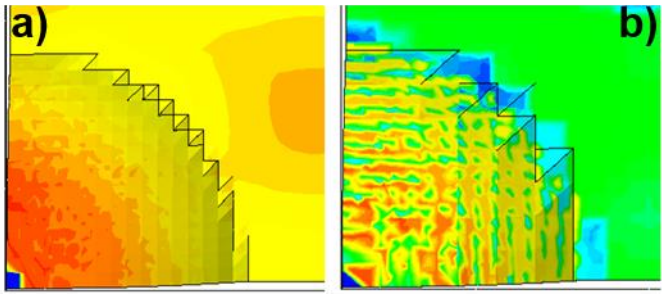

Figure A3: Impact of extrapolation on the interface generation rate (*G*). *a)* - with extrapolated generation. *b)* - without extrapolated data.

The resolution of the discretized mesh was increased until the numerical integration of the generation rate J_{PH} converged. This provided a sufficiently accurate spatially resolved representation of the generation data provided by the optical simulations (see Chapter 5) while keeping the required computational effort to run the simulations manageable. To focus on the effect of the interfaces between the absorber and HTL / ETL, the physical parameters were chosen such as to minimize effects due to other factors impacting the device performance, e.g. band energy mismatch or low mobility in the ETL. Outside the perovskite layer, the device can be considered idealized, except for a serial resistance of 3.3 $m\Omega cm^{-2}$.

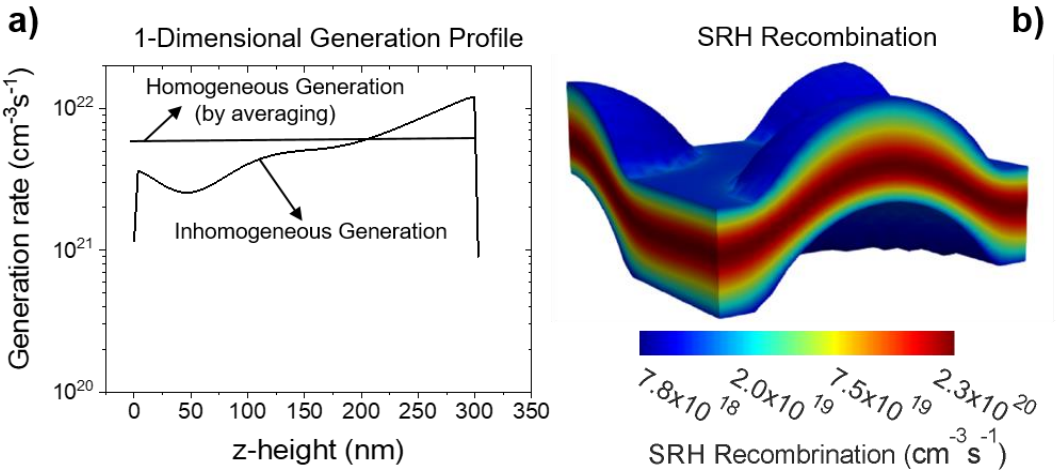

Figure A4: The normalized 1D generation profiles (a) across the absorber thickness, as well as the SRH recombination profile (b) at the maximum power point obtained in Sentaurus Tcad electrical modelling.

Figure A4,a shows an example of the normalized 1D generation profiles of the inhomogeneous and homogeneous (averaged constant field) generation functions that were created from the 3D-optically computed *G(x,y,z)* data, by first planarizing the 3D generation profile, *G*, and then integrating along the in-plane directions *(x,y)*. Such profiles were used for the 1D electrical simulations in Sentaurus Tcad in sub-section 5.3.2.3 of Chapter 5. Figure A4,b depicts the cross-section of the SRH recombination profile across the perovskite absorber, and in the

HTL/ETL interface surfaces, resulting from the 3D electrical simulations in Sentaurus Tcad in sub-section 5.3.2.3.

Table A4: Parameters used for the electrical simulations in sub-section 5.3.2.3, considering the PSC structure of Chapter 5 with a 300 nm thick perovskite absorber.

Material	Parameters	Value	Unit
Perovskite Absorber	Conduction band minimum	-4.0	eV
	Valence band maximum	-5.6	eV
	Bandgap	1.6	eV
	Effective density of states of conduction band	$5x10^{18}$	cm^{-3}
	Effective density of states of valence band	$5x10^{18}$	cm^{-3}
	Dielectric permittivity (relative)	25	
	Electron mobility	10	$cm^2 (Vs)^{-1}$
	Hole mobility	10	$cm^2 (Vs)^{-1}$
	Radiative recombination coefficient	10^{-11}	$cm^3 s^{-1}$
	SRH lifetime bulk	$2.5x10^{-7}$	s
Absorber/HTL or ETL Interface	SRH surface recombination velocity, S_0	140	$cm\ s^{-1}$

A.3 Fast Fourier Transform analysis

The Fourier-series of a surface structure is based on its aperture function, defined as a binary matrix A whose non-zero elements (alias apertures) are 1. If one pixel stands for a 5 nm width in real space, A contains as many copies of the unitcell-array in its rows and columns as necessary to span an area of ca. 500 µm². After a fast Fourier transform of $e^{i\pi A}$, the Fourier-components are found by shifting the zero-frequency to the center of the array. For instance, the following FFT profile of modulated grating lines by 60-degree rotation is shown in Figure A5.

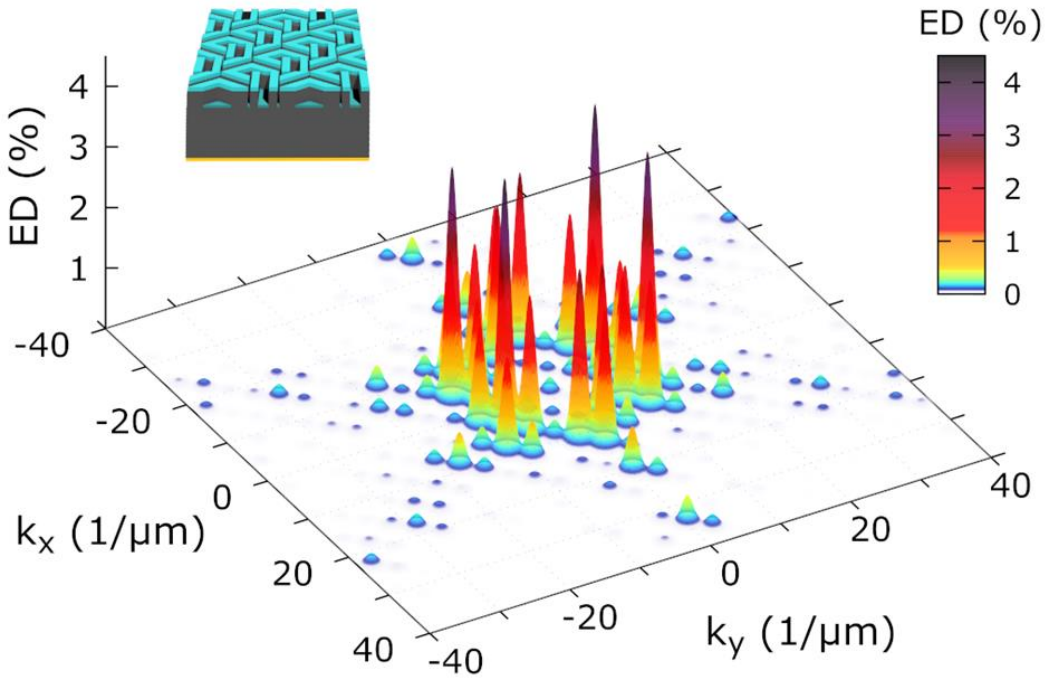

Figure A5: Modulating grating lines not by a 90-degree rotation, as the checkerboard pattern in Chapter 6, but by a 60-degree rotation yields a star-like diffraction pattern. Here, the optimised parameters of the checkerboard pattern are adopted: 242 nm line width, 575 nm grating period and 925 nm domain length; the unit cell thus has a size of 2.775 x 2.775 µm². The increase in surface area is 85% with respect to the flat 1 µm c-Si reference slab. The short-circuit currents are 5.37 mA/cm² for the surface structure and 22.81 mA/cm² for the bulk layer, generated by carriers within and beyond 190 nm depth, respectively.

The following two tables were used to identify four criteria that correlate with current gains for CB pattern in thin film silicon solar cells (see Chapter 6).

Table A5: The Fourier-series of a surface structure defines a diffraction pattern in k-space. Here, the energy distribution *(ED)* quantifies the components' contribution to the total diffracted energy. We list the contribution by the strong components as ED_{strong} and the contribution of the inner k-region as $ED_{\text{k<21/µm}}$ with $k = \sqrt{k_x^2 + k_y^2}$. A strong component contains at least 15% of the global peak value. The surface area factor (*SAF*) quantifies the increase in surface area compared to the unstructured slab while respecting the periodic boundary conditions. The bulk- and surface-current refer to the carriers generated only beyond and within the etching depth d of a textured crystalline silicon slab with 1 µm total thickness, respectively. The X-factor is given by Eq. 6.

	*peak height		*surface area factor			- - - - - - - - mA/cm² - - - - - - - -		
Name	**# strong components**	**ED_{strong}**	**$ED_{k<21}$**	**SAF***	**X**	**bulk**	**surface**	**total**
	≥15% PH*	strong only	∀k < 21	factor	factor	d > 190nm	d < 190nm	1 µm
Planar Ref					0.98	10.10	4.63	14.73
2D-0.96	1	0.992	0.993	1.053	1.00	10.20	4.70	14.90
2D-0.92	1	0.970	0.972	1.106	1.01	10.25	4.72	14.98
2D-0.88	1	0.942	0.948	1.159	1.01	10.47	4.78	15.25
2D-0.84	1	0.894	0.915	1.211	1.03	10.83	4.90	15.74
2D-0.80	1	0.846	0.888	1.264	1.06	10.31	6.03	16.35
1D-0.04	1	0.834	0.849	1.661	1.08	14.86	0.58	15.44
1D-0.96	1	0.834	0.849	1.661	1.08	11.85	5.14	16.99
2D-0.76	1	0.777	0.861	1.317	1.10	11.83	5.17	17.00
1D-0.08	1	0.682	0.741	1.661	1.12	14.95	1.05	16.00
1D-0.92	1	0.682	0.741	1.661	1.12	12.84	5.34	18.18
2D-0.72	1	0.714	0.845	1.370	1.16	12.51	5.33	17.84
2D-0.04	1	0.689	0.716	2.269	1.16	16.16	1.17	17.33
1D-0.12	1	0.572	0.685	1.661	1.17	14.96	1.84	16.80
1D-0.88	1	0.572	0.685	1.661	1.17	13.55	5.61	19.16
PhC_a300_0.1	1	0.896	0.901	2.791	1.19	10.57	4.83	15.41
2D-0.08	1	0.445	0.545	2.216	1.24	16.52	2.02	18.55
2D-0.68	1	0.629	0.834	1.423	1.25	13.30	5.57	18.86
1D-0.48	2	0.807	0.809	1.661	1.26	15.98	3.99	19.96
1D-0.52	2	0.807	0.809	1.661	1.26	15.76	4.40	20.16
1D-0.44	2	0.785	0.798	1.661	1.28	15.80	3.92	19.72
1D-0.56	2	0.785	0.798	1.661	1.28	14.70	5.61	20.31
1D-0.42	2	0.757	0.785	1.661	1.29	15.95	3.57	19.52
PhC_a300_0.2	1	0.605	0.674	3.228	1.29	12.44	5.53	17.97
1D-0.24	5	0.854	0.652	1.661	1.30	15.51	2.70	18.21
1D-0.76	5	0.854	0.652	1.661	1.30	15.29	5.43	20.72
1D-0.28	5	0.870	0.674	1.661	1.30	15.34	2.97	18.32
1D-0.72	5	0.870	0.674	1.661	1.30	15.71	5.45	21.16
PhC_a300_0.4	4	0.624	0.312	4.276	1.30	14.83	5.76	20.59
1D-0.40	2	0.733	0.773	1.661	1.31	15.52	3.92	19.45
1D-0.60	2	0.733	0.773	1.661	1.31	15.76	4.78	20.54
1D-0.20	5	0.824	0.640	1.661	1.33	15.90	2.33	18.23
1D-0.80	5	0.824	0.640	1.661	1.33	14.81	5.45	20.27
1D-0.32	5	0.873	0.709	1.661	1.33	15.73	3.13	18.86
1D-0.68	5	0.873	0.709	1.661	1.33	15.86	5.24	21.10
2D-0.64	1	0.538	0.831	1.476	1.35	14.10	5.69	19.79
1D-0.16	5	0.798	0.648	1.661	1.36	15.71	2.18	17.89
1D-0.84	5	0.798	0.648	1.661	1.36	14.37	5.55	19.93
2D-0.12	1	0.295	0.472	2.163	1.38	17.20	3.50	20.69
1D-0.36	5	0.860	0.747	1.661	1.39	15.95	3.27	19.21

1D-0.64	5	0.860	0.747	1.661	1.39	15.77	5.02	20.79
2D-0.60	1	0.462	0.832	1.529	1.45	15.20	5.91	21.11
QR32_E8-E12	174	0.477	0.033	3.884	1.47	18.23	6.44	24.67
PhC_a300_0.3	9	0.824	0.442	3.752	1.47	13.79	5.85	19.64
2D-0.16	13	0.769	0.443	2.110	1.50	18.94	3.98	22.92
2D-0.20	13	0.776	0.457	2.057	1.50	19.43	4.23	23.66
2D-0.24	9	0.698	0.504	2.005	1.52	18.86	4.76	23.62
2D-0.28	8	0.702	0.556	1.952	1.53	18.87	5.15	24.02
QR32_E6-Einfi	560	0.535	0.020	4.756	1.55	16.50	6.45	22.94
PhC_a300_0.5	5	0.615	0.444	4.713	1.56	13.51	6.60	20.11
2D-0.32	12	0.771	0.627	1.899	1.62	19.39	5.45	24.84
2D-0.56	5	0.677	0.831	1.582	1.64	16.33	6.12	22.45
2D-0.48	9	0.810	0.810	1.687	1.65	18.44	6.14	24.58
2D-0.52	5	0.664	0.826	1.634	1.65	17.52	6.19	23.71
2D-0.44	9	0.786	0.786	1.740	1.65	18.78	6.27	25.05
2D-0.42	9	0.761	0.761	1.765	1.65	19.31	5.91	25.22
2D-0.40	9	0.741	0.741	1.793	1.66	18.69	6.28	24.96
2D-0.36	13	0.786	0.694	1.846	1.66	19.43	5.61	25.04
Spiral	17	0.610	0.387	2.993	1.68	19.50	5.03	24.54
QR-inverse	236	0.551	0.087	3.634	1.76	18.40	6.32	24.72
CBx2-0.54	17	0.735	0.769	1.822	1.78	20.83	6.15	26.98
CBx2-0.57	17	0.763	0.802	1.822	1.78	19.86	6.23	26.09
CBx2-0.51	21	0.765	0.754	1.822	1.78	21.52	6.17	27.69
CBx2-0.48	21	0.748	0.748	1.822	1.79	22.18	6.04	28.22
CBx2-0.60	5	0.452	0.861	1.514	1.79	18.61	6.09	24.70
CBx2-0.45	25	0.762	0.753	1.822	1.80	22.44	5.95	28.39
CBx2-0.42	24	0.751	0.763	1.823	1.81	22.66	5.76	28.42
CBx2-0.39	22	0.734	0.771	1.823	1.81	22.91	5.38	28.29
CBx2-0.36	23	0.747	0.783	1.822	1.81	22.86	5.21	28.07
CBx2-0.30	23	0.740	0.780	1.822	1.81	22.73	4.57	27.30
CBx2-0.33	23	0.744	0.784	1.822	1.81	22.94	4.87	27.81
QR8b-V	13	0.554	0.822	1.716	1.84	22.29	4.18	26.47
QR32_E0-E3_Real	29	0.719	0.785	1.914	1.85	21.50	4.64	26.14
CBx3	24	0.603	0.742	1.850	1.85	22.81	5.37	28.18
QR32_E3-Einfi	514	0.500	0.085	4.529	1.87	19.01	6.88	25.89
QR8b	58	0.632	0.667	2.219	1.90	21.83	6.86	28.70
QR8b-VI	47	0.605	0.751	1.861	1.90	22.16	6.18	28.34
QR32b	128	0.640	0.473	2.925	1.91	22.85	6.67	29.52
QR32_E0-E7a	131	0.676	0.559	2.502	1.92	23.03	6.18	29.21
QR32_E0-E7b	137	0.682	0.569	2.479	1.92	22.78	6.17	28.95
QR32_E0-E6	119	0.668	0.640	2.503	1.93	22.98	6.00	28.97
QR54-Random	967	0.447	0.097	4.472	1.93	19.33	6.71	26.04
L Limit					2.24	23.28	10.38	33.65

Table A6: The correlation coefficient R between X (Eq. 1) and the FDTD-calculated J_{tot}/J_{ref} of 83 different structures is greater than 0.96 for all n<21 and k^*<22. The #-marked columns also include five additional photonic crystal structures with a square unit cell size of 300 nm only.

Correlation Matrix for q = √2 and p = √3.5

n \ k*	16	17	18	19	20	21	22	23	24	21#	22#	23#	24#	k* / n
10	0.9607	0.9604	0.9646	0.9663	0.9667	**0.9696**	0.9416	0.9421	0.9418	**0.9639**	0.9260	0.9271	0.9272	10
11	0.9589	0.9586	0.9627	0.9644	0.9648	**0.9678**	0.9380	0.9385	0.9382	**0.9618**	0.9221	0.9232	0.9232	11
12	0.9579	0.9576	0.9617	0.9635	0.9639	**0.9669**	0.9368	0.9373	0.9370	**0.9608**	0.9234	0.9245	0.9245	12
13	0.9611	0.9607	0.9647	0.9664	0.9668	**0.9698**	0.9387	0.9391	0.9388	**0.9633**	0.9249	0.9259	0.9259	13
14	0.9608	0.9605	0.9645	0.9661	0.9665	**0.9695**	0.9389	0.9393	0.9390	**0.9630**	0.9250	0.9260	0.9260	14
15	**0.9640**	**0.9636**	**0.9674**	**0.9690**	**0.9693**	**0.9721**	**0.9427**	**0.9430**	**0.9426**	**0.9653**	**0.9284**	**0.9293**	**0.9292**	**15**
16	0.9638	0.9635	0.9673	0.9688	0.9691	**0.9719**	0.9426	0.9429	0.9425	**0.9651**	0.9282	0.9291	0.9291	16
17	0.9634	0.9631	0.9669	0.9685	0.9687	**0.9715**	0.9421	0.9424	0.9420	**0.9648**	0.9277	0.9286	0.9286	17
18	0.9634	0.9630	0.9668	0.9684	0.9687	**0.9715**	0.9420	0.9423	0.9419	**0.9649**	0.9278	0.9287	0.9287	18
19	0.9631	0.9628	0.9666	0.9682	0.9684	**0.9713**	0.9420	0.9423	0.9419	**0.9647**	0.9279	0.9288	0.9287	19
20	0.9629	0.9625	0.9663	0.9679	0.9682	**0.9710**	0.9419	0.9422	0.9418	**0.9645**	0.9278	0.9287	0.9287	20

2022

SIRAZUL HAQUE

LIGHT MANAGEMENT IN PEROVSKITE SOLAR CELLS WITH PHOTONIC STRUCTURES AND LUMINESCENT DOWN-SHIFTING LAYERS